Characterisation of Local Mechanical Properties in Living Tissues

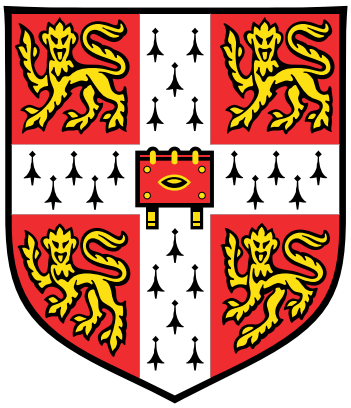

Qian Cheng

Department of Engineering
University of Cambridge

This dissertation is submitted for the degree of
Doctor of Philosophy

Emmanuel College

May 2017

According to Philip Stanhope, 4th Earl of Chesterfield:
"Whatever is worth doing is worth doing well."

Declaration

I hereby declare that except where specific reference is made to the work of others, the contents of this dissertation are original and have not been submitted in whole or in part for consideration for any other degree or qualification in this, or any other university. This dissertation is my own work and contains nothing which is the outcome of work done in collaboration with others, except as specified in the text and Acknowledgements. It is an account of work undertaken under the supervision of Dr Alexandre Kabla in the Department of Engineering between October 2013 and December 2016. This thesis contains fewer than 65,000 words including references, footnotes, tables, captions and equations and has fewer than 150 figures.

All animal work was approved by Local Ethical Review Committee at the University of Cambridge and performed according to the protocols of UK Home Office license PPL 80/2198.

Qian Cheng
May 2017

Acknowledgements

First and foremost I would like to express my special appreciation and thanks to my supervisor Dr Alexandre Kabla, you have been a tremendous mentor for me. You have been providing me with a definite direction, professional guidance, and constant encouragement from the beginning of my PhD study. I cannot forget every moment when I was down and you encouraged and inspired me. I would like to thank you for all your contributions of time and ideas. I'm also thankful for his support in the application for PhD studentship. I am thankful to the Engineering and Physical Sciences Research Council (EPSRC) UK for funding my research, making it possible for me to pursue a doctoral degree at Cambridge.

I am immensely thankful to Dr Richard Adams, Dr Thierry Savin and Dr Julien Dumortier for their helpful discussions and suggestions which lead to the betterment of work. Thanks go to Dr Radu Tanasa for his input and recommendations during the development of the magnetic tweezers and his patience in discussions on various topics. I am also grateful to my examiners, Dr Michael Sutcliffe and Dr Alexander Fletcher, for their thorough reading of my thesis, their valuable comments and an enjoyable viva examination.

Additionally, the English teachers at the Language Unit of the Department of Engineering: Denise Chappell, Nicola Cavaleri and Sheila Dodds deserve my thanks for the support on academic writing and speaking.

A special thanks to my family and friends. Words cannot express how grateful I am to my beloved parents, Hongbin and Lixia, my dearest buddy Songyin, my sister Wei and brother-in-law Hao, my sister Bai, and my closest friends, Xiao, Jiyao, Kaiou, Yangting, Linqing, Difan, Wen and Tianpeng, for their priceless love and continuous support during the most difficult time. I also thank my lab mates within Alex's research group, Joel Jennings, Pierre Recho, Adrien Hallou, Nishit Srivastava, Fergus Riche and Victoire Cachoux, and the collaborators, Aleksander Chmielewski and Tom Wyatt, for providing both on- and off-topic discussions. Thanks to my friends at Cambridge, Longzhu, Bo, Xiong, Yushuang

and Mingfei, for listening, offering me advice, and supporting me.

This journey would not have been possible without the support of all of you.

March 2017, Cambridge, United Kingdom.

Qian Cheng

Abstract

The process of a single cell evolving into a complex organism results from a series of coordinated movements of cells and tissues, especially during early embryo development. Although a wealth of morphological data characterises the shapes and movements of cells in embryos, how these movements are driven, patterned and controlled, and how this patterning is related to the mechanical properties of tissues remains unknown.

Four-pole electromagnetic tweezers have been developed to probe the mechanical properties of living embryonic tissues that are undergoing active morphogenetic development. The device is capable of generating magnetic forces in the order of nano-Newtons on a grafted magnetic bead. The local passive mechanical properties of the tissues can be characterised by measuring the three-dimensional bead movement and analysing cell shape changes and cell rearrangement in response to this externally applied force.

The magnetic device is used to probe the rheology in early zebrafish embryos between high stage (3.3 hpf) and the onset of gastrulation (5.3 hpf) when rapid cell cycles give way to a hollow sphere of cells. The tissue response to the applied force is modelled as linear viscoelastic. The embryo becomes stiffer and more viscous during this period of development, showing that a loose collection of cells becomes cohesive tissues.

A computational model is used to explore how cells respond to local or global mechanical perturbations in two systems. First, the model simulates the movement of the bead within an embryo, and the results illustrate the generation, patterning and relaxation of the local cell stress around the bead. Second, the model reproduces the autonomous changes in mitotic cells within a stretched monolayer, and the results show that propensity of cells to divide along their long axis facilitates stress relaxation and contributes to tissue homoeostasis.

Table of contents

List of figures

List of tables

List of Abbreviations

1D	One-dimensional
2D	Two-dimensional
3D	Three-dimensional
ABS	Acrylonitrile Butadiene Styrene
AFM	Atomic Force Microscopy
ANP	Anterior Neural Plate
AP	Animal Pole
CAM	Cell Adhesion Molecule
ECM	Extracellular Matrix
EPC	Electromagnetic Pulling Cytometry
ETC	Electromagnetic Twisting Cytometry
EVL	Enveloping Layer
FEP	Fluorinated Ethylene Propylene
GP	Gaussian Process
hpf	hours post fertilisation
LSFM	Light Sheet Fluorescent Microscopy
MAPE	Mean Absolute Percentage Error
MDCK	Madin-Darby Canine Kidney II

MMF	Magnetomotive Force
NS	Non Stretched (monolayer)
PDE	Partial Differential Equation
S	Stretched (monolayer)
SD	Standard Deviation
SPIM	Selective Plane Illumination Microscopy
TCJ	Tricellular Junctions
VP	Vegetal Pole
WT	Wild Type

Chapter 1

Introduction

1.1 Morphogenesis

An animal organism is developed from a single fertilised egg. This development starts from a zygote undergoing division and differentiation, and this process involves coordinated control and action of hundreds to thousands of cells. Figure 1.1 shows the development of animal embryos from fertilisation to a developed organism, through a series of cell divisions, cell growth, and cell migration. The formation of the organism is controlled by the embryo both spatially and temporally. The cellular behaviour and the underlying mechanisms during this complex development are yet to be unravelled.

Morphogenesis is the biological process that causes an organism to develop its shape and controls cell growth and cellular differentiation. During embryo development, cell–cell interactions determine the fabric of the tissue and in consequence determine the mechanical properties of tissues. At the tissue scale, a biological tissue is a collection of interconnected cells that perform a similar function within an organism. Local tissue displacement and deformation are driven by local and distant forces acting through tissues [23, 86]. We propose a hypothesis that force imbalances induced by differences in the mechanical properties of tissues are responsible for these morphogenetic movements in the embryo. In the thesis, we are interested in how cells within the tissue move and change shape, how forces are generated, directed and patterned to guide these cell movements, how the cellular mechanical properties change during development, and how cells respond to local or global mechanical perturbations. Before examining these questions, we first look at the properties of cells and the cell division cycle.

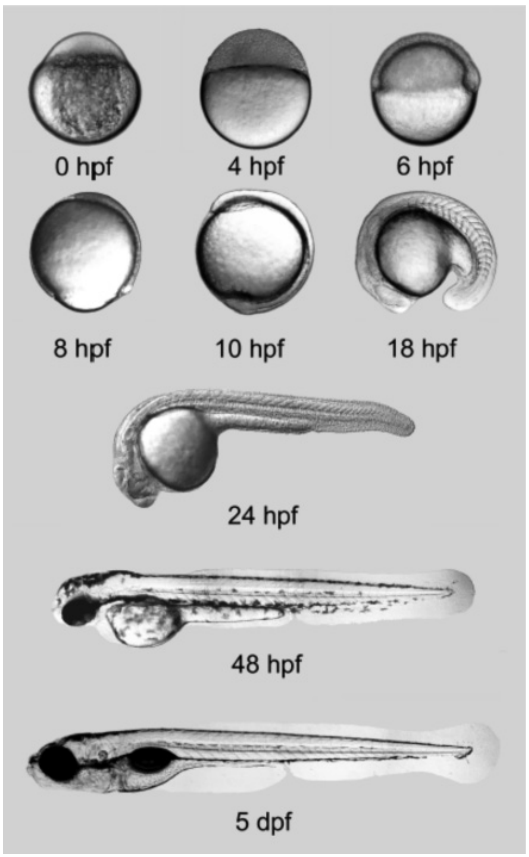

(A)

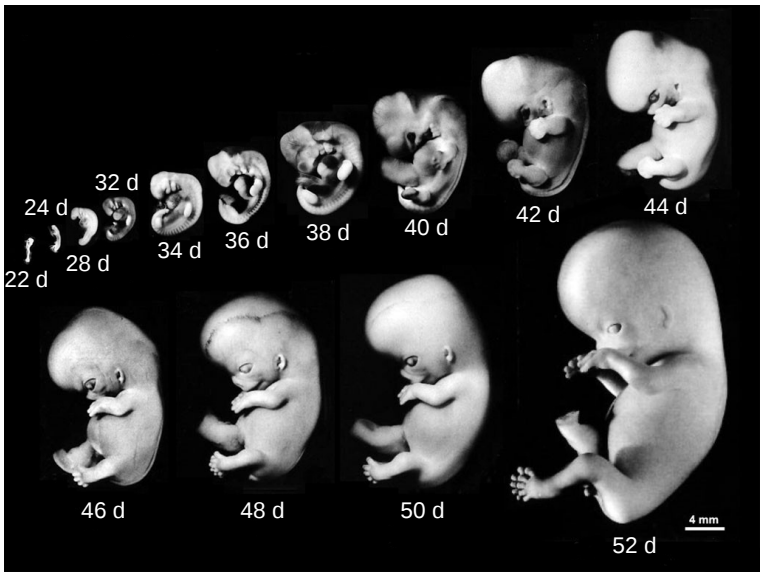

(B)

Fig. 1.1 Images of developing animal embryos. (A) A developing zebrafish embryo from fertilisation to a larva. The image is taken from Lin [58]. (B) A developing human embryo from 22 days to 52 days after fertilisation. Scale bar: 4 mm. The image is taken from Shigehito Yamada [88].

1.2 The Cell

The cell is the fundamental structural, functional and biological unit that is responsible for all the processes of life in all known living organisms. Animal tissue is an ensemble of eukaryote cells [70]. Hence, the study of tissue properties requires an understanding of cellular functions and behaviours. The following discussion introduces the cellular properties which are of interest to this study and is guided by O'Connor et al. [70], Alberts et al. [1], Boal and Boal [11] and Lodish et al. [59].

1.2.1 Components of a Cell

Figure 1.2 illustrates the internal structure of most eukaryotic cells. Cells are surrounded by the cell membrane or the plasma membrane, which provides a clear boundary between the cell's internal and external environments. The nucleus, other organelles and subcellular structures that perform specialised functions are surrounded by cytoplasm within the cell membrane. The nucleus plays the most prominent role in a eukaryotic cell. It is separated from the cytoplasm by two concentric membranes that form the nuclear envelope, and it contains molecules of DNA which store the genetic information of the organism. This DNA contains the instructions for how to create each protein in the cell. Proteins provide the cell with shape and structure, and they constitute most of the cell's dry mass. Some long, fine protein filaments, which form an intricate network that extends throughout the cytoplasm, determine the mechanical properties of the cells. This system of filaments is called the cytoskeleton.

1.2.2 Cytoskeleton

Cells acquire their shape from their internal structure, the cytoskeleton. The cytoskeleton is a highly dynamic structure which maintains cell shape, and drives cell motions, inter-cellular transport and cell division. It is composed of three types of protein filaments: intermediate filaments, microtubules, and actin filaments, each of which has different protein subunits and distinct mechanical properties. These protein filaments together control the shape and the mechanical properties of the cell.

Intermediate filaments are rope-like fibres made of long, twisted strands of protein, with a diameter of $\sim$ 10 nm (Figure 1.3 (A)). They are the toughest of the three types of cytoskeletal filament and have the greatest tensile strength. They play a role in enabling cells to withstand the mechanical stress when cells are subjected to stretch. In addition, they bind to the

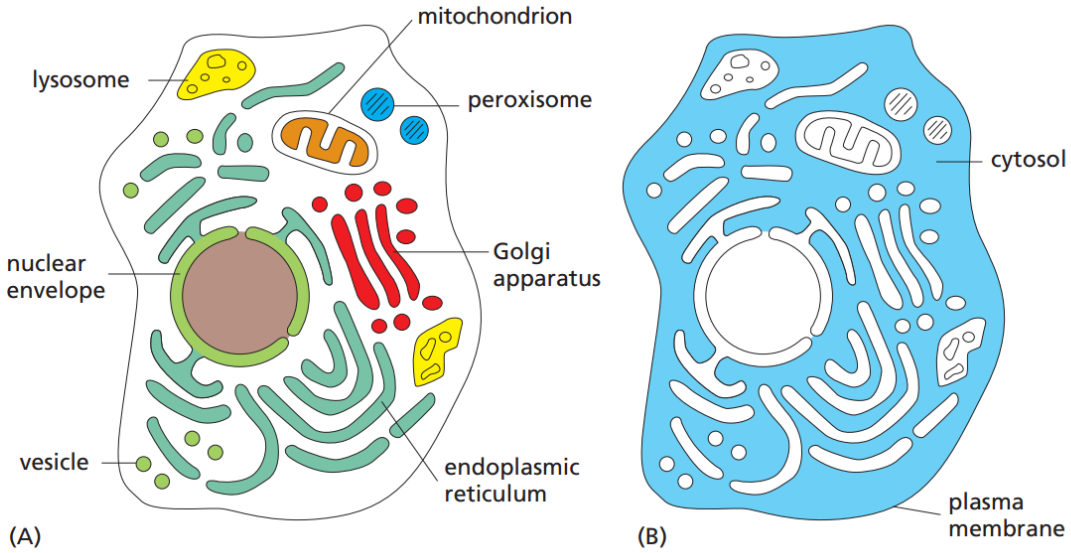

Fig. 1.2 An illustration of the internal structure of a typical animal cell. Membrane-enclosed organelles are distributed throughout the cytoplasm. (A) The organelles are labelled. (B) The cytosol is coloured in blue. The figure is adapted from Alberts et al. [1].

desmosomes, which are the proteins in the cell membrane forming the cell–cell junctions that connect cells. Different types of intermediate filaments can be found in different types of cells, for example, keratin filaments are found in epithelial cells, neurofilaments in nerve cells, and nuclear lamins, which strengthen the nuclear membrane, are found in all animal cells.

Microtubules are long and relatively rigid hollow cylinders of protein which are able to fast disassemble in one location and reassemble in another (Figure 1.3 (B)). The subunit in microtubules is the repeating protein tubulin. They grow out from the centrosome which is close to the centre of the cell. They have an outer diameter of 25 nm and are responsible for controlling the movement of organelles and other cell components, and guiding intracellular transport. During cell mitosis, the cytoplasmic microtubules disassemble and then form the mitotic spindle, which segregates the chromosomes equally into the two daughter cells.

Actin filaments are the thinnest of these filaments and are hence known as microfilaments (Figure 1.3 (C)). They are two-stranded helical polymers of the protein actin, with a diameter of 5–9 nm, and form a variety of linear bundles and networks, which are more rigid than the individual filaments. As they are flexible, actin filaments can bind to other proteins to form stable structures in cells and have different mechanical properties. Actin associates with the protein myosin, and binds to and hydrolyzes ATP to form contractile bundles, which are essential for cells crawling along the contact surface. Cells are able to apply stresses to

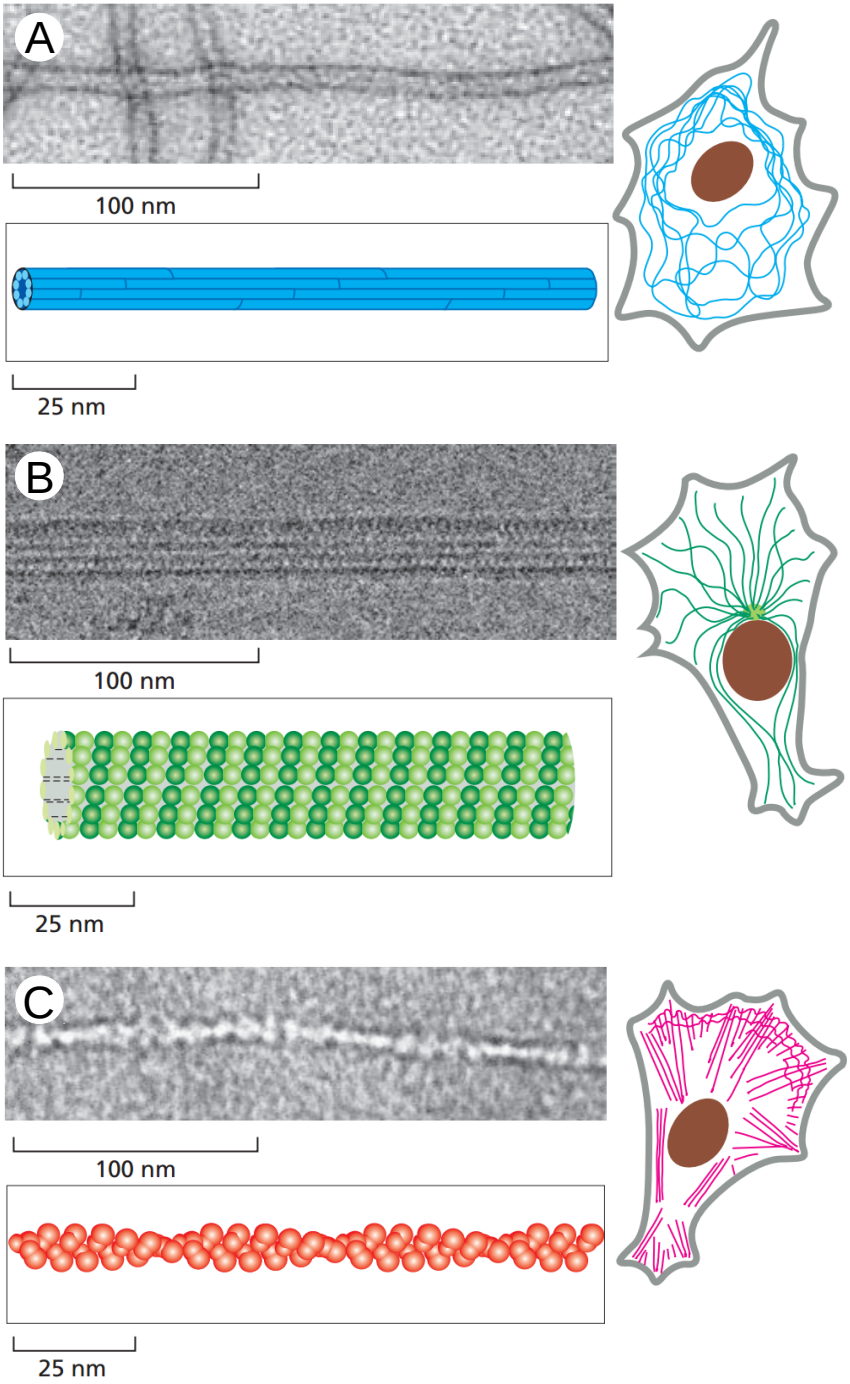

Fig. 1.3 An illustration of the three major types of protein filaments. (A) Intermediate filaments. (B) Microtubules. (C) Actin filaments. The figure is adapted from Alberts et al. [1].

neighbouring cells and/or the substrate by protrusive activities. For example, the lamellipodia attach to other cells or the substrate and allow the cell to apply a force, such as extension, binding and subsequent pulling by using myosin motors [50, 104].

In addition to the cytoplasm, a high concentration of actin is found in a layer just beneath the plasma membrane, which is known as the cell cortex. In this region, actin filaments are associated with actin-binding proteins, forming a meshwork that supports the outer surface of the cell to give it mechanical strength. This cortical actin mesh governs the shape and mechanical properties of the plasma membrane and the cell surface. The rearrangement of actin filaments within the cortex provides the molecular basis for changes in cell shape and cell motion.

1.2.3 Cell Adhesions

Cells tend to adhere to things that they come into contact with, for instance, other cells and extracellular matrix (ECM). Cellular adhesion is responsible for maintaining multicellular structure. Cells stick to other cells by employing specific cell adhesion molecules (CAMs) on their surfaces. The extracellular matrix, which is secreted by cells themselves, is also involved in assembling cells to construct biological tissue. Stress can be transmitted by cell–cell adhesive junctions to other cells or by cell–matrix adhesive junctions to the substrate. These cell adhesion proteins not only hold cells together to construct biological tissue, but also play important roles in cell–cell and cell–environment biochemical signalling [2].

As different types of cells have different cadherins (calcium-dependent adhesion proteins) and other adhesion molecules in their plasma membranes, cell adhesion is selective by homophilic binding to other cells of the same type. They may also form selective attachments to certain other cell types or to specific extracellular matrix components. Selective cell adhesion ensures that cell types are not chaotically mixed within a tissue.

1.2.4 Cell Motility

Cell motility is defined as cell migration along a surface or through a tissue by consumption of energy. For example, cells move from one location to another in an embryo during embryonic development [1, 17].

Cell migration can be realised by the protrusive behaviour of cells. Cells are able to apply forces to neighbouring cells and/or the substrate, such as extension, binding and subsequent pulling. These movements are mediated by the cytoskeleton and are powered by molecular motors that move along the cytoskeleton. This mechanism is used for most forms of intra-

cellular movement [50, 104]. Moving cells are able to migrate in a specific direction, in response to an external signal such as the signalling molecules. Cells sense the concentration of the chemical and move in the direction of increasing concentration of the signal. This directional movement is responsible for much of the cell migration during tissue formation [1, 17].

These proteins within the cell form the structure of the cell, and consequently the mechanical properties of cells. Next we discuss cell division, the essential mechanism by which all living things reproduce.

1.2.5 The Cell Division Cycle

The development of an organism results from the growth of cells, and from spatially and temporally organised cell divisions. A cell reproduces by duplicating its contents and then dividing into two daughter cells. This cycle of duplication and division is called the cell cycle. The key function of the cell cycle is to duplicate accurately the genetic information in DNA in the chromosomes and then distribute the copies into genetically identical daughter cells. A typical eukaryote cell cycle consists of four phases, beginning at the start of one cell division and ending at the start of another. They are the M phase, the S phase, the G_1 phase and the G_2 phase, as shown in Figure 1.4.

Mitosis is the process whereby the cell nucleus is replicated and divided into two identical nuclei containing genetically identical material. Mitosis comprises four main phases: prophase, metaphase, anaphase and telophase. Metaphase is when the chromosomes are lined up along the plate, and anaphase is when the centromere of each chromosome is pulled apart by spindle fibres [21, 47, 94].

Following mitosis is the cytokinesis phase, when the cell's cytoplasm divides into two, creating two daughter cells. Each of the daughter cells receives one of the new nuclei, genetically identical to the parent cell [21, 47]. Mitosis and cytokinesis together constitute the **M phase** of the cell cycle. For a typical mammalian cell, the time duration of the M phase is about an hour, which is only a small fraction of the total time for the whole cell cycle.

Interphase is for cell growth and division preparation, and it is the period between one M phase and the next. It is the longest phase (about 90% of the time) in the cell cycle, and is made up of three stages. The **S Phase** (S = synthesis) is when the cell is committed to division, and chromosomes including DNA begin to replicate in the nucleus. This replication

produces two sets of DNA which will be divided between the new daughter cells. The *S* phase takes place in between two phases in which the cell continues to increase in size. The **G_1 Phase** (G = gap) is the intermediate phase between the completion of the *M* phase and the beginning of the *S* phase. During this period, the cell grows and develops. No division takes place. The **G_2 phase** lies between the end of the *S* phase and the beginning of the *M* phase. Organelles and other materials required for cell division are replicated or formed during the G_2 phase [94].

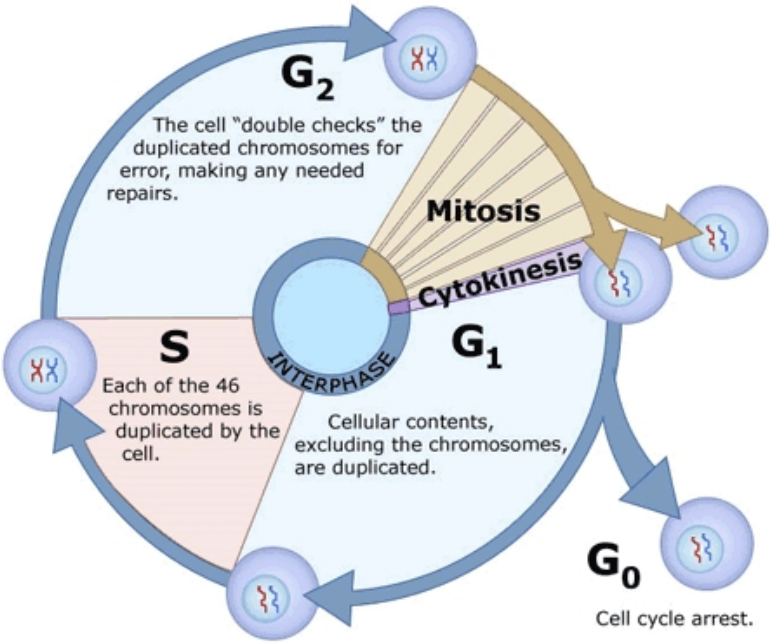

Fig. 1.4 An illustration of a typical cell division cycle. The figure is an adaption from Sumner [94].

Hence, the interphase includes gene transcription, protein synthesis and mass growth. In some special cases, the time for interphase is sufficient for cells to replicate DNA without growing in size. As a result, the tissue shrinks with each division. This happens during the first cell divisions after fertilisation, which are called cleavage divisions. In these embryonic cell cycles, the G_1 and G_2 phases are short, and the cells do not grow before they divide. Hence, a giant egg is rapidly subdivided into a cluster containing a large number of small cells.

1.2.6 Morphogenetic Movements

During morphogenesis, changes in the cellular properties can result in tissue deformations including elongation, thinning and folding. Figure 1.5 describes two major types of cell movement that occur during early developmental processes in various organisms. Epiboly (Figure 1.5 (A)) occurs at the onset of gastrulation. It is characterised as a thinning and spreading of cell layers. When a sheet has several cell layers, epiboly occurs through intercalation. The sheet becomes thinner by changes in the positions of cells. Convergent extension, or convergence and extension, is realised via cell intercalation (Figure 1.5 (B)). During intercalation, two or more rows of cells move between one another, creating a longer but thinner cell array. The change in tissue shape results from cell rearrangement. Convergent extension refers to the process by which the tissue converges along one axis and extends along a perpendicular axis, resulting in an overall extension in a specific direction [42]. In this movement, the cells of a tissue become narrower and longer.

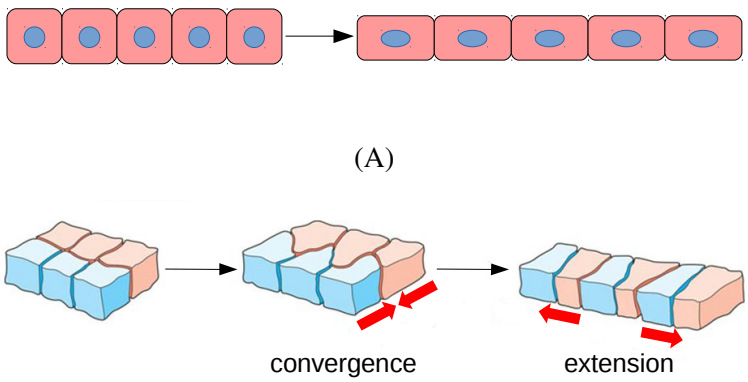

Fig. 1.5 Typical morphogenetic tissue movement: (A) Epiboly. (B) Convergence and extension. The diagram is adapted from Hardin [42].

Tissue level behaviour is influenced by changes in the cellular properties, including cell stiffness, cell–cell adhesion and cell motility. These concepts discussed throughout this thesis are simplifications of complex cell–internal dynamic processes. Next, a method is introduced that has been used to describe and quantify morphogenetic events.

1.3 Characterising Morphogenesis: Tissue Tectonics

Techniques for characterising dynamic developmental processes have been developed in recent years to quantify cell movements and cell shapes. These tools help us understand what is happening during morphogenesis. A kinematic framework that can be used to analyse the morphological data extracted from a developing embryo was described in Blanchard et al. [10]. The deformation of a tissue is quantified by two mesoscopic cell behaviours, namely tensorial rates of cell shape change, and cell intercalation (cell rearrangement). These two fundamental cellular behaviours account for a wide range of tissue shaping behaviours. They can be either active cell-autonomous behaviours, or passive deformations (elastic or plastic) in response to external forces.

1.3.1 Tissue Strain Rate

Morphogenetic deformation is a consequence of the change in cell relative positions. At the tissue scale, deformations are quantified by tracking small groups of cells or domains over a short time interval. A variety of types of tissue-scale deformation are shown in Figure 1.6. Each domain consists of a central cell and a small number of coronae of neighbouring cells. When the domain moves as a whole in space and behaves as a rigid block, the average translation velocity of the domain is calculated in Figure 1.6 (a), and the angular velocity for a rotating domain is calculated in Figure 1.6 (b). The strain rate tensor measures how the domain itself deforms. The domain in Figure 1.6 (c) can be characterised as a balanced convergence and extension, as the tissue narrows along one axis and elongates along a perpendicular axis, or a pure shear deformation. A simple shear results from a combination of rotation and a pure shear (Figure 1.6 (d)). To further understand tissue deformation in terms of the local cell behaviours within each domain, we move on to the cellular scale.

1.3.2 Cell Shape and Cell Intercalation Strain Rates

Two complementary components were identified at the cellular scale: cell shape change and cell intercalation. Three simulated cases were considered. In the first two cases, tissue convergence and extension were equal but resulted from cell shape change (Figure 1.7 (a), (d)–(f)) or cell intercalation (Figure 1.7 (b), (g)–(i)), respectively. In the third case, no tissue deformation was found as the effects of cell shape change and cell intercalation mutually cancelled (Figure 1.7 (c), (j)–(l)). *In vivo*, it is expected that morphogenesis combines both cell shape change and cell intercalation which vary with tissue, time and location. The shape

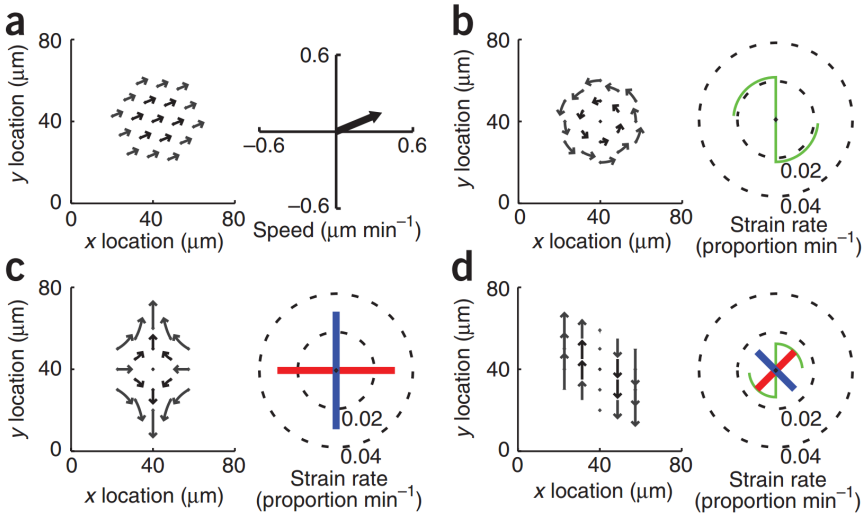

Fig. 1.6 These figures illustrate the measured tissue strain rates in simulated data. In each simulated domain (number of coronae, $n_c = 2$; and time interval, $dt = 9$ min), the plots on the left show the trajectories and the plots on the right describe either domain translation (a) or tissue strain rates (b–d). Principal strain rates are represented by orthogonal line segments with length equal to the strain rate amplitude (blue, positive and red, negative). Rotation is represented by a green scythe motif, with the radius indicating radians per minute on the same scale as the strain rates. The blades point in the direction of rotation (anticlockwise in b and clockwise in d). (a) Translation with uniform velocities. (b) Pure rotation. (c) Balanced convergent extension, or pure shear. (d) An equal combination of pure shear and rotation, or simple shear. The figure is taken from Blanchard et al. [10].

of each cell can be estimated by fitting the cell outlines to an ellipse. Using this fitting, the average cell shape strain rate for a patch ($\dot{\varepsilon}_c$) can be calculated. The tissue strain rate can then be calculated from the cell centroid trajectories ($\dot{\varepsilon}_t$). In terms of cell intercalation, it was proposed that cell intercalation results from the continuous sliding of the bulk of neighbouring cells past each other. This local rate and the principal directions of sliding are directly represented by the cell intercalation strain rate tensor ($\dot{\varepsilon}_i$). This can be calculated from the following relationship, which explains that the intercalation rate is related to the difference between the tissue rate and the cell shape change rate:

$$\dot{\varepsilon}_i = \dot{\varepsilon}_t - \dot{\varepsilon}_c. \tag{1.1}$$

This definition is true for both two and three dimensions. As Figure 1.7 (c) shows, during intercalation the convergence rate in one direction is balanced by an identical rate of extension in the perpendicular direction so that the area in 2D and the volume in 3D are preserved.

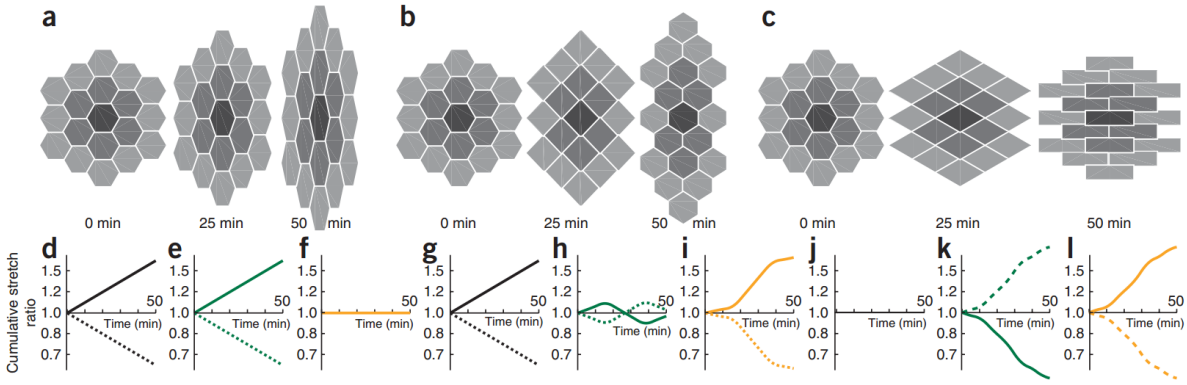

Fig. 1.7 These figures illustrate different modes of tissue morphogenesis. Black (d,g,j) and green (e,h,k) graph lines represent tissue and cell cumulative stretch ratios, respectively. Yellow (f,i,l) graph lines show cell intercalation. Dotted and solid lines represent horizontal and vertical directions, respectively. (a,d,e,f) show tissue deformation caused entirely by cell shape change with no intercalation. (b,g,h,i) show tissue deformation caused by intercalation. (c,j,k,l) show no tissue deformation but horizontal elongation of the cells purely through intercalation. The figure is adapted from Blanchard et al. [10].

1.3.3 A Biological Application

The above model can be used to explore how the cellular behaviours are patterned in time and space. Four main quantities are examined: cell shape, cell intercalation, tissue strain rates and tissue rotation rate.

These quantities were used to quantify convergence and extension in a single domain of zebrafish trunk neuroectoderm. Tissue strain rates indicated that the convergence and extension was unbalanced (Figure 1.8 (c)), with extension biased to the anterior-posterior (AP) axis. An ellipse was used to represent the shape of the cells (Figure 1.8 (f)). The average cell shape change rate ε_c and tissue strain rate ε_t were calculated. Hence the strain that was not reflected by cell shapes was the intercalation rate, ε_i, which could be calculated from Equation (1.1). For any tissue of interest, these quantities can be extracted over time from local cell data to study how they vary across the tissue and vary with time.

1.3.4 Research Updates

The tissue tectonics method developed by Blanchard et al. has quantified a set of core behaviours of cells underlying different morphogenetic events [10], however, this method has not been made public to others with well-documented libraries. Recent studies have proposed new approaches for tissue tectonics.

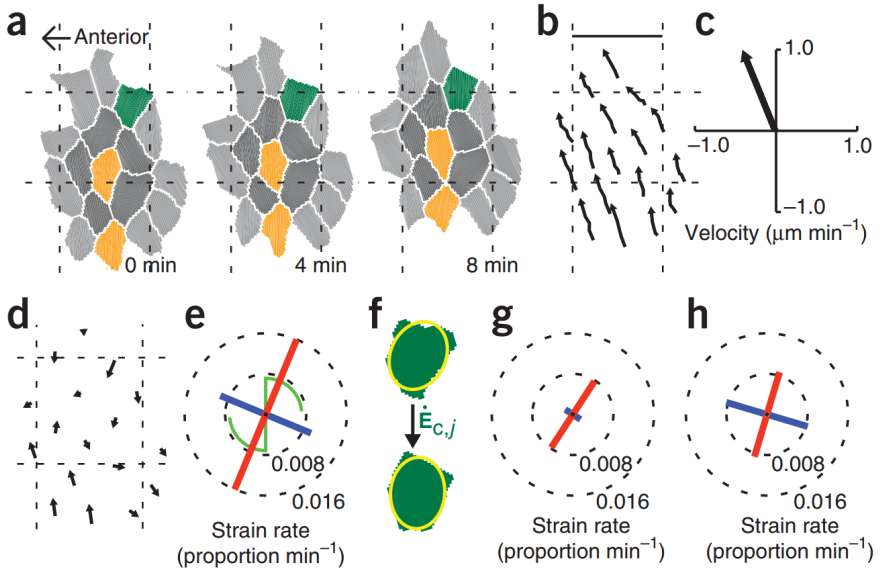

Fig. 1.8 These figures present the strain rates in a domain ($n_c = 2$, $dt = 4$ min) of zebrafish neuroectoderm. (a) Cell shapes over time. Cell colours show first (dark gray) and second (light gray) coronae of neighbours around the focal central cell, with examples of cell shape change (dark green) and intercalation (orange). (b) Cell centroid trajectories. Scale bar: 25 mm. (c) Average translation velocity of the domain. (d) The velocity field. (e) Tissue strain and rotation rates. (f) Cell shapes are approximated to their best-fit ellipses (yellow) and strain rates that must be applied to account for a cell's shape evolution from time t - dt to t + dt are calculated for all cells of the domain. (g) Area-weighted average cell shape strain rates. (h) Cell intercalation strain rates. The figure is adapted from Blanchard et al. [10].

Etournay et al. [30] developed a multi-scale analysis toolkit to quantify how cellular processes create tissue dynamics in 2D, which is called TissueMiner. This computational framework has a database storing cellular connectivity and geometric information of epithelial tissues under tension, and uses computational tools to interrogate it and perform multi-scale analysis of morphogenesis. The procedure of the analysis of epithelial morphogenesis within TissueMiner is in three steps. Firstly, all epithelial cells of the tissue are segmented as segmentation masks that contain information about cell geometry, cell neighbour topology and cell ancestry, and automatically tracked over time. Secondly, a TissueMiner automated workflow is used to extract cell information from the images and store it in a relational database. An example of visualisation and quantification of anisotropic cell and tissue deformation by TissueMiner is shown in Figure 1.9. Finally, cell properties and behaviours between different movies and subregions of the tissue are quantitatively compared by visualising the data using TissueMiner's library of tools. In particular, TissueMiner enables us to visualise time-lapse information on the tissue, which reveals spatial and

temporal patterns of core cell behaviours. In order to quantitatively compare regions within the same tissue or compare how the tissue behaves across replicates or various conditions, tools are developed to define regions of interest, synchronise movies in time and align all tissues to a common orientation.

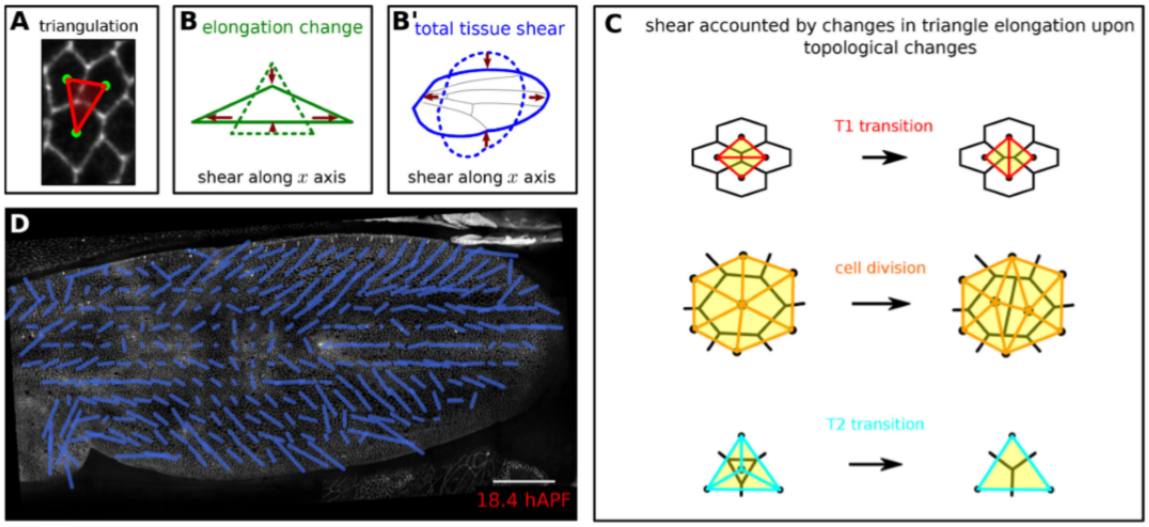

Fig. 1.9 Visualisation and quantification of anisotropic cell and tissue deformation. (A) Triangulation of the cell network: each triangle vertex corresponds to a cell center. (B–B') Cartons depicting triangle pure shear and total tissue shear along the x axis. (C) Cartons depicting shear due to T1 transition, cell division and extrusion. (D) Pattern of local tissue shear rate obtained from the triangulation method. Scale bar: 50 microns. The figure is adapted from Etournay et al. [30].

The TissueMiner toolbox allows us to quantify cell state properties and cell dynamics, their spatial patterns and their time evolution in a fast, easy and flexible way. This multi-scale physical model was originally used for quantifying cellular contributions to wing blade deformation during wing morphogenesis and demonstrating how the interplay between epithelial tension and cell dynamics reshapes the pupal wing [31].

Another new approach was carried out by Guirao et al. [41] to characterise cellular behaviours including cell divisions, rearrangements, cell size and shape changes, and apoptoses in epithelial tissue during development. To understand how the behaviours of each individual cell can act together to generate a large and reproducible change at the scale of entire tissues and organs, a multi-scale formalism was developed to provide maps that reveal how much each cell process contributes to tissue growth and morphogenesis.

This novel formalism is valid in both 2D and 3D. The four main cell behaviours, including cell divisions, cell rearrangements, cell shape and size changes and apoptoses, are unam-

biguously distinguished and independently quantified by four measurements **D**, **R**, **S** and **A**, respectively. These four measurements quantify the changes in link length or orientation as well as link appearances or disappearances due to their respective cell processes. As a result, these measurements accumulate to the local tissue rate of deformation measuring the rate of tissue growth and morphogenesis (**G**) due to these four cell processes (Figure 1.10 (a)). In addition, introducing cell divisions and apoptoses naturally enables the addition of the other cell processes changing the number of cells such as the integration of new cells in epithelium sheets, the fusion (coalescence) of cells and the in/outward cell flux, representing the cells entering and exiting the microscope field of view or the boundaries of the tissue of interest.

If tissue deformation is only associated with cell divisions, cell rearrangements, cell size and shape changes and apoptoses, the tissue can be characterised by a balance equation where the deformation rate of a region in the tissue is decomposed of the sum of the deformation rates associated with each cell process:

$$\mathbf{G} = \mathbf{D} + \mathbf{R} + \mathbf{S} + \mathbf{A}. \tag{1.2}$$

In the equation, when divisions, rearrangements and apoptoses are absent, which is $\mathbf{D} = \mathbf{R} = \mathbf{A} = 0$, the formalism therefore yields an exact equality between the rates of tissue deformation **G** and of cell size and shape changes **S**. This method enables us to understand how animals from different species develop from a single cell to a variety of shapes and sizes and may facilitate understanding how certain diseases affect the development of tissues.

Tissue tectonics can be used to describe these cellular behaviours that can drive different aspects of development. However, the underlying forces generated by these cellular processes were not determined. To investigate how cellular forces are generated and how these forces link to tissue-level and cellular-level mechanical interactions, we need to combine the quantified observations with experimental measurement, and compare the effects of perturbations in phenotypes and mutants to indicate the acting forces.

1.4 Techniques for Investigating Tissue Mechanical Properties

To further understand the developmental processes, an experimental technique is required to probe the mechanical properties of the tissues in developing embryos. Recent studies have used different approaches to explore the intrinsic properties of biological tissues. The

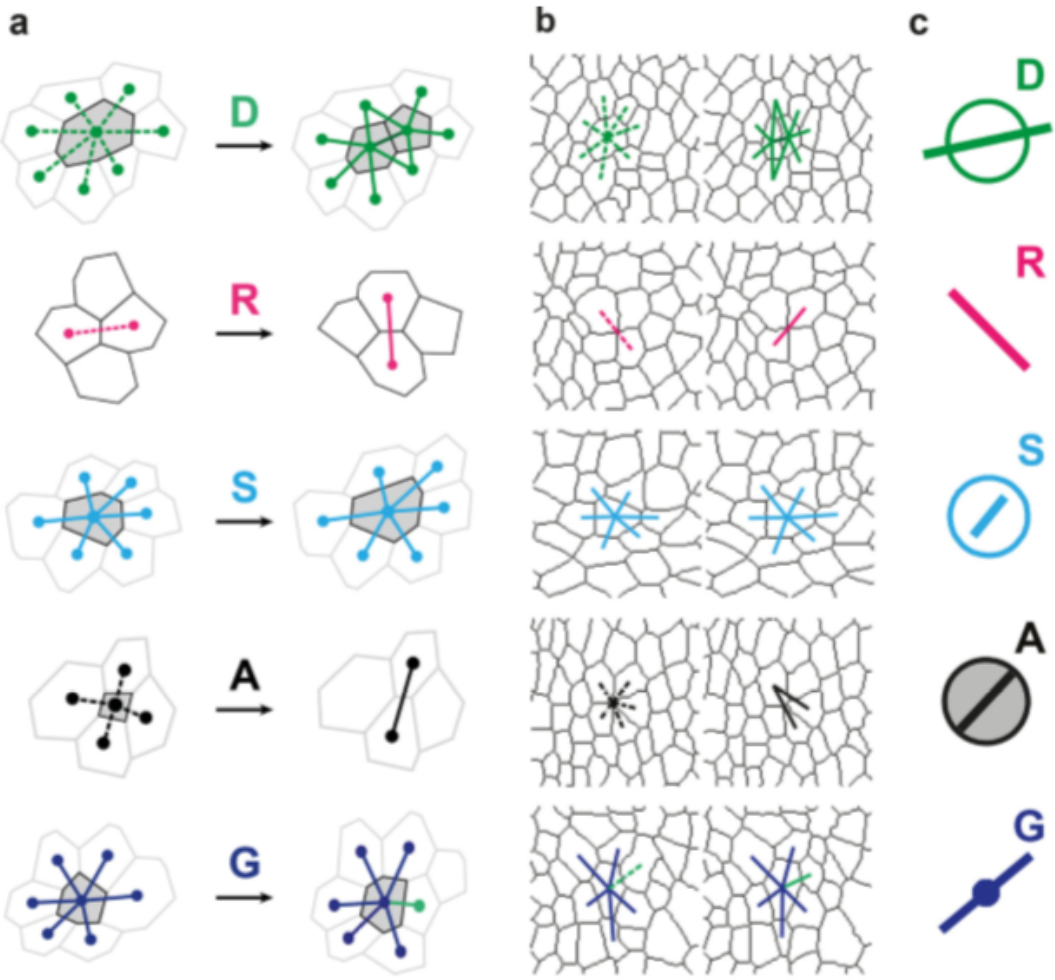

Fig. 1.10 Definitions of the main formalism quantities. (a) Characterisations of the four main elementary cell processes and of tissue deformation: **D**, divisions (green; and dark green for the link created between the daughter cells); **R**, rearrangements (magenta); **S**, size and shape changes (cyan); **A**, apoptosis/delaminations (black). They make up the tissue deformation rate **G**, the measurement of which is based on geometric changes of conserved links (dark blue links) excluding nonconserved links (green). Dots indicate cell centroids. Lines are links between neighbour cell centroids. (b) Measurements of the four elementary main cell processes rates and of tissue deformation rate. Same as (a), this time showing cell-cell links on two actual successive segmented images extracted from experimental time-lapse movies. (c) Representation with circles and bars of the quantitative measurements performed on (b). The figure is adapted from Guirao et al. [41].

following sections discuss the principles of these techniques and establish the direction of our research.

1.4.1 Local Measurement Techniques

Brodland et al. [107] measured the tensile properties of embryonic epithelium using a pair of cantilever wires glued to the surface of an embryo, as shown in Figure 1.11. One wire is fixed while the other moves, under the control of computer to stretch the tissue at a constant strain rate. The force in the specimen can be measured from the wire deflection. The specimen and the two wires are monitored by a real-time camera which produces images with high magnification and resolution. This approach is highly invasive, and it is difficult to measure tissue dynamic properties *in vivo* during the development of the embryo.

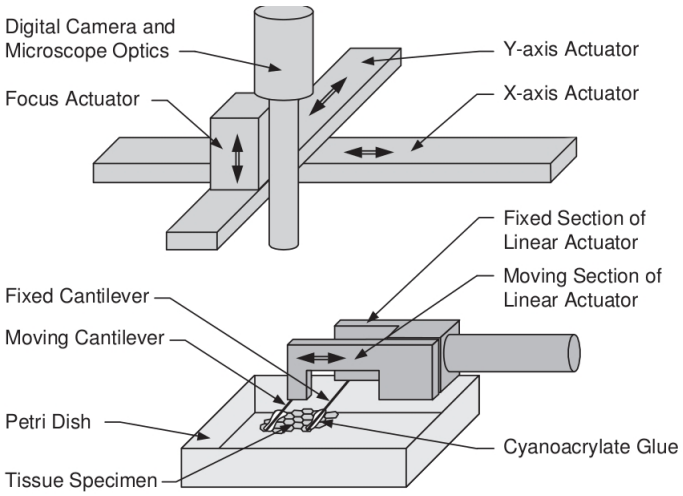

Fig. 1.11 A schematic diagram of the two-wire tissue property measurement instrument. The diagram is adapted from Wiebe and Brodland [107].

Laser ablation techniques are capable of capturing tissue mechanics during development at both cellular and tissue levels. The forces can be revealed by ablating cellular or subcellular structures, such as cytoskeletal filaments and cell junctions, by pulsed laser [78]. A force imbalance is produced at the cut position by the highly focused laser. Consequently, this sudden force imbalance causes a change in cellular geometry between the ablated point and non-ablated point [89]. Experiments have been performed to explore the anisotropy of stresses around the cell by measuring the initial velocity of cell junctions after ablation. The stress anisotropy could be indicated by the differences in tension. Similarly, tissue scale properties can be examined by ablating cells in the tissue and comparing the initial velocity of the wound margin after ablation [13, 14]. Martin et al. [63] used lasers to focus on the

surface of the embryo to ablate actomyosin structures. Point ablations took $\sim$ 670 ms while line ablations took $\sim$ 6.4 s. These time-lapse methods are limited, as information, such as the tension in the tissue, is unrecognised. The available information on ablation time and tissue movement is insufficient to calculate forces or stiffness.

Campas et al. [19] used a quantitative approach to measure cellular forces. This new technique has been developed to quantify cell-generated mechanical forces within living embryonic tissues by fluorescent oil microdroplets, which are similar in size to individual cells [19]. The droplets are coated with adhesion receptor ligands. The mechanical properties of the oil droplets are known before injection. When a fluorescent microdroplet is injected into the intercellular space of living embryonic tissue, adjacent cells adhere to the surface receptor ligands on the oil droplet and exert force on it. As a result, the droplet is deformed by cellular forces (Figure 1.12). Then the tensional and compressional stresses that cells apply at every point on the droplet surface can be quantified by time-lapse fluorescence microscopy and imaging analysis tools. This method could be adapted for many different applications to explore in 3D the local stresses generated by individual cells or group of cells. However, the method is restricted to measuring the isotropic component of the stresses, since large-scale tissue flows may also be driven by tissue-scale spatial variations in the tissue pressure.

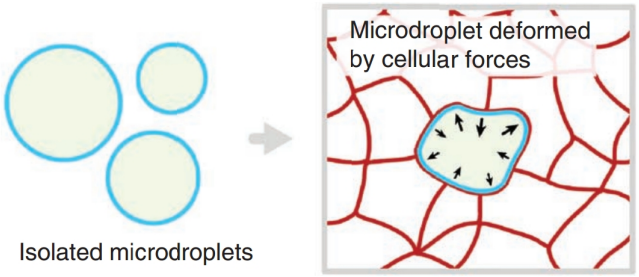

Fig. 1.12 Oil microdroplets as force transducer. The droplet is embedded between cells in embryonic tissue. The diagram is adapted from Campàs et al. [19].

1.4.2 Direct Measurement Techniques

Direct measurement techniques apply a remote force to the specimen. The applied force is known as a priori or measured directly, and can be manipulated to probe the mechanical properties in living tissues. Optical tweezers, atomic force microscopy (AFM) and magnetic tweezers are used to measure the viscoelastic properties of cells by observing cellular responses to the applied force over time. Micro-needle aspiration can be used to probe surface tension.

Optical Tweezers

Optical tweezers or laser tweezers use a highly focused laser beam, which is typically focused by sending it through a microscope objective lens. The laser beam manages to trap small round beads, which are dielectric particles of sizes in the range of nanometres to microns, by an attractive or repulsive force (typically in the order of piconewtons). As shown in Figure 1.13, the beam waist has a very strong electric field gradient. The dielectric particles are captured to the centre of the beam, where the electric field is the strongest [109]. In addition, since the particles absorb or scatter photons and the momentum should be conserved, the laser light exerts forces on these particles along the propagation of the beam. The particles are displaced slightly downstream from the exact position of the beam waist. Therefore, the force can be calibrated by evaluating the deflection distance of the particle relative to the laser focus [4, 109]. Forces on the particles could stretch the cells, and the elastic properties of cells can be calculated from the cell shape changes. Nevertheless, optical tweezers can release high energy with heating effects and cause radiation damage to the specimen samples [26, 44].

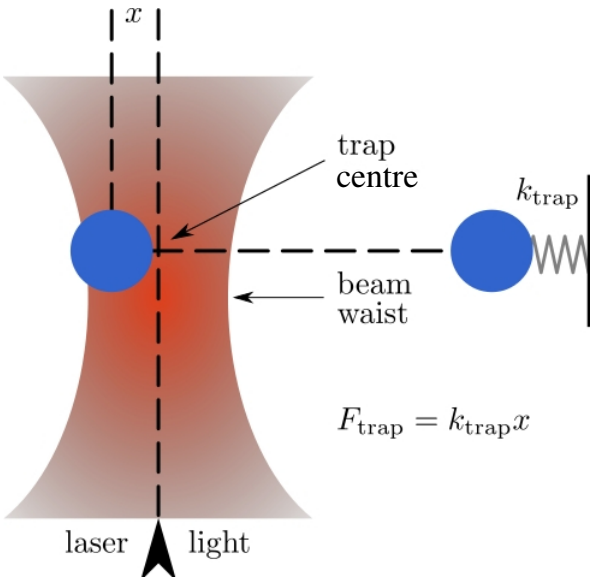

Fig. 1.13 The schematic illustration of optical tweezers. Dielectric particles are attracted to the centre of the beam, slightly above the beam waist. The diagram is adapted from Wu et al. [109].

Atomic Force Microscopy

Atomic force microscopy (AFM) has a high demonstrated resolution in the order of fractions of a nanometre. Figure 1.14 shows the basic principles of AFM. The probe is at the sharp tip of a flexible cantilever ($\sim$ 10 nm), which is attached to a piezo positioner and adheres to the surface of a specimen. The force between the probe and the sample is reflected by the deflection of the cantilever [9]. One of the methods to measure the deflection is to use a laser beam reflected from the top surface of the cantilever and collected by a position-sensitive detector (an array of photodiodes) [64]. The output signal of these diodes is brought into a differential amplifier. The amplifier produces a signal which takes the difference between the signals from the photodiodes normalised by their sum, which is proportional to the deflection of the cantilever. Another widely-used method is piezoelectric detection. The cantilever is made from piezoelectric materials which are able to directly detect deflection as an electrical signal. Cell surface mechanical properties, such as the elastic property and the strength of cell adhesion, can be derived from the pressing force and deflection of the cantilever in AFM [75]. Sharper tips and more sensitive cantilevers are required for higher resolution detections by AFM [109].

Micropipette Aspiration

Micropipette aspiration can be used to measure cellular mechanical properties by quantifying cell deformation upon pressure suction [55]. Figure 1.15 describes a micropipette aspiration system with two micropipettes in a cell suspension chamber. The movement of the micropipette in 3D is controlled by a pneumatic manipulator. The internal diameter of the pipette is smaller than the diameter of the sample. In this approach, the micropipette attaches to the sample and controllable suction pressure is applied until a cell is aspirated. The suction pressure generated in the micropipette is measured by a pressure gauge. The resultant forces are from 10 pN to 10^4 nN. Time-lapse images of cell deformation are recorded by a camera [46, 55]. This technique has been used in different ways to analyse passive material properties, such as cortical tension in cells [32] and the visco-elastic properties of cell aggregates [40].

Magnetic Tweezers

Tissue mechanical properties can also be probed by applying known forces to magnetic beads attached to or injected into the sample. A magnetic particle placed in a magnetic field gradient will experience a force directed towards the source of the field. Magnetic

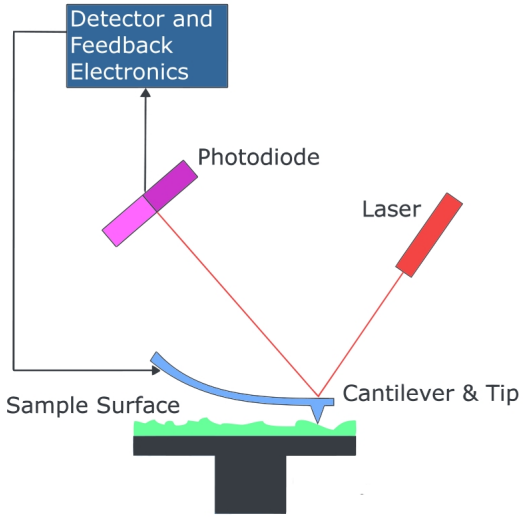

Fig. 1.14 The schematic illustration of AFM beam deflection detection system. The diagram is adapted from Wu et al. [109].

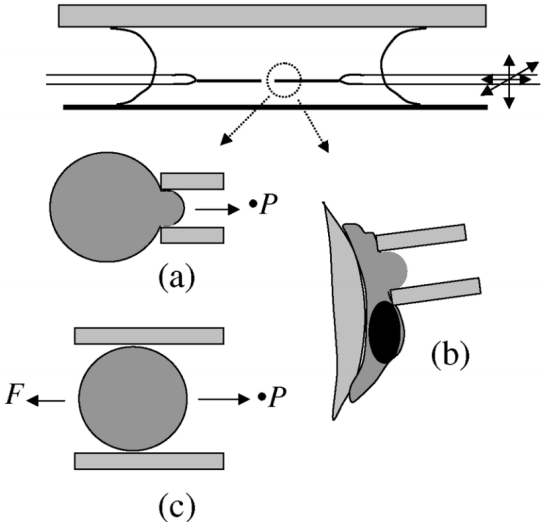

Fig. 1.15 The schematic diagram illustrates the micropipette aspiration system. There are two micropipettes in a chamber. The movement of the micropipette is controlled by a micromanipulator. At static conditions, the attachment force, F, is determined by the multiplication of the suction pressure and the cross-sectional area of the pipette. (a) A spherical cell is aspirated into a micropipette. (b) An attached cell being aspirated into a pipette. (c) A cell or bead could move freely in a pipette by the applied pressure. The size of the cell or bead is closely fit to the internal diameter of the pipette. The image is from Lee and Liu [55].

fields can be generated from either permanent magnets or electromagnets (Figure 1.16). Magnetic materials have a non-zero magnetic moment in the presence of a magnetic field. Paramagnetic/superparamagnetic and ferromagnetic materials are two major types that can be used for a magnetic probing test. Paramagnetic materials acquire a magnetic moment only when an external magnetic field is applied, and are entirely nonmagnetic in a zero field. In comparison, once exposed to a magnetic field, ferromagnetic materials become magnetized and retain a certain fraction of their magnetization even after the field has been removed [96]. A set of direct measurement techniques have been developed based on magnetic forces.

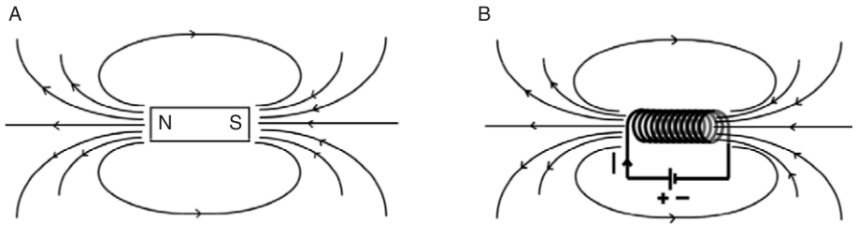

Fig. 1.16 The schematic description of magnetic field profiles for (A) permanent magnet and (B) an electromagnetic solenoid. The diagram is from Tanase et al. [96].

Savin et al. [85] developed a method for characterising the tensile properties of biological tissues at the mesoscale (Figure 1.17 (A)). A calibrated uniaxial tensile force is applied to a steel bead, which is attached to the sample by a permanent magnet. The attractive magnetic forces are in the range of micro- to milli-Newton. The extension of the sample is monitored by a camera. Hence, the elastic modulus can be derived from the stress-strain relationships.

Overby et al. [71] used a technique known as electromagnetic pulling cytometry (EPC) to explore cell rheology (Figure 1.17 (B)). The EPC uses magnetic beads which are coated in ligand and attached to receptors on the cell sample. The electromagnet is a coiled conductive microneedle with a sharp pole tip, which gives a larger gradient and force [96]. A pre-calibrated force is applied to the magnetic bead. The viscoelastic properties of cells are measured by observing bead displacement and cell deformation. Similarly, Laurent et al. [74] used another technique known as electromagnetic twisting cytometry (ETC) for measuring the mechanical properties in a monolayer of adherent cells (Figure 1.17 (C)). ETC uses coated ferromagnetic microbeads which are attached to the actin cytoskeleton. A magnetic twisting device applies a magnetic torque directly to the cell surface via the microbeads [105]. The attached cells are deformed by rotation of the beads. The elastic modulus of the cell can be calculated from the pre-calibrated magnetic moment and the angle of rotation of the bead.

The most advanced magnetic measurement technique is magnetic tweezers. Typical magnetic tweezers consist of four to six coils. The magnetic flux is generated by the current

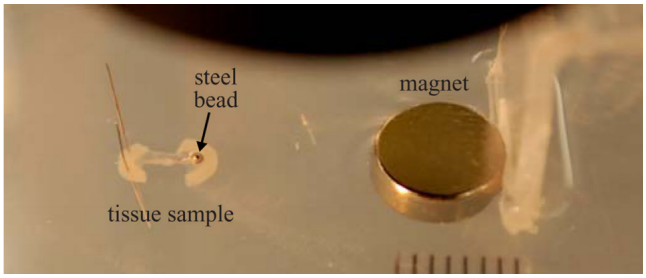

(A)

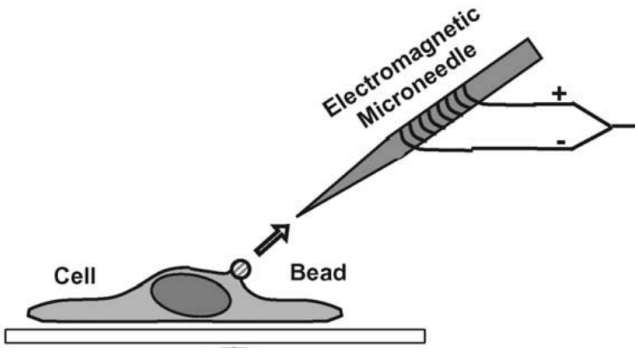

(B)

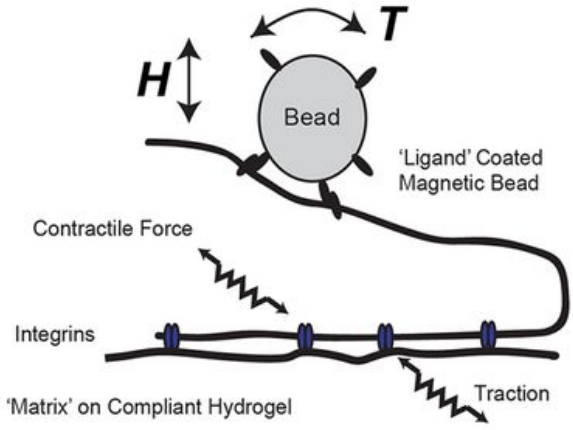

(C)

Fig. 1.17 The diagrams illustrate magnetic measurement techniques using permanent magnets or electromagnets in different studies. (A) The tensile test setup with the tissue sample and the magnet. The picture is from Savin et al. [85]. (B) The experimental setup for electromagnetic pulling cytometry. The diagram is adapted from Overby et al. [71]. (C) The experimental setup for magnetic twisting cytometry. The diagram is adapted from Muhamed et al. [68].

in the coils and passes through a magnetic circuit. Fisher et al. [35] proposed a tetrapolar electromagnet for *in-vitro* study of chromatin stretching, which is able to produce a 3D force on the magnetic beads in the sample. This idea of using magnetic tweezers for probing the mechanical properties of living tissues was adopted in our research, which is introduced in Chapter 3.

1.4.3 Summary

We propose to build an instrument by which we could measure the mechanical properties of a developing animal embryo in non-stationary and heterogeneous conditions. This section has discussed multiple tools for the measurement of tissue mechanical properties. For the purposes of direct measurement, Table 1.1 compares optical tweezers, AFM and magnetic tweezers.

Table 1.1 Comparison of single-molecule force spectroscopy techniques [69].

	Optical tweezers	Electromagnetic tweezers	AFM
Measurement time (s)	10^{-4}	10^{-4}	10^{-3}
Probe size (μm)	0.25–5	0.5–60	100–250
Stiffness (pN.nm^{-1})	0.005–1	10^{-4}	10–10^5
Force range (pN)	0.1–100	0.01–10^4	10–10^4
Displacement range (nm)	0.1–10^5	5–10^5	0.5–10^4
Typical applications	3D manipulation Tethered assay Interaction assay	3D manipulation	High force pulling Interaction assay
Features	Low noise	Force clamp Apply torsion	High resolution
Limitations	Photodamage Sample heating	Force hysteresis	Large high-stiffness probe Large minimal force

In order to avoid severe damage to the tissue, to exert mechanical forces and probe the rheology inside the living embryo, and to achieve rapid and direct manipulation, magnetic

tweezers were selected as the candidate for *in-vivo* interaction with embryonic tissues. Preliminary experiments were carried out which implanted a super-paramagnetic bead with a diameter of 20 μm into zebrafish embryos. The magnetic force on the bead was generated by a simple, single-pole electromagnet with a magnitude of $\sim$ 100 pN. No obvious disruption of normal development was detected after the injection of the beads. The complete design of the magnetic tweezers and the procedure for calibration of the magnetic forces are detailed in Chapter 3. The experiment of probing the tissue rheology of the early-stage zebrafish embryo is described in Chapter 4.

1.5 The Scope of the Work

Local tissue displacement and deformation are the result of a combination of local and distant force generating processes that act through the largely-unknown mechanical properties of tissues. The aim of this thesis is to investigate how the mechanical properties of embryonic tissues influence cell movement during morphogenetic development, and how the tissues respond to perturbations in passive systems.

To address these questions, direct mechanical measurement and manipulation accompanying numerical modelling are our approach to the question. The Wild Type and mutant early-stage zebrafish embryos and the Wild Type Madin-Darby canine kidney II (MDCK) epithelial monolayers were used as the biological model. A mechanical model, which was originally developed by Jennings [49], was used to simulate the mechanical experiments. The projects involved in the thesis were highly collaborative. The personal contribution to work is claimed in the introduction section of each chapter.

1.6 Thesis Overview

The thesis is divided into seven chapters. This chapter gives a summary of the thesis structure, and introduces the background, the available techniques for characterisation of the local mechanical properties of tissue and the purpose of the research.

Chapter 2 introduces the methods that can be used for modelling tissue mechanics. These methods include the linear rheological model which models the behaviour of viscoelastic materials, and a computational model for multi-cellular biological systems.

Chapter 3 details the development of the magnetic tweezers for micromechanical measurement in living embryos. The design of the magnetic tweezers setup, the force calibration imaging system, the force calibration algorithm and the complete design with light sheet

fluorescent microscopy are also described. Chapter 4 discusses the first application of the device to characterise the local rheology of a zebrafish embryo at early development stages by applying forces to grafted magnetic beads. We combine both experimental observation and the fitted rheological model to explore the time evolution of mechanical properties during early embryo development.

In Chapter 5 and Chapter 6, the mechanical model introduced earlier in Chapter 2 is further developed to investigate two different questions. In Chapter 5, the model is used to simulate the bead probing test in a zebrafish embryo. We obtain data of cell stress from a large group of simulations to statistically investigate local cell stress heterogeneity in response to external perturbations. In Chapter 6, cell division, one of the cell active processes that shape animal tissues, is implemented in the mechanical model. Experimental evidence shows that oriented divisions in an epithelium dissipate tissue-scale stress and maintain cell packing. This model is used to simulate oriented and mis-oriented cell divisions in the epithelium under uni-axial stretch. Statistical significance shows that the results qualitatively and quantitatively duplicate the experiment observations.

The final chapter discusses and draws conclusions from the findings of the experimental and modelling work, and proposes future work for continuing the research.

Chapter 2

Models for Tissue Mechanics

Introduction

In the previous chapter, we introduced the experimental methods for probing material properties. To model the behaviour of a viscoelastic material, such as the embryonic tissues [8, 91], the linear rheological model is the simplest one that predicts both phenomena. It assumes that the materials are homogeneous and exhibit as a continuum.

In addition to experimental techniques, the tissue can be simulated by a computational model that can control the cell-level processes and boundary conditions to explore how the observed tissue level behaviours are generated and driven by cellular processes and surrounding tissues.

In this chapter, we focus on the methods that we used in the thesis to model tissue mechanics. These methods include the standard linear solid model for viscoelastic materials, and a novel mechanical model for testing hypotheses of dynamic processes within tissues which was developed by Jennings [49] .

2.1 Linear Rheological Model

The linear rheological model is an approach to model the viscoelastic properties of materials by using a linear combination of springs and dashpots to indicate the elasticity E and viscosity η, respectively (Figure 2.1). The model assumes that a constantly applied force (stress) σ produces a constant deformation (strain) ε in a spring and a constant deformation (strain) rate $\dot{\varepsilon}$ in a dashpot [81].

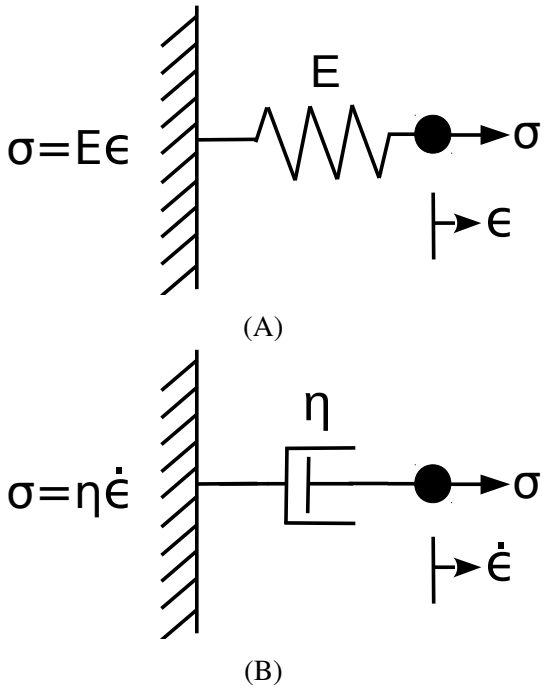

Fig. 2.1 The linear rheological model. (A) The spring represents the elastic property. (B) The dashpot represents the viscous property. The equations describe the stress-strain relationship.

The spring undergoes an instantaneous elastic deformation upon loading. It maintains that strain as the load is applied and completely recovers upon removal of the applied force. In comparison, the deformation on the dashpot increases linearly and without bound as the stress is applied. The slope of the creep is $\frac{\sigma}{\eta}$. When it is unloaded, there is no stress to move the piston back through the fluid, hence the deformation is permanent [72, 81].

Springs and dashpots could be connected to one another in different forms to represent different viscoelastic material behaviours. Two simplest forms are the Kelvin-Voight model and the Maxwell model (Figure 2.2). The Kelvin-Voight model consists of a spring and a dashpot in a parallel arrangement. The total stress applied to the system is shared by the spring and the dashpot and the deformation of both components is equal. The Maxwell model is comprised of a spring and a dashpot in a series. The stress on the spring and the dashpot is equal to the applied stress and the resulting strain is the sum of the strains of each component [72].

In the Kevin-Voight model, if a load σ is applied, the spring is held back by the dashpot as the dashpot cannot react immediately. Hence, the spring is at its resting length. The strain-time curve initially starts from 0 with an initial slope $\frac{\sigma}{\eta}$. As strain occurs, the stress is transferred from the dashpot to the spring. The slope of the creep curve is decreasing, until

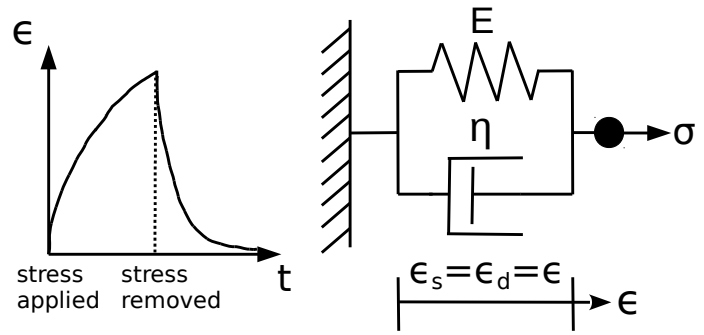

(A)

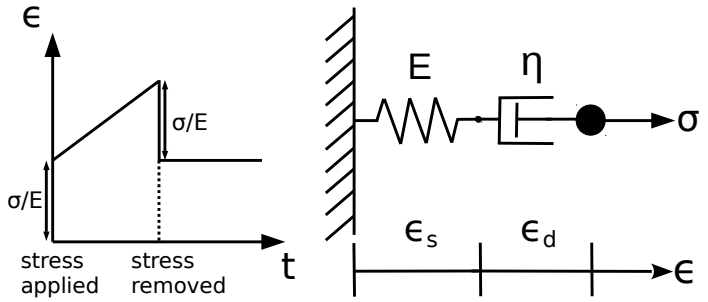

(B)

Fig. 2.2 The Kevin-Voight model (A) and the Maxwell model (B). The plots on the left of each model describe the time evolution of the strain. ε_s: the strain of the spring, ε_d: the strain of the dashpot.

the stress in the dashpot reaches 0. The maximum strain is $\frac{\sigma}{E}$. When the model is unloaded, the spring is held back by the dashpot and it cannot contract immediately. Eventually, the spring will pull the dashpot back to its original zero position and the deformation recovery is anelastic. There is no instantaneous or permanent strain [81].

In the Maxwell model, when the model is subjected to a stress σ, the spring stretched immediately and the dashpot needs time to respond to the load. The initial strain is $\frac{\sigma}{E}$. The slope of the creep curve is $\frac{\sigma}{\eta}$. When the load is released, the spring contracts immediately, however, the deformation in the dashpot will remain since it has no tendency to recover. The rapid elastic recovery is $\frac{\sigma}{E}$. There is no anelastic recovery, but there is a permanent strain in the end [81].

In summary, material behaviours could be indicated by different forms of the linear rheological model. The four fundamental models illustrated in this section help us understand the tissue behaviour and explore appropriate combinations of the model components to represent the tissues. By deriving the constitutive equations of the model, the fitted parameters

could be obtained to explain the mechanical properties of the tissues. In the following chapters, the rheological model is used to discuss both experimental and simulation results.

2.2 A Computational Model for Multi-cellular Biological System

A cell-based two-dimensional computational model has been developed by Jennings [49]. The model aims to investigate the mechanical properties of a cell and intercellular interactions within tissues. In the model, the Maxwell model is assumed to represent the viscoelastic behaviours of the tissue. The spring component and dashpot component are used to model the properties of cell cytoskeleton and the passive cell intercalation, respectively [67]. The model was implemented in C++. In this section, we discuss the main features of the model including cell morphology, dynamics through cell-cell dissipation, passive cellular properties and boundary conditions. The following discussion is guided by Jennings [49].

2.2.1 Cell Morphology

In the model, cell morphology is modelled by the dual representation of the cell as strain tensor and the Voronoi tessellation (Figure 2.3). An ellipse in two dimensions, represented by the strain tensor, indicates the shape of the cell by showing both the directions and the values of elongation or contraction. It is assumed that the ellipsoid, as a simplified representation of cell shape, is able to capture the cell dynamics and the effects of cell morphology on large scale tissue movements. A logarithmic strain model is used. Hence, the eigenvectors and the exponentials of the eigenvalues of the strain tensor represent the directions of the major and minor axes of the ellipse and the magnitudes of these axes, respectively.

The Voronoi tessellation divides the tissue into polygons associated with each cell [12]. Forces are acted on the edges of each polygon which define the cell–cell interface. On average, each cell has six neighbours. In the simulation, the two configurations of cells are calculated at each time step. The Voronoi tessellation is calculated from the position and shapes of cells to calculate the force balance, and the ellipse map is updated from the Voronoi polygon. The model used a logarithmic strain or true strain model. The strain ε in 1D is given by:

$$\varepsilon = ln(\frac{l}{L}), \tag{2.1}$$

where l and L are the current and rest lengths of the deformed object. With the logarithmic model, the eigenvectors of the strain tensor represent the directions of the major and minor axes of the ellipse and the exponentials of the eigenvalues represent the magnitudes of these axes [82]. This representation is not capable of exploring sub-cellular level behaviours.

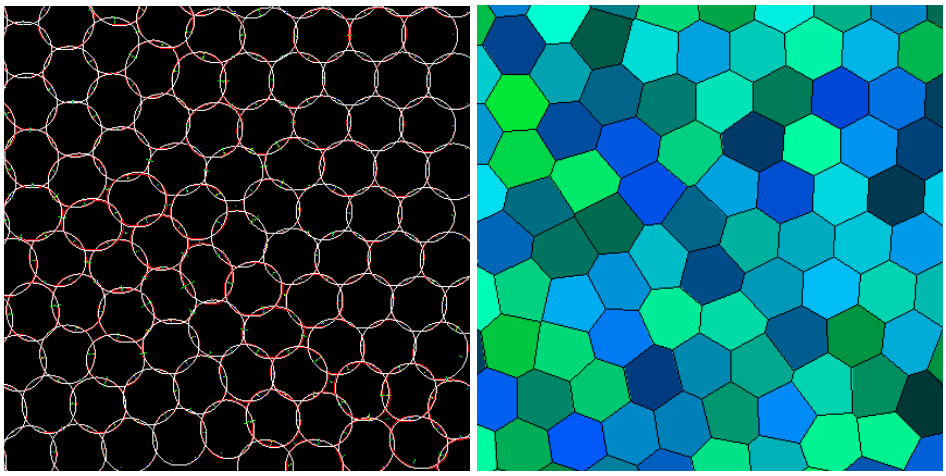

(A) (B)

Fig. 2.3 The two representations of cell morphology in the computational model for the same tissue. (A) ellipses (strain tensor). (B) Voronoi tessellation (polygons).

In the model, a linear elastic relationship is used to show the elasticity of cells. The linearly elastic constitutive relationship between the stress and strain in 2D is:

$$\sigma = K\varepsilon_A + 2G\varepsilon_s. \tag{2.2}$$

In Equation (2.2), σ is the stress tensor of elasticity, K is the bulk modulus showing the ability of cells to change their size, G is the shear modulus describing how difficult it is to change the cell shape at a constant cell size, the ε_A is the variation of cell area and ε_s shows the cell deformation at a constant cell area. This relationship provides a simple link between the cell shape and the stress.

2.2.2 The Algorithm

In the model, cells are represented as ellipses and Voronoi polygons in the plane. When the cells move relative to one another, this motion is resisted by the viscous force at the cell–cell interface. The changes in cell shapes in response to applied forces are captured by linear, isotropic elasticity. Boundary conditions are controlled using a finite element method so that the stresses over the tissue are balanced. The algorithm is summarised in Figure 2.4.

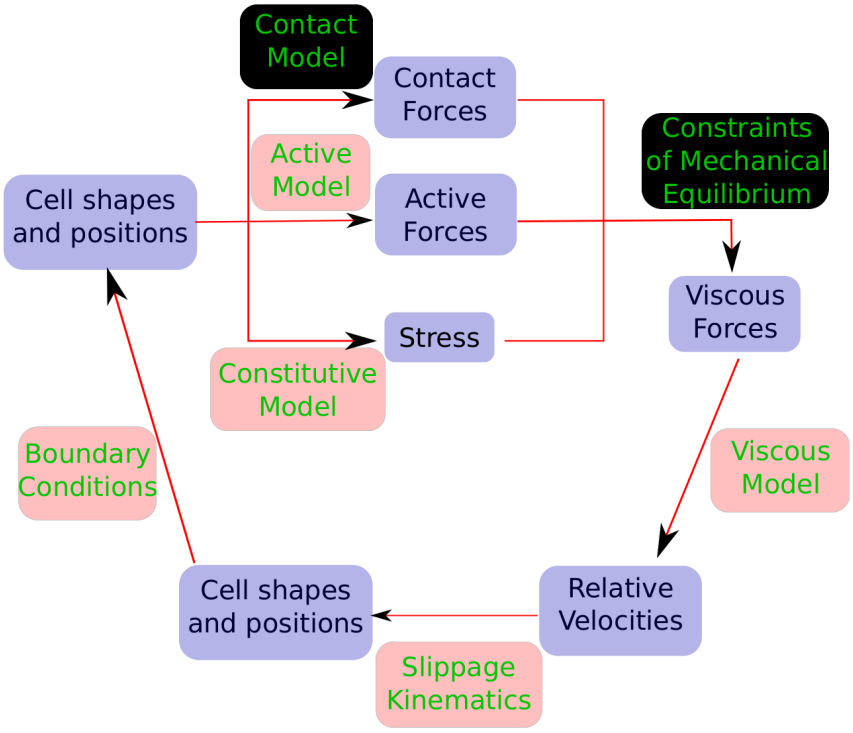

Fig. 2.4 A schematic diagram of the algorithm used for generating dynamics. Blue boxes represent the outputs/inputs of the model, the green text boxes represent the method used to calculate each output from the inputs. Red boxes indicate the requirements we set out and black boxes represent methods that have been introduced to create the algorithm. The figure is adapted from Jennings [49].

Starting with a configuration of cells, the contact forces and active forces are calculated from the shapes and positions of the cells. Viscous forces are then calculated from the contact forces and active forces using constraints of mechanical equilibrium including force balance, torque balance and that the internal stress of a cell must reflect the distribution of forces acting on it.

A velocity field of slippages at each cell–cell interface is calculated at each time step using the viscous force model. This result is used to update the cell positions and shapes.

The finite element method is applied to ensure that the boundary conditions are correct in the system. The new cell shapes and positions can then be used to calculate the contact forces in the next time step. The process continues in this way. Next we will discuss the forces, the constraints of mechanical equilibrium and the boundary conditions in the model.

2.2.3 Assembling the Model

The Forces

A cell in the tissue experiences body forces and surface forces. Cell–cell interaction is realised by defining surface forces, including contact forces, viscous forces and active forces. In the original model, body forces were not taken into account.

When cells move relative to one another within the tissue, they experience dissipative forces that resist this motion at the interface. Figure 2.5 illustrates the effects of a shear force on the interface between two cells. In this model, forces that only relate to the sliding between two cells were considered. Cell–cell dissipation is a consequence of the **viscous force** when any cell moves relative to another by a relative velocity $\mathbf{v}$. The model captures cell slippage at the interface for both cell shape change and cell motion in the absence of a substrate. For an interface of length l, the resistive force for the entire interface is described by the total energy expended divided by the distance the cell has moved through, and is controlled by a single viscosity parameter η. The viscous force model is described as:

$$\mathbf{F}^{\mathbf{v}} = \eta l \mathbf{v}. \tag{2.3}$$

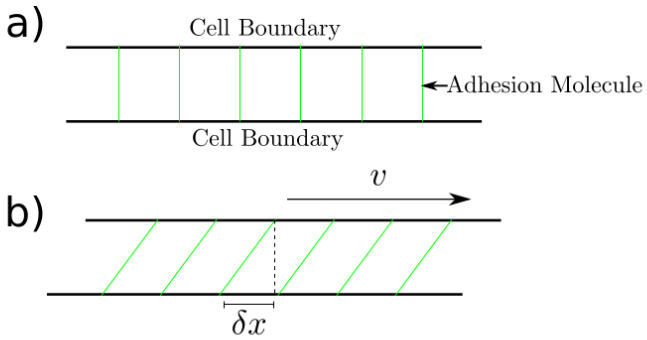

Fig. 2.5 Description of the viscous model: a) The cell boundaries with adhesion molecules before a shear is applied. b) The cell boundaries and adhesion molecules after a shear due to a relative velocity v, the net displacement of the endpoints of an adhesion molecule is given by δx. The figure is adapted from Jennings [49].

For cells at zero-stress configuration or equilibrium state, the pressure due to isotropic compression is given by:

$$p = -K\frac{A - A_0}{A_0}, \tag{2.4}$$

where K is the bulk modulus, A_0 is the initial cell area and A is the current cell area.

In the model, to capture the effects on cell areas, the area of the ellipse A_{ell} is fixed as its stress free state and the area of the Voronoi polygon associated with each cell A_{vor} which represents the current area of the cell controls the pressure of the cell:

$$p = -K\frac{A_{vor} - A_{ell}}{A_{ell}}. \tag{2.5}$$

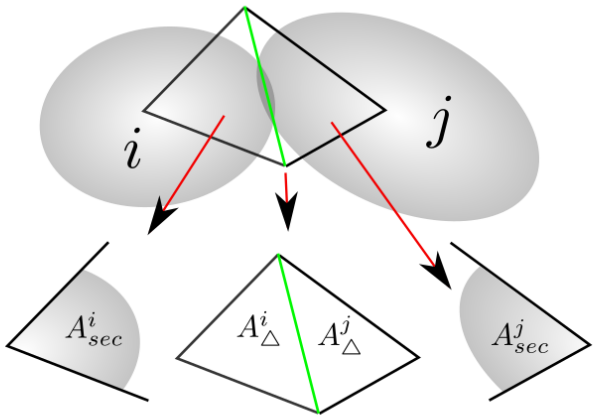

Fig. 2.6 The contact model between cell i and cell j illustrated in green. The areas of the sectors A_{sec} and the Voronoi triangles associated with the contact A_{Δ} are shown. These terms are used to calculate the contact force associated with local configuration effects. The figure is adapted from Jennings [49].

Figure 2.6 shows the algorithms of calculating the contact forces between two adjacent cells. When the current area A_{vor} is the same as the initial area A_{ell}, the pressure is zero. Based on this, the **contact force** is to describe the forces that act normal to the cell–cell interfaces and to capture the pressure effects, which can be expressed by:

$$\mathbf{F^c_{ij}} = CG^i\left(\frac{A^i_{\Delta}}{A^i_{Vor}} - \frac{A^i_{sec}}{A^i_{ell}}\right) + CG^j\left(\frac{A^j_{\Delta}}{A^j_{Vor}} - \frac{A^j_{sec}}{A^j_{ell}}\right). \tag{2.6}$$

In this equation, the local configuration effects can be seen as higher order deformations on the shape of the ellipse and scaled by the shear modulus G. Another parameter, the jamming contact parameter C, is defined to indicate the ability of cells to move past one

another. A higher contact parameter results in larger resistance to the cell rearrangement. The system is updated by calculating the viscous forces from the contact forces, and then calculating the new cell positions and shapes from the viscous forces and slippages.

Active forces occur when cell protrusive behaviours take place. The cell moves itself by applying an active force μ to two of its neighbouring cells. This force is equally balanced between its neighbours (Figure 2.7). In the thesis, cellular active behaviours are not considered.

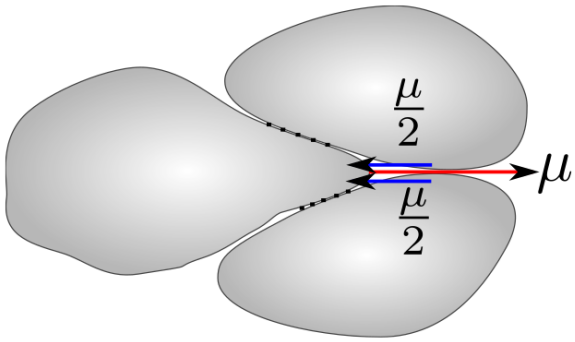

Fig. 2.7 The active force model. The active cell finds the gap between two neighbouring cells, and applies an equal force $\frac{\mu}{2}$ to each of them to pull itself forwards with force μ. The direction of such behaviour is fixed and the active cell searches for the gap between cells that is closest to this preferred direction at a given time. The figure is adapted from Jennings [49].

Constraints of Mechanical Equilibrium

Each cell within the model is subject to physical constraints. Cells are modelled as objects with no inertia, therefore, forces and torques on the cell must be balanced. Cell i within the model can experience any distribution of forces due to cell–cell interactions. A surface force density vector $\mathbf{T}_i(\theta)$ can be used to represent this distribution. The constraint of stresses is that an integral which guarantees that the total distribution of forces on the cell is consistent with its stress. The stress constraint equation is:

$$\sigma = \frac{1}{\pi}\int_0^{2\pi} \mathbf{T}(\theta) \otimes \hat{\mathbf{e}}_r(\theta) d\theta = \frac{1}{\pi}\int_0^{2\pi} \begin{pmatrix} T_x cos\theta & T_x sin\theta \\ T_y cos\theta & T_y sin\theta \end{pmatrix} d\theta, \tag{2.7}$$

where $\mathbf{T}(\theta) = (T_x(\theta), T_y(\theta))$. According to force balance, torque balance and consistent shape of cells, we have:

$$\mathbf{0} = \frac{1}{\pi}\int_0^{2\pi} \mathbf{T}(\theta) d\theta. \tag{2.8}$$

$$\sigma = \frac{1}{\pi}\int_0^{2\pi} \begin{pmatrix} T_x cos\theta & T_x sin\theta \\ T_y cos\theta & T_y sin\theta \end{pmatrix} d\theta. \tag{2.9}$$

The viscous forces can be calculated from the contact and active forces within the model. For cell i, with neighbours indexed by j, this gives the form of the constraints as (the active forces are neglected):

$$-\sum_j \mathbf{F}_{ij}^c = \sum_j \mathbf{F}_{ij}^v. \tag{2.10}$$

Equations 2.8–2.10 are solved for each time step to determine the viscous force to update the system. Then the viscous forces and slippages can be used to calculate the new positions and shapes of cells at the next time step. In the model, it is more efficient to calculate the new positions and shapes directly from the contact forces by solving a system of simultaneous linear equations. This is solved through *QR factorisation* to perform the linear least squares regression to determine the best fit for the system of equations.

Large-scale Force Balance

The model is in accordance with the large-scale force balance within a continuous body subject to an external force $\mathbf{F}$, given by the partial differential equation (PDE):

$$\nabla \cdot \sigma(\mathbf{x}) = \mathbf{F}. \tag{2.11}$$

In the two-dimensional continuous body model, the stress function $\sigma(\mathbf{x})$ is defined for any point $\mathbf{x}$ in the plane as constant across each Voronoi polygon by the stress tensor σ^i of cell i corresponding to that Voronoi polygon. The PDE is solved by finite element analysis. The PDE is written in a *weak form*. A point within the elastic body is considered. The work done against forces moving along a *virtual displacement* path is called the *virtual work*. In static equilibrium, the virtual work done for all virtual displacements is zero, which is called *the principle of virtual work*.

The virtual displacements of points within the body are denoted by $\delta\mathbf{u}(\mathbf{x}) = (\delta u_1, \delta u_2)$. The virtual work done by body forces F_i and surface forces T_i^n on a body, with volume V and surface S is given by:

$$\delta W = \int_S T_i^n \delta u_i dS + \int_V F_i \delta u_i dV. \tag{2.12}$$

Using Gauss' Theorem and definitions of the traction vector T_i^n, the virtual work function can be expressed as:

$$\int_V \sigma_{ij}\delta\varepsilon_{ij}dV = \int_S T_i^n \delta u_i dS + \int_V F_i \delta u_i dV. \tag{2.13}$$

The next step for the finite element method is meshing and interpolation. The Voronoi tessellation of the cells provides a very natural meshing of the plane into polygons, which can easily be split into collections of triangles using the centre of the cell and the edges of the polygon (Figure 2.8).

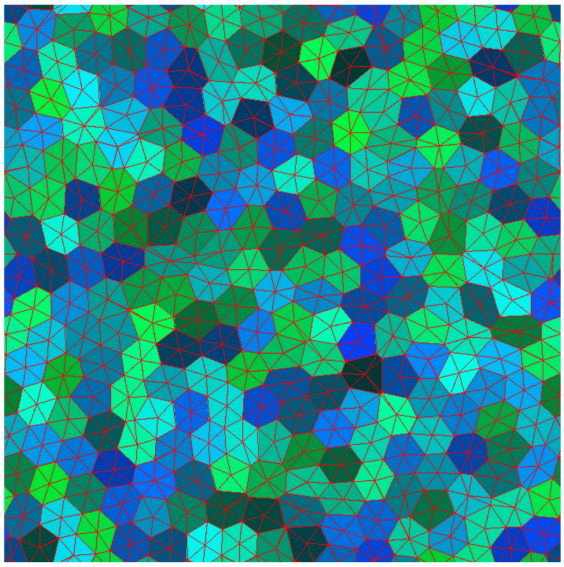

Fig. 2.8 The Voronoi tessellation with the meshing of the system into triangular elements in red. The figure is adapted from Jennings [49].

A linear function $u(x,y) = c_1 + c_2x + c_3y$ is used to define the displacement for each point on a triangle. A *Lagrange interpolation function* for a triangle is used and therefore, the strain tensor across each element is constant. In 2D, we are interested in finding the displacement vector (u,v) for each of the nodes within the mesh. The strains can be represented as:

$$\mathbf{e} = \begin{pmatrix} \varepsilon_{xx} \\ \varepsilon_{yy} \\ 2\varepsilon_{xy} \end{pmatrix} = \begin{pmatrix} \partial/\partial x & 0 \\ 0 & \partial/\partial y \\ \partial/\partial y & \partial/\partial x \end{pmatrix} \begin{pmatrix} u \\ v \end{pmatrix} = B\mathbf{U}. \tag{2.14}$$

The finite element method calculates the new positions of each node within the model to maintain stress balance throughout the system. Each triangular element has a pre-stress shape, which can be defined by the strain tensor of the cell $\mathbf{e_0}$. According to Hooke's Law, we have:

$$\sigma = M(\mathbf{e} + \mathbf{e_0}), \tag{2.15}$$

where M is the elasticity matrix. This equation can be substituted into the virtual work equation (Equation 2.13) to calculate local solutions to the PDE for one element. The local solutions can then be combined to construct the global solution. Each node within the mesh is associated with roughly six triangular elements. The global solution can be expressed as:

$$\bar{K}\bar{\mathbf{U}} = \bar{\mathbf{Q}} - \bar{\mathbf{S}} + \bar{\mathbf{B}}, \tag{2.16}$$

where the bars over the symbol $\bar{()}$ represent the global terms, $\bar{K}$ is the global stiffness matrix, $\bar{\mathbf{Q}}$ is the global traction vector, $\bar{\mathbf{S}}$ is the global pre-stress vector and $\bar{\mathbf{B}}$ is the body force vector. For instance, the displacement vector $\bar{\mathbf{U}}$ is defined as:

$$\bar{\mathbf{U}}^T = (u_1, v_1, u_2, v_2 ... u_n, v_n), \tag{2.17}$$

where n denotes the number of nodes within the mesh. This system of equations is linear and the displacement vector can be determined by inverting the square, symmetric matrix $\bar{\mathbf{K}}$.

Boundary Conditions

In the model, system of cells with periodic boundary conditions is considered. Periodic boundary conditions mean that the configurations of cells is wrapped so that the right edge is connected with the left edge while the top edge is connected with the bottom edge. Therefore, each cell only interacts with other cells rather than the boundaries. However, periodic boundary conditions require large system of cells to avoid artefacts that might arise from the periodicity of the system. In the thesis, we use two different systems containing 256 cells and 1024 cells, respectively. In these simulations, such effects are neglected.

Major Parameters

In the thesis, we explore the behaviour of the model in different conditions. The applied conditions to the model are determined mainly by the different parameters of the system. The major parameters of the model used throughout the thesis are listed in Table 2.1. The model is a non-dimensional system. In the table, we give estimates of the order of the magnitude of these parameters from experimental measurements and the units for each parameter.

2.2.4 Passive Cellular Properties

The computational model considers cells in a discrete manner. However, when the passive behaviour of the model system is assessed, the discrete-to-continuum bridge is made by

Parameter	Definition	Estimate
G	Shear elastic modulus of the cell	$\sim 10^6 Nm^{-1}$
K	Elastic bulk modulus of the cell	$\sim 10^7 Nm^{-1}$
η	Cell–cell sliding viscosity	$\sim 10^{11} Nm^{-1}s$
C	Jamming contact parameter	Scaling factor
R	Cell radius	$\sim 10^{-5}m$
F_m	Magnitude of the external force	$\sim 10^{-9}N$
t	Time step	s

Table 2.1 The major parameters and their definitions in the model

assuming that local cell displacement can be mapped homogeneously at the tissue scale. Hence, the continuum mechanics fits to the discrete model, showing that under stress the tissue exhibits viscoelastic behaviour which is consistent with the Maxwell model (Figure 2.2 (B)). Two major modes of deformation of the passive tissue were explored: isotropic compression and expansion, and pure shear.

Isotropic compression (or expansion) reduces (or increases) the sizes of the tissue in both the x- and y-direction by an equal amount. Consequently, the overall area of the system decreases (or increases) isotropically. This system does not generate cellular dynamics. The forces generated by compression or expansion are normal to the cell–cell interfaces, as the elastic pressure exactly matches the pressure calculated from the contact forces. There is no cell intercalation. This behaviour is controlled by the bulk modulus K which represents the overall compressibility of each cell.

When a large and instantaneous step strain is applied to the system of cells, the tissue is stretched with an instantaneous tissue strain (Figure 2.9 (B)). Cells are elastically deformed by the strain exactly matching the stretch applied to the boundaries of the tissue. Hence, initially, the stretch is entirely accounted for by cell elongation. The average strain of the cells is identical to the tissue strain. These stretched cells then start to relax by cell intercalation and rearrangement. Cells slowly become more circular and finally reach a plateau (Figure 2.9 (C,D)). Nevertheless, the tissue strain is non-reversible.

In the model system, the timescale for the relaxation of the cell strain is determined by the characteristic time parameter τ. The relaxation of the cell strain for different parameters is shown in Figure 2.10 (A). There are four distinct paths in these responses, according to the values of τ. Since the viscous forces account for the stress of the cell in its elongated

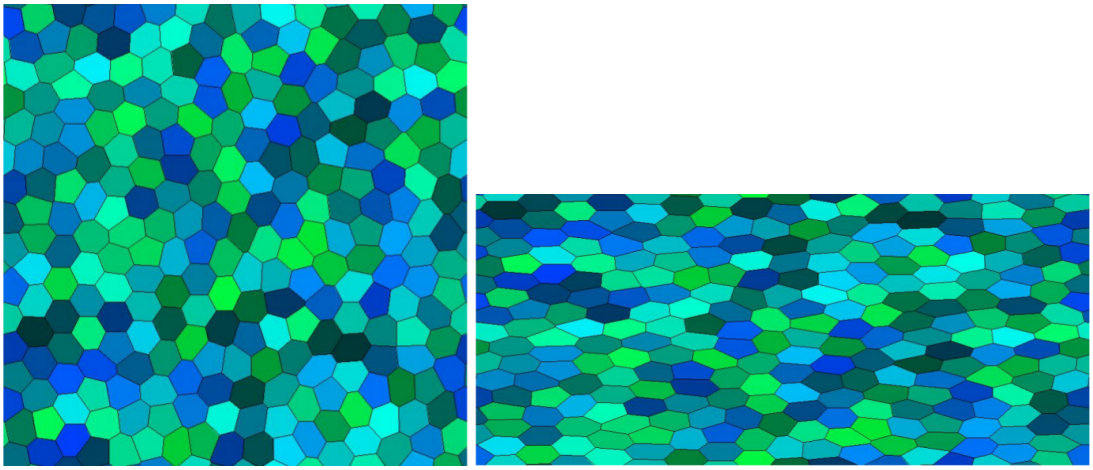

(A) (B)

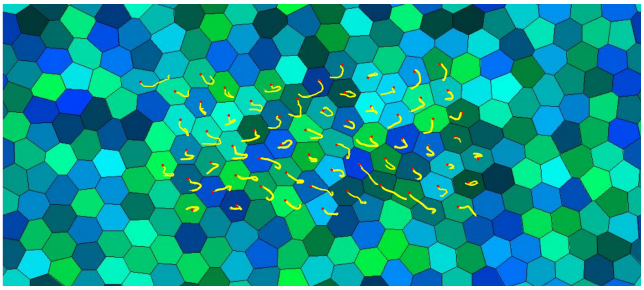

(C)

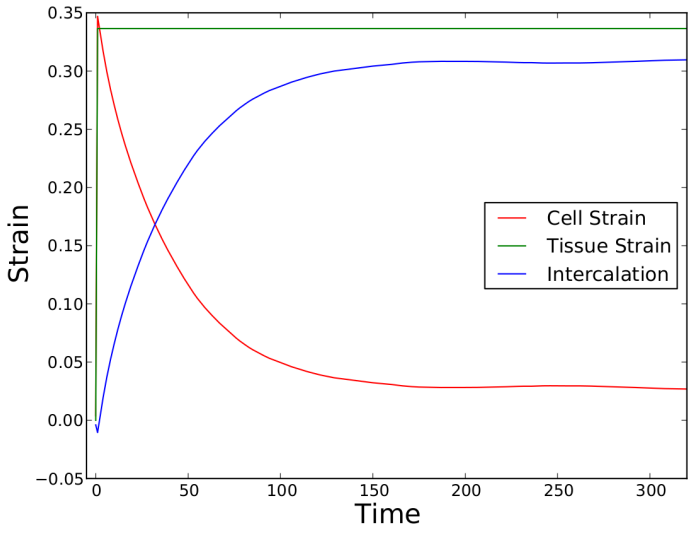

(D)

Fig. 2.9 A step strain applied to the model system. (A) The pre-strained system of cells. (B) A large step strain applied to a system of cells. (C) The system after long relaxation by cell intercalation. The red dots show the cell centres after intercalation and the yellow paths describe the cell trajectories. (D) The response of the system to a step strain which is measured in the direction of the stretch. These figures are adapted from Jennings [49].

state, the magnitude of viscous forces are associated with the cell stiffness G. We have described that the slippage is controlled by the cell–cell viscosity η. Hence, the speed of cells to rearrange to relax cell shape $\dot{\varepsilon}$ is related to the current cell shape ε:

$$\eta R\dot{\varepsilon} \sim -G\varepsilon. \tag{2.18}$$

And therefore:

$$\varepsilon \sim e^{-t/\tau}, \tag{2.19}$$

where $\tau = \dfrac{\eta R}{G}$. It shows that doubling the cell shear stiffness has identical effects to halving the cell–cell viscosity. It indicates that the tissue behaves viscoelastically as elastic cells interact with other cells through viscous dissipation. If the time is scaled by τ, all of the curves collapse to a single characteristic curve (Figure 2.10 (B)). The bulk modulus of the cells K does not influence the behaviour of the system since the overall area of the system does not change. The average cell strain maintains a small residual strain as cells do not have enough elastic energy to overcome local forces and continue relaxing their shapes (Figure 2.9 (D)). Further analysis has shown that this residual strain depends approximately linearly on the jamming contact parameter C.

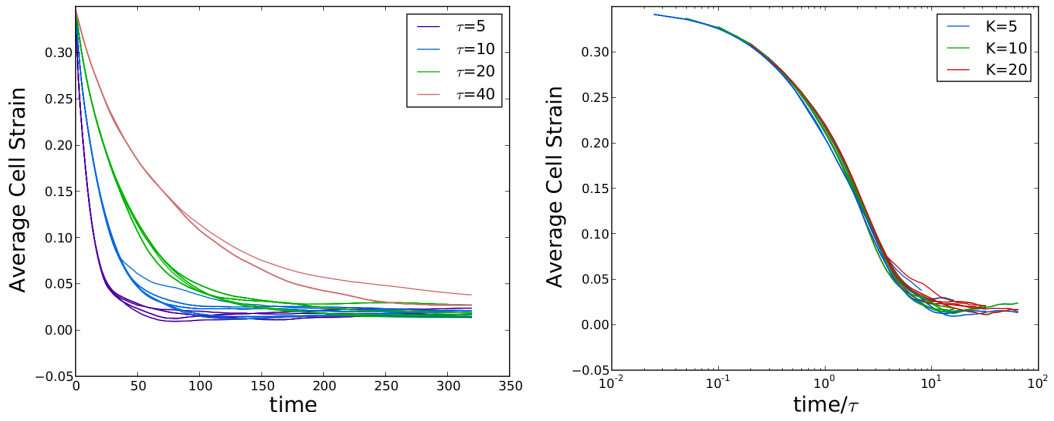

(A) (B)

Fig. 2.10 Time evolution of the average cell strain. (A) The relaxation of the strain of the cells over time through intercalation. Curves are coloured by their timescale parameter $\tau = \eta R/G$. (B) The collapse of average strain relaxation curves after scaling time with τ plotted with a logarithmic time axis. Curves are coloured by the value of the bulk modulus K for each simulation. These figures are adapted from Jennings [49].

In summary, in a passive system, the viscoelastic response is controlled by the characteristic timescale τ, the residual strain is determined by the jamming contact parameter C,

and the elastic pressure under isotropic compression and extension is controlled by the bulk modulus K.

2.2.5 Applications in the Thesis

The model could be applied to explore the physical processes underlying different development processes by adjusting the values of these parameters to simulate different cell properties. In the thesis, we used the modelling platform originally established by Jennings to solve two practical problems. In addition to the calculations described above, two novel features are added to the model: the external body force, and cell growth and division. An external force, which pulls one cell to move in the tissue to produce local perturbations, was incorporated in the model. We discuss how cell stiffness G and cell–cell viscosity η influence the movement of the cell and how surrounding cells respond to the local deformation in Chapter 5. Besides, cell growth and cell division were implemented within the model to explore the role of cell divisions on stress relaxation within monolayer tissues. This is described in Chapter 6.

In the next chapter, we will introduce the measurement techniques which we used to explore embryonic tissue mechanics.

Chapter 3

Electromagnetic Tweezers: Instrument for Three-Dimensional Micromechanical Measurement

3.1 Introduction

In the previous chapter we compared different techniques for measuring the mechanical properties of tissues. The key objective of our research is to measure the mechanical properties within the developing animal embryo in non-stationary and heterogeneous conditions. The tool should be able to apply a remote force on injected probes without disrupting normal development of the embryo. Magnetic tweezers are capable of generating three-dimensional (3D) forces of adequate magnitude to appropriate magnetic beads, which fits this purpose.

Magnetic tweezers must be accommodated with the biological specimen and the imaging system, such as light sheet fluorescent microscopy (LSFM). The device should be calibrated to establish the relationship between electrical currents in the coils and the magnitude and direction of the resulting forces on the magnetic bead. A control programme is needed to control the electrical current in each coil, to produce a pre-determined magnetic field and to synchronise image acquisition of the bead and the surrounding tissue.

This interdisciplinary work was a collaboration between Dr Alexandre Kabla's group in the Department of Engineering, Dr Richard Adams' group in the Department of Physiology, Development and Neuroscience, and Professor Clemens Kaminski's group in the Department of Chemical Engineering and Biotechnology at the University of Cambridge. Instrument development was carried out with Radu Tanasa. The chamber, sample mount and reference

system of the magnetic tweezers to accommodate the light sheet fluorescence microscopy (LSFM) were designed with Radu Tanasa and Aleksander Chmielewski. The calibration samples were prepared by Julien Dumortier. Bead trajectories were collected by Radu Tanasa. I designed the control programme in the Arduino controller, developed the calibration model and conducted calibration data analysis.

In this chapter, we introduce the development of the instrument, the procedure for magnetic force calibration and the application of a learning algorithm to the calibration data.

3.2 Instrument Development

The tool which was used to experimentally investigate tissue mechanics was the magnetic tweezers. Our modified version of magnetic tweezers includes an imaging chamber compatible with both the microscope and the tweezers, a heating unit to control sample temperature and a sample mount. Details are introduced in this section.

3.2.1 Magnetic Tweezers

A multipolar device with at least four poles is required to generate magnetic forces in arbitrary directions in 3D space to manipulate magnetic beads in living tissues [3]. The original design of a tetrapolar electromagnet from Fisher et al. [36] is a four-pole electromagnetic tweezers. These four magnetic poles are arranged in the shape of a flattened tetrahedron, two of which point vertically up and the other two point vertically down. As shown in Figure 3.1, the pole axis angles from horizontal are 22.5°. The distance from each pole to the centre is 517 μm. The coils are repositioned to locations removed from the optical path, and the magnetic poles are connected together through an optimised arrangement of flux return frames with coils, encircling parts of the return path rather than the poles. The coils are wound on cylindrical bobbins and consist of 340 turns of magnetic wire. During a 3 min test, the temperature of the coils at 3 A increased by 22.7°C. On the whole, this design is able to apply versatile, significant forces to microscopic structures with good heat control by allocating space for the cooling system to remove excess heat. Further, the optical microscope can easily provide access to the biological sample at the centre of the magnetic poles.

In order to use the device with light sheet fluorescent microscopy (LSFM) for high image resolution of cells in the embryo, a modified version of magnetic tweezers is used (Figure 3.2). The spacing between the top poles is increased to 2.42 mm, and between the bottom poles is increased to 1.5 mm. This allows enough space for a zebrafish embryo and mounting

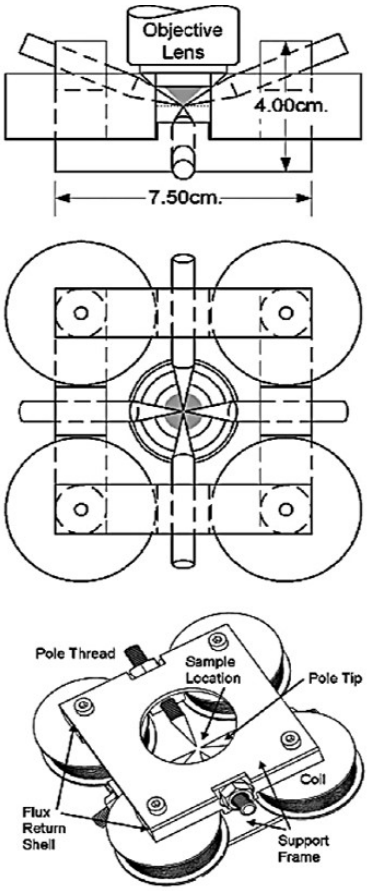

Fig. 3.1 Schematic diagrams of the design of the tetrapolar electro-magnet with four coils: side view, bottom-up view and perspective view, respectively. The first two views include the objective lens. The biological samples are placed in the central space between the pole tips. The figure is adapted from Fisher et al. [36].

chamber. The angle of each pole to the horizontal line is increased from 22.5° to 30°. The number of windings is around 400 turns in each coil so as to produce forces in the order of a few pico-newtons to nano-newtons on beads with diameters of 20 to 50 μm. Each coil is connected to one output of a multi-channel DC current supply, through an electrical relay switch. The relay enables us to change the direction of the current through the coil simply by altering the state of the relay, and hence change the orientation of the magnetic field generated by the coils.

3.2.2 Magnetic Beads

Super-paramagnetic beads are widely used in biological applications. They are composed of a polystyrene particle matrix with homogeneously incorporated nanometre-sized iron

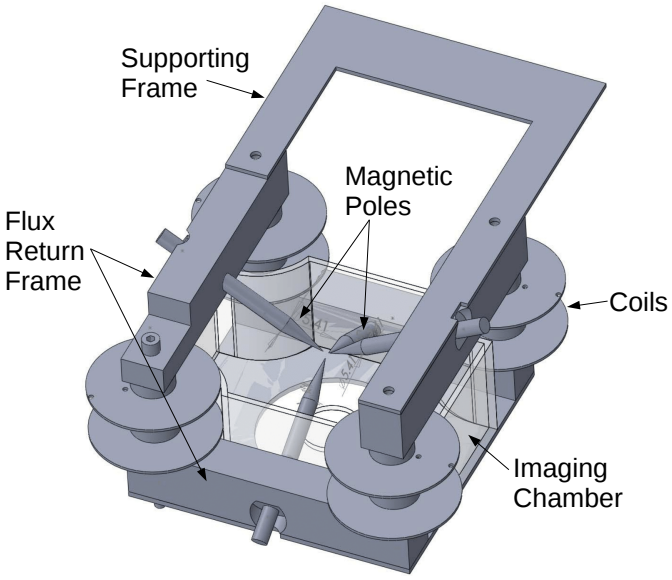

(A)

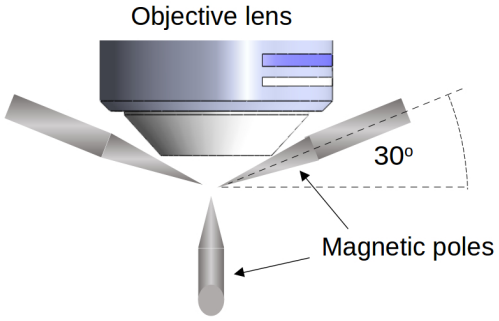

(B)

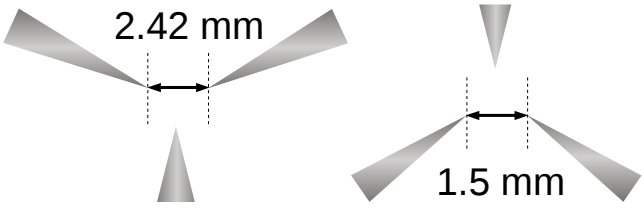

(C)

Fig. 3.2 The schematic diagram of the modified version of magnetic tweezers. (A) The magnetic tweezers with imaging chamber. (B) The angle of the poles to the horizontal line is 30 °. (C) The spacing is 2.42 mm for the top poles and 1.5 mm for the bottom poles.

oxide. Within a sufficiently strong magnetic field (> 0.5 T) produced by permanent magnets or electromagnets, the beads are magnetised [66]. The available sizes of magnetic beads are 18.82, 41.14 and 67.40 μm. The 41.14 μm bead size was chosen for the zebrafish experiments. The ability of magnetic tweezers to exert forces on the bead has been tested by injecting the bead into the specimen volume filled with a Newtonian fluid of known viscosity. In the experiment, only one bead is grafted in the embryo.

3.2.3 Magnetic Force

When an electrical current passes through the wire of the coil, a magnetic field is generated. The direction of the magnetic north pole can be determined by the thumb direction when wrapping the right hand around the solenoid with the fingers in the direction of the electrical current, which is known as the right hand rule [6]. Figure 3.3 demonstrates an example of the magnetic flux within the flux return frames and the poles, when the two coils take electrical current identical in both magnitude and direction.

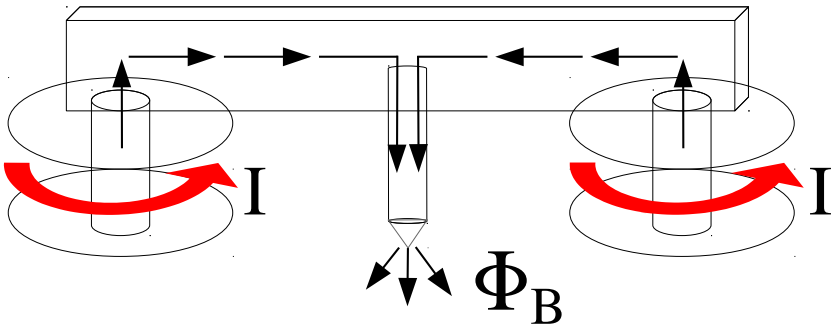

Fig. 3.3 The diagram describes the magnetic flux generated by electrical currents passing through the coil within the frame and the poles. The magnitudes of the currents are identical and the direction is counterclockwise.

The force on a magnetic bead is caused by the interaction between its magnetic dipole moment $\mathbf{m}$ and the gradient of an incident magnetic field $\nabla \mathbf{B}$. The magnetic moment is induced by the incident field and subject to the saturation properties of the super-paramagnetic materials in the bead:

$$\mathbf{m} = \frac{\pi d^3}{2\mu_0}\left(\frac{\mu_r - 1}{\mu_r + 2}\right)\mathbf{B}, \tag{3.1}$$

where the permeability of free space $\mu_0 = 4\pi \times 10^{-7}$ N A^{-2}, μ_r is the relative permeability of the bead, and d is the diameter of the bead. The magnetic force generated on the bead is:

$$\mathbf{F} = (\mathbf{m} \cdot \nabla)\mathbf{B}. \tag{3.2}$$

Substituting Equation (3.1) in Equation (3.2) we have [35, 48]:

$$\mathbf{F} = \frac{\pi d^3}{2\mu_0}\left(\frac{\mu_r - 1}{\mu_r + 2}\right)(\mathbf{B} \cdot \nabla)\mathbf{B}. \tag{3.3}$$

3.2.4 The Chamber and The Sample Mount

To image the zebrafish embryo, we used water-immersion objectives in order to minimise the difference in refractive index between the medium and the biological sample. A chamber, which could fill the entire space inside the magnetic tweezers, was designed to hold the culture medium for the zebrafish embryos (Figure 3.4). It was 3D printed on a MakerBot replicator 2X machine using Acrylonitrile Butadiene Styrene (ABS) filaments. Windows on each of the four side walls allowed us to observe the sample during positioning. They were cut from 2-mm thick acrylic sheets. Two of these windows had holes for the bottom poles to be screwed into the frames. At the bottom of the chamber, a fifth window was added for additional imaging during chamber positioning. The windows were sealed using silicone rubber and the assembled chamber was sealed with reusable pressure-sensitive adhesive Blu-tack.

A zebrafish embryo sample was mounted in an FEP capillary. The capillary was connected to the end of a cantilever, which could be horizontally slid into the chamber along the y-axis and rotated to a vertical position to fit between the magnetic poles. A thermistor was suspended near the chamber and a heating element (Silicone matt) was placed at the bottom of the chamber. A temperature controller was connected to them to keep the sample at its optimal temperature (28.5°C for zebrafish embryos).

The mounting and the sample size determine the spacing between the magnetic poles. In the final design, the vertical distance between the top poles and the bottom poles and the horizontal distance between the bottom poles were 1.5 mm. The space in the centre of the poles permitted the part of the embryo containing the magnetic bead to be adjusted and positioned at the centre. A camera (Raspberry Pi camera module) was attached to the bottom of the chamber to provide images through the bottom window, which helped to place the sample in the right position.

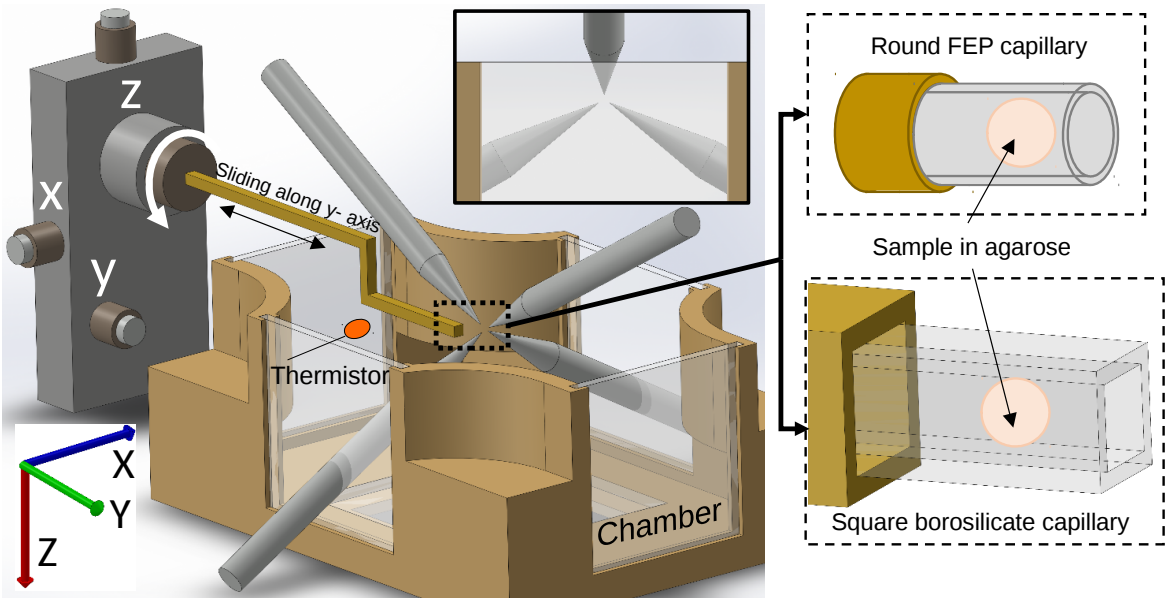

Fig. 3.4 This diagram illustrates a chamber designed to be compatible with magnetic tweezers. This design allows for immersion of the sample and objective lenses under LSFM. The cantilever, which is in the shape of a step in yellow, can be slid into the chamber along the *y*-axis horizontally and rotated to a vertical position by the XYZ translator and rotator. In the zoomed box, the sample could be mounted either in a round FEP capillary or a rectangular borosilicate capillary which is connected to the end of the cantilever. Images by courtesy of Radu Tanasa.

3.2.5 Final Design with LSFM

Light sheet fluorescence microscopy uses a thin plane of light which is able to section and observe tissues with sub-cellular resolution. The microscope is called a selective plane illumination microscope (SPIM). The fundamental idea of this type of microscopy is to illuminate the object perpendicularly to the direction of the observation axis. As shown in Figure 3.5 (A), the angle between the detection bead path and the illumination bead path is 90°. The illumination path consists of a laser source and cylindrical lens to focus the beam into a thin sheet of light. The expanded laser beam is focused in only one direction by this cylindrical lens. The laser light illuminates a fluorescently labelled sample from the side. Only fluorophores within the focal plane of the detection objective are excited [24, 80]. The excitation plane is then imaged by a wide-field detector system.

The specimens are exposed to only a thin plane of light, and, as a result, the signal to noise ratio is increased while specimen photobleaching and phototoxicity are minimised. The microscopy provides deep images of thicker transparent tissues or whole organisms

[83]. Hence, the LSFM is an ideal imaging tool to obtain 3D high resolution images of the zebrafish embryo. LSFM permits fast imaging for tracking the movement of the magnetic beads and long term imaging due to its low phototoxicity, which poses no restrictions for the study of changes in tissue dynamics during zebrafish embryo development. Our modified version of the magnetic tweezers successfully accommodated the microscopes, as shown in Figure 3.5 (B) and (C).

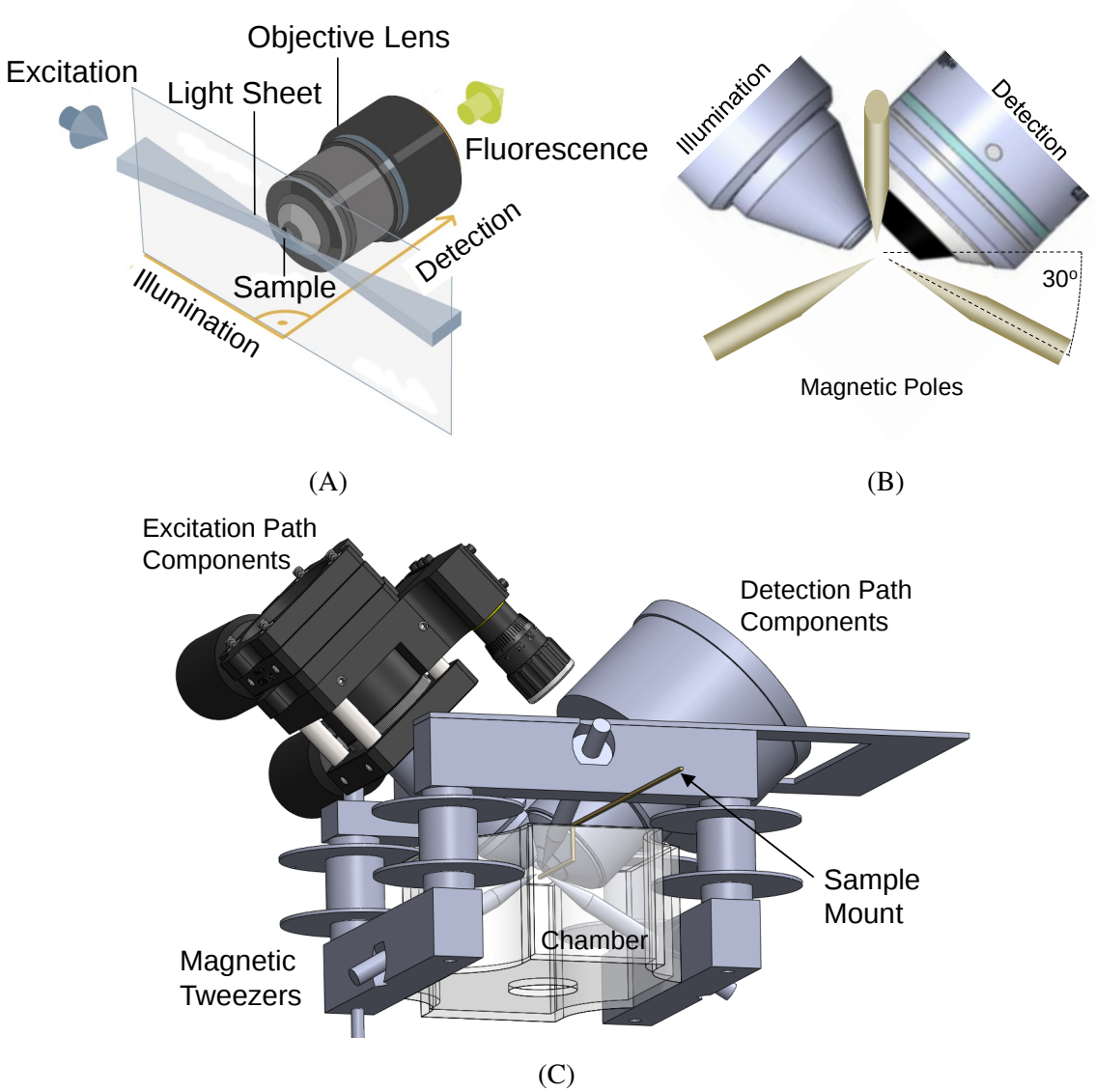

Fig. 3.5 The principles of LSFM and the final design of magnetic tweezers accommodated to LSFM objectives and the chamber. (A) In LSFM, the detection bead path is placed perpendicular to the illumination beam path. The figure is taken from Selchow and Huisken [87]. (B) The angle between the magnetic pole and horizontal plane is 30°. (C) The magnetic tweezers accommodated to LSFM objectives and the chamber.

3.3 Magnetic Force Calibration

Force calibration aims to determine a relationship between the configurations of electrical currents in the coil and the magnetic force vector acting on a bead in the specimen volume.

To calibrate the magnetic forces, beads were injected into a transparent silica rectangular capillary. The inner diameter of the capillary is 1.0 mm and the capillary wall has a thickness of 0.2 mm. The capillary is filled with silicone oil $(-Si(CH_3)_2O-)_n$, a transparent liquid with a viscosity of 49.2 cSt [1] at 25°C. It has a small variation with temperature and a 2% decrease in viscosity by a change in temperature of 1°C. The temperature around the capillary during calibration is measured by a thermistor to calculate the accurate kinematic viscosity. We will first introduce the imaging system for bead tracking, and then describe the magnetic force calculation.

3.3.1 Control Software and Bead Tracking

The purpose of the software is to control the electrical current in each coil. Hence, the electrical current from the DC power supply is controlled through serial communication by an Arduino microcontroller (ARDUINO DUE R3). Serial commands are sent from the software to the power supply to alter the magnitude and polarity of the current output. The produced heat is checked in real-time by evaluating the changes in the resistance of the coils. When the resistance is beyond the calibrated threshold, which indicates a high temperature, the coils are automatically disconnected from the power supply.

In order to track the position of the bead in 3D, a calibration microscope system was designed to visually observe the bead in the capillary and to track the position of the bead during bead movement (Figure 3.6). An objective lens (4× magnification) was mounted on a 3-axis micrometer manual translation stage (Thorlabs PT3/M, 25 mm motion range) on a vibrational isolation table. The vertical direction of the stage was actuated by a linear motor (The LTA-HS 50 mm High Speed Motorized Actuator). Two tube lenses were used, each connected to a camera (AVT Guppy F-503C) with a resolution of 2588 × 1940 pixels and a maximum frame rate of 13 fps. Each pixel corresponded to a distance of 0.5 μm, which was much smaller than the bead diameter. The light beams from the objective lens were added to the second camera by a beam splitter and a mirror. The capillary was held horizontally and moved under the microscope by another 3-axis micrometer manual translation stage. We managed to observe the same field of view with the same resolution from the two cameras by an off-focus distance of around 100 μm.

[1] 1 cSt = 1 $mm^2s^{-1} = 10^{-6}$ m^2s^{-1}.

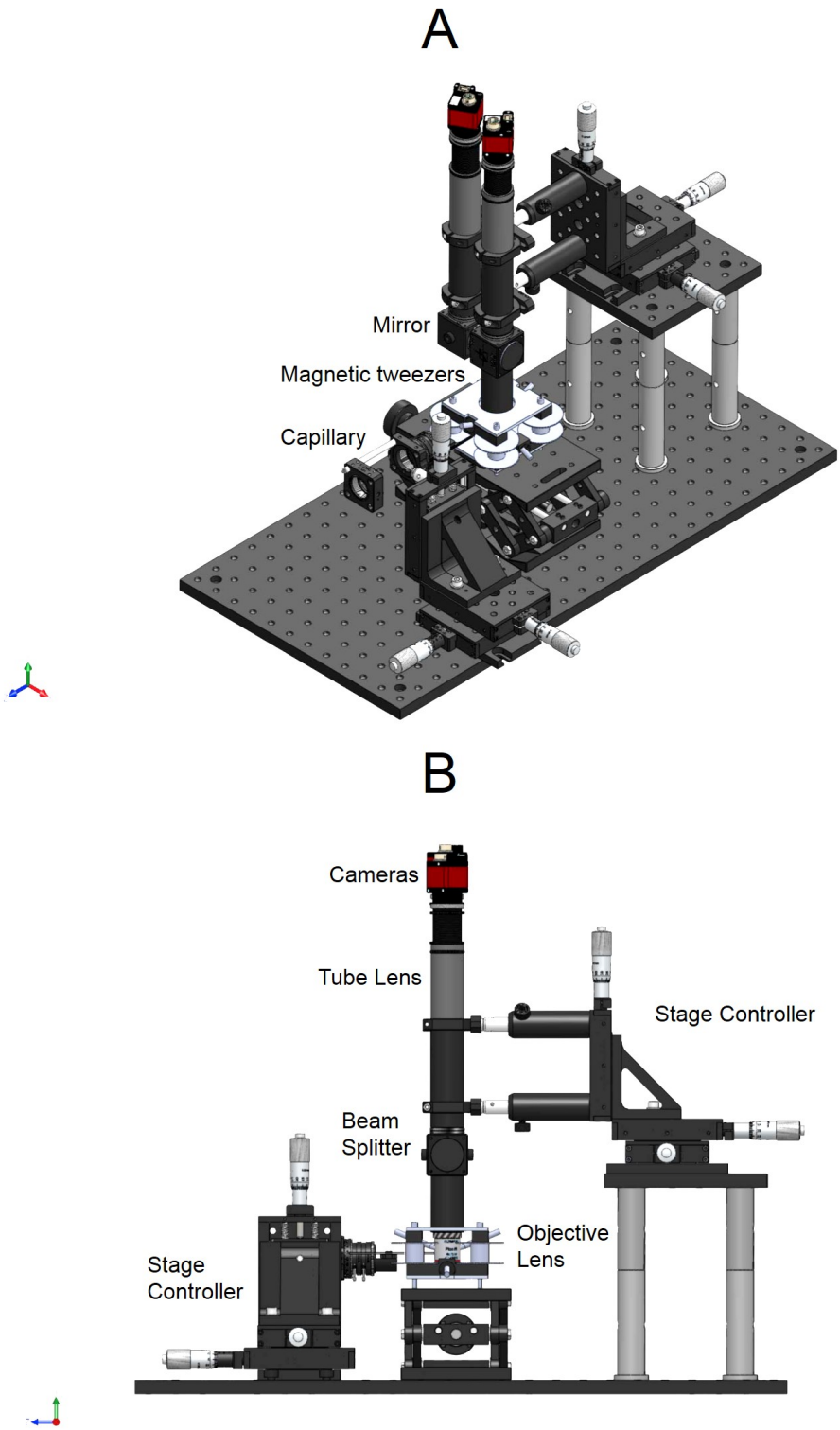

Fig. 3.6 Diagram of the layout of the calibration setup with optical imaging systems mounted. (A) Perspective view. (B) Side view. Images by courtesy of Radu Tanasa.

The imaging volume is defined as the interest space for embryo manipulation. The size of the volume is 300 μm $\times$ 300 μm $\times$ 300 μm around the centre of the poles. A Cartesian coordinate system is imposed on the imaging volume with the origin at the centre of the poles. The y-axis is along the line of the capillary and the x-axis is perpendicular to it. The z-axis is defined as positive vertically upwards. The coordinate system follows the right handed coordinate convention.

Bead detection was achieved using open source computer vision libraries (OpenCV). Images were cropped to an area of twice the bead diameter (hereinafter referred to as "cropped image"). The Sobel edge detection algorithm [102] was applied to the cropped images (hereinafter referred to as "filtered image"). The coordinates of the bead in the x-y plane are calculated by counting the pixels from the centre of the detected bead to the origin of the imaging volume (Figure 3.7 (A)). The bead position on the z-axis is determined by the focus parameters [95]. A focus parameter characterises how in focus the bead images is. It is defined as the ratio of the standard deviation of pixel values and their mean. If the initial image of the bead is sharp, the edges of the bead in the filtered image becomes thinner and brighter. In this case, the focus parameter is large because of a high standard deviation and a low mean. By taking a stack around the bead, a Lorentzian distribution of the focus parameter along the detection axis was revealed. We have obtained these distributions for both cameras and stored them in the control software (Figure 3.8 (A)). During bead tracking, focus parameters were calculated for both images and these values were stored in the profiles.

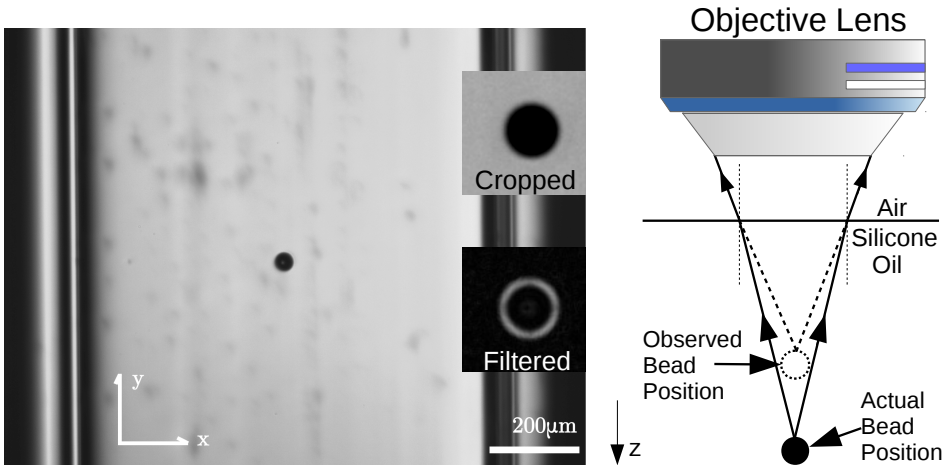

(A) (B)

Fig. 3.7 Bead observation and bead tracking in 3D. (A) An example image of the bead sample with indication of the coordinate system in the x-y plane. Scale bar: 200 μm. (B) The observed bead position in the live image and the actual position of the bead, as a result of different refractions in the air and in the silicone oil.

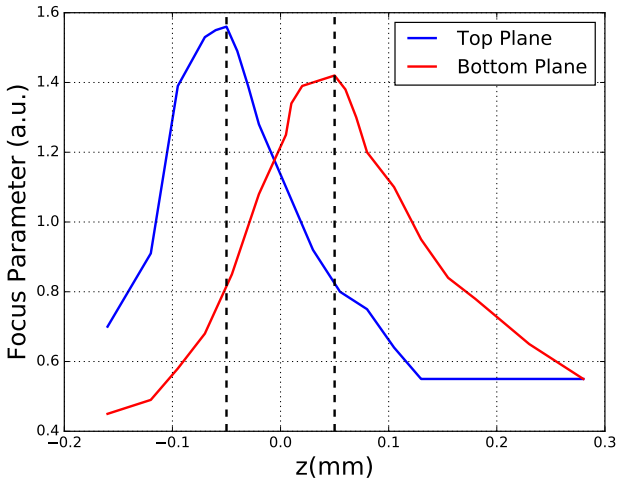

(A)

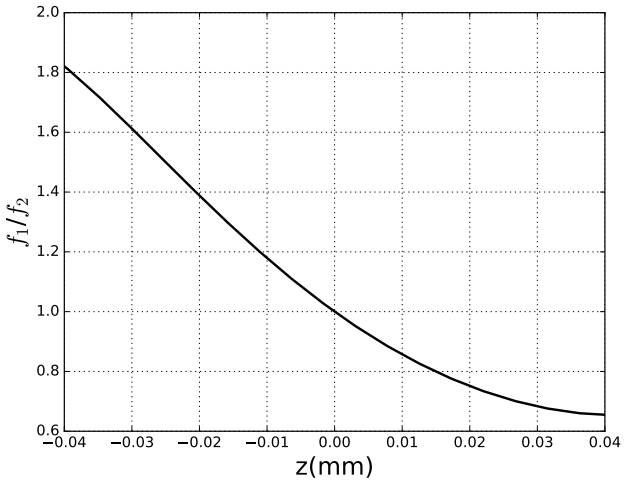

(B)

Fig. 3.8 Bead tracking in the direction of the z-axis. (A) The calibrated data of the focus parameters of the two tube lenses. (B) The bead position on the z-axis is detected by calculating the ratio of the two focusing parameters and fitting to the calibrated data.

Initially the cameras are moved manually in the z-axis until the bead is between the two planes and is visible in both camera images. The two focus parameters, f_1 for the cropped image and f_2 for the filtered image, are calculated. The bead position in the z-axis can be searched by fitting the ratio of f_1/f_2 to the calibrated data (Figure 3.8 (B)). When the bead moves away from the central line between the two image planes by more than 20 μm, the mechanical actuator will reposition the microscope to relocate the bead to the centre of the two planes.

However, the refraction in silicone oil is different from that in air. The refractive index of silicone oil is 1.40. Hence, the movement of the objective lens by the actuator, with the image plane movement, is corrected. For instance, by moving the objective lens (image planes) by 100 μm, the actual movement of a bead in the silicone oil will be 140 μm (Figure 3.7 (B)).

Finally, control software[2] is implemented in Python to integrate all the features described above, including controlling the electrical current, displaying and processing the image from the cameras, communicating with the electronic components in the setup, and operating the feedback loop.

3.3.2 Orientation and Reference

The coordinate system of the imaging from the LSFM objectives is different from that in the calibration imaging acquisition system. Hence, a referencing system is required to permit the switch between coordinate systems of the LSFM and the calibration microscope.

During calibration, a coordinate system of the calibration imaging system was defined according to the relative positions of the magnetic poles. A reference sample was needed that did not change position during the switch between two microscopes, as shown in Figure 3.9. A strip was cut from a glass cover slip with magnetic beads adhered to the top surface. The strip was attached to the mounting cantilever. One of the beads was selected as the reference bead, which was positioned in the centre of the magnetic tweezers. When the centre position was determined, the cantilever remained stationary. The whole experimental setup, including the magnetic tweezers and the sample holder, were attached to an optical breadboard and moved to the LSFM.

In the LSFM system, the selected central bead was located and positioned close to the centre of the image. During post processing, the exact location was calculated. The translational (along the x- and z-axis) and rotational (a 45° rotation around the y-axis) transformation were then determined between the two coordinate systems (Figure 3.9). The reference procedure had to be repeated every time a new calibration was carried out. Therefore, the magnetic force at each position in the LSFM images could be determined from the calibration model (Section 3.5) by transforming the coordinates to the corresponding coordinates in the calibration system.

In summary, we are able to get bead positions in either defined Cartesian coordinate system from the calibration microscopes or the LSFM microscopes. Next, we will measure the velocity of bead movement in the viscous fluid and calculate magnetic forces exerted on the

[2]The control procedure and calibration were designed with Radu Tanasa and Aleksander Chmielewski. Radu Tanasa implemented the GUI of the control software in the Python environment.

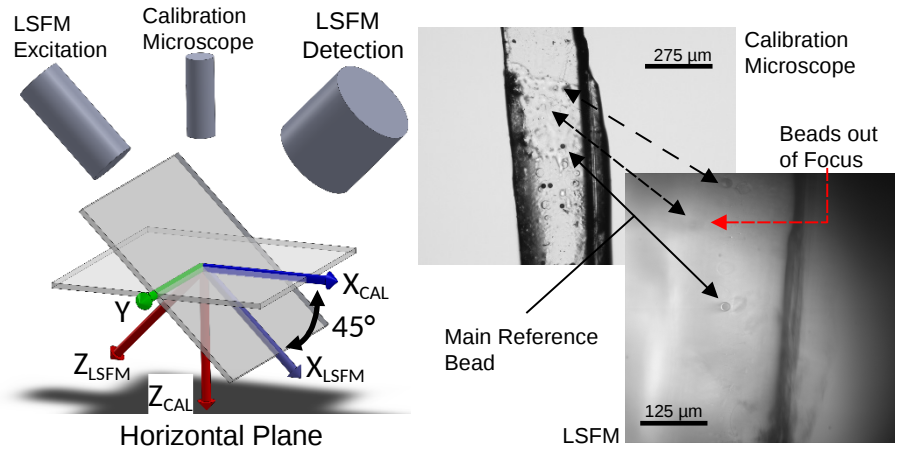

Fig. 3.9 The figure illustrates the orientation and reference procedure. The schematic diagram on the left shows the interplay between the LSFM coordinates system and the calibration microscope coordinates system. X_{CAL} and Z_{CAL} are the x and z coordinates for the calibration microscope, respectively, and X_{LSFM} and Z_{LSFM} are the x and z coordinates for the LSFM, respectively. The two coordinate systems have common y-axis. The diagram on the right shows the images of magnetic beads attached to the glass strip. Images by courtesy of Radu Tanasa.

beads according to bead force equilibrium. We first apply a range of current combinations to analyse the general bead motion and force vector. Then we focus on six current configurations which are able to move the bead in different directions in the specimen volume.

3.3.3 Magnetic Force Measurement

When there is no electrical current in the coil, a bead in the silicone oil is suspended if the gravitational force is identical to the buoyancy. If the bead moves in the liquid by a driven force, it experiences viscous drag force, the direction of which is opposite to the direction of the motion. The bead will then achieve a constant terminating (or setting) velocity. The viscous drag force can be determined by the Navier-Stokes equation [7]:

$$F_d = 6\pi\mu R v, \tag{3.4}$$

where F_d is the drag force acting on a small spherical particle with radius R, v is the velocity of the bead and μ is the dynamic viscosity of the fluid. The dynamic viscosity is obtained from $\mu = \nu\rho_l$, where ν is the kinematic viscosity of the fluid and ρ_l is the fluid density. For instance, if the bead sinks in the liquid, the viscous drag force is equal to the difference of the weight and the buoyancy on the bead:

$$F_d = \frac{3}{4}\pi R^3(\rho_b - \rho_f)g, \tag{3.5}$$

where ρ_b and ρ_f are the mass density of the bead and the fluid, respectively, and g is the gravitational acceleration.

When the electrical current is switched on and a magnetic force is exerted on the bead, the bead velocity in each dimension can be calculated by differentiating the bead displacement (change in position) by the number of image frames it takes (indicating the time). In the experiment, the magnetic force is in the order of nano-newtons and the maximum terminal velocity of the bead is around several microns per second. Calculations show that the acceleration period for the bead to reach the terminating velocity is far less than the time interval between frames. In this case, we assume that the bead moves at the terminating velocity between two consecutive frames so as to calculate the magnetic force from the force equilibrium:

$$\vec{\mathbf{F}} = \mathbf{0}. \tag{3.6}$$

In our measurement, the bead was moved by forces generated by various current combinations in silicone oil. Based on this broad investigation, six basic current configurations were selected. By applying these current configurations, we were able to move the bead in the direction of $\pm x$, $\pm y$ and $\pm z$, respectively, within the imaging volume. For example, with a simple feedback monitor of bead positions, it is possible to move the bead to achieve complicated trajectories, as shown in Figure 3.10. The details of these calibrated current configurations are introduced in Section 3.5.

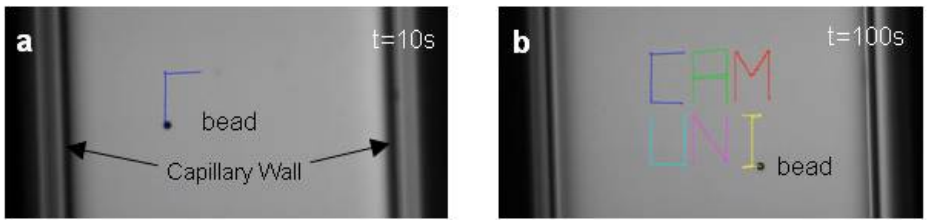

Fig. 3.10 Control of bead motion. A bead in the silicone oil is moved using the six principal current configurations. A simple feedback control is used to move the bead to the desired positions by switching on and off the current. (a) The bead is moved by the magnetic force. (b) The bead motion completes six letters 'CAM UNI' (Cambridge University) in two rows.

Next the bead was moved manually by the six current configurations to sample the specimen volume by applying the six principal current configurations, and the positions of

bead were tracked by the calibration microscope. A vector field of magnetic forces was calculated. These vectors are classified for each current configuration.[3]

The objective of data interpolation is to find a function which interprets the relationship of magnetic forces on the bead and the bead position in the specimen volume for each principal current configuration:

$$(F_x, F_y, F_z) = \mathbf{f}(x, y, z). \tag{3.7}$$

We know that the magnetic force depends on the magnetic moment of the bead and the gradient of the magnetic field (Equation (3.2)). The distribution of the magnetic field generated by the electromagnets is nonlinear. Furthermore, it is very time consuming to get the magnetic force vectors for every point in the imaging volume to establish a lookup table containing coordinates and corresponding force vectors. Hence, in the next section, we describe a machine learning algorithm which could be used to interpolate field vectors within the volume based on a limited number of data points.

3.4 3D Data Interpolation Algorithm

In the previous section, we introduced that the magnetic force vectors were sampled in the imaging volume for each principle current configuration. We are interested in interpolating the relationship between any position of the bead and the corresponding magnetic force vector from the limited measurement data. In this case, a non-parametric regression algorithm could be used to construct a 3D force field based on calculated force vectors, without the need to find fitting parameters. Besides, the dimensional components F_x, F_y and F_z in the force vector were measured independently according to the bead displacement in each dimension. The question can be simplified as three independent models which find the relationship between one component in the force vector and the bead position. In this section, the principle of the algorithm and its application for data interpolation are introduced.

3.4.1 Introduction

A nonparametric regression algorithm is a type of regression analysis in which the predictor takes no predetermined formula, but is built on information derived from the data. It is called supervised machine learning, which considers learning a relationship from inputs to

[3]The current configuration analysis and magnetic force sampling experiments for basic configurations were performed with Radu Tanasa.

outputs. Since it is a data-based learning process, it requires a large input sample size which must provide the model structure. Gaussian Process regression is the most commonly used learning method, and has been used for modelling magnetic field in many different studies [22, 84, 103].

Gaussian Process

Gaussian Process (GP) is a form of continuous stochastic process which is capable of modelling spatially correlated measurements. It extends multivariate Gaussian distributions to infinite dimensionality. In a GP, data are generated and located throughout some domain such that any finite subset of the range follows a multivariate Gaussian distribution. For example, suppose we have a set of arbitrary variables indexed by a continuous variable as a random function $f(x)$. A number of random function variables $f = \{f_1, f_2, ..., f_N\}$ and their corresponding inputs $X = \{x_1, x_2, ..., x_N\}$ are known. The set of random function variables follow a multivariate Gaussian distribution:

$$\begin{bmatrix} f_1 \\ f_2 \\ \vdots \\ f_N \end{bmatrix} \backsim \mathcal{N}(\mu, \mathbf{K}), \tag{3.8}$$

$$\mu = \begin{bmatrix} \mu_1 \\ \mu_2 \\ \vdots \\ \mu_N \end{bmatrix}, \tag{3.9}$$

$$\mathbf{K} = \begin{bmatrix} K_{11} & K_{12} & \cdots & K_{1N} \\ K_{21} & K_{22} & \cdots & K_{2N} \\ \vdots & & & \vdots \\ K_{N1} & K_{N2} & \cdots & K_{NN} \end{bmatrix}, \tag{3.10}$$

where $\mathcal{N}(\mu, \mathbf{K})$ describes a Gaussian distribution with mean μ and covariance $\mathbf{K}$. The mean function and the covariance function drive the entire Gaussian Process to specify a particular GP prior. Normally GPs assume that $\mu = 0$ everywhere, since any offsets and simple trends are subtracted out before modelling. The covariance function $\mathbf{K}$ (a.k.a.

kernel) characterises the correlations between different points in the process. It determines the properties of the functions such as smoothness, lengthscales, amplitudes, noise level, etc. In our approach, we aim at modelling the smooth magnetic force field function with coordinates of beads as the input and the scalar force magnitude in one dimension as the output. The squared exponential (SE) covariance function is the most common choice in machine learning.

The SE covariance function can generate smooth sample functions which are infinitely differentiable:

$$k(x,x') = {\sigma_f}^2 \exp\left(\frac{-(x-x')^2}{2l^2}\right), \tag{3.11}$$

where ${\sigma_f}^2$ and l are two hyperparameters which govern the properties of sample functions. l is the expected length-scale of variation of the target learning function. This should be a large value to cover a wide range for the function. ${\sigma_f}^2$ is the maximum allowable covariance. When $x \approx x'$, the covariance function approaches its maximum, indicating that $f(x)$ is perfectly correlated with $f(x')$. If the distance between x and x' is large, $k(x,x') \approx 0$, showing that these two points are far away from each other.

The observation data are often noisy due to measurement errors. Therefore, each observation data y could be related to a random function $f(x)$ through a Gaussian noise model:

$$y = f(x) + \mathcal{N}(0, {\sigma_n}^2) \tag{3.12}$$

Then a noise term in the covariance function is included:

$$k(x,x') = {\sigma_f}^2 \exp\left(\frac{-(x-x')^2}{2l^2}\right) + {\sigma_n}^2 \delta(x,x'), \tag{3.13}$$

where $\delta(x,x')$ is the Kronecker delta function, which is $\delta(x,x') = 0$ when $x \neq x'$, and $\delta(x,x') = 1$ when $x = x'$.

In summary, we could use the Gaussian Process to generate smooth spatial field data with a zero mean squared exponential covariance function (kernel). Next we will introduce how to regress using GP.

Gaussian Process Regression

A Gaussian Process regression is an algorithm of interpolation for which the interpolated targets are modelled by a Gaussian Process governed by prior covariances. Starting from

Equation (3.8), assume that we have n training input and output data pairs $(\mathbf{X}, \mathbf{y})$ and a new input location X_*, at which we are going to make predictions. Then we could write as:

$$\begin{bmatrix} \mathbf{y} \\ y_* \end{bmatrix} \backsim \mathcal{N}\left(\mathbf{0}, \begin{bmatrix} K & {K_*}^T \\ K_* & K_{**} \end{bmatrix}\right), \tag{3.14}$$

where $K = \begin{bmatrix} k(x_1,x_1) & k(x_1,x_2) & \cdots & k(x_1,x_n) \\ k(x_2,x_1) & k(x_2,x_2) & \cdots & k(x_2,x_n) \\ \vdots & & & \vdots \\ k(x_n,x_1) & k(x_n,x_n) & \cdots & k(x_n,x_n) \end{bmatrix}$, $K_* = [k(x_*,x_1) \quad k(x_*,x_2) \quad \cdots \quad k(x_*,x_n)]$

and $K_{**} = k(x_*,x_*)$. The diagonal element of K is ${\sigma_f}^2 + {\sigma_n}^2$. Then we will investigate the conditional probability $p(y_* \mid \mathbf{y})$. The probability could be defined as the likelihood of the prediction for y_* when given $\mathbf{y}$. In a GP, the probability also follows a Gaussian distribution:

$$y_* \mid \mathbf{y} \backsim \mathcal{N}(K_* K^{-1}\mathbf{y}, K_{**} - K_* K^{-1} K_*^T). \tag{3.15}$$

The best estimation for y_* is the mean of the distribution:

$$\overline{y_*} = K_* K^{-1}\mathbf{y}, \tag{3.16}$$

and the variance shows the uncertainty in the estimation:

$$var(y_*) = K_{**} - K_* K^{-1} K_*^T. \tag{3.17}$$

The GP model is a probabilistic model that allows us to select covariance hyperparameters directly from the training data. If these parameters $\eta = \{l, \sigma_f, \sigma_n\}$ are not suitably selected, the result will be nonsense. However, it is not analytically possible to place a prior and compute the posterior probability on hyperparameters since we know little about what these parameters should be. As an alternative solution, the marginal likelihood is calculated as a cost function and the aim is to maximise the *log* marginal likelihood $\mathscr{L}$ with respect to the hyperparameters [61, 77, 106]:

$$\mathscr{L} = \log p(\mathbf{y}|\mathbf{x}, \eta) = -\frac{1}{2}\mathbf{y}^T K^{-1}\mathbf{y} - \frac{1}{2}\log|K| - \frac{n}{2}\log 2\pi. \tag{3.18}$$

In summary, we use covariance functions with a limited number of hyperparameters to control the fitted function. The optimisation is not done with the function variables directly but integrating over uncertainty. The computational cost for the marginal likelihood

maximisation depends largely on the choice of covariance function and the size of the training data. However, the quality of solutions is influenced by the number of training data and the sampling frequency over the domain, as most non-parametric regression models have. In our study, we use the Gaussian Process Regression Model in the $scikit-learn$ library in Python. Next, we investigate the effects of different parameters on the performance of the GP regression model in Python.

3.4.2 Regression Parameter Selection

In this section, we define a Gaussian Process regression model with squared exponential covariance function in Python. The main parameters in this model are the standard deviation of noise (noise level) σ_n and the characteristic length-scale of the learning function l. The optimised prediction of Gaussian regression is a result of the maximisation of the marginal likelihood estimation for the given parameters. In the Gaussian model, the uncertainty of estimation is shown by the variance (Equation (3.17)). The model calculates the variance for each predicted result. In the following examples, we plot the 95% confidence level in each figure to indicate the uncertainty of the estimation.

Here we examine these parameters with three sets of training data: a single-variate function with noiseless data, a single-variate function with noisy data, and a multi-variate function with noisy data, respectively.

Single-Variate Interpolation

The length-scale of variation l is first examined using a single-variate function with no noise. A simple noise-free linear function is defined as $f(x) = x$. A number of test data x and corresponding $f(x)$ are selected between the interval [0, 15] as the training data (Figure 3.11). The values of l are [10^{-1}, 1, 10], ranging from a tiny distance to the range of the interval. In Figure 3.11 (A), when l is small, the maximum likelihood is estimated only with the closest neighbours. Good fitting is obtained between consecutive training data points, however, the prediction on the points where no training data is given is poor ($5 < x < 10$, $x < 1$ and $x > 12$). The variance of the predictor is high. In Figure 3.11 (B), l is increased but is smaller than the range of the training data. In Figure 3.11 (C), l is increased to 10 which covers the range of the training data. The prediction and expectation curves coincide. A lower level of variance yields narrow confidence intervals and more precise estimates of the function. From this example, it can be concluded that the quality of Gaussian Process

regression depends largely on the choice of length-scale. Short length-scales result in a rapidly growing predictive variance, while large length-scales introduce irrelevant features.

Next we examine the effects of the noise level σ_n on the fitting of the same target linear function. Similarly, a number of test data x and corresponding $f(x)$ are selected between the interval [0, 15] as the training input (Figure 3.12). Each training data $f(x)$ is added with random noise which follows a normal distribution with zero mean and standard deviation σ_n = 0.5. In the python model, a parameter *nugget* is added to the diagonal of the correlation matrix between training points. In the squared exponential correlation function, the normalisation is equivalent to specifying a fractional variance in the input, which is defined as

$$nugget_i = [\frac{\sigma_i}{y_i}]^2, \tag{3.19}$$

where i is the index of the data point [73]. In this experiment, a proper length-scale l is selected for all tests. In Figure 3.12 (A), the noise parameter is not taken into account and, as a result, the prediction is noisy. In Figure 3.12 (B) and (C), the selected standard deviation of noise is [0.1, 0.5]. The results show that a reasonable noise parameter which reflects the noise level of the training data can produce smooth and precise fitting.

Multi-Variate Interpolation

Previous examples have shown that Gaussian Processes can be used as a robust learning method for noisy data recovery of a single variate linear function. In our calibration problem, the nonlinear magnetic force function has three variables (x,y,z) and 3D output (F_x,F_y,F_z). As the force data in each dimension is measured independently, the Gaussian model could be split into three sub-models, each of which takes the bead position (x,y,z) as the input and one of the dimensional components F_n as the output.

To investigate the performance of the Gaussian Process regression model with three input variables, a nonlinear function $f(x,y,z) = x^2 + y^2 + z^2$ is defined. A number of input vectors (x,y,z) between the interval [-1.0, 1.0] and the corresponding output values $f(x,y,z)$ are selected as the training data (Figure 3.13). The output training data $f(x,y,z)$ is added to random noise which follows a normal distribution with zero mean and standard deviation σ_n = 0.1. The characteristic parameters are: the length-scale $l = 3$ and the standard deviation of noise σ_n = 0.1.

Figure 3.13 gives an explicit presentation of the fitted function on each axis in 3D. In each dimension, within the range of [-1, 1], the inferred data is close to the expectation. However, the predicted results in the ranges of [-1.5, -1.0] and [1.0, 1.5] are poor. The input training

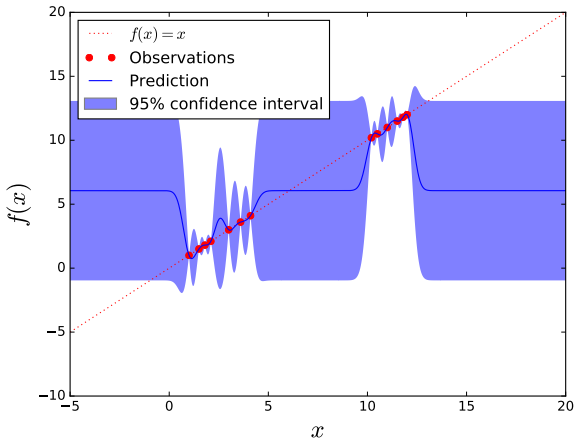

(A)

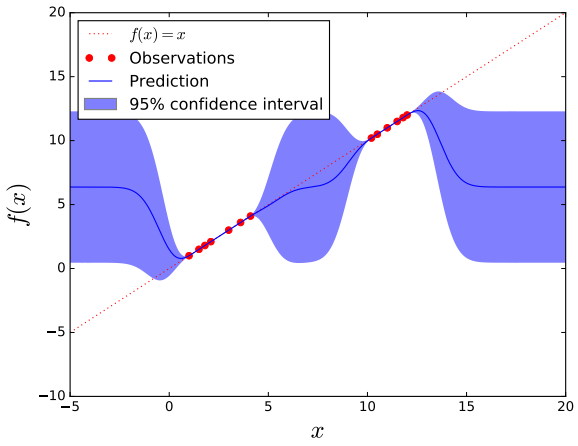

(B)

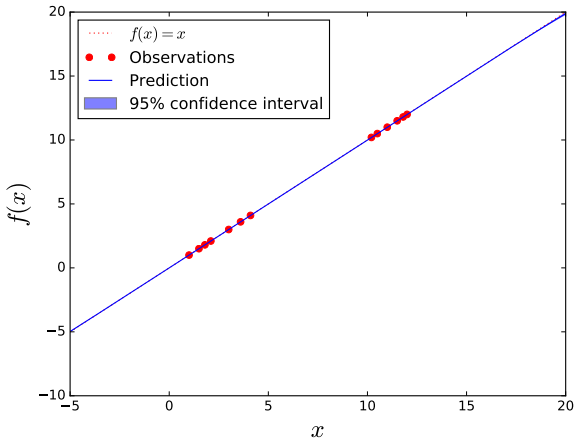

(C)

Fig. 3.11 Prediction by Gaussian Process regression model of linear noise-free observation data. The figures illustrate the expected function (red dashed line), the observations (red dots), the predicted function (blue line) and the probabilistic nature in the form of a pointwise 95% confidence interval. (A) Poor fitting with short length-scale. (B) Fitting with larger length-scale but not necessarily covering the range of the input data. (C) Good prediction with good selection of length-scale.

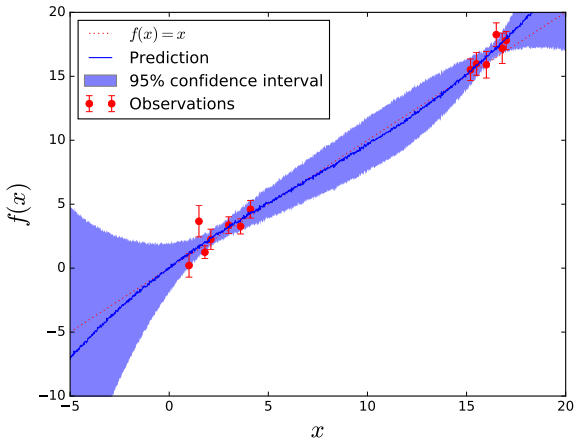

(A)

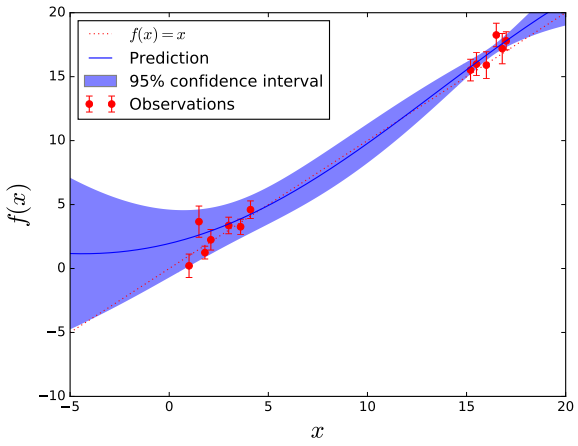

(B)

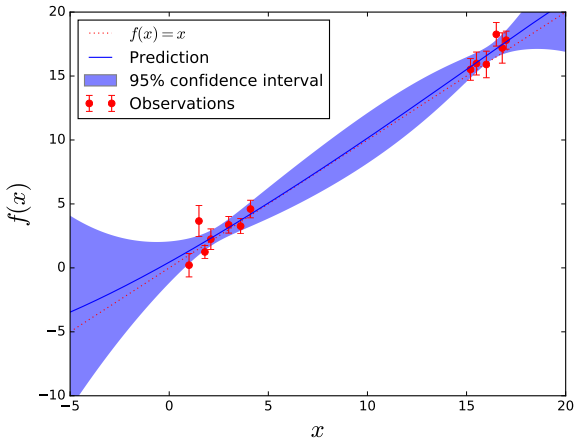

(C)

Fig. 3.12 Prediction by Gaussian Process regression model of linear observation data with noise. The figures illustrate the expected function (red dashed line), the observations (red dots), the predicted function (blue line) and the probabilistic nature in the form of a pointwise 95% confidence interval. (A) Noise is not taken into account. (B) Noise level is underestimated. (C) Noise level is reasonable and the fitting is smooth and precise.

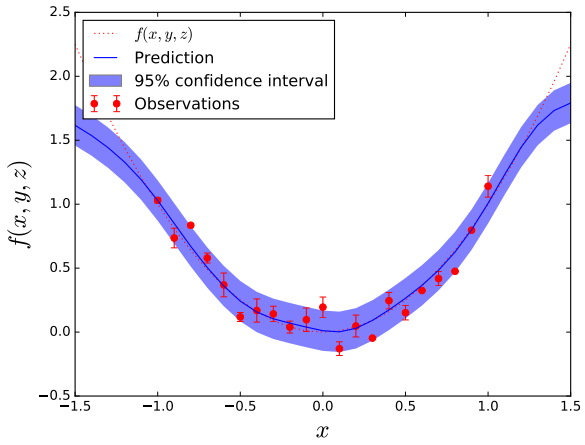

(A)

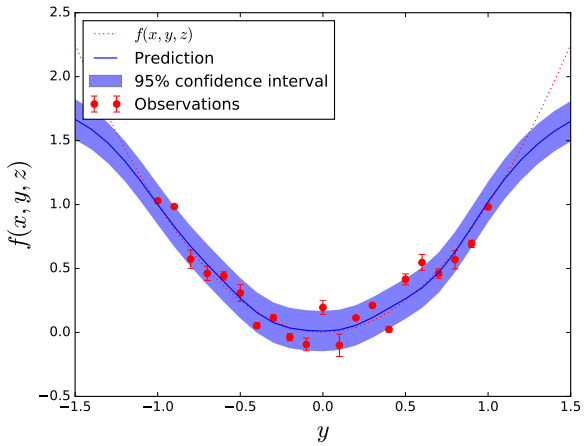

(B)

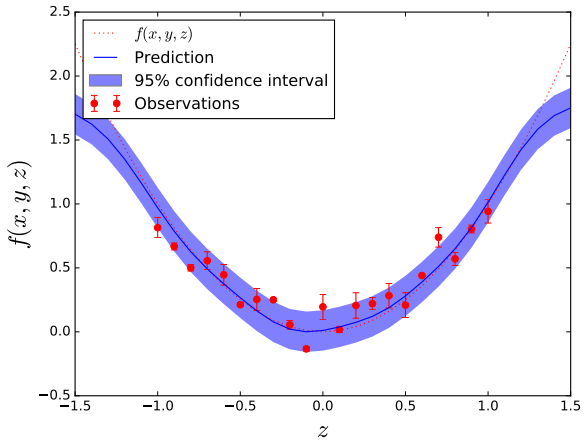

(C)

Fig. 3.13 Prediction by Gaussian Process regression model of three-dimensional non-linear observation data. The figures illustrate the expected function (red dashed line), the observations (red dots), the predicted function (blue line) and the probabilistic nature in the form of a pointwise 95% confidence interval. (A) Prediction of $f(x,y,z)$ on the x-axis. (B) Prediction of $f(x,y,z)$ on the y-axis. (C) Prediction of $f(x,y,z)$ on the z-axis.

data is not included in these intervals, and as a result, the model does not have sufficient learning information. The precision of the prediction decreases and the relative percentage error between the true value and the inferred value is around 30%. This result indicates that Gaussian Process is not robust for extrapolation with nonlinear functions.

In summary, these three regression examples provide evidence that the Gaussian Process regression model can be used for the purpose of 3D magnetic force calibration. For the calibration, we aim to obtain smooth and continuous magnetic force field vectors in the specimen volume. In our GP regression model, the input training data are the coordinates of the bead (x, y, z) and the output training data is the magnetic force vector [F_x, F_y, F_z]. The magnetic force at any position in the volume can then be inferred by the model. The details are introduced in the next section.

3.5 GP model for Magnetic Force Calibration

In the procedure for magnetic force measurement, the coils were numbered, as shown in Figure 3.14. The positive flow direction of the electrical current was defined as counter-clockwise. We have chosen six basic current configurations which can exert forces on the bead to move it in the imaging volume. The diameter of the bead used in the calibration experiments was 18.82 μm. The bead was moved by these six configurations of current to sample the imaging volume. The magnetic force vectors at each sampling point on the bead trajectories were calculated for each current configuration. In this section, we build a Gaussian Process regression model to establish the magnetic force map for these six current configurations. The demonstration is aided by examples of data collection for current configuration [2.5 A, 2.5 A, 0, 0].

3.5.1 Building the Model

Data from each current configuration is treated with separate models. The training input data for the model are the bead position coordinates in the calibration imaging system, and the training output data is the corresponding magnetic force in each dimension. The model learns from the training data and predicts the magnetic forces for any given positions within the specimen volume. This is described as:

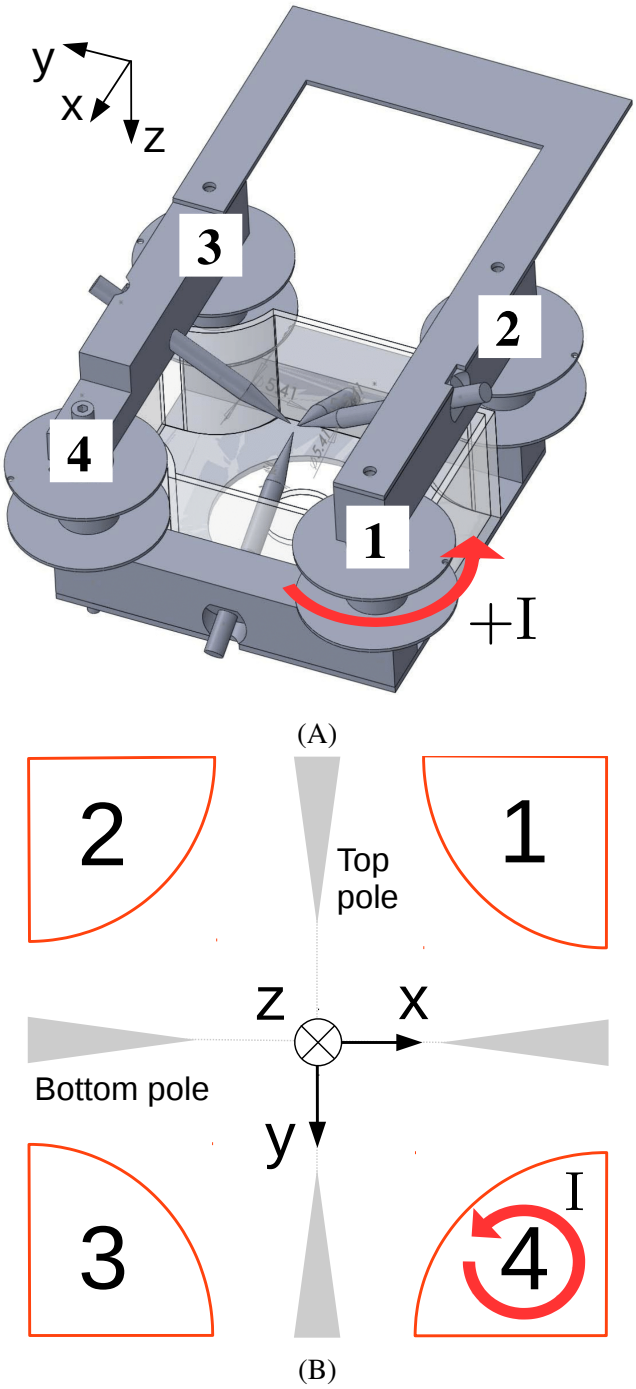

Fig. 3.14 The diagram shows the indices of the coils (1, 2, 3, 4), the poles, the positive flow direction of the electrical current (counter clockwise) and the coordinate system in the calibration system. (A) The prospective angle. (B) The view of the calibration image from the bright field camera.

$$F_x = GP(x,y,z), \tag{3.20}$$

$$F_y = GP(x,y,z), \tag{3.21}$$

$$F_z = GP(x,y,z), \tag{3.22}$$

$$|\,\mathbf{F}\,| = \sqrt{F_x^2 + F_y^2 + F_z^2}, \tag{3.23}$$

where F_x, F_y and F_z are the dimensional components of the predicted magnetic force $\mathbf{F}$, and *GP* is the Gaussian Process regression model which is built on the training data.

The training data were carefully selected. In the process of bead tracking, the selected frame rate of the camera is 10 frames per second. As a result, each trajectory contains data points in high density (Figure 3.15 (A), current configuration [2.5 A, 2.5 A, 0, 0]). The distance between trajectories is much larger than the distance between two adjacent points on the same trajectory. Furthermore, the number of data points on each trajectory exceeds the maximum number required for learning. The model cannot detect significant variations from two adjacent points and predict the values at points not included within the bead trajectories. In this case, the data points used as training data were selected according to a distance of equal lengths. The number of data points on each trajectory were reduced to 10% of the full data points to create evenly distributed data points in the specimen volume (Figure 3.15 (B)). The average distance between adjacent data points was $\sim 10\ \mu$m.

Figure 3.16 shows the predicted results by the reduced number of training data points for current configuration [2.5 A, 2.5 A, 0, 0]. At the centre of the imaging volume, the force is directed towards -*y* with a magnitude of around 1.0 nN. The asymmetry of the magnetic force field is a consequence of the unbalanced number of turns in the coils.

3.5.2 Validating the Performance of the Model

In the Gaussian regression model, the only known information is the measured magnetic forces. We could use the measured data to validate the performance of the prediction on these trajectories. However, the prediction results at positions which were not measured cannot be validated.

To validate the prediction performance, two different approaches have been used. First, the positions of the training data points in each configuration were used to generate similar training data using a 3D analytical force model, for which the true values were known, and calculated the MAPE between the inferred values and the true values. In addition, we selected

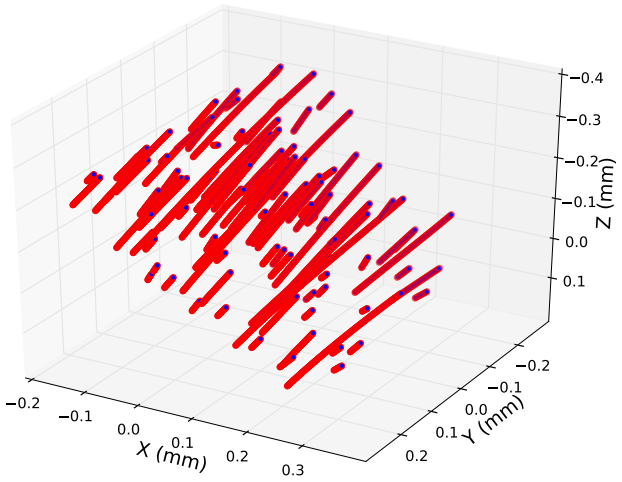

(A)

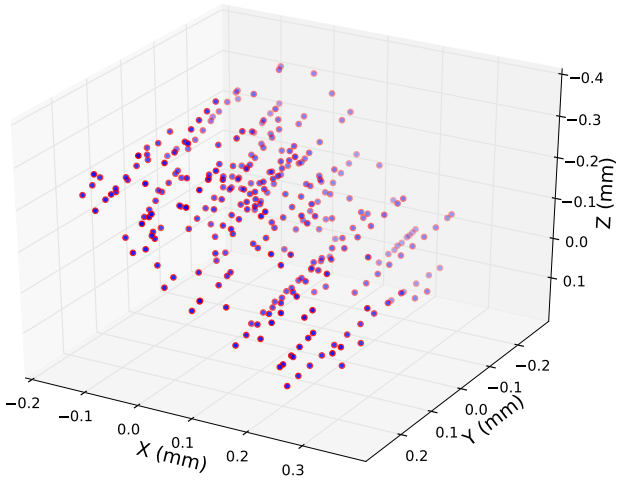

(B)

Fig. 3.15 The diagrams present the bead trajectories and the training data points for current configuration [2.5 A, 2.5 A, 0, 0]. (A) The full bead trajectories sampling the specimen volume. (B) The reduced number of data points in the specimen volume used as the training data sets for the GP model. In this case, the total number of data points is reduced to 10% of the initial raw data.

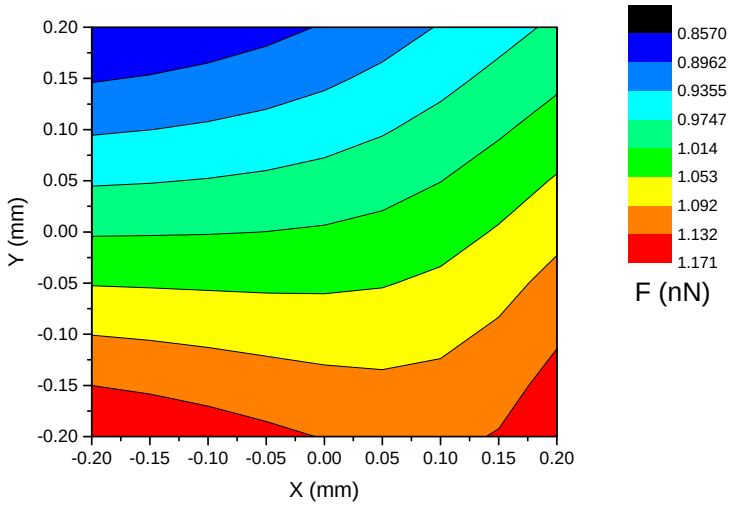

(A)

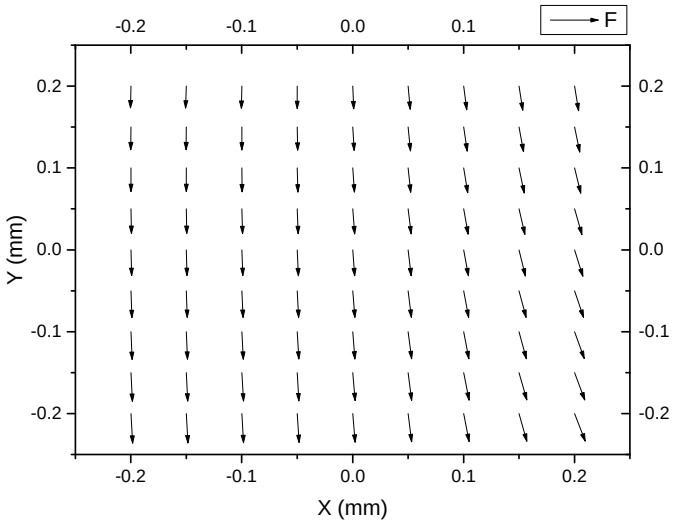

(B)

Fig. 3.16 Prediction of magnetic force field by Gaussian Process regression model for current configuration [2.5 A, 2.5 A, 0, 0]. The dominant direction of the magnetic force is -*y*. (A) The contour map illustrates the variations of the force in the *x*-*y* plane and *z*=0. (B) The quiver plot indicates the direction of the force vectors on the same plane as (A).

a number of data points on the bead trajectories as evaluation data which were not used for learning purposes, and examined the MAPE between the predicted forces and the measured forces.

The mean absolute percentage error (MAPE), or the mean absolute percentage deviation (MAPD), is used to assess the accuracy of a prediction method. The MAPE between the expectation and the prediction is calculated as:

$$MAPE = \frac{100}{n}\Sigma_{i=1}^{n}\left|\frac{F_i - \hat{F}_i}{F_i}\right|, \tag{3.24}$$

where F_i is a vector of n actual values and $\hat{F}_i$ is a vector of n predictions. The absolute value of the relative error is summed for every predicted point and divided by the number of fitted points n. Multiplying by 100 makes it a percentage error. A small MAPE value demonstrates a small deviation to the expectation [98]. Next, the analytical force model is introduced.

Analytical Force Model

Vicci [101] shows that monopole approximation is solely reasonable if the pole has a symmetrical tetrahedral geometry (Figure 3.17 (A)). In this configuration, four monopoles represent the four physical poles in the magnetic tweezers. Figure 3.17 (B) shows the example geometry of monopole configuration which approximates our physical pole system. The monopoles are located at the positions of the pole tips. Generally, the excitation strength of a magnetic field generated by 4 monopoles is:

$$\mathbf{B} = \sum_{j=1}^{4}\frac{q_j}{r_j^2}\mathbf{u_j}, \tag{3.25}$$

where r_j is the distance between the bead and the j^{th} monopole, $\mathbf{u_j}$ is the unit vector towards the monopole, and q_j is the strength of the monopole. Since there is no experimental evidence showing the existence of monopoles, the total strengths of the monopoles should be zero:

$$\sum_{j\neq i}^{4} B_j = -B_i. \tag{3.26}$$

Hence, the magnetic force on the bead can be determined by:

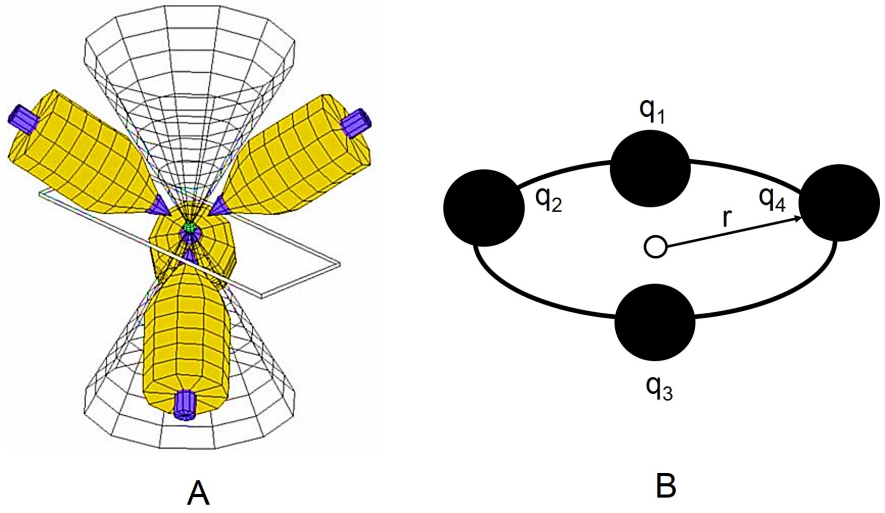

Fig. 3.17 3D analytical bead force model (magnetic monopole model). (A) Four cylindrical magnetic iron cores converge towards it from the centres of the four faces of the tetrahedron Vicci [100, 101]. (B) Schematic diagram of the monopole representation showing the geometry.

$$\mathbf{F} = (\mathbf{B} \cdot \nabla)\mathbf{B} = \sum_{j,k} \frac{2q_j q_k \mathbf{u_j} \cdot \mathbf{u_k}}{r_j^2 r_k^2} (\frac{\mathbf{u_j}}{r_j} + \frac{\mathbf{u_k}}{r_k}). \tag{3.27}$$

Similar to the bead trajectories in the experiments in the previous section, we generated 3D force data with noise by the monopole model by assigning proper values to the parameters. The positions of the training data points were the same as those in Figure 3.15. Figures 3.18 and 3.19 show the expected data (A), the training data (B) and the prediction (C) in the x-y plane and the x-z plane. Tests were performed with the positions of the training data for all six configurations. The MAPE between the true values and the predicted values in the imaging volume is always $< 10\%$, which indicates that the selected training data provides sufficient information for the learning algorithm.

Evaluation Data from Bead Trajectories

Another 10% of data points on the bead trajectories were selected as evaluation data. These data points were not used for the learning process. The quality of the prediction was validated by calculating the MAPE between the values of the measured force and the predicted values at these bead positions. The MAPE for each configuration was calculated and was always $<$ 5%.

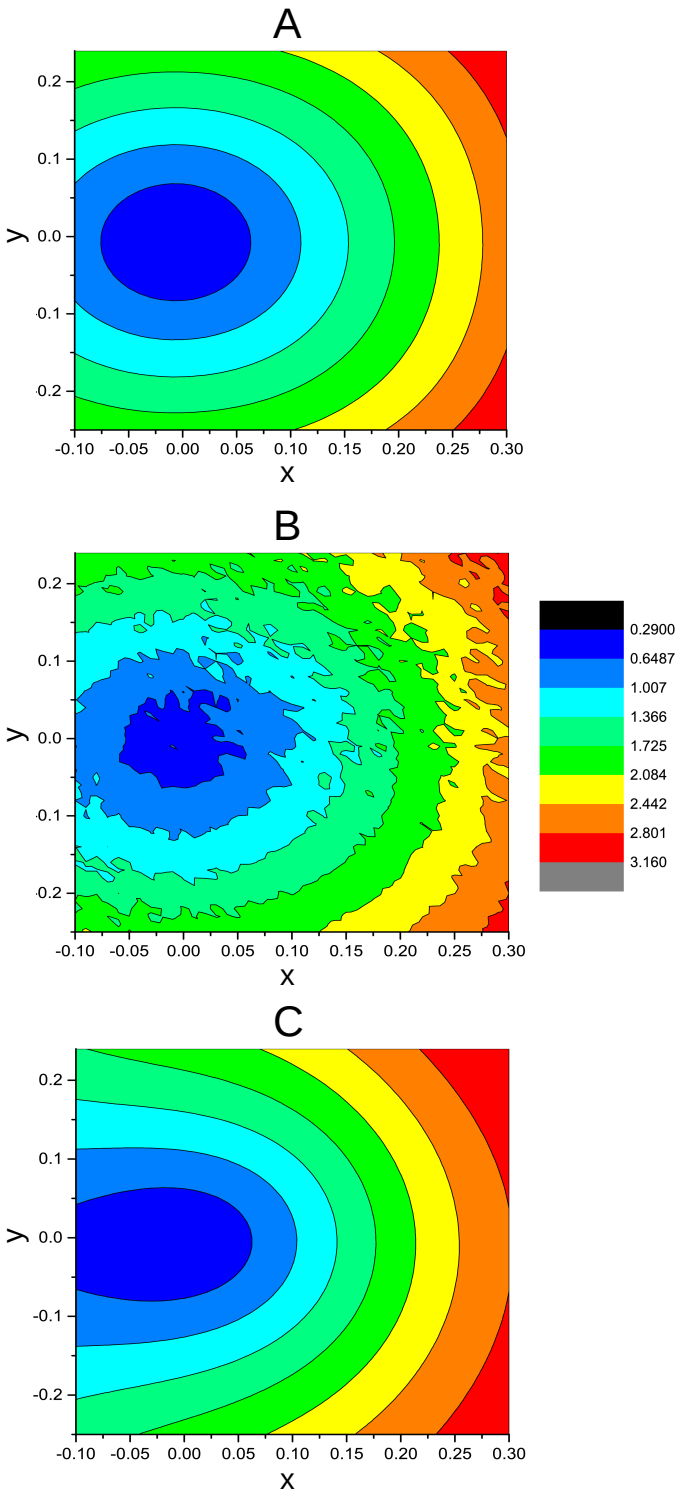

Fig. 3.18 Interpolation by Gaussian Process regression model of monopole force data. The figures illustrate the force contour map in the *x*-*y* plane. (A) The expected force contour map calculated from the monopole. (B) The training data added with random noise (noise variation is 0.1). (C) The predicted force contour map in the same plane by the Gaussian Process regression model.

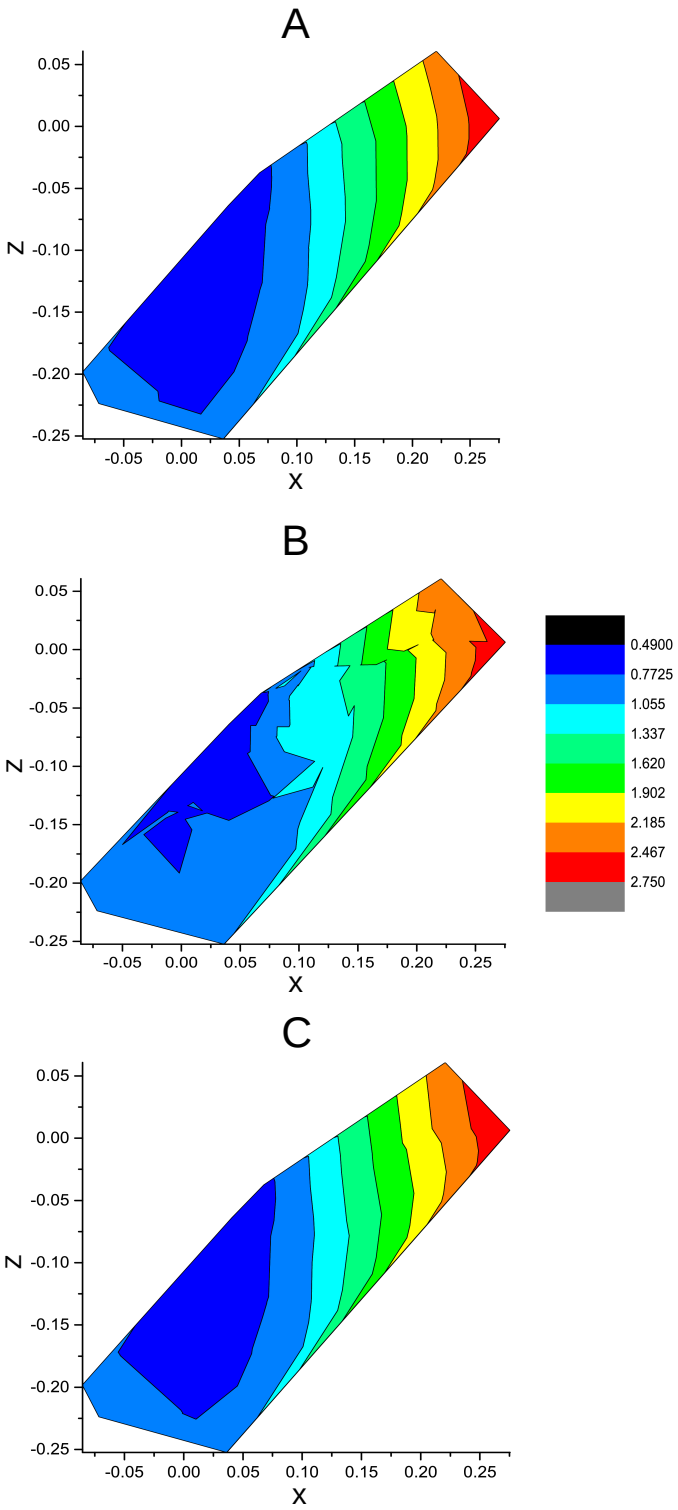

Fig. 3.19 Interpolation by Gaussian Process regression model of monopole force data. The figures illustrate the force contour map in the x-z plane. (A) The expected force contour map calculated from the monopole. (B) The training data added with random noise (noise variation is 0.1). (C) The predicted force contour map in the same plane by the Gaussian Process regression model.

3.6 Summary

This chapter presented the development process of the electromagnetic tweezers for 3D micromechanical measurement. The main function of the magnetic device is to apply a 3D force vector to the magnetic bead and to manipulate the bead movement in biological tissues to measure the mechanical properties of cells during morphogenesis. The design of the device geometry was required to allocate sufficient space for the sample specimen and the microscopes. The bead should be tracked in the images from the microscopes and hence the 3D positions of the bead can be derived. Finally, magnetic forces should be calibrated to establish the relationship between the electrical current in the coils and the resulting force on the bead in the imaging volume.

The original design of the magnetic device from Fisher et al. [35] was modified to allow more space for the sample and mounting chamber, and to accommodate the LSFM microscopes. The length of the flux return frame was increased from 7.5 cm to 10 cm, and the angle of each pole to the horizontal line was changed to 30°. Furthermore, the distance between the tips of the poles was also increased. Different configurations of electrical currents were applied to explore the range of magnetic forces generated in the volume. The results showed that the new device is able to generate forces in order of a few pica-newtons to nano-newtons on beads with a diameters of 20 to 50 μm.

Two imaging systems were used for observing the bead: the calibration imaging system and the LSFM. The calibration microscopes included one objective lens and two tube lenses, each of which was connected to a camera. A Cartesian coordinate was imposed on the imaging volume. The x-axis and y-axis were in the horizontal plane and perpendicular to each other. The two vertical cameras provided the images of the x-y planes, from which the x and y coordinates of the bead were derived. A focus parameter was defined as the ratio of the standard deviation of pixel values and their mean to characterise the focus intensity of the bead images. The two focus parameters were calculated when the bead was located between the focus planes of the two cameras. The bead position in the z-axis was obtained by fitting these two parameters to the pre-calibrated data. The coordinate system in the LSFM system is different from the pre-defined coordinate system for the calibration system. Hence, an orientation and reference system was designed to provide consistent position information during the switch between the two imaging systems. A reference bead was selected and positioned in the centre of the magnetic tweezers. The translational (along the x- and z-axis) and rotational (a 45° clockwise rotation around the y-axis) transformations were determined in the post processing.

The process of magnetic force calibration consists of force measurement and data regression. The force vector was measured by moving the bead in the viscous liquid and calculating the velocity at each location. For each current configuration, the bead was dragged by the magnetic forces to sample the imaging volume, which was 300 $\times$ 300 $\times$ 300 (μm) at the centre of the magnetic tweezers. Next, a multi-variate Gaussian Process regression model was developed based on the Gaussian Process, the typical non-parametric regression algorithm. The input of the model was the training data, which were the measured 3D force vectors and the corresponding bead coordinates. The output of the model was the predictor, which could generate the magnitude of magnetic force in 3D for any given points in the imaging volume. In total, we have calibrated the forces for six basic current configurations. These force data were sufficient for the experiments which examined the mechanical properties of living tissues.

Table 3.1 summarises the six calibrated current configurations with the 18.82 μm bead. The magnetic forces in the table are the forces at the centre of the imaging volume. Although the current configuration is symmetrical, the magnetic force is not symmetrical, for instance in Configuration I and Configuration II. This asymmetry comes from a number of factors. First, the number of turns in each coil is different. One of the flux return frames in the tweezers is shorter. Moreover, the manufacturing of the iron pole is not perfect as the tips are not 100% sharp. These factors lead to magnetic flux leakages. Hence, in the calibration process, we took a direct measurement method, rather than by means of some simulation models.

Table 3.1 The calibrated current configurations and magnetic forces on 18.82μm bead. The unit of the current is A. The unit of the force is nN.

Current Configuration	I_1	I_2	I_3	I_4	F_x	F_y	F_z
I	2.5	2.5	0	0	0.073	**-0.94**	-0.38
II	0	0	2.5	2.5	0.13	**1.07**	-0.35
III	1.25	2.5	2.5	1.25	**-0.57**	0.068	0.43
IV	2.5	1.25	1.25	2.5	**1.18**	0.07	0.70
V	-1	-1	1	1	0.25	-0.03	**1.5**
VI	-2.5	2.5	2.5	-2.5	-0.19	0.18	**-1.05**

In the next chapter, we introduce the application of the magnetic tweezers to investigate the mechanical properties of a zebrafish embryo at early development stages.

Chapter 4

Tissue Rheology of Living Zebrafish Embryo at Early Developing Stages

4.1 Introduction

The development of animals from a single cell to a complex organism is a consequence of synchronised cell movements and tissue morphogenesis. The development of the embryo at early stages involves morphogenetic changes in the cellular structure and the way cells interact in tissues. It has been shown that force generation and transmission by cells in the tissue are essential for tissue morphogenesis [54]. To understand how the forces perform in these morphogenetic phenomena, the tissue mechanical properties must be known. Previous studies have shown that certain embryonic tissues are viscoelastic materials [8, 37, 91]. However, these experiments were carried out on embryonic cell aggregates rather than living embryos, and the time evolution of the patterning of mechanical properties of embryos during development was not unravelled.

In the previous chapter, we have introduced the development of the magnetic tweezers which can apply 3D magnetic forces to the magnetic bead. Here, we propose to probe the mechanical properties in early zebrafish embryo in which the superparamagnetic bead is grafted. This interdisciplinary work was a collaboration between Dr Alexandre Kabla's group in the Department of Engineering, Dr Richard Adams' group in the Department of Physiology, Development and Neuroscience, and Professor Clemens Kaminski's group in the Department of Chemical Engineering and Biotechnology at the University of Cambridge. The preparation of zebrafish embryo, including bead injections, was performed by Julien Dumortier. The probing experiments were performed with Radu Tanasa and Julien Dumortier. The post-processing of data was carried out with Radu Tanasa.

In this chapter, we first introduce the mechanical probing experiments with zebrafish embryo, followed by the interpretation of the measured data and the explanation of tissue mechanical properties by a linear viscoelastic model. This model leads to a discussion on the rheological parameters that control the morphological movements occurring in developing embryos.

4.2 Experimental Protocols

The choice of the biological model in our experiment is the zebrafish embryo. The reasons for this selection are threefold; the ease of magnetic bead implantation in its soft tissues, the heterogeneous characteristics of cell behaviour and its transparent colour for good quality of microscopic imaging deep within the tissue. Zebrafish embryos are complex biological specimens providing research opportunities on a wide range of developmental processes which are often closely related to those in humans. From an ethical point of view, the fertilisation can be done *in vitro*, hence there is no need to dissect the parent. Table 4.1 summarises the earlier staging series for zebrafish with their time period and the principal events [51].

Figure 4.1 shows the aspect ratio of the experimental zebrafish embryo from 1k stage to sphere stage. The distance between the vegetal pole (VP), where the highest concentration of yolk is, and the animal pole (AP), which consists of small cells, is marked as R_1. At the AP, the embryo is covered by an epithelial monolayer known as the enveloping layer (EVL). The perpendicular axis is marked as R_2. At the onset of gastrulation, the embryo transforms from an elliptical to a spherical shape. At high stage, the ratio R_1/R_2 is around 1.2. Then the ratio gradually decreases with development time and gets closer to 1.0 at sphere stage. The underlying mechanism of this transition is not known. We suggest that there is a change in tissue mechanical properties when the embryo is shaping into a sphere. Hence, the experiment aims at measuring the time evolution of the rheological properties *in vivo* with the magnetic tweezers.

In the experiment, a fluorescent (green-AlexaFluor 488) paramagnetic bead with a diameter of 41.14 μm was transplanted in zebrafish transgenic Tg (beta-actin: mCherry-CAAX) embryo at 1k-cell stage (3 hpf)[1]. The bead was placed among the largely non-adherent deep cells. The zebrafish embryo was suspended in low melting point agarose and sucked into a fluorinated ethylene propylene (FEP) tube with an outer diameter of 1 mm and an inner diameter of 0.8 mm. The embryos were mounted at high stage (3.3 hpf)

[1]The embryo process and bead injection were performed by Julien Dumortier

Table 4.1 Periods of early development of zebrafish [51].

Period	Start Time (hpf)	Main Events
Zygote	0	Newly fertilised egg. 1-cell stage. Cytoplasm streams toward animal pole to form blastodisc.
Cleavage	$\frac{3}{4}$	Cell division with no significant growth, producing a cluster of cells that is the same size as the original zygote, which are 3 regular tiers of blastomeres.
Blastula	$2\frac{1}{4}$	Rapid cell cycles give way to a hollow sphere of cells. Embryo flattens to a spherical shape. The border between blastodisc and yolk is flat. Epiboly then begins in the late blastula. Blastoderm forms an inverted cup of uniform thickness [90].
Gastrula	$5\frac{1}{4}$	Morphogenetic movements of involution, convergence, and extension through the end of epiboly.
Neurula	24	Transformation of the neural plate into the neural tube.
Hatching	48	Completion of rapid morphogenesis of primary organ systems. Hatching occurs.
Early Larva	72	Completion of most morphogenesis and continuation of rapid growing. The total body length is 3.5 mm.

at a temperature of 28.5°C. The probing period was between high stage and the onset of gastrulation (5.3 phf), in order to avoid the effects of too many factors and complex tissue movements on the results. We have observed that embryos with a bead were able to develop without being perturbed by the introduction of the bead. The bead and the surrounding cells were imaged for extensive periods.

To measure the rheological properties of the blastoderm, known forces were applied to the bead. The current configuration is shown in Table 4.2. The dominant force component in these two configurations is the force in the y-axis, directed either to the AP or to the VP. The displacement of the bead in the embryo in the y-axis was recorded. The purpose of applying forces in opposite directions was to verify if the difference in force direction brings about a

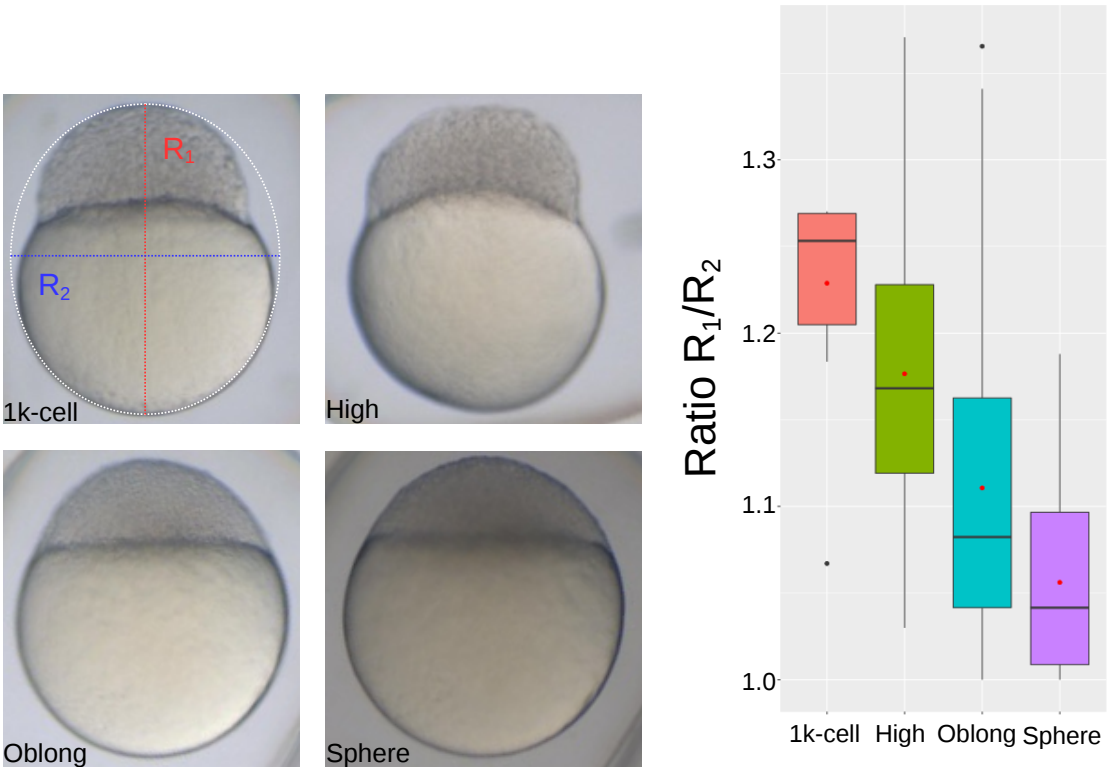

(A) (B)

Fig. 4.1 The figure (A) shows the shapes of a wild type zebrafish embryo at four different developing stages: 1k-cell stage, high stage, oblong stage and sphere stage. R_1 and R_2 are two axes of the ellipse shape of the embryo. The aspect ratio is R_1/R_2. The box plot (B) shows the average embryo aspect ratio in these four developing stages. The figures are adapted from the experimental images by courtesy of Julien Dumortier.

distinctive behaviour in tissue mechanics. Further, the influence of the cells in EVL and the yolk cells on the deep cells in the embryo was also examined.

Table 4.2 The calibrated current configurations and magnetic forces on 41.14 μm bead. The unit of the current is A. The unit of the forces is nN.

Current Configuration	I_1	I_2	I_3	I_4	F_x	F_y	F_z
VP	0.45	0.45	0.9	0.9	0.8	**9.3**	-3.1
AP	0.9	0.9	0.45	0.45	-0.4	**-10.5**	-3.5

A set of tests were performed within each embryo as it developed. Each test lasted for a total of 210 seconds. In the first 30 seconds, magnetic force was not applied. Then the current was switched on for 1 minute and switched off for an additional 2 minutes. According to the

position of the bead, the magnitude of the magnetic forces was obtained from the calibration model. The calibration model provided the information of the magnetic forces: at the initial position of the bead, the force towards the AP was -0.4 nN in the x-direction, -10.5 nN in the y-direction and -3.5 nN in the z-direction, and the force towards the VP was 0.8 nN in the x-direction, 9.3 nN in the y-direction and -3.1 nN in the z-direction (Figure 4.2). The figure shows that the magnitude of forces had small variations when the bead moved in the embryo. The variations were < 0.5 nN, which was 5% of the initial value. Hence, the force in the y-direction was assumed to be constant.

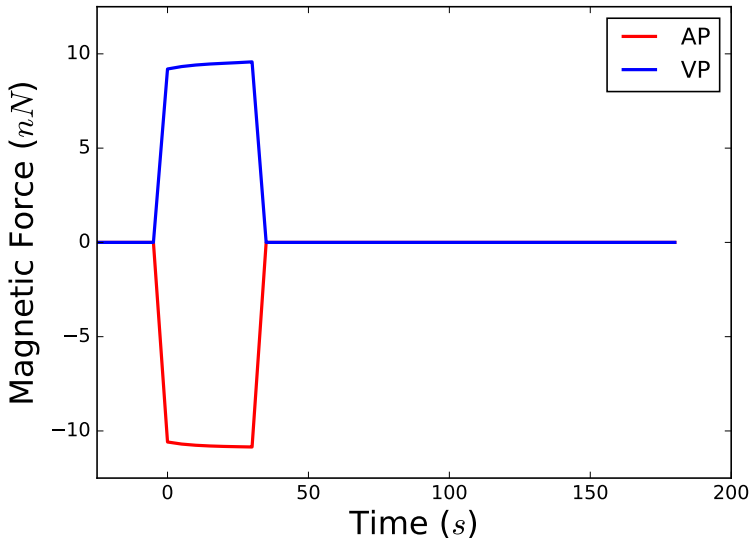

Fig. 4.2 The figure illustrates the time evolution of the magnitude of the magnetic force exerted on the bead in the y-direction. The force pointing to the animal pole is in coloured red and to the vegetal pole in blue. When the current is switched off, the force on the bead is zero. The magnitude of the force has small variations with the bead position.

Figure 4.3 presents the image of an experiment on a wild-type (WT) zebrafish embryo at high stage. The bead was grafted in deep cells. In the absence of a magnetic field, bead remained stationary in the embryo. When the current was switched on, the bead moved towards the animal pole. The displacement was around 60 μm. When the current is switched off, the bead moved back towards the yolk. The bead position at the end of the recorded images was not the initial bead position.

In total, twelve tests were carried out with the force towards AP and eleven tests were carried out for the force towards VP on the same embryo. These tests were performed at continuous time points to examine the changes of mechanical properties at different

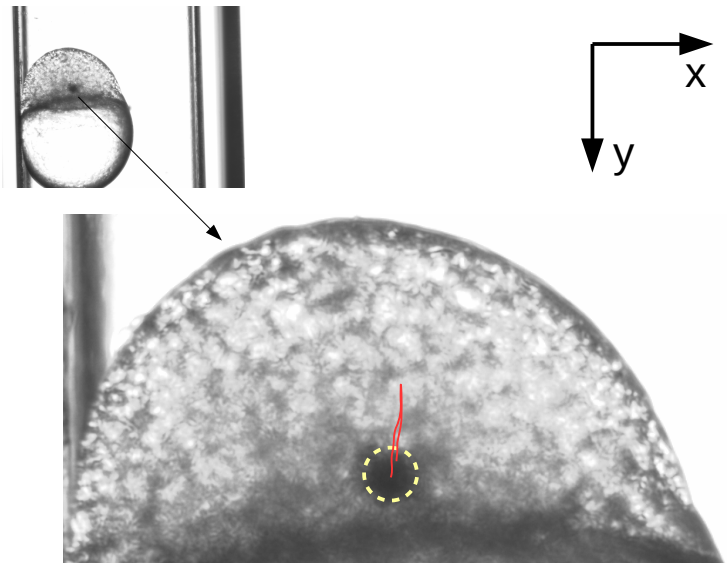

Fig. 4.3 The figure shows the experimental image taken by the calibration microscope at the Engineering Department. The small picture on the upper left corner is a full image of the embryo in the capillary. The coordinates on the upper right corner show the directions in the imaging plane. The bead is marked by a circle in white in the zoomed-in picture. The red line records the trajectories of the bead when the current is switched on.

developing stages. Next, we will explore the tissue behaviours by measuring the bead displacement.

4.3 Characterisation of Tissue Properties

4.3.1 Bead Displacement

The dominant component of the force vector is the force in the y-direction in the focused plane. The displacement of the magnetic bead in this direction is shown in Figure 4.4, for both AP force and VP force at a different developing time. The maximum displacement in each curve is different from one another, but the overall trend is consistent.

Figure 4.5 shows one of the bead trajectories. When the current is switched on ($t = 0$), an initial rapid displacement (d_1) in the first few seconds is observed. Then the bead creeps at a lower but constant velocity (v). The displacement during creep is comparatively slow and linear until the current is switched off. Once the force is released, the bead retracts towards its initial position in a reversal of the initial fast displacement (d_2). The timescale of this relaxation is unknown. Then the bead displacement is retained since the bead does not move back to the initial position. We suppose that these bead displacement curves have described

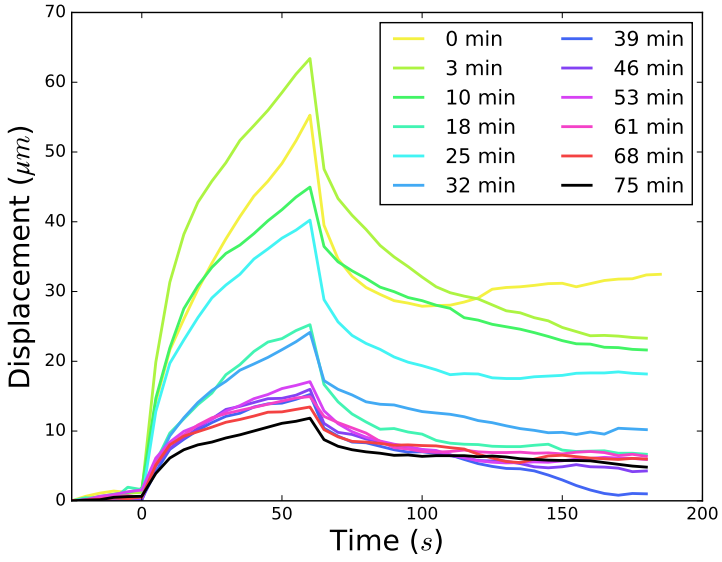

(A)

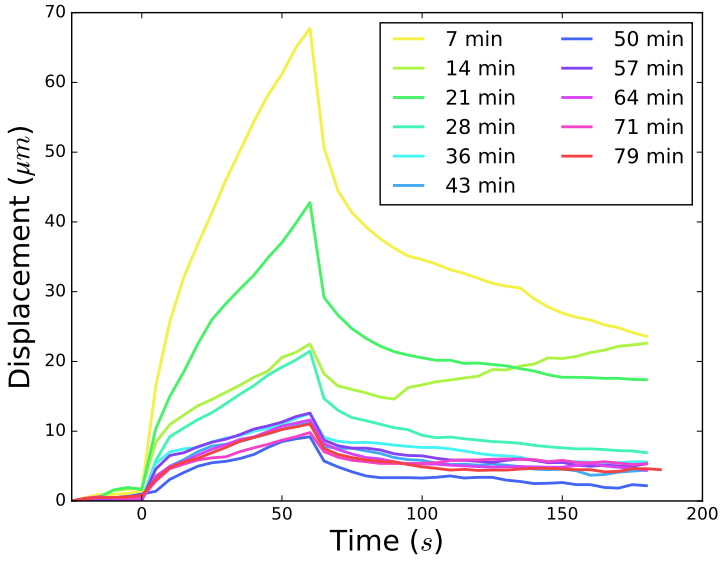

(B)

Fig. 4.4 The time evolution of bead displacement in the direction of y-axis. The direction of the force is to the AP (A) and to the VP (B). The current is switched on at $t = 0$. The first experiment starts at 0 min. The time in the legends indicates the time point when the experiment was conducted.

the viscoelastic properties of an early developing zebrafish embryo subjected to external stresses.

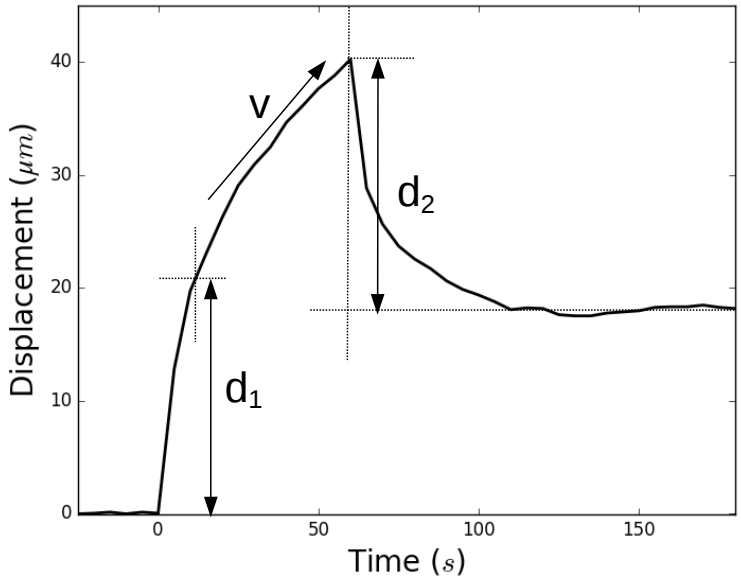

Fig. 4.5 The graph describes different phases in the bead displacement. d_1 is the initial rapid displacement, v is the speed of the slow creep, d_2 is the retraction upon release.

To quantify and further analyse the bead displacement, we fitted each bead displacement curve to a one-dimensional rheological model which characterises the material mechanical properties. The model consists of a Kelvin-Voigt model, which has a spring and a dashpot connected in parallel, and another dashpot in series (Figure 4.6). The Kelvin-Voigt model contributes to a cell level response correlated with cell shape changes, and the second dashpot interprets the cell–cell interaction, correlated with cell adhesion. Next, we will derive the strain-stress relationship for this model and find the fitted rheological parameters for each curve.

4.3.2 Linear Rheological Models

In this section, we derive the equation of strain in the linear rheological model. Connecting a spring and damper in parallel yields a model of a Kelvin–Voigt material, which describes the viscoelastic property of the material. The second dashpot is in series with the Kelvin-Voigt model. Hence, the stress is identical for the two components and the total strain in the model is the sum of the strain of the two components.

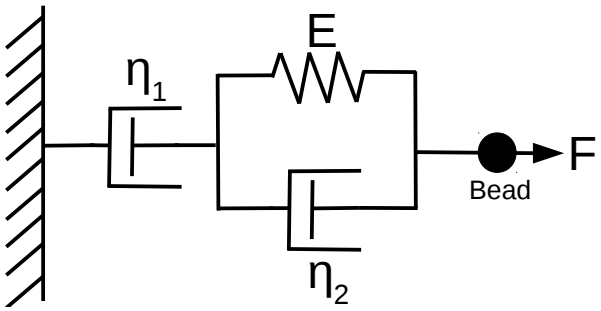

Fig. 4.6 The graph describes a linear solid model combining elastic spring and viscous dashpots. The model consists of a Kelvin-Voigt model, which has a parallel spring and dashpot, and the second dashpot in series. E is Young's Modulus of the spring component, η_1 and η_2 are the viscosity of the dashpot component and F indicates the force on the magnetic bead. It can be transformed to the applied stress σ.

The model is described by the following parameters: dynamic viscosities η_1 and η_2 and elastic stiffness E. When stress σ is applied to the material, which in our experiment is the stress on the bead caused by the magnetic force, the strain ε is quantified by the displacement of the bead. The stress phase (when $\sigma \neq 0$) and the recovery phase (when $\sigma = 0$) are evaluated separately. The stress phase starts from the equilibrium state at $t = 0$ when a constant force is applied instantaneously on the bead and lasts for 1 minute. The recovery phase begins at the end of stress phase $t = t_1$ when the force is released. The bead displacement is monitored for two minutes.

In the Kelvin–Voigt model [81], the linear spring is described by:

$$\varepsilon_2 = \frac{1}{E}\sigma_E, \tag{4.1}$$

while a dashpot by:

$$\dot{\varepsilon_2} = \frac{d\varepsilon_2}{dt} = \frac{1}{\eta_2}\sigma_{\eta_2}. \tag{4.2}$$

The stress for the Kelvin–Voigt model is:

$$\sigma = \sigma_E + \sigma_{\eta_2} = E\varepsilon_2 + \eta_2\dot{\varepsilon_2}. \tag{4.3}$$

Taking the integral of ε_2 in time in the equation with the initial condition $\varepsilon_2 = 0$ at $t = 0$:

$$\varepsilon_2 = \frac{\sigma}{E}\left(1 - \exp(-\frac{E}{\eta_2}t)\right). \tag{4.4}$$

Similarly, the strain for dashpot η_1 with initial condition $\varepsilon_1 = 0$ at $t = 0$ is:

$$\varepsilon_1 = \frac{\sigma}{\eta_1} t. \tag{4.5}$$

Therefore, knowing that $\varepsilon = \varepsilon_1 + \varepsilon_2$, the strain for the stress phase could be described by:

$$\varepsilon = \frac{\sigma}{\eta_1} t + \frac{\sigma}{E} \left(1 - \exp(-\frac{E}{\eta_2} t) \right). \tag{4.6}$$

The recovery phase starts from t_1 when the force is zero: $\sigma = 0$. The total strain for this phase is given by the strain of dashpot η_1 and the relaxation of the Kelvin-Voigt model. The strain for the dashpot η_1 has no recovery. For the Kelvin-Voigt model, we have:

$$0 = E\varepsilon_2 + \eta_2 \dot{\varepsilon}_2. \tag{4.7}$$

The initial condition of ε_2 at $t = t_1$ is:

$$\varepsilon_2 \mid_{t=t_1} = \frac{\sigma}{E} \left(\exp(\frac{E}{\eta_2} t_1) - 1 \right). \tag{4.8}$$

Taking the integral of ε_2 in time, the equation becomes:

$$\varepsilon_2 = \frac{\sigma}{E} \left(\exp(\frac{E}{\eta_2} t_1) - 1 \right) \exp(-\frac{E}{\eta_2} t). \tag{4.9}$$

Therefore, for the second phase, the strain is described by:

$$\varepsilon = \frac{\sigma}{\eta_1} t_1 + \frac{\sigma}{E} \left(\exp(\frac{E}{\eta_2} t_1) - 1 \right) \exp(-\frac{E}{\eta_2} t). \tag{4.10}$$

In general, combining Equation (4.6) and (4.10), the time evolution of the strain for the linear model is:

$$\varepsilon = \begin{cases} \dfrac{\sigma}{\eta_1} t + \dfrac{\sigma}{E} \left(1 - \exp(-\dfrac{E}{\eta_2} t) \right), & t \leq t_1 \\ \dfrac{\sigma}{\eta_1} t_1 + \dfrac{\sigma}{E} \left(\exp(\dfrac{E}{\eta_2} t_1) - 1 \right) \exp(-\dfrac{E}{\eta_2} t), & t \geq t_1 \end{cases}$$

4.3.3 Rheological Parameters

In this section, we find the fitted parameters in the strain equation to further establish the relationships between the rheological parameters and the underlying biology. The stress could be derived from the elastic response of the tissue due to the bead displacement. According to the solution of a point force in an infinite isotropic medium [33, 53, 97], the displacement **d**

in cylindrical coordinates (ρ, y) for a point force F_y located at the origin and directed along y-axis is given by:

$$\mathbf{d} = \frac{F_y}{4\pi\mu R}\left[\frac{1}{4(1-\nu)}\frac{\rho y}{R^2}\hat{\rho} + \left(1 - \frac{1}{4(1-\nu)}\frac{\rho^2}{R^2}\right)\hat{y}\right], \tag{4.11}$$

where R is the radius of the bead, $\hat{\rho}$ and $\hat{y}$ are the unit vectors, μ is the shear modulus (at constant volume) and ν is the Poisson's ratio. To explore the deformations along the direction of the applied force where $\rho = 0$, the equation could be reduced to:

$$d_y = \frac{F_y}{4\pi\mu R}. \tag{4.12}$$

In the close proximity of the radius of the bead, Equation (4.12) could be written as:

$$\frac{d_y}{R} = \frac{1}{4\mu}\frac{F_y}{\pi R^2}. \tag{4.13}$$

If we replace 4μ by E, the equation becomes:

$$\varepsilon = \frac{\sigma}{E}, \tag{4.14}$$

where the stress is defined as:

$$\sigma = \frac{F}{\pi R^2}, \tag{4.15}$$

and the strain in this case is defined as the bead displacement scaled by the bead radius:

$$\varepsilon = \frac{d}{R}. \tag{4.16}$$

Similarly, the viscous force on the moving bead could be described by Stokes' law:

$$F = 6\pi\eta' R v = 6\pi\eta' R\frac{dD}{dt}, \tag{4.17}$$

where η' is the viscosity and D is the bead displacement. By dividing πR^2 on both sides of the equation, we have:

$$\frac{F}{\pi R^2} = \frac{6\pi\eta' R}{\pi R^2}\frac{dD}{dt}. \tag{4.18}$$

Since we know the stress in Equation (4.15), we have:

$$\sigma = 6\pi\eta'\frac{d}{dt}\left(\frac{D}{R}\right). \tag{4.19}$$

Hence, if we replace $6\eta'$ by the coefficient of a dashpot η, we have:

$$\sigma = \eta\dot{\varepsilon}. \tag{4.20}$$

Next, the fitted rheological parameters E, η_1 and η_2 were estimated. Figure 4.7 shows the experimental and the fitted bead displacement data for high stage, oblong stage and sphere stage, respectively.

In total, experiments were performed on nine WT early-stage zebrafish embryos by the same protocol. In each experiment, the developing time was recorded. Each bead displacement curve was fitted to the rheological model and the corresponding parameters were obtained. Figure 4.8 to Figure 4.10 describe the time evolution of these rheological parameters. The value of the parameters at each developing time is the mean taken from nine experiments. Over a developing time of ~ 75 min, E increased by 3.1 times, η_1 increased by 4.6 times and η_2 increased by 4.1 times. In each plot, we see that these parameters increase approximately linearly with time. In comparison, no significant difference is observed between the rheological properties of the embryo when the force is towards AP and towards VP.

A characteristic time constant τ of the Kelvin-Voigt model is defined as

$$\tau = \frac{\eta_2}{E}. \tag{4.21}$$

This constant controls the relaxation time of the material and is a measure of the time taken for the recovery of the deformation. Figure 4.11 shows the time evolution of τ. Although E and η_1 increased, the time constant τ remains relatively constant within the hour of the experiment. The approximation lines of the time constant in forces to the AP and forces to the VP collapse. This suggests that the embryonic tissue may contain a self-regulation mechanism which has a time constant of τ, or both E and η_2 are determined by a common parameter during this development period.

4.4 Discussion

In this chapter, we have shown that the magnetic tweezers could be optimal for studying the mechanical properties of tissues as it exerts 3D forces on the magnetic bead with known magnitudes. The device was used to measure the mechanical properties of the early-stage zebrafish embryo. During the period of development, it was observed that the embryo flattened to a spherical shape. The response of the embryonic tissues to an external force was

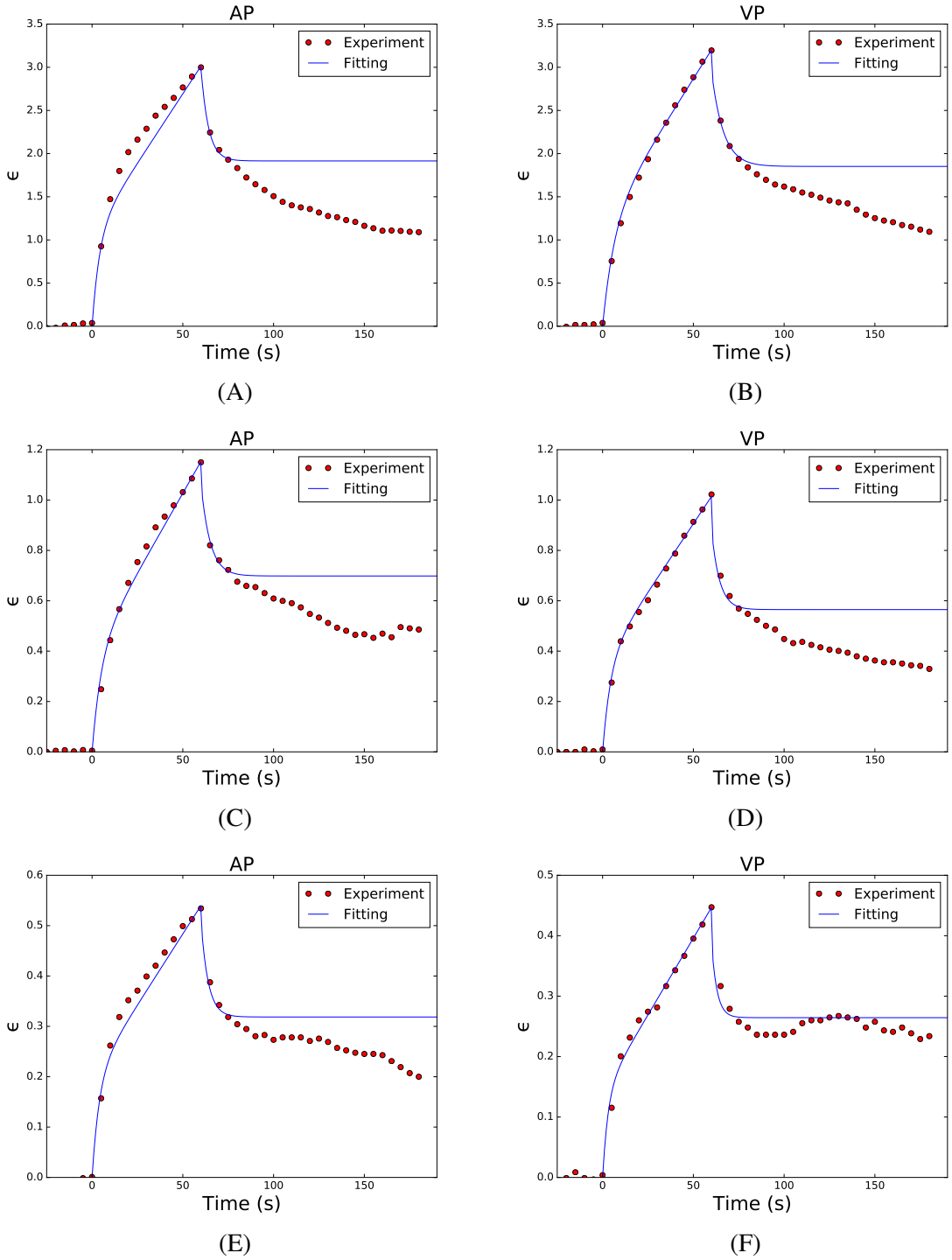

Fig. 4.7 The bead displacement curve from the experimental tracking (dots in red) and the fitted rheological model (line in blue): high stage of the zebrafish embryo with force towards the animal pole (A) and force towards the vegetal pole (B); oblong stage of the zebrafish embryo with force towards the animal pole (C) and force towards the vegetal pole (D); sphere stage of the zebrafish embryo with force towards the animal pole (E) and force towards the vegetal pole (F).

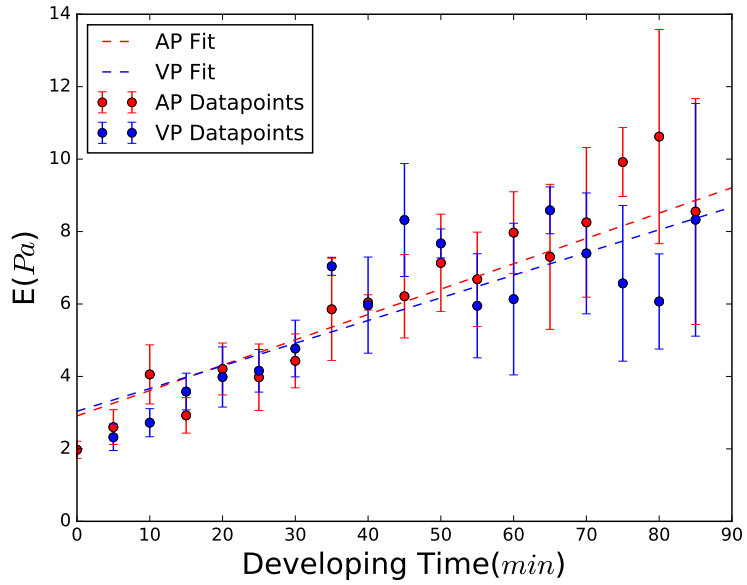

Fig. 4.8 The time evolution of the elastic parameter E. The force direction is to the AP (red) and to the VP (blue). The datapoints indicate the mean value at each time step and the error bars denote the standard deviation (SD). The dashed line is the linear approximation.

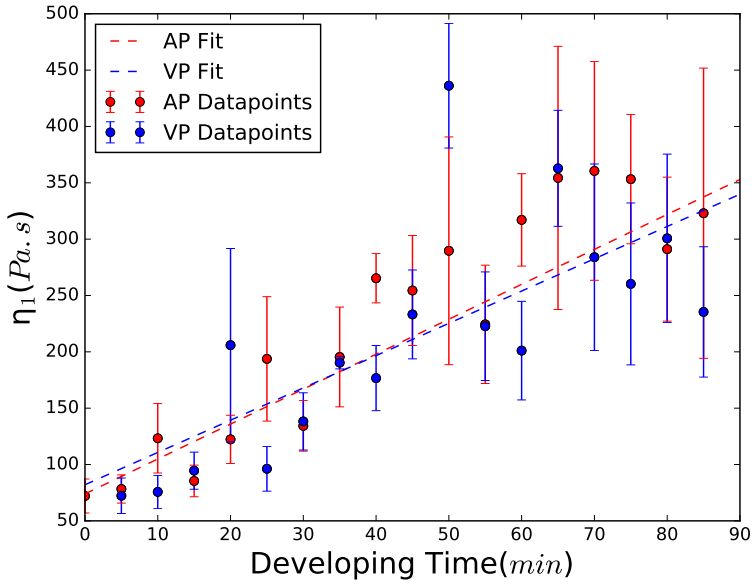

Fig. 4.9 The time evolution of the viscous parameter η_1. The force direction is to the AP (red) and to the VP (blue). The datapoints indicate the mean value at each time step and the error bars denote the standard deviation (SD). The dashed line is the linear approximation.

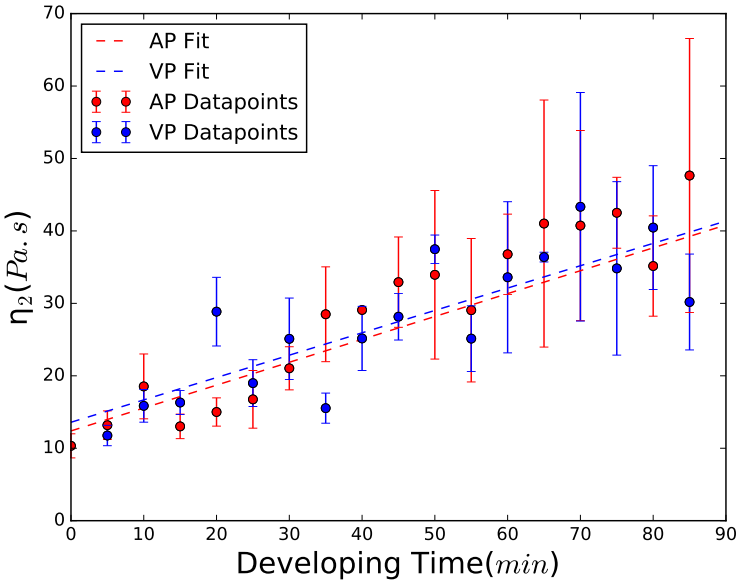

Fig. 4.10 The time evolution of the viscous parameter η_2. The force direction is to the AP (red) and to the VP (blue). The datapoints indicate the mean value at each time step and the error bars denote the standard deviation (SD). The dashed line is the linear approximation.

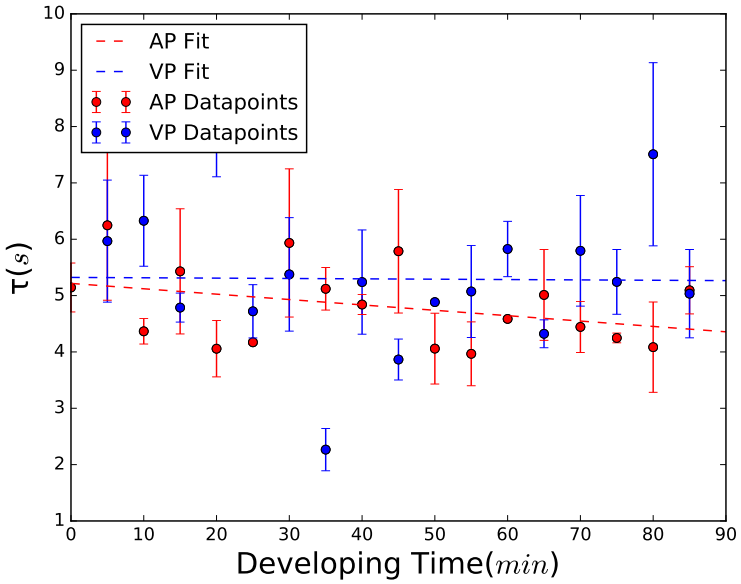

Fig. 4.11 The time evolution of the characteristic time constant τ. The force direction is to the AP (red) and to the VP (blue). The datapoints indicate the mean value at each time step and the error bars denote the standard deviation (SD). The dashed line is the linear approximation.

consistent with a linear viscoelastic model. The fitted rheological model describes that the tissue consists of two mechanical components, a soft viscoelastic component and a more viscous component. These two key contributions form the passive mechanical properties of the embryo. The rapid increase and decrease of the bead displacement within several seconds when the current is switched on and off shows the elastic property of cells. The creep is a form of energy dissipation, which is non-reversible [65]. Statistical results have shown that all three parameters increase with developing time. The hypothesis could be that the Maxwell model interprets cell mechanics and the dashpot represents cell–cell adhesion.

To further approach this question, measurements have been accomplished in embryos in which cellular mechanical properties were experimentally modulated [2]. These properties include cell motility, cell adhesion and cell cortex tensions, which are known to be dependent respectively on Rac1, E-Cadherin and MyosinII activities. The time evolution of the rheological parameters in different types of embryos is shown in Figure 4.12 to Figure 4.15.

Cell adhesion was reduced by weakening the expression of E-cadherin by a knock-down Morpholino approach (MoECad) [27, 99]. As a consequence, the embryos failed to obtain a spherical shape. The measured rheological parameters indicate that MoECad-treated embryos have lower stiffness and viscosity. These embryos are softer and less viscous than WT embryos over the period of time.

Cell protrusive activity was knocked down by a dominant-negative Rac1 construct (DNRAC) [27, 108] and the activation of molecular motor myosin-2 was reduced by a dominant-negative Rho-kinase construct (DNROCK) [16, 27]. DNRAC treatment led to less spherical shapes, while DNROCK treatment led to a faster rounding up. Rheological parameters show that DNRAC embryos fail to increase stiffness and viscosity while DNROCK embryos become stiffer and more viscous than WT embryos.

Based on these results, we suggest that the changes in the rheological parameters of the embryo during development are closely related to the cellular mechanical properties during that stage. The mechanical properties of cells, cell migration and morphogenesis are linked and impact each other, even at really early steps of embryonic development. We could use LSFM to produce high-resolution images at cellular levels to measure the changes in cell shape. Figure 4.16 presents the images of a magnetic bead in the embryo produced by LSFM at three different phases: the initial state with no forces applied (A), 10 sec after the current was switched off (B) and 120 sec after the current was switched off (C). When the current is switched off and the elastic deformation is recovered, it could be observed that the shape

[2]The embryo process was performed by Julien Dumortier. The probing tests were performed with Radu Tanasa and Julien Dumortier.

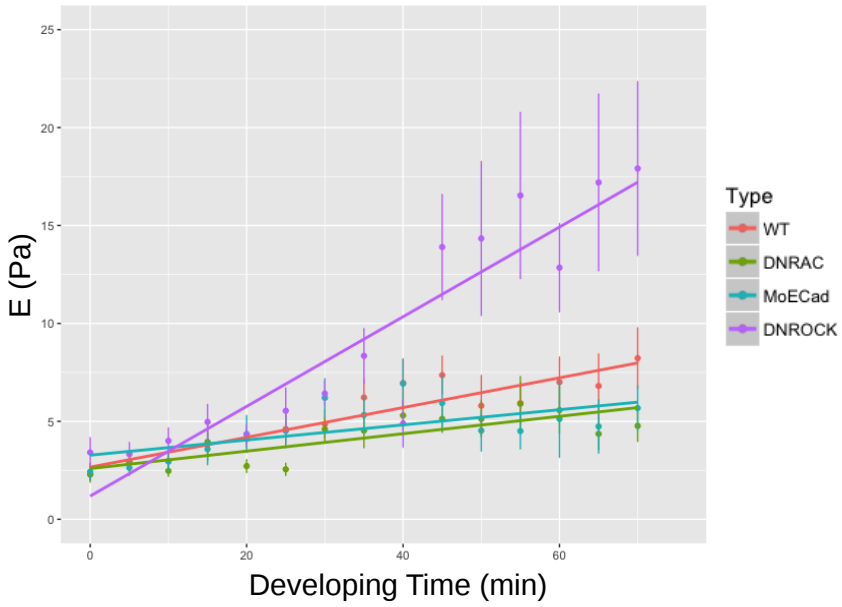

Fig. 4.12 The time evolution of the elastic parameter E in WT embryo and mutants. The datapoints indicate the mean value at each time step and the error bars denote the standard deviation (SD).

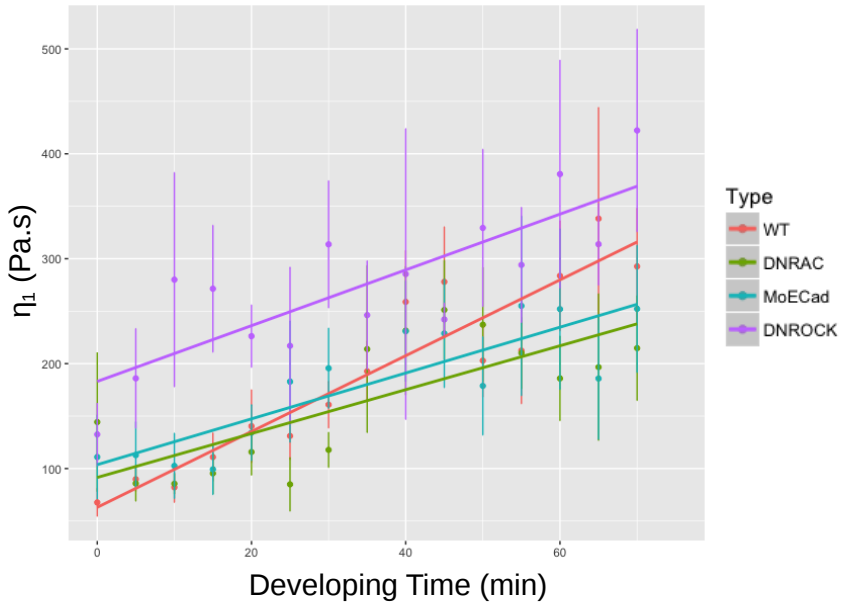

Fig. 4.13 The time evolution of the viscous parameter η_1 in WT embryo and mutants. The datapoints indicate the mean value at each time step and the error bars denote the standard deviation (SD).

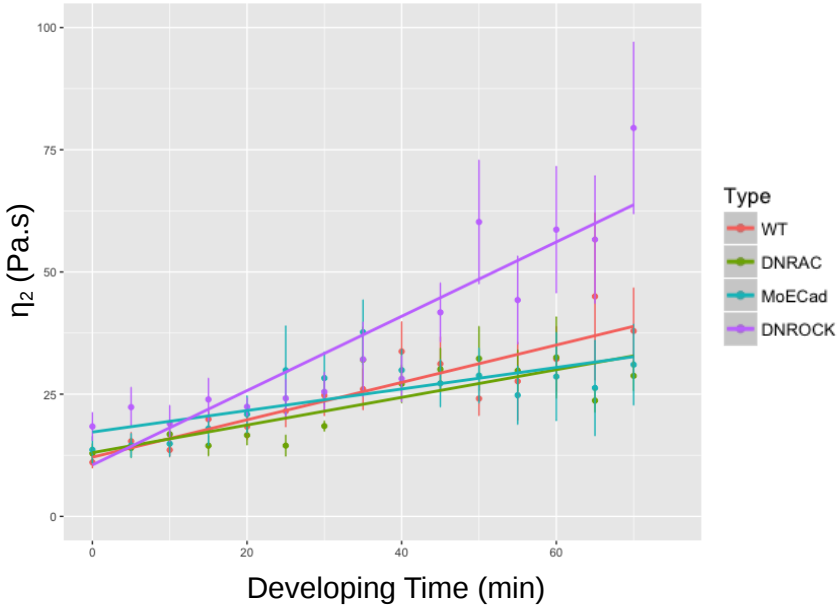

Fig. 4.14 The time evolution of the viscous parameter η_2 in WT embryo and mutants. The datapoints indicate the mean value at each time step and the error bars denote the standard deviation (SD).

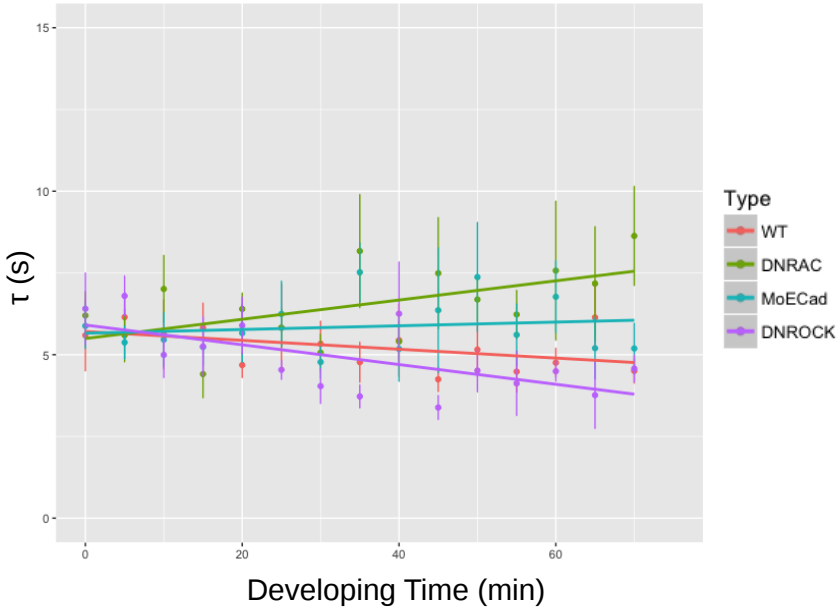

Fig. 4.15 The time evolution of the characteristic time constant τ in WT embryo and mutants. The datapoints indicate the mean value at each time step and the error bars denote the standard deviation (SD).

of cells in the vicinity of beads have changed (B), compared with cells in the resting state (A). Cell 1 is compressed while Cell 5 is elongated. The deformations result from bead creep. According to the linear rheological model, these deformations caused by the slow creep should not be reversible. However, if we define the cell aspect ratio as the ratio of the length in y-axis and the length in x-axis, the average aspect ratio of Cell 1 to 3 (front cells) has increased from 0.97 to 1.00, and the average aspect ratio of Cell 4 and 5 (rear cells) has decreased from 1.04 to 1.02 in (C), compared with cell aspect ratio in (B). The mechanisms behind these changes were not clear.

In summary, the rheological model shows that the tissue is only able to recover the elastic deformation and the relaxation time is determined by the time constant τ. The slow creep is not reversible. Ideally, the bead should stay at the position where the elastic deformation is fully recovered, as shown by the blue curves in Figure 4.7. However, a long and slow relaxation is observed in all the bead displacement curves. Regardless of the developmental stages or the direction of the external forces, this mismatch exists in all of these curves. This mismatch could result from unknown cellular movements, or it might be controlled by unknown timescale parameters. On the other hand, the relaxation process might simply come from cell intercalation. We suggest that bead creep would cause local tissue disorder. The relaxation would be a result of cell intercalation which dissipates the heterogeneous stress remained in the vicinity of the bead. Experimental data are not sufficient to quantify the local stress around the bead. In the next chapter, we will use a computational model to test our hypothesis of the observed relaxation in the embryo.

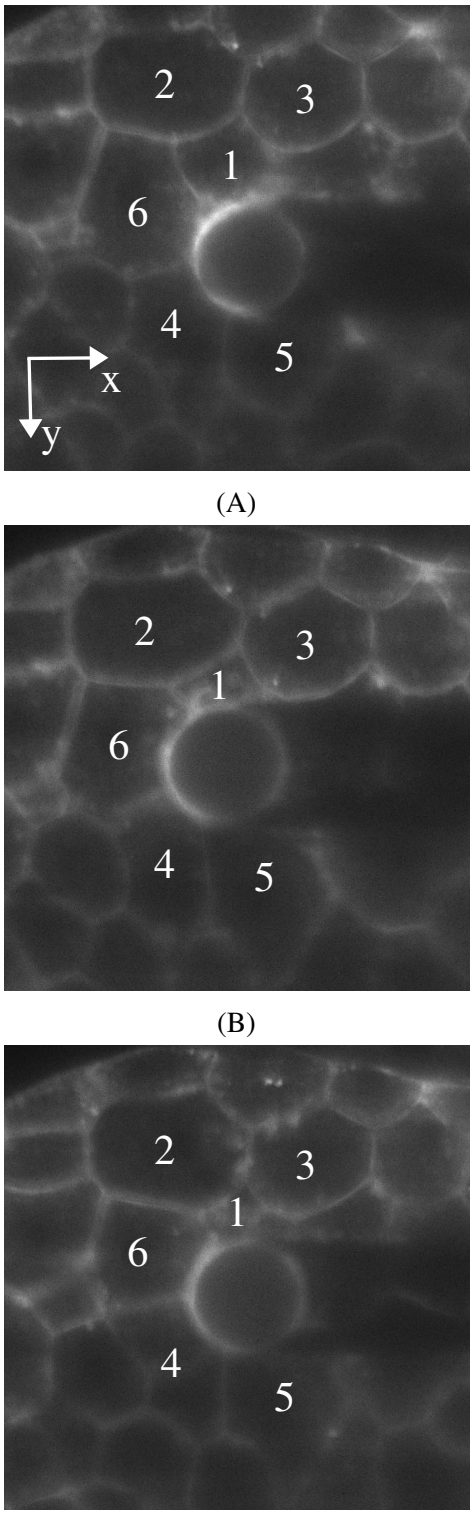

Fig. 4.16 Experimental images produced by the LSFM microscopes. Local cells are numbered from 1 to 6. (A) Before the current is switched on. There is no force on the bead. (B) The image is taken 10 sec after the current is switched off. (C) The image is taken 120 sec after the current is switched off.

Chapter 5

Cellular Stress Heterogeneity in Response to Local Perturbations

5.1 Introduction

In the previous chapter, experimental results indicated that the zebrafish embryonic tissue during the early development stages is viscoelastic. The experimental curves were fitted using a simple rheological model. Regardless of development time, a significant mismatch between the fitted curve and the experimental curve was observed during the relaxation phase when the current was switched off. The experimental curves had a long and slow relaxation phase after the elastic deformation was recovered. With the same values of the fit parameters for the rheological model, the fitting curves did not match this secondary relaxation. The difference between the two curves showed that there might be unknown changes in the tissue.

Combining the observation of cell shape changes and the bead displacement curves, we are interested in the causes of the local disorder and the control parameters of the secondary relaxation. However, the amount of experimental data is limited and cell stress is difficult to quantify from these images. We propose a hypothesis that the secondary relaxation is induced by the local stress disorder caused by bead creep, and the relaxation is controlled by the characteristic time of cell intercalation.

To test this hypothesis and provide supporting evidence for the experiment, we used a computational model developed by Jennings [49], which was introduced in Chapter 2. In the model, we could simply reproduce the experimental observations and vary the control parameters to predict how external forces affect the tissue behaviour in a passive system. Furthermore, in the experiment, the embryonic tissue is a small-scale system. In comparison,

the model allows us to investigate local effects in a larger-scale system. The simulation and data analysis described in this chapter were my individual work.

5.2 Modelling

The mechanical model captures the viscoelastic properties of the tissue. It is used to simulate the tissue behaviour in the experiment, where the force is applied to the bead to move it through the passive cells. A single cell (hereinafter referred to as "bead") is modelled as the mechanical probe, and an external force, similar to the magnetic force exerted on the bead, is applied to it.

5.2.1 Body Forces Implementation

Body forces were not taken into account in the initial design of the model. A body force $\mathbf{F_m}$ is implemented at the centre of a selected cell. Hence, the bead is driven by the external force and experiences cell–cell viscous forces and contact forces. The net force on the bead is the external force $\mathbf{F_m}$. In order to keep the system at the equilibrium, ensuring that tissue rotation, local twisting or tissue movement are avoided, the net force and net torque in the large-scale system should be zero. To achieve this, we introduce a pair of bead cells in a large system containing 1024 cells. The two beads are aligned and separated by a distance of half the length of the tissue, so the movement of one bead has negligible effects on the neighbour cells around the other bead. The body force on the two cells at each timestep has the identical magnitude but in opposite directions, along the axis of the two beads. An example of the bead pair is illustrated in Figure 5.1.

The model is in accordance with the large-scale force balance within a continuous body subject to an external force $\mathbf{F}$, given by the partial differential equation (PDE):

$$\nabla \cdot \sigma(\mathbf{x}) = \mathbf{F}. \tag{5.1}$$

The details of the solution to the PDE by finite element method have been introduced in Chapter 2.

The elastic deformation caused by the introduction of the external force in the model is obtained by solving the force balance equations by finite element methods. The viscous property of the tissue is reflected by bead creep when the bead slides through the cells and experiences cell–cell viscous force. In the analysis, the average effects of the bead pair were taken into account. For each individual simulation, we rotated the region associated with the

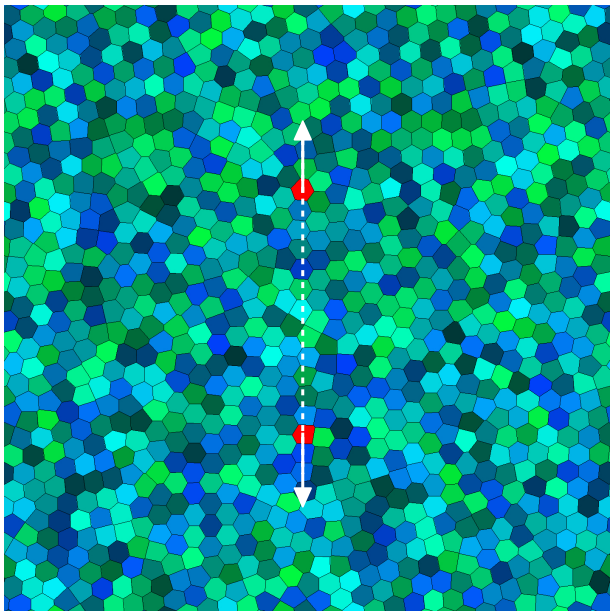

Fig. 5.1 A system of 1024 cells by Voronoi configuration. The red polygon indicates the bead pair which takes the external force. A pair of beads are separated by a distance of half of the dimension of the system. The white dashed line shows the axis of the beads. The external forces on the cells are in opposite directions.

second bead by 180 degrees and superimposed the data in this region with the data in the region of the first bead. A single simulation is very noisy as the cell displacement and stress around the bead cell depend on the particular environment through which the cell moves. To examine the statistical significance, we performed 100 simulations for each combination of parameters. In each simulation, a different pair of beads was selected at different locations to sample the plane of the model system.

5.2.2 Bead Displacement

In the simulation, the magnitude of the applied external force is constant (Figure 5.2 (A)) and the direction depends on the position vector of the pair bead. A typical bead displacement curve is shown in Figure 5.2 (B). The displacement is the distance which the bead moves in the direction of the force. We have discussed that the mechanical model corresponds to a spring and dashpot in series connection, which is known as the Maxwell model. The expected bead response given by the Maxwell model is shown by the red dashed line. However, a nonlinear curve during creep and a slow relaxation phase were noticed in the simulation. The non-linearity in bead displacement during creep is caused by updating cell positions by the transition between cell configurations. The slow relaxation strongly corresponds to the

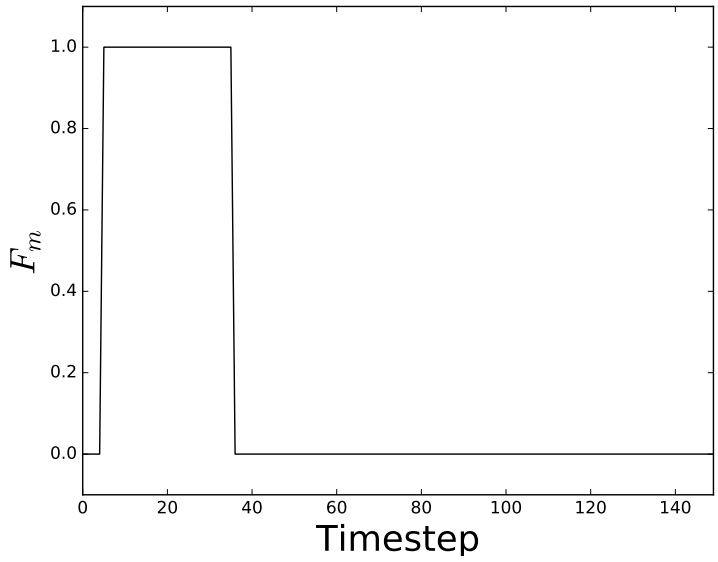

(A)

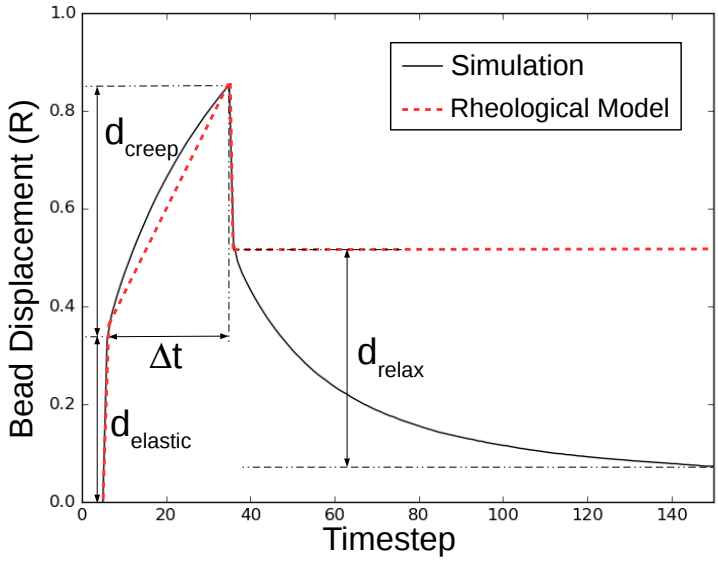

(B)

Fig. 5.2 The graphs describe the external force and the bead displacement in the simulation. (A) The external force against time. The magnitude is constant. (B) An example of the bead displacement curve. $d_{elastic}$ is the rapid elastic deformation, d_{creep} is the displacement that the bead creeps in the cells, d_{relax} is the displacement that bead moves towards its starting point during relaxation, and Δt is the duration of the creep.

bead displacement curve obtained in the experiment. Next, we will explore the relationship between the model parameters and these three displacement components: a rapid elastic stretch $d_{elastic}$, the creep distance d_{creep}, and the long relaxation displacement d_{relax}.

5.2.3 Major Parameters

By incorporating body forces, the model provides a simple system which can model *in-vivo* systems such as the experiments carried out to investigate the mechanical properties of the embryonic tissues in the previous chapter. The major parameters that control the behaviour of the model within this chapter are shown in Table 5.1. We also know that the characteristic time of the system τ is formed by G, η and the cell radius R as $\tau = \frac{\eta R}{G}$. Note that a reference unit length in the simulation is the radius of the cell $R = 1$. Therefore, for obvious demonstration, we use R as a unit to indicate the dimension in 2D and displacement in figures of the simulation results. We first explore how the external force and the properties of passive cells affect bead displacement.

Parameter	Definition	Estimate
G	Shear elastic modulus of the cell	$\sim 10^6 Nm^{-1}$
η	Cell–cell sliding viscosity	$\sim 10^{11} Nm^{-1}s$
R	Cell radius	$\sim 10^{-5}m$
F_m	Magnitude of the external force	$\sim 10^{-9}N$
t	Time step	s
Δt	The duration of bead creep	s

Table 5.1 The major parameters used in this chapter and their definitions

5.3 Mechanical Properties of Cells

In this section, we first investigate how cell mechanical properties affect the bead displacement in the model. Figure 5.3 shows an example of the simulation. The pair of beads is coloured in red. The simulation results showed that the cells in front of the bead are compressed, and the rear cells are pulled by the bead and elongated (Figure 5.3 (A)). The bead then creeps through the tissue by a short distance (Figure 5.3 (B)). When the force is removed, the elastic deformation of cells is recovered (Figure 5.3 (C)) but the shape of

the surrounding cells is significantly different compared with the resting state. After a long period of relaxation, the cells return to fully relaxed packing (Figure 5.3 (D)). In this case, we divide the whole procedure into four phases: elastic deformation, creep, elastic recovery and long relaxation. We examine the bead displacement during the elastic phase $d_{elastic}$, creep d_{creep} and relaxation d_{relax}, respectively.

5.3.1 Elasticity

The displacement $d_{elastic}$ is the length of elongation or compression in a linear elastic spring. The application of the external force causes cells to undergo an instantaneous elastic strain upon loading. The strain is maintained as long as the load is applied. The cells then undergo an instantaneous de-straining upon removal of the load. The viscous property of individual cells is not captured in the model. Therefore the deformation is instantaneous, unlike the slope in the experimental curves. To examine the effects of the parameters on the elastic behaviour of the cells, an identical force F_m is applied with cell stiffness $G = [1, 2]$. Then with the same G, the external force is varied $F_m = [1.0, 1.5, 2.0, 2.5, 3.0]$.

The instantaneous displacement of the bead cell increases linearly with the external force. When cells are stiffer, the displacement is smaller, as the displacement at $G = 2$ is half of that at $G = 1$ (Figure 5.4 (A)). When the force is scaled by the stiffness, the two curves collapse, as shown in Figure 5.4 (B). Therefore, we could conclude that the elastic deformation depends on the magnitude of the external force and the stiffness of cells. Figure 5.4 (C) shows the consistency of the model that when the amount of deformation is normalised by the external force, the data points overlap. The relationship is:

$$d_{elastic} \sim \frac{F_m}{G}. \tag{5.2}$$

5.3.2 Creep Velocity

The velocity of the bead v during creep is defined as the total displacement in the direction of the force d_{creep} divided by the number of timesteps in the simulation. The only force that can resist the external force moving the bead through the tissue is the viscous force F_v that occurs as the bead moves through the passive cells. Because of force balance on the cells we have $F_m \sim F_v$. From the viscous force model, we know that $F_v \sim R\eta v$, where R is the cell radius and η is the cell–cell viscosity. This means that we expect to have $F_m \sim R\eta v$, or written as:

$$v \sim \frac{F_m}{R\eta}. \tag{5.3}$$

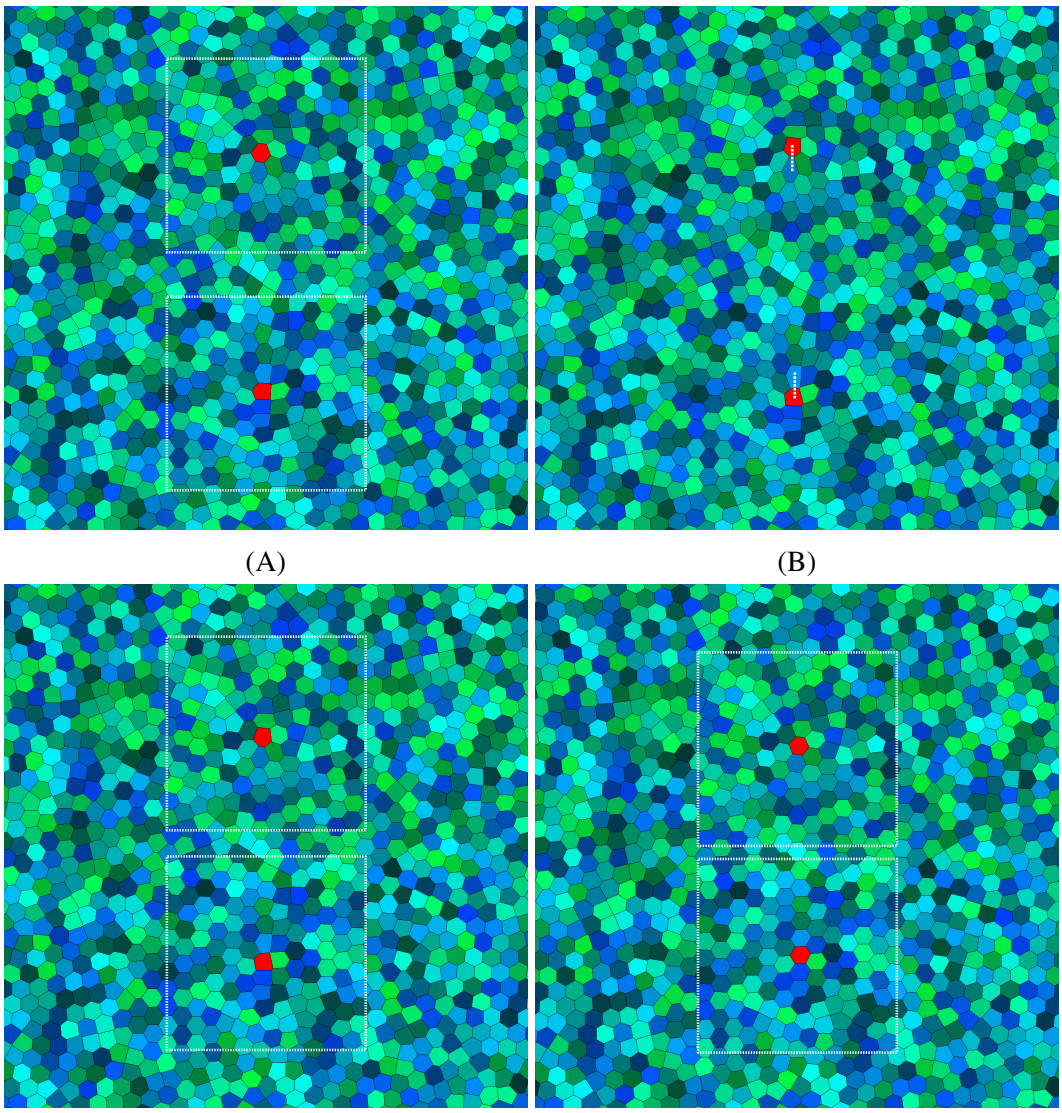

Fig. 5.3 A system of 1024 cells. The red cells experience external forces with identical magnitudes but in opposite directions. (A) When the force is applied, the local cells are elongated, causing local deformation. (B) The bead cells move through the cells. The white dashed line shows the trajectories. (C) The external force is removed. (D) The tissue returns to its normal state.

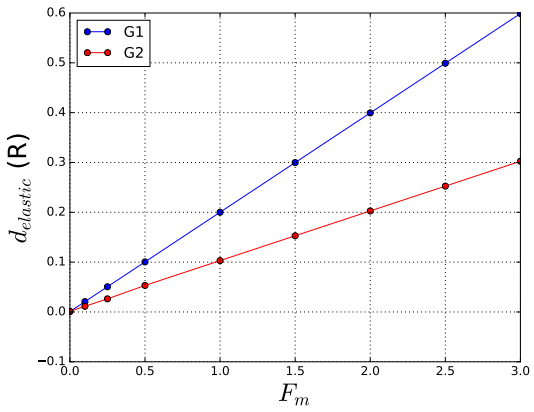

(A)

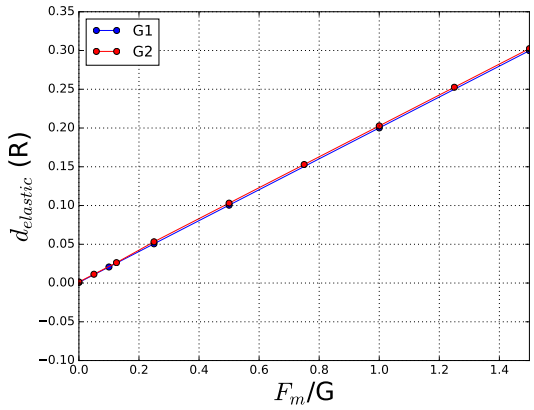

(B)

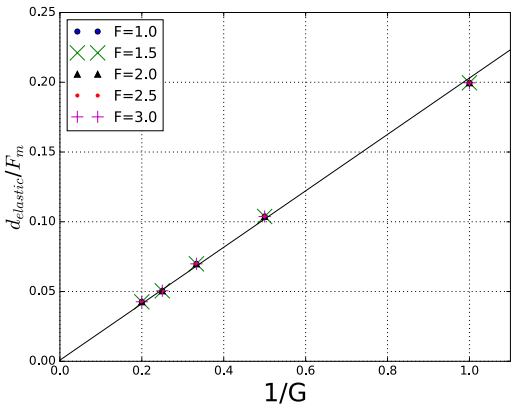

(C)

Fig. 5.4 Graphs demonstrating the elastic deformation. (A) The elastic displacement of the bead under a range of external forces. The stiffness of cells are $G = 1$ (blue) and $G = 2$ (red). (B) The same plot as (A) but the external force is scaled by the stiffness G. Then the two lines collapse. (C) The relationship of elastic displacement and the reciprocal of the stiffness. The elastic displacement is scaled by the external force.

To examine the effects of the parameters on the elastic behaviour of the cells, an identical force F_m is applied with viscosity η = [5, 10, 15, 20, 25, 30]. Then we looked at how the velocity varies with the cell stiffness G = [0.5, 1.0, 1.5, 2.0, 2.5] at η = [10, 20].

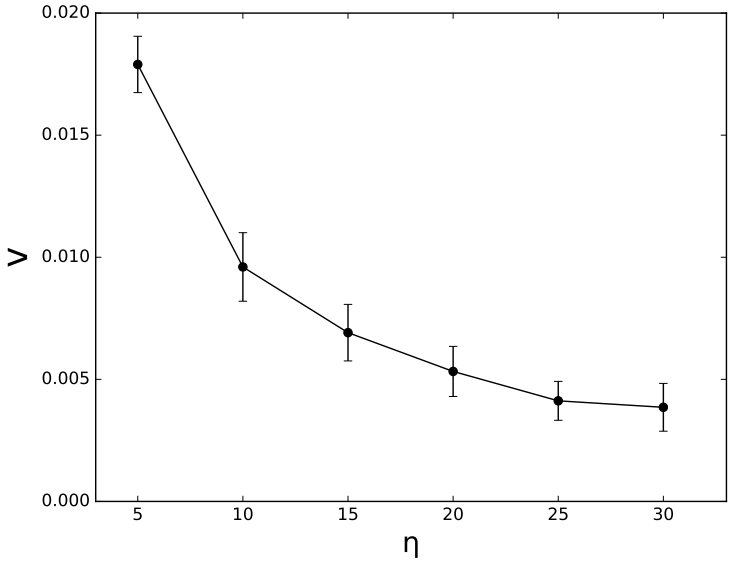

(A)

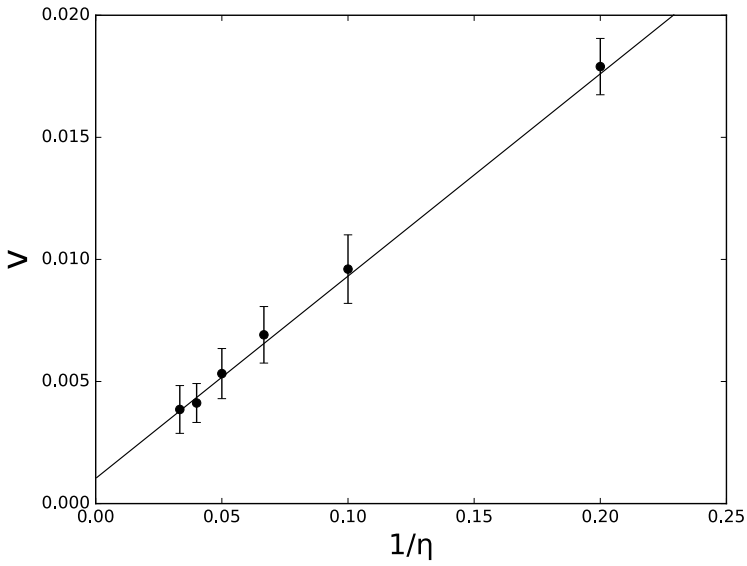

(B)

Fig. 5.5 The graph shows how the creep velocity is controlled by the cell–cell viscosity. The datapoints indicate the mean and the error bars denote the standard deviation (SD). The creep velocity is calculated as the average displacement per unit time step. (A) The velocity is plotted against the viscosity. (B) The velocity is plotted against the reciprocal of the viscosity.

Figure 5.5 shows that, as expected, the creep velocity decreases with an increased viscosity. We have noticed that the velocity plateaus when the viscosity is increased (Figure 5.5 (A)) but there is a slight movement when the viscosity is infinitely high (when $\frac{1}{\eta}$ is close to 0; 5.5 (B)). This is the noise generated from updating the position of the cells alternately from the Voronoi configuration to ellipses. However, we could conclude that the speed of the bead cell creeping through the cells is inversely proportional to the cell–cell viscosity:

$$v \sim \frac{F_m}{\eta}. \tag{5.4}$$

Figure 5.6 shows that the velocity of the bead is influenced by the cell stiffness. In stiffer tissue, a bead is less able to move. Stiffer cells are less deformed by the bead and retain a rounder shape. They provide resistance to the bead creep. In contrast, during the experiment, the magnetic bead was much stiffer than the cells and no significant deformation was observed on the bead. Hence, in our analysis, in order to see the effects of bead movement on the local cells, we neglected the effects of the stiffness of the bead and made the bead as stiff as the other cells.

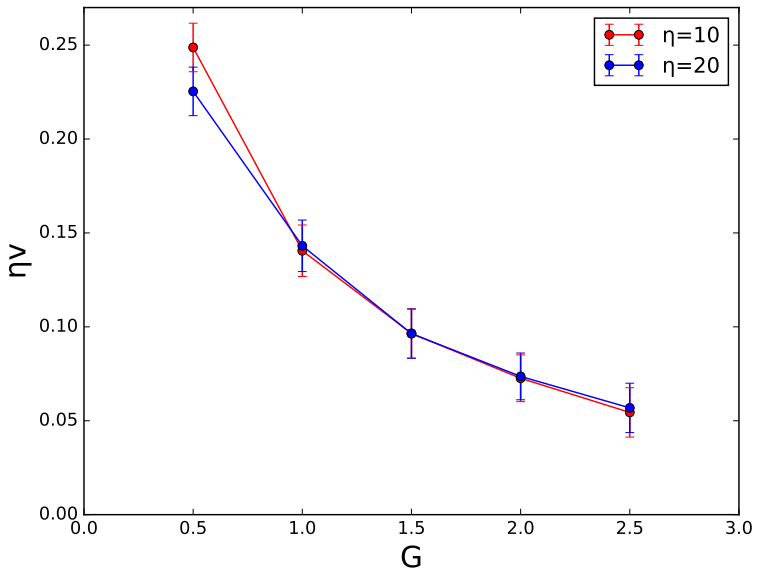

Fig. 5.6 The graph shows how the creep velocity is affected by cell stiffness. The velocity is multiplied by the cell–cell viscosity $\eta = 10$ (red) and $\eta = 20$ (blue). The datapoints indicate the mean and the error bars denote the standard deviation (SD). The curves show that the velocity decreases in stiffer tissue. The two curves tend to collapse.

5.3.3 Relaxation Displacement

We have introduced that the tissue behaviour in the model could be represented by an elastic spring and a dashpot in series if the applied stress is above the yield stress. Figure 5.2 (B) shows that the expected bead displacement curve has no recovery of the strain in the dashpot. However, when the external force is removed, there is a long relaxation. This tissue response suggests that cells rearrange their positions, which makes the bead move by a distance of d_{relax}.

The characteristic time constant of stress relaxation by cell rearrangement depends on the cell stiffness and cell–cell viscosity, since it is easy for cells to change neighbours when the viscosity is small. To examine the effects of cell–cell viscosity η and cell stiffness G on the bead relaxation displacement d_{relax}, an identical force F_m is applied to the same configurations of cells with viscosity η = [5, 10, 15, 20, 25, 30] and stiffness G = [0.5, 1.0, 1.5, 2.0, 2.5, 3.0].

Figure 5.7 (A) shows that the relaxation displacement linearly decreases with cell–cell viscosity. A higher viscosity makes the cells less able to rearrange. In comparison, cell stiffness has minor effects on the relaxation displacement (Figure 5.7 (B)). We suggest that the relaxation displacement is a result of cell intercalation and is correlated with the creep displacement. To investigate this relationship, an identical force is applied with the duration of the creep Δt = [0, 1, 5, 10, 20, 30, 40, 50, 60, 70, 80, 90, 100, 110, 120, 130, 140, 150]. As bead creep velocity is determined by the viscosity, the creep displacement d_{creep} linearly increases with the duration of the applied force.

Figure 5.8 describes the relationship between the creep and the relaxation. When there is no bead creep and the elastic deformation is immediately recovered, no relaxation behaviour is observed. Before the bead creep displacement reaches around 1.7, the relaxation displacement linearly increases with creep distance. Beyond that, though the bead creeps further, the relaxation displacement remains the same. There are no significant differences between tissues which have different cell stiffness and viscosity.

In the model, when a constant strain rate is applied to the passive system, cells start to intercalate when the cell stress reaches the yield stress. As a result, this allows the system to extend without increasing the cell strain and the average cell strain remains in a steady state [49]. The bead movement during creep is similar to a constant strain rate applied to the tissue. We suggest that when the local cell stress reaches the yield stress, the local stress disorder stays unchanged in a steady state. As a result, cell relaxation displacement does not increase when the bead moves further. Hence we suggest that the relaxation displacement is

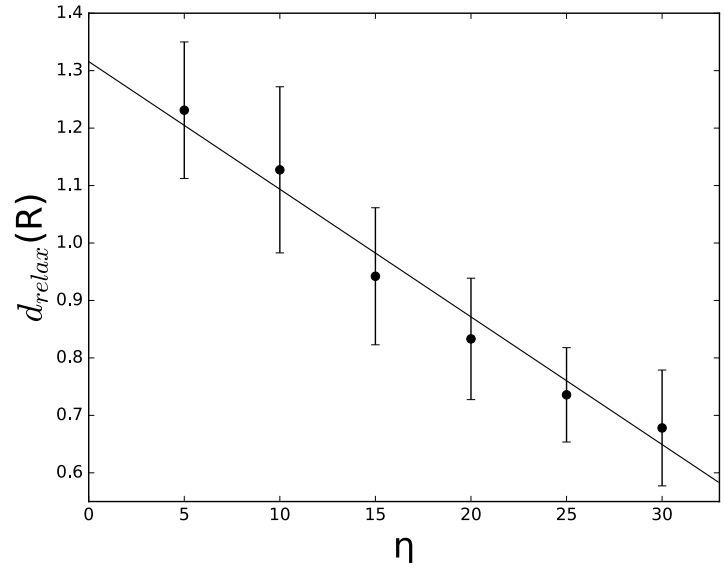

(A)

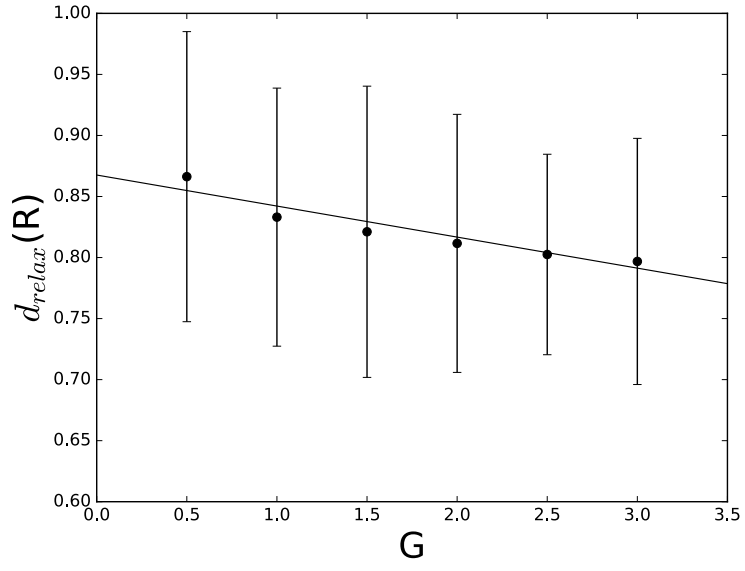

(B)

Fig. 5.7 The graph shows the relationship between the relaxation displacement and cell–cell viscosity and cell stiffness. The datapoints indicate the mean and the error bars denote the standard deviation (SD). (A) When the viscosity is higher, cells are less able to rearrange. As a result, the bead moves less in more viscous tissue. (B) The effect of cell stiffness on the relaxation displacement is not significant.

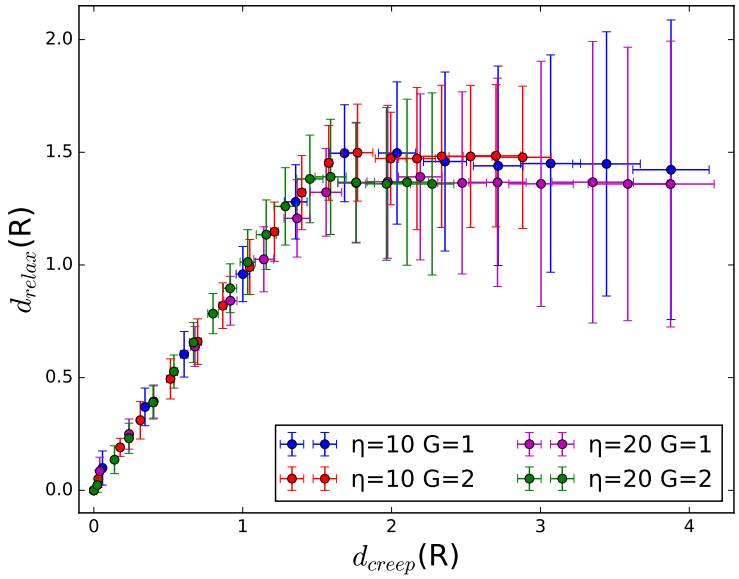

Fig. 5.8 The graph demonstrates the relationship between relaxation displacement and the creep displacement in four different tissue systems. The datapoints indicate the mean and the error bars denote the standard deviation (SD). There is no significant difference between these tissues.

related to the local stress distortion caused by the movement of the bead cell, rather than how far the bead creeps. We will examine the local cell stress in Section 5.5.

5.3.4 Summary

Simulation results have shown that the model is capable of capturing qualitatively the viscoelastic properties of the zebrafish embryo at an early development stage. We have examined the movement of the bead pulled by an external force in the passive tissue, and proved the relationships:

$$d_{elastic} \sim \frac{F_m}{G} \tag{5.5}$$

and

$$v \sim \frac{F_m}{\eta}. \tag{5.6}$$

The long relaxation is induced by the bead creep. The displacement during relaxation is mainly controlled by cell–cell viscosity. The relationship between the creep displacement and

the relaxation displacement reveals that the relaxation depends on the local stress disorder. In the following sections, we will investigate the cell displacement and the evolution of local cell stress over the experiment time.

5.4 Cell Displacement Field

We have shown in the previous section that the tissue mechanical properties affect the bead movement. Here we explore the displacement of cells in the vicinity of the bead in the tissue over the time when the force is applied. To avoid the influence of random factors in individual simulations, we plotted the average displacement field from 100 different sets of data.

Figures 5.9 – 5.11 describe the average displacement field of the cells during rapid elastic deformation, slow creep and rapid elastic recovery, respectively. In the plots, the applied force is directed in the negative y-direction. To calculate the mean displacement, the origin of the plane is translated to the position of the bead in each simulation. A region with an area of 10×10 (R) is divided into grids with a size of 2×2 (R). The bead is located in the central grid. Cells are assigned to each grid according to their coordinates, and hence the mean displacement vector in each grid is calculated. The plot in (A) shows the average displacement vector. The direction is indicated by the arrow and the magnitude by the colour. In (B), the standard deviation of the mean displacement in each grid is plotted.

The average displacement of the cells during rapid elastic deformation (Figure 5.9) and rapid elastic recovery (Figure 5.11) exhibits the same magnitude but in opposite directions. When the force is applied, cells on the axis of the force move in the same direction as the force. The rear cells move towards the bead and the front cells move away from the bead. The displacement decreases with increasing distance from the bead (Figure 5.9 (A)). When the force is released, cell displacement is in the opposite direction (Figure 5.11 (A)). If there is no time for creep, cells return to their initial position due to their elastic properties. In both cases, cell displacement is symmetrical along the axis of the force. The plot of standard deviations in (B) shows that the variations of cell displacement between simulations in both phases are small.

By contrast, the variations of cell displacement during creep between simulations in both x- and y-axis are greater than the elastic phases (Figure 5.10 (B)). No significant trend of cell displacement was observed in individual simulations. Nevertheless, the average displacement of cells is notably interpretable (Figure 5.10 (A)). The average displacement over this period of creep of the bead is 0.16. Cells around the bead have a larger displacement (around 0.10) while other cells move a small distance (around 0.03). Similar to the displacement field of

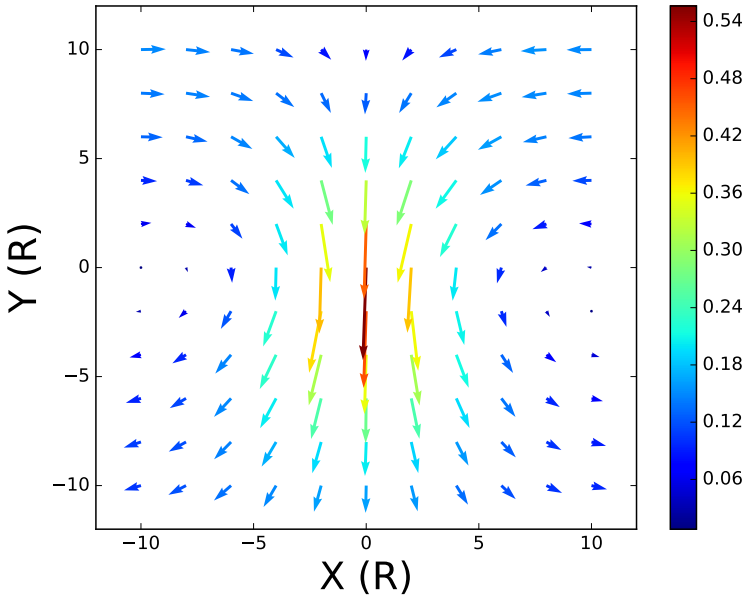

(A)

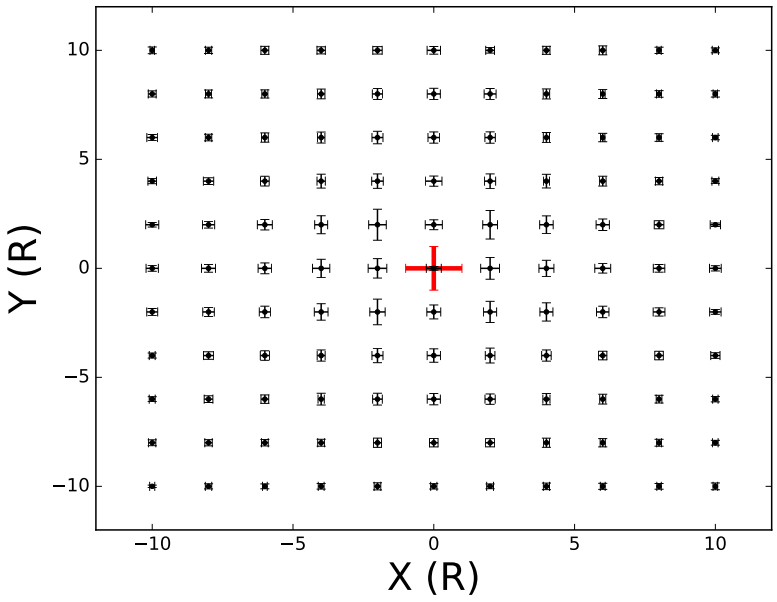

(B)

Fig. 5.9 Average cell displacement field for the rapid elastic deformation. (A) The mean displacement of cells around the bead. The arrow shows both direction and magnitude of the displacement of cells in each grid. (B) The standard deviation of the mean displacement of cells around the bead in the *x*- and *y*-axis, respectively. The scale bar in red colour represents a standard deviation of 0.1.

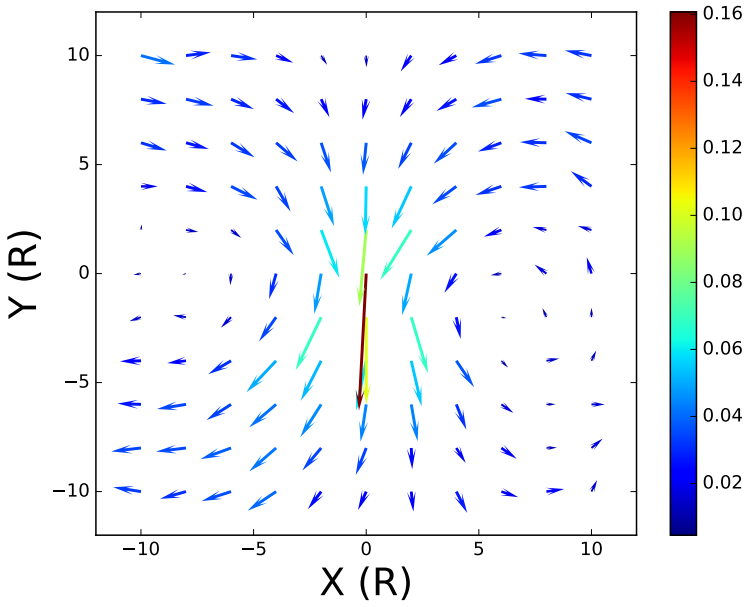

(A)

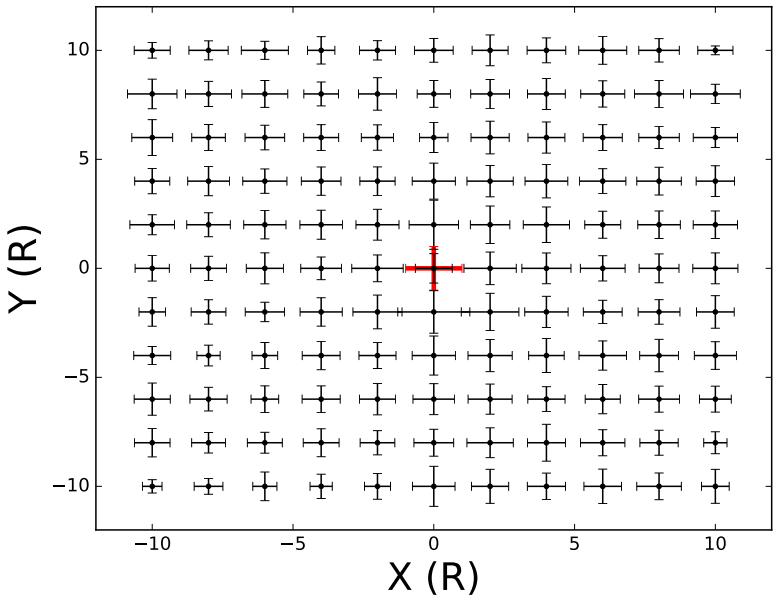

(B)

Fig. 5.10 Average cell displacement field for the slow creep. The duration of the creep in this plot $\Delta t = 20$ timesteps. (A) The mean displacement of cells around the bead. The arrow shows both direction and magnitude of the displacement of cells in each grid. (B) The standard deviation of the mean displacement of cells around the bead in the x- and y-axis, respectively. The scale bar in red colour represents a standard deviation of 0.1.

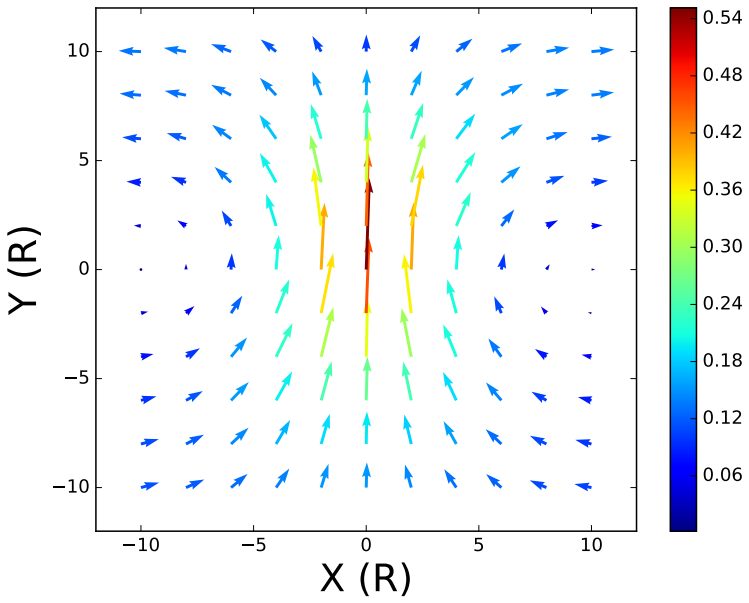

(A)

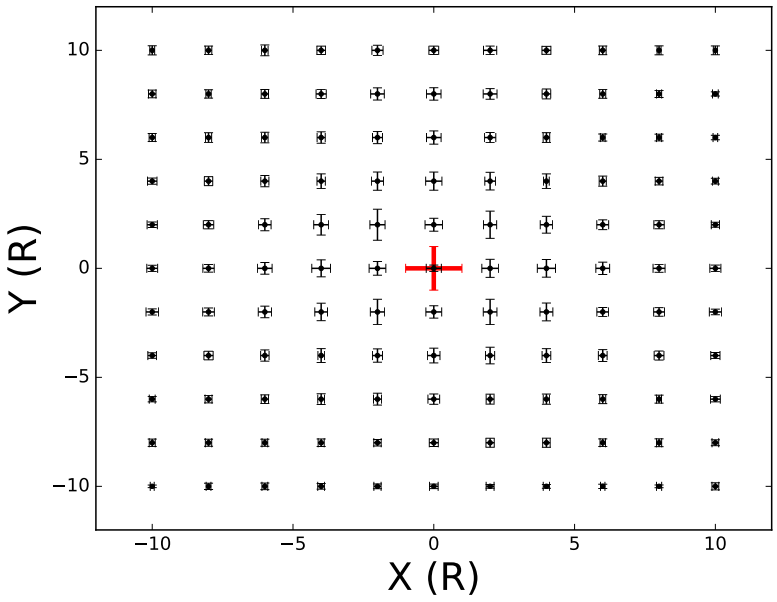

(B)

Fig. 5.11 Average cell displacement field for the rapid elastic recovery phase. (A) The mean displacement of cells around the bead. The arrow shows both direction and magnitude of the displacement of cells in each grid. (B) The standard deviation of the mean displacement of cells around the bead in the *x*- and *y*-axis, respectively. The scale bar in red colour represents a standard deviation of 0.1.

the elastic phase, the front cells are pushed and the rear cells are pulled in the direction of the creep. The average displacement is approximately symmetrical along the axis of the creep.

In the previous chapter, we discussed that the rheological model shows that the displacement during creep is not reversible. The bead creeping through cells causes local perturbation which remains in the tissue. However, in both experiments and simulations, we have noticed that a slow relaxation takes place when the elastic deformation is recovered. The patterns of local cell stress are yet to be defined. In the following section, we investigate how surrounding cells respond to the external perturbation by analysing the changes in cell stress.

5.5 Local Heterogeneous Stress

In this section, we investigate the cause, the patterns, and the relaxation timescale of the heterogeneous stress around the bead when the external force is released.

5.5.1 Local Stress Disorder

To explore the local stress disorder caused by bead creep, the cell stress around the bead is examined at relevant timesteps (Figure 5.12 (A)). If the force is applied at t_a and removed at t_b, the slow creep begins at t_a^+ and ends at t_b^-. The creep displacement along the force direction is $d_b - d_a$. The stress disorder caused by elasticity is the difference between stress at t_a^+ and t_a^-, and the stress disorder caused by creep is the difference between stress at t_b^+ and t_a^-, which eliminates the stress effect caused by elasticity.

Next, we define a circular plane where the bead is located at the centre. We are interested in the surrounding cells around the bead. Hence, the radius of the circular plane is $r = 5R$, where R is the radius of the cell. The area of the plane covers two layers of cells. The plane is then divided into four domains (Figure 5.12 (B)). In each simulation, the bead is located at the centre and cells are assigned to different domains according to their coordinates. The mean stress tensor of each domain is:

$$\bar{\sigma}_{\mathbf{k}}(t) = < \sigma_{\mathbf{i}}(t) >_{i \in D_k}, \tag{5.7}$$

where $\bar{\sigma}_k(t)$ is the mean stress tensor in domain D_k at timestep t, the index of the domains $k = 1,2,3,4$ for the circular plane, and $\sigma_i(t)$ is the stress tensor of cell i which lies in the domain k at timestep t. The change of stress between any two time steps (from t_1 to t_2) could be calculated as:

$$\Delta\bar{\sigma}_{\mathbf{k}}(t_1,t_2) = \bar{\sigma}_{\mathbf{k}}(t_2) - \bar{\sigma}_{\mathbf{k}}(t_1). \tag{5.8}$$

Then the norm of the change in stress tensor is:

$$\bar{\sigma}_k(t_1,t_2) = \| \Delta\bar{\sigma}_{\mathbf{k}}(t_1,t_2) \|, \tag{5.9}$$

where the norm is the Frobenius Matrix Norm, defined as the square root of the sum of the absolute squares of its elements for an $m \times n$ matrix $\mathbf{A}$:

$$\| \mathbf{A} \|_F = \sqrt{\sum_{i=1}^{m}\sum_{j=1}^{n} | a_{i,j} |^2}. \tag{5.10}$$

Finally, the integrated norm of stress changes all over the plane is:

$$\bar{\sigma}_{\sum}(t_1,t_2) = < \bar{\sigma}_k(t_1,t_2) >, k = 1,...,n. \tag{5.11}$$

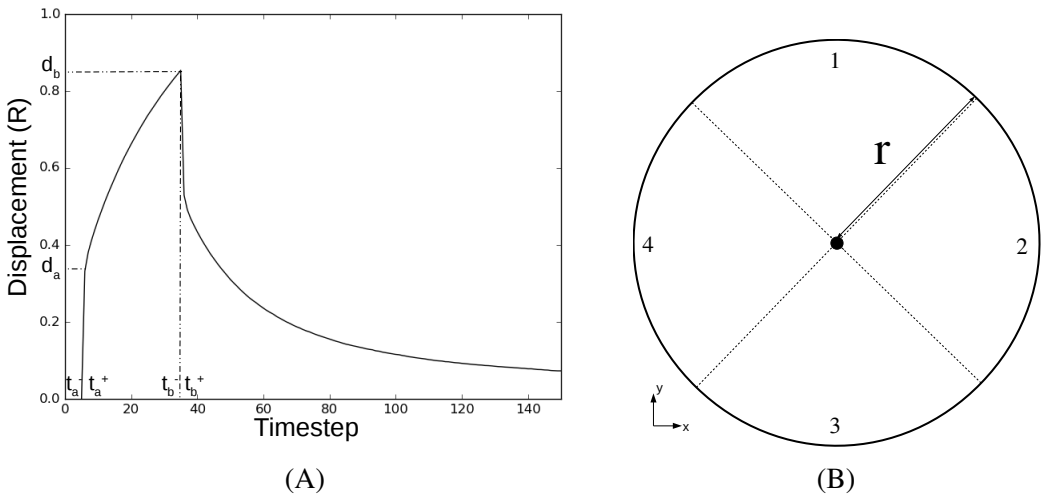

(A) (B)

Fig. 5.12 The analysis of heterogeneous stress caused by bead movement. (A) The external force is applied at t_a and removed at t_b. At t_a^+ the bead starts to slide through the cells. The creep displacement is calculated as the difference between the bead displacement d_b at t_b^- and the bead displacement d_a at t_a^+. (B) A circular plane is defined to analyse the local cell stress. The bead is at the centre. Cells in all simulations are assigned into each domain (1, 2, 3, 4) according to their coordinates with reference to the bead position. The radius of the plane is $r = 5R$.

Next, we investigate the correlation of bead creep displacement, the bead relaxation displacement, and the mean stress change in surrounding cells. In the simulation, we use

a configuration of 1024 identical cells with shear moduli $G = 1$ and cell–cell viscosities η = [10, 20], and the force F_m is constant for all simulations with the duration of the applied force being Δt = [0, 1, 5,10, 20, 30, 40, 50, 60, 70, 80, 90, 100, 110, 120, 130, 140, 150]. The bead pair was selected at different positions in the system and 100 simulations in total were taken into account.

We have illustrated the relationship between the creep displacement and the relaxation displacement in Figure 5.8. The change in the mean cell stress caused by the bead creep at each creep distance is shown in Figure 5.13. Though the bead moves at a different velocity in tissues with different cell–cell viscosities, the local stress disorder is only correlated with how far the bead moves, rather than how fast it moves. Initially, the mean stress increases with the movement of the bead. When the bead creeps for a distance of approximately 1.7 ($d_{creep} = 1.7(R)$), the value reaches a plateau, which means that the value of the mean cell stress comes to a steady state.

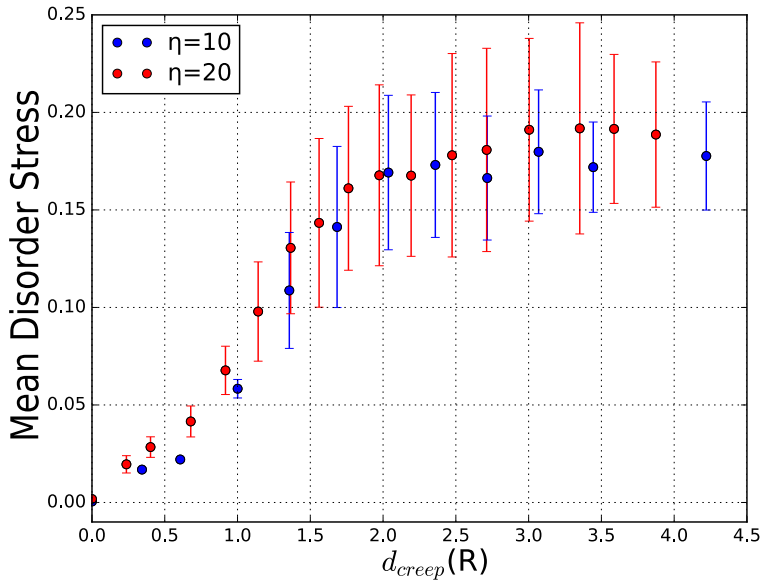

Fig. 5.13 The graph shows how the change of cell stress around the bead varies with bead creep displacement. The datapoints indicate the mean and the error bars denote the standard deviation (SD). The curve of $\eta = 10$ (blue) tends to collapse with the curve of $\eta = 20$ (red). When the bead moves by one cell size, the value of stress reaches a plateau.

We then examine the relationship between the change in mean cell stress around the bead and the relaxation displacement (Figure 5.14). The fit lines suggest that the relaxation displacement is correlated with the stress disorder around the bead. Hence, Figure 5.13 and 5.14 give evidence that the secondary relaxation could result from the change in local cell

stress which is caused by the bead creep. When the disorder reaches the yield stress of cells, the local stress remains in the steady state. We will now investigate the cell behaviour during relaxation and how it depends on the timescale of the system.

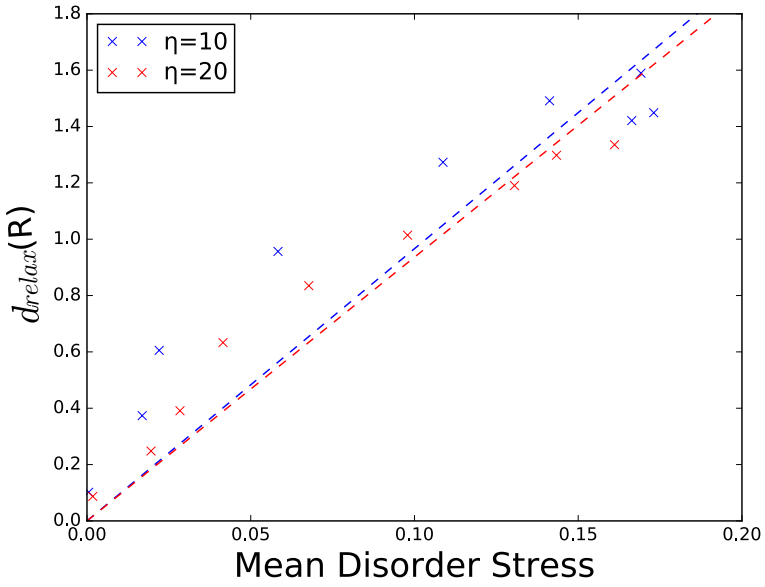

Fig. 5.14 The graph shows how the relaxation displacement of the bead varies with the change of cell stress around the bead. Cell–cell viscosity if $\eta = 10$ (blue) and $\eta = 20$ (red). The two fit lines tend to collapse.

5.5.2 Stress Relaxation Time

To examine the effects of the parameters on the relaxation time of the system, a constant force with fixed magnitude is applied to all simulations. The characteristic time $\tau = [\frac{10}{3}, 5, \frac{20}{3}, 10, 20]$ with different cell stiffness G and cell–cell viscosity η. The change in the mean cell stress is calculated for the relaxation period from $t = t_b^+$. Figure 5.15 shows the time evolution of the change in the mean cell stress caused by bead creep. In the previous section, we showed that the change in the mean cell stress is determined by the creep displacement. In order to compare the relaxation time for different cell parameters, the system is relaxed from identical history of stress disorder, which means that the bead creeps for the same amount of displacement in all simulations.

The relaxation of the cell stress is shown in Figure 5.15 (A). We can see that the system follows distinct paths according to the value of time constant τ. Initially, the change in stress is caused by the movement of the bead. The model defines the stress tensor as:

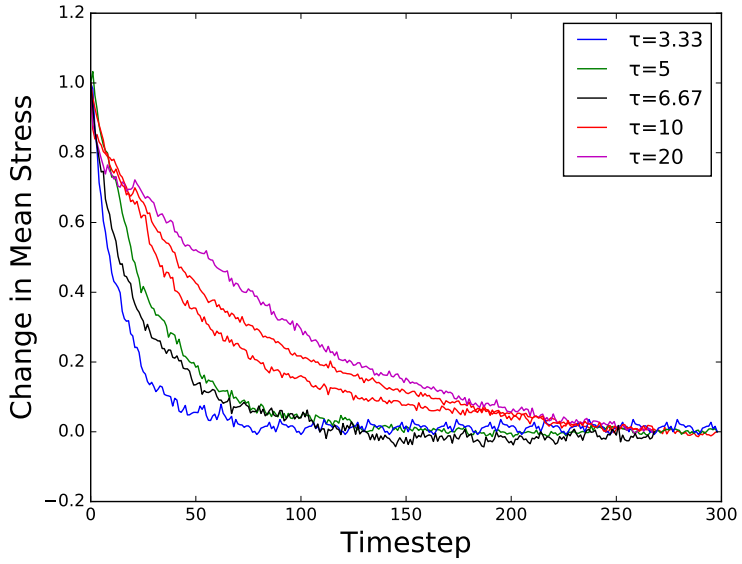

(A)

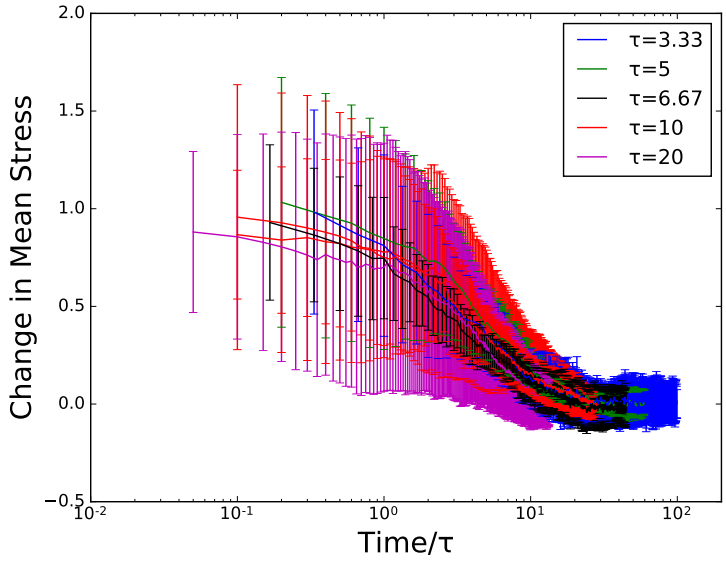

(B)

Fig. 5.15 The time evolution of the change of mean cell stress during relaxation. (A) The relaxation of local cell stress over time through intercalation. Curves are coloured by their timescale parameter $\tau = \eta R/G$. (B) Collapse of the local stress relaxation curves after scaling time with τ plotted with a logarithmic time axis. The error bars denote the variations of the stress around the bead by the standard deviation (SD).

$$\sigma = 2G\varepsilon, \tag{5.12}$$

where G is the stiffness of the cells. The cell shape ε during relaxation is determined by:

$$\varepsilon \backsim e^{-t/\tau}, \tag{5.13}$$

where $\tau = \eta R/G$. Therefore, the relaxation speed of the local heterogeneous stress is controlled by the timescale parameter. As shown in Figure 5.15 (A), the system with a smaller time constant τ relaxes faster.

Then we plot the time evolution of the change of mean cell stress and scale the time by the characteristic time for each simulation (Figure 5.15 (B)). We see that all of the curves collapse. Statistical significance has proved that the relaxation time is also controlled by the timescale parameter $\tau = \eta R/G$ of the system.

Having examined the short time response of the system on the cell stress heterogeneity, we will now look at the cell stress patterns around the bead cell and how they evolve with time.

5.5.3 Cell Stress Patterns

In this section, we investigate the patterns of cell stress in the tissue at each time step. The bead position is sampled in the same tissue which has a configuration of 1024 identical cells to generate 100 different simulations. A rectangular plane with a size of 10×10 (R) is defined, where the bead is at the origin. The plane is divided into 2×2 (R) grids. Cells are assigned to the grid according to their coordinates with reference to the bead cell.

To examine the stress patterns in the plane, the mean cell stress tensor was calculated for each grid. The stress tensor of each cell is represented as:

$$\sigma = \begin{bmatrix} \sigma_{xx} & \sigma_{xy} \\ \sigma_{yx} & \sigma_{yy} \end{bmatrix}, \tag{5.14}$$

where σ_{xx} and σ_{yy} are the normal stress in the x- and y-direction, and σ_{xy} and σ_{yx} are the shear stress. The mean stress tensor in each grid is calculated by taking the average of the stress tensor of each cell which lies in the grid. The averaged stress tensor of each grid is diagonalised to obtain the principal stress:

$$\bar{\sigma} = \begin{bmatrix} \bar{\sigma}_x & 0 \\ 0 & \bar{\sigma}_y \end{bmatrix}. \tag{5.15}$$

The pure shear stress for each grid is defined as:

$$\tau = \frac{1}{2} \mid \bar{\sigma}_x - \bar{\sigma}_y \mid, \tag{5.16}$$

and the normal stress component or pressure as:

$$\sigma_n = \frac{1}{2}(\bar{\sigma}_x + \bar{\sigma}_y). \tag{5.17}$$

Figure 5.16 uses ellipses to represent the mean stress tensor at t_a^-, t_a^+, t_b^-, t_b^+ and $t \to \infty$, respectively. The two axes of the ellipses and rotation angles are explicitly presented. Since cell stress is proportional to cell strain in the model, the ellipses in these plots are also a description of cell shape.

Initially, the system is fully relaxed and cells maintain normal regular shape (Figure 5.16 (A)). When an external force is applied to the central bead in the direction of -y, a rapid movement of the bead causes elastic deformation of the local cells. The cells in front of the bead are compressed while the cells behind the bead are elongated. The cells on both sides are deformed by shear forces, and the stress is symmetrical along the force axis (Figure 5.16 (B)). We have discussed that the average cell displacement during creep is symmetrical along the axis of the force. At the end of the bead creep, cell deformation reaches the maximum (Figure 5.16 (C)). When the external force is removed, there is no external force in the tissue and the elastic deformation is recovered. Compared with the relaxed state (Figure 5.16 (A)), significant stress heterogeneity remains in the tissue (Figure 5.16 (D)). The ellipses are symmetrical along the y-axis. After a long period of relaxation, the cells return to their normal regular shapes by dissipating stress through cell rearrangement (Figure 5.16 (E)).

Next we use a heat map with hexagonal presentation to describe the evolution of cell stress in the tissue. The normal stresses σ_{xx} and σ_{yy}, the shear stress σ_{xy}, the pressure σ_n and pure shear τ are plotted at t_a^-, t_a^+, t_b^-, t_b^+ and $t \to \infty$, respectively (Figure 5.17 to Figure 5.21).

Normal stress in the x-direction σ_{xx} is a result of cell movement. There are no significant patterns, but a rough symmetry along the x-axis can be observed (Figure 5.17). As the external force is on the negative y-axis, normal stress of cells in the y-direction σ_{yy} is more significant. It is symmetrical along the y-axis with opposite signs. The stress in the direction of the force increases at the end of creep (Figure 5.18 (C)).

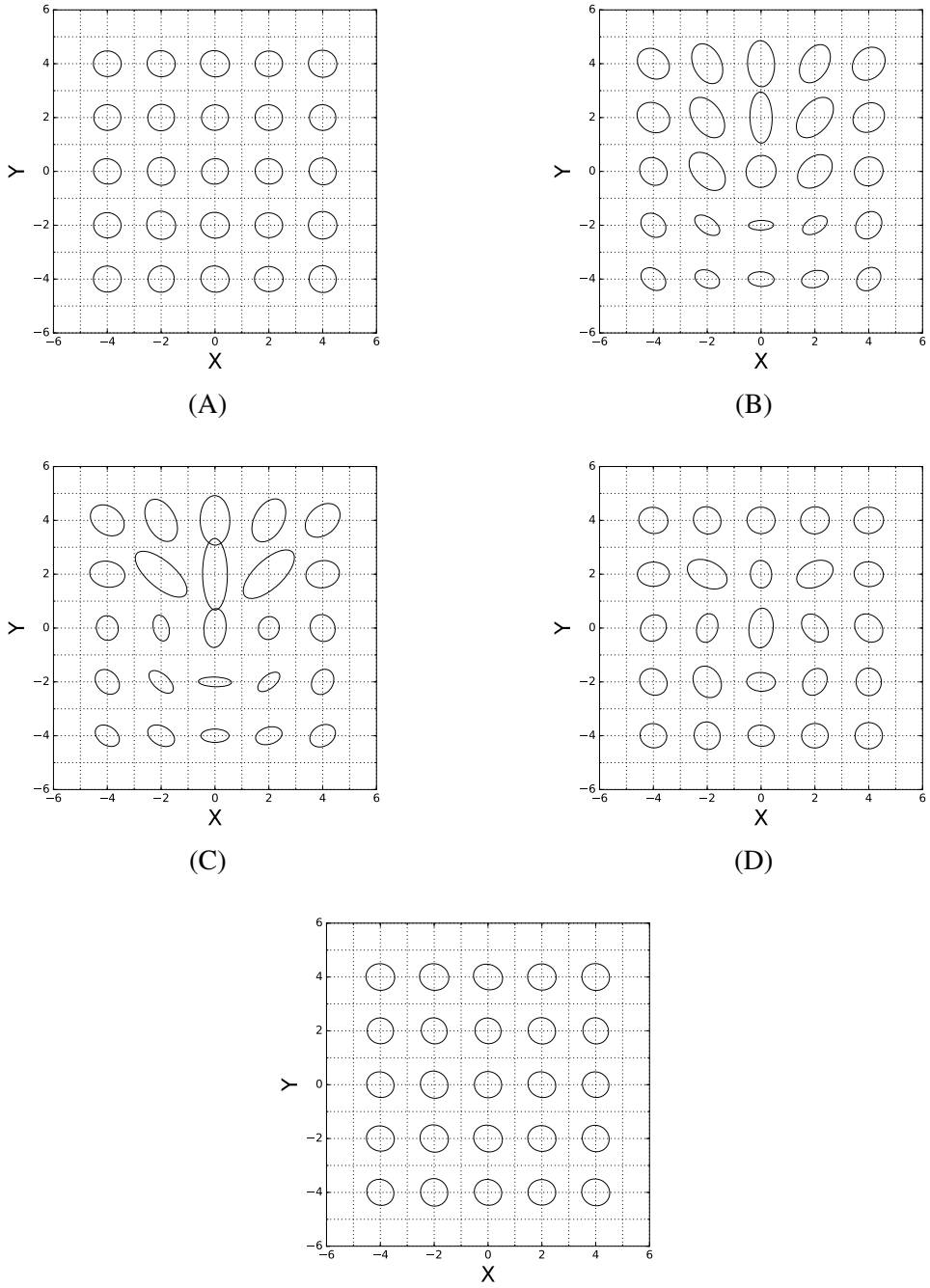

Fig. 5.16 Elliptical representation of cell stress tensors in the plane which is divided into grids. The bead is positioned at the centre. The timestep of each plot is (A) Relaxed system before the force is applied: t_a^-, (B) Rapid elastic deformation: t_a^+, (C) The end of the creep before the force is removed: t_b^-, (D) Right after the force is removed: t_b^+ and (E) The system is relaxed for a long period of time: $t \to \infty$.

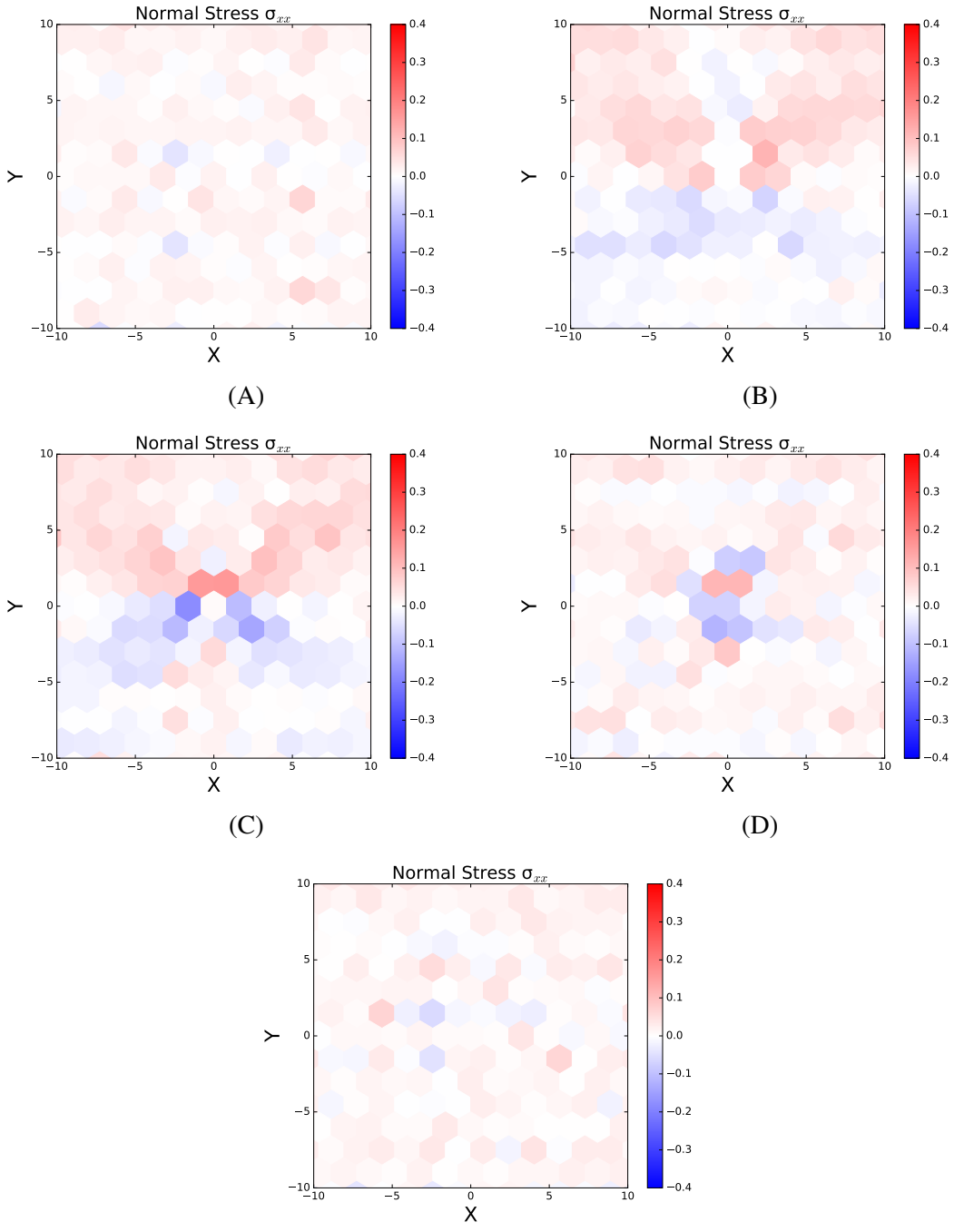

Fig. 5.17 The map for the normal stress in the x-direction σ_{xx}. The brightness of the colour indicates the value of the stress: positive (red), negative (blue) and 0 (white). The bead is positioned at the origin. The timestep of each plot is (A) Relaxed system before the force is applied: t_a^-, (B) Rapid elastic deformation: t_a^+, (C) The end of the creep before the force is removed: t_b^-, (D) Right after the force is removed: t_b^+ and (E) The system is relaxed for a long period of time: $t \to \infty$.

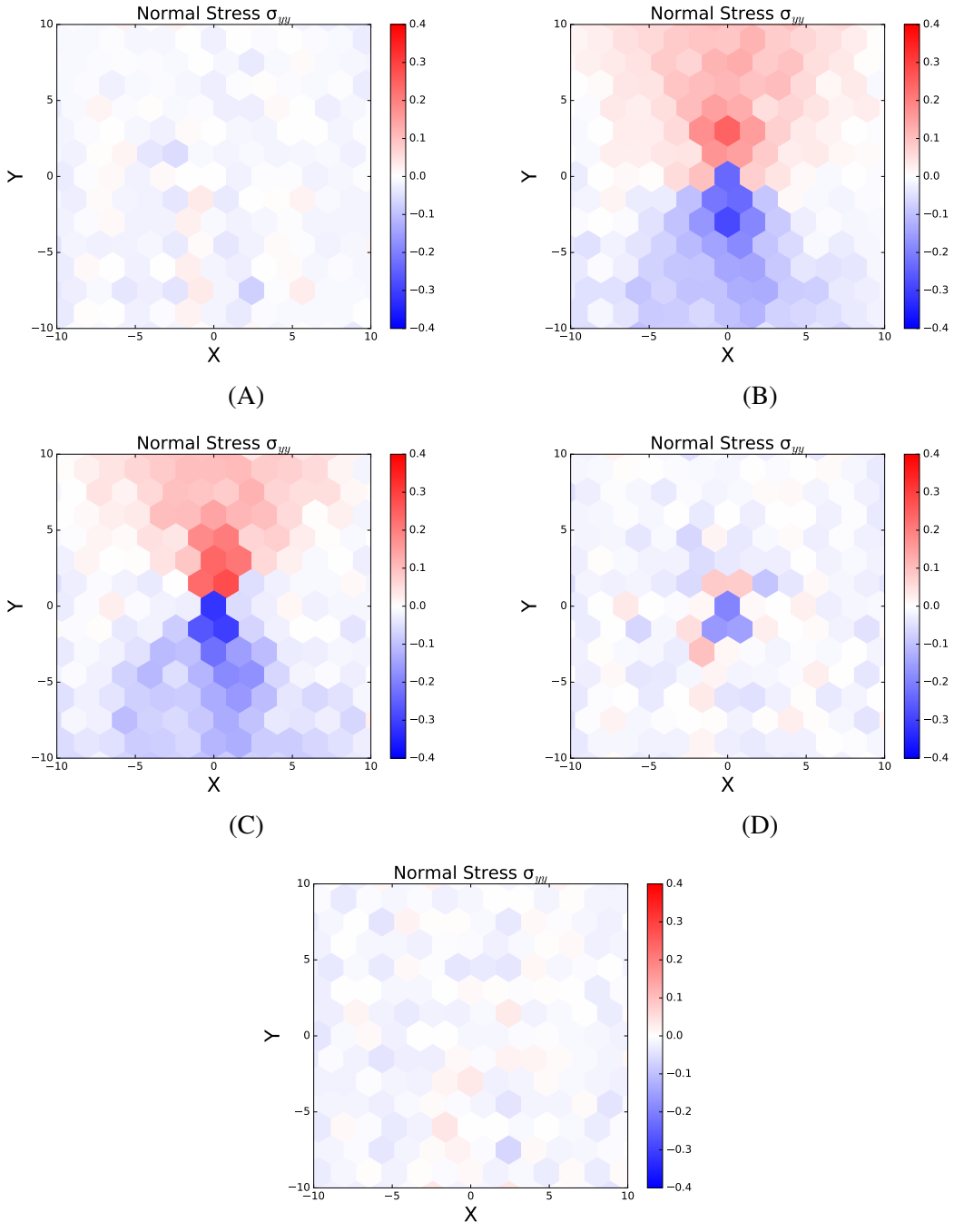

Fig. 5.18 The map for the normal stress in the y-direction σ_{yy}. The brightness of the colour indicates the value of the stress: positive (red), negative (blue) and 0 (white). The bead is positioned at the origin. The timestep of each plot is (A) Relaxed system before the force is applied: t_a^-, (B) Rapid elastic deformation: t_a^+, (C) The end of the creep before the force is removed: t_b^-, (D) Right after the force is removed: t_b^+ and (E) The system is relaxed for a long period of time: $t \to \infty$.

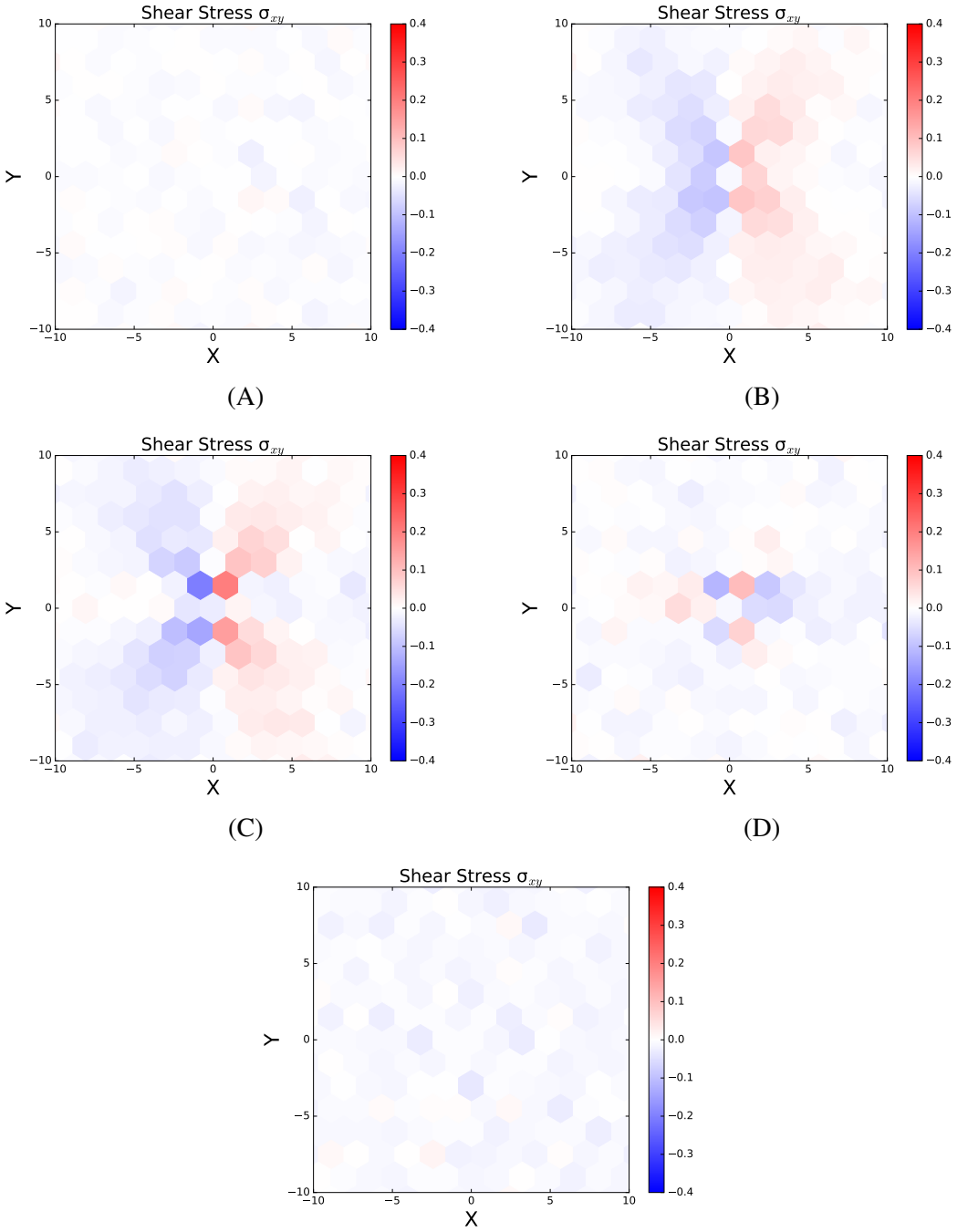

Fig. 5.19 The map for the shear stress σ_{xy}. The brightness of the colour indicates the value of the stress: positive (red), negative (blue) and 0 (white). The bead is positioned at the origin. The timestep of each plot is (A) Relaxed system before the force is applied: t_a^-, (B) Rapid elastic deformation: t_a^+, (C) The end of the creep before the force is removed: t_b^-, (D) Right after the force is removed: t_b^+ and (E) The system is relaxed for a long period of time: $t \to \infty$.

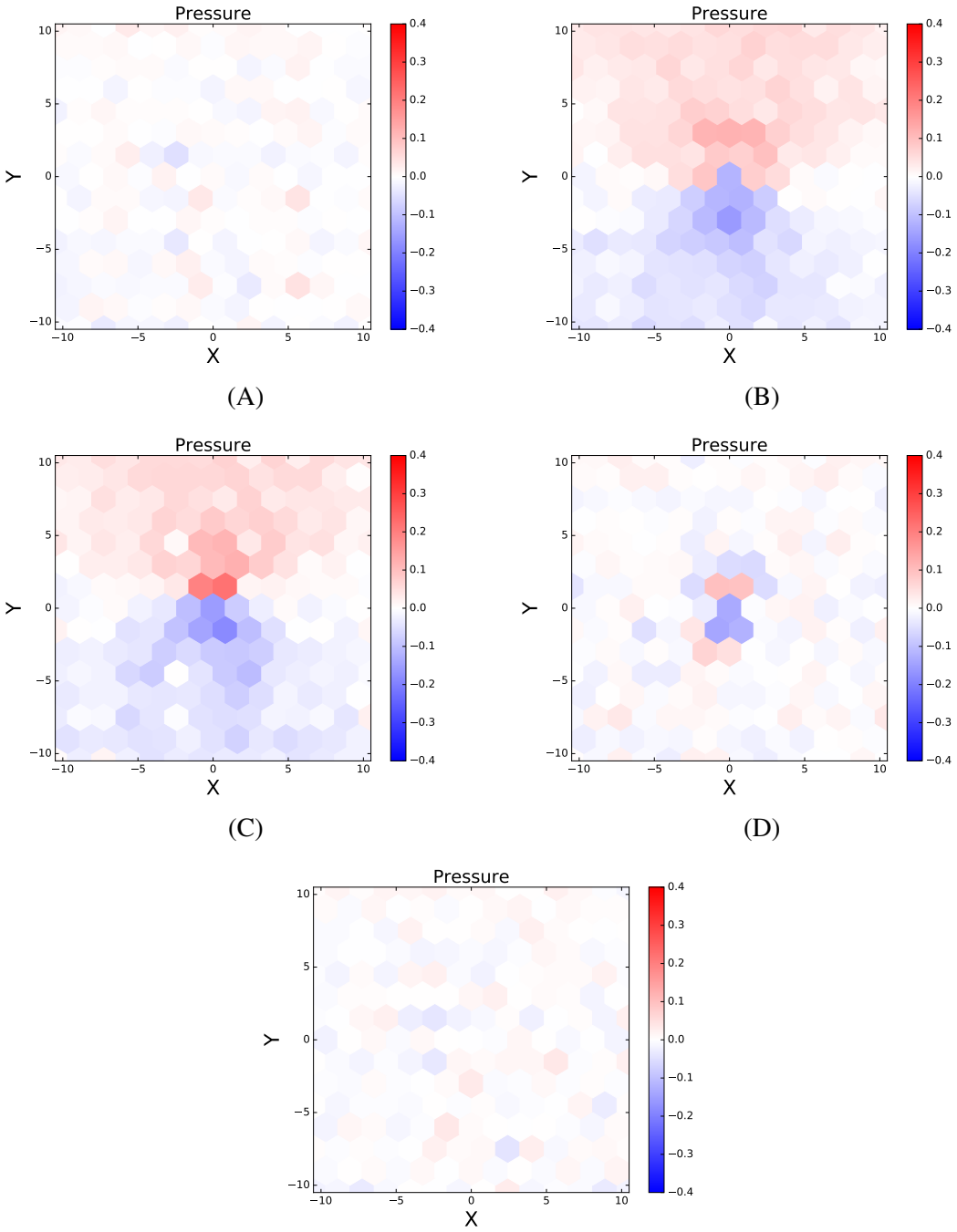

Fig. 5.20 The map for the pressure σ_n. The brightness of the colour indicates the value of the stress: positive (red), negative (blue) and 0 (white). The bead is positioned at the origin. The timestep of each plot is (A) Relaxed system before the force is applied: t_a^-, (B) Rapid elastic deformation: t_a^+, (C) The end of the creep before the force is removed: t_b^-, (D) Right after the force is removed: t_b^+ and (E) The system is relaxed for a long period of time: $t \to \infty$.

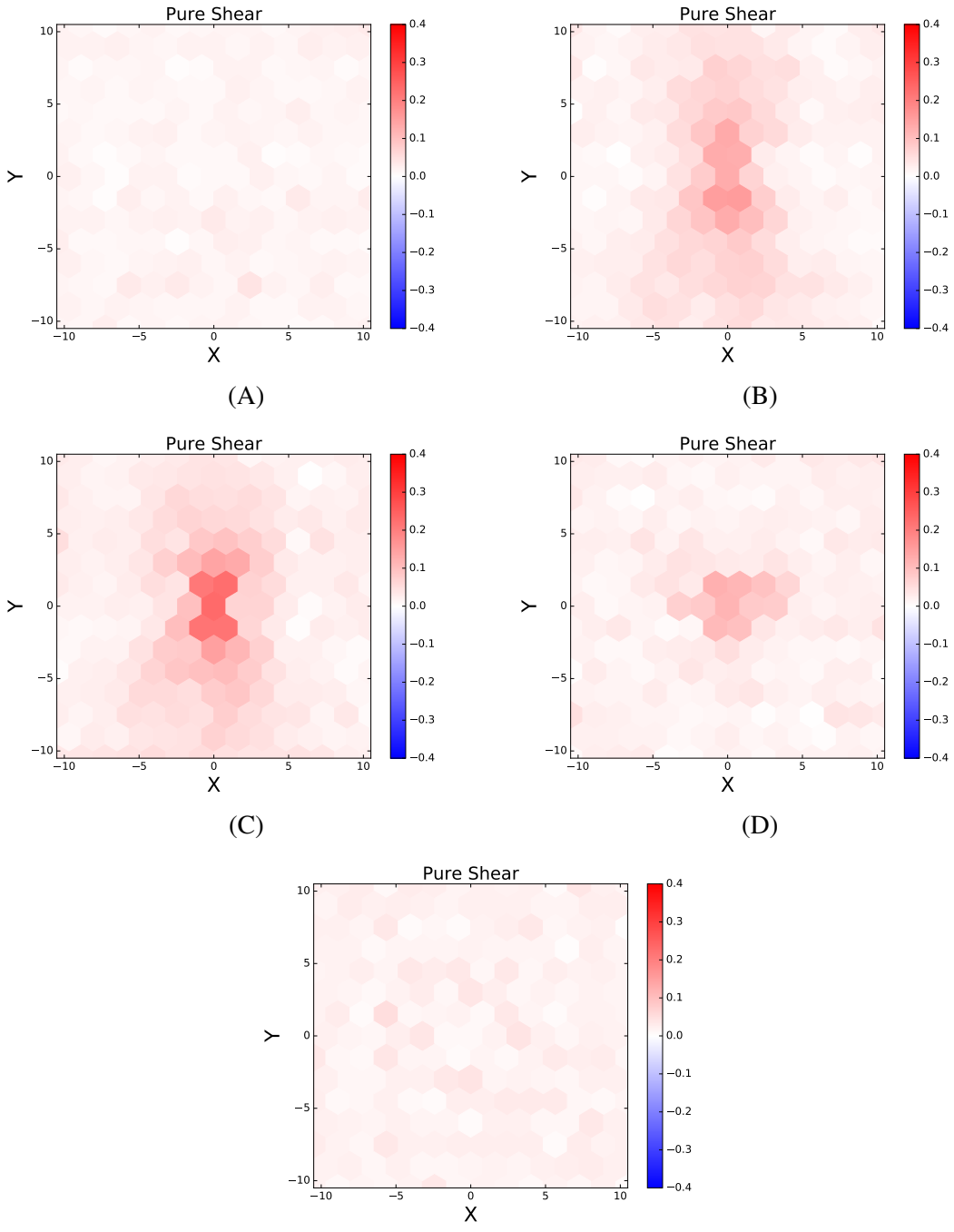

Fig. 5.21 The map for the pure shear stress τ. The brightness of the colour indicates the value of the stress: positive (red), negative (blue) and 0 (white). The bead is positioned at the origin. The timestep of each plot is (A) Relaxed system before the force is applied: t_a^-, (B) Rapid elastic deformation: t_a^+, (C) The end of the creep before the force is removed: t_b^-, (D) Right after the force is removed: t_b^+ and (E) The system is relaxed for a long period of time: $t \to \infty$.

The shear stress of cells σ_{xy} is symmetrical along the y-axis but has opposite signs. Cells on the y-axis have no significant shear effects (Figure 5.19 (B)). The magnitude of the shear stress decreases when the distance between the cell and the bead is increased. When the force is removed, heterogeneous shear stress is observed in the central region with a size of 5×5 (R) (Figure 5.19 (D)). In the simulation, the bead creeps for a distance of one cell size. In this case, the bead movement has the most significant effects on the closest layer of cells. The change in the pure shear in Figure 5.21 (C) and (D) shows that the increased shear stress around the bead is the consequence of bead sliding through neighbouring cells.

The pressure σ_n is an indication of the change in cell size. When the force is applied, cells in the tissue are deformed. As shown in Figure 5.20 (B), the front cells are compressed, indicated by negative pressures, and the rear cells are elongated, indicated by positive pressures. At the end of the bead creep (Figure 5.20 (C)), the pressure on the cells in the direction of the applied force is increased, however, the pressure on the cells on both sides is decreased. It suggests that distant cells are less influenced by the creep and the cell stress is relaxed by cell rearrangement. When the force is released (Figure 5.20 (D)), the notable pressure on the surrounding cells shows that local cells remain deformed.

Figure 5.17 – Figure 5.21 (E) have presented a common feature of different stress components, that after a long period of relaxation, the heterogeneous stress recovers and the tissue reaches the normal relaxed state.

5.6 Summary

In this chapter, we have first examined the behaviour of the mechanical model when an external body force is incorporated. The simulation result is qualitatively similar to the experimental measurement. The displacement of the bead consists of four phases: the rapid elastic deformation, the slow creep, the rapid elastic recovery and the long relaxation. The main control parameters are the magnitude of the external force, the cell stiffness and the cell–cell viscosity. The bead displacement in the fast increase phase and retraction phase reflected the elastic property. The displacement was controlled by the magnitude of the external force and the cell stiffness. The slow creep described the viscous property. The bead moved at a constant speed which was determined by the magnitude of the external force and the cell–cell viscosity. The effect of stiffness on creep was minor. Since the model was consistent with a Maxwell model, the bead displacement should have remained the same after the fast elastic retraction. However, a long relaxation was observed in the simulated curve,

which was qualitatively similar to the experimental results. This result implied that the local cell stress disorder caused by bead creep might induce the observed secondary relaxation.

To test this hypothesis, we analysed the time evolution of the average stress of the local cells around the bead. The results show that the change in the local cell stress was a result of bead creep, and the average cell stress increased with the creep distance until it reached a threshold. Furthermore, bead displacement during relaxation was correlated with the change in the cell stress caused by the bead movement. The early-stage embryo illustrated mechanical properties similar to history dependent materials. During relaxation, the time was controlled by the characteristic time constant of the system. The patterns of local cell stress during creep indicated that the main stress experienced by cells in the line of the applied force was elastic stresses, while on both sides of the bead the main stress was shear stresses.

Figure 5.22 illustrates the patterns of forces which the bead experiences during creep. The front and rear cells are analogous to elastic springs with stiffness G. The cells on the left and right sides of the bead produce friction when the bead slides through them. The viscous force is represented by a dashpot with a coefficient η at the contact surfaces. When the external force is applied (Figure 5.22 (A)), the bead slides through the cells. The front cells are compressed and the rear cells are elongated. The front cells push the bead and the rear cells pull the bead. Cells on the left and right sides of the bead experience shear stress produced by the viscous forces. The viscous force on the bead is in the opposite direction to the movement. At the time when the force is released (Figure 5.22 (B)), the tissue tends to retract. Hence, the front cells push the bead and the rear cells pull the bead. The elastic deformations on these four cells recover rapidly. When the bead moves back, it experiences viscous forces at the contact surfaces with the cells. The direction of the viscous forces is in the opposite direction to the bead movement.

In summary, the simulation results provide evidence that the secondary relaxation could be a result of cell intercalation, without involving other complex cell movements. Based on these ideas from the simulation, the correlation between the creep displacement and the relaxation displacement in the experimental data can be explored to examine the behaviours of cells during the relaxation. In the next chapter, we explore the mechanical behaviour of cells when cell division takes place. The mechanical model is used to simulate cell division in an epithelial monolayer.

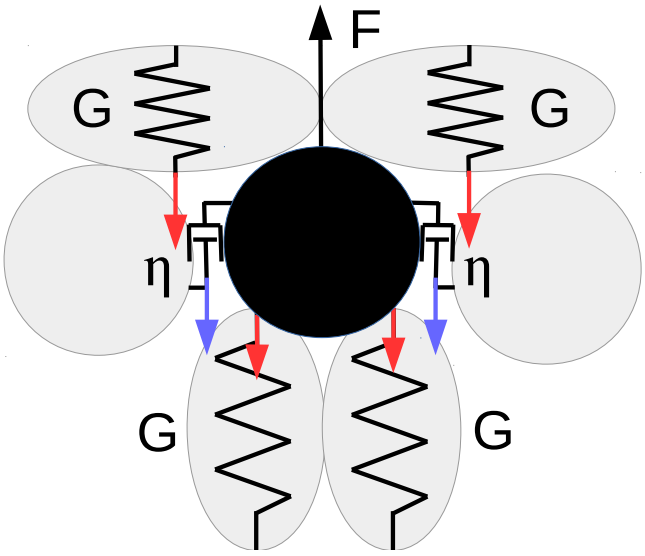

(A)

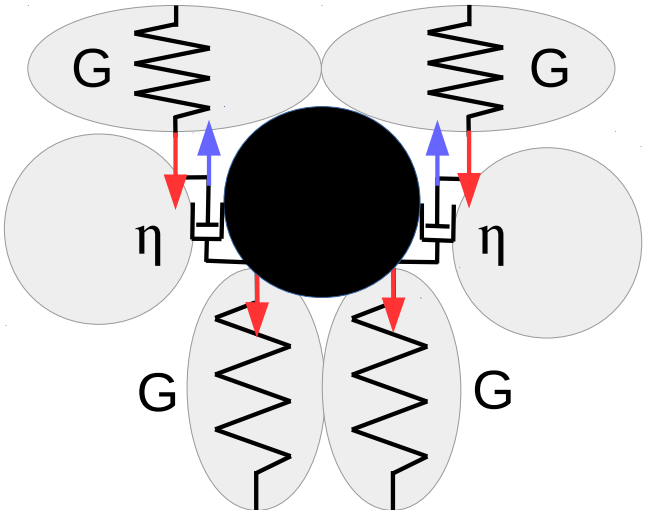

(B)

Fig. 5.22 The schematic schematic diagram describing the bead and surrounding cells with rheological models. The elastic stiffness of the springs is G. The viscosity of the dashpot is η. F denotes the direction of the applied force on the bead. The arrows describe the reaction forces produced by the cells: elastic force (red) and viscous force (blue). (A) During bead creep. (B) When the external force is released.

Chapter 6

Oriented Division Along Long Cell Axis as a Mechanism for Tissue-scale Stress Dissipation

6.1 Introduction

Cell division is one of the active events that drives the tissue to deform by the changes in the shape of participating cells. It plays an important role in shaping animal tissues. Several studies have suggested that cell division can account for much of the topological disorder observed in epithelia [38], can drive tissue elongation [5, 25, 62], and can facilitate the return to homeostatic cell packing following a deformation [18, 39]. In each of these processes, the effect of cell division depends critically on the orientation of divisions. Further, experiments have suggested that the proliferation rate of animal cells tend to change with existences of extrinsic forces and both intrinsic and extrinsic factors may change the choice of the axis for division [5, 25, 62].

At the cellular level, simple rules govern division orientation. Hertwig [45] showed that cells from early animal embryos divide along their long cell axis so as to reduce the length of their long axis. Rappaport [76] proposed that anti-parallel microtubules emanating from anaphase spindle poles specify the division plane in animal cells. However, more recent studies looked at division orientation in cells adhering to micropatterned substrates and found that both the geometrical arrangement of integrin-mediated cells-substrate adhesions and extrinsic mechanical forces orient cell division [34]. These biological and mechanical signals appear to guide division orientation both *in vivo* [60] and in epithelial monolayers in

developing embryos [56, 62]. Hence, in the study, we investigate how cell shape and extrinsic mechanical tension on the tissue contribute to the orientation of division, how tissues respond to these effects, and how cell divisions change the stress around the cell in an epithelial tissue.

Both live imaging and mechanical perturbations were used to examine the effects of cell shape changes during mitosis and cell division in stretched monolayers in the absence of cell intercalation. In addition, these behaviours were quantitatively reproduced by the mechanical model which could simulate the autonomous changes within a stretched monolayer. This interdisciplinary work was a collaboration between Dr Alexandre Kabla's group in the Department of Engineering at the University of Cambridge, Prof Guillaume Charras' group and Dr Buzz Baum's group in UCL. The experiments were performed and analysed by Tom Wyatt and Andrew Harris. The simulation and data analysis were my individual work. In this chapter, we first introduce the experimental protocols and the experimental results, followed by the computational model and the discussion on cell mechanics from both experimental and simulation data.

6.2 Experimental Protocols

Harris et. al. [43] developed an experimental equipment to characterise the tensile planar mechanical properties of epithelial cell monolayers in isolation from their substrate (Figure 6.1). The system consists of two micromanipulators, two test rods, one of which is soft and the other stiff, and a top-down macroscope to image the position of the test rod. Monolayers are suspended between the extremities of these two test rods. A manual micro-manipulator keeps one rod fixed and the other micro-manipulator slowly moves the other rod apart by a motor with known forces, of which the magnitude can be measured by monitoring the deflection of the soft test rod. As a result, the suspended monolayers are extended. In the experiment, monolayers are required to be free from their substrate as we only interpret the stress-strain response of the load-bearing monolayers. Initially, cells are cultured on a substrate generated by polymerising a drop of collagen between the two rods. The monolayer extends from one test rod to the other. Before the experiment, the collagen substrate is removed by enzymatic digestion, leaving the monolayer freely suspended. During monolayer extension, live microscopy imaging at both cellular and subcellular level is recorded for analysis.

With this force measurement device, the division orientation and the underlying mechanism can be explored [110]. Wild Type Madin-Darby canine kidney II (MDCK) epithelial monolayers were generated through collagenase treatment [43] devoid of a continuous load-

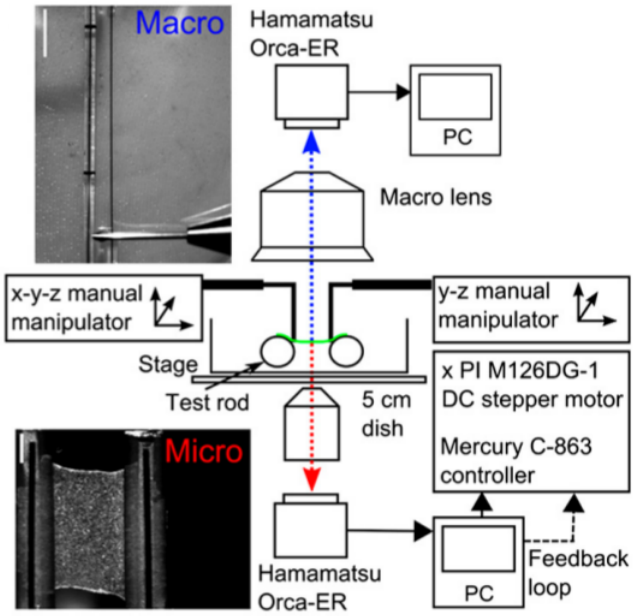

Fig. 6.1 The experimental system for mechanical testing. Petri dishes containing monolayer culture devices were mounted onto the microscope stage. The motorised micro-manipulator arm was brought into contact with the soft test rod and the manual micro-manipulator arm with the fixed rod. The device test rods could be moved apart to stretch the monolayer. The motorised manipulator is used to control over extension and strain rate. Monolayer extension was imaged with an inverted microscope (red light path giving the bottom left image) and the positions of the test rods were monitored with a top-down macroscope (blue light path giving the top left image) allowing measurement of strain and stress. A feedback loop was implemented to achieve constant stress or constant strain. Scale bars: 1 cm (Macro) and 1 mm (Mirco) [43].

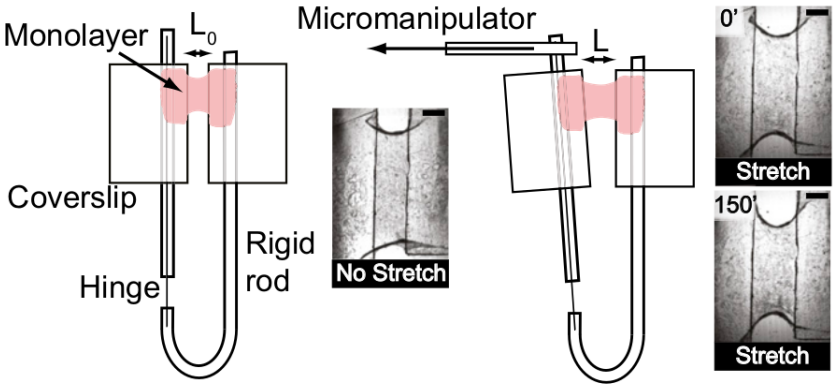

Fig. 6.2 The schematic diagrams of the modified experimental equipment with the suspended monolayer pre- (left) and post-stretch (right), along with bright-field images at three different stages in the experiment. Scale bars: 1 mm. Image by courtesy of Tom Wyatt.

bearing substance as a model system. For the stress relaxation measurement, a motorised micro-manipulator was used to subject the monolayers to stretch and produced a 30-35% strain on the monolayer, of which the central part was suspended between the two testing platforms, over a time course of several hours (Figure 6.2). Monolayer strain was held constant by altering the magnitude of the applied force. In comparison, another monolayer with no extrinsic stretch on it was used as a control group.

The cell shape was measured by the best-fitted ellipse of the cell outline. The cell aspect ratio was measured as the ratio of ellipse major axis over the minor axis, and the cell orientation was described by the ellipse orientation. The orientation of cell division was determined as the angle perpendicular to the angle of the new junction formed between daughter cells at the first time point that it was visible. In the next section, we present the significant findings of this approach and propose a hypothesis of the underlying mechanism from the experimental result.

6.3 Experimental Results

6.3.1 Post-stretch Cellular Elongation and Monolayer Stress

After the stretch was applied, no neighbour exchange event in the epithelium was observed as cell–cell junctions were stable at their initial positions. Instead of rearranging their position, cells elongated in the direction of the applied force by a strain approximately identical to that at the tissue level. The extension led a decrease in the thickness of the monolayer and a small decrease in tissue width [43]. Before cell division, cells remained elongated (Figure 6.3 (A) and (B)).

Since these monolayers lacked ECM but had apicobasal polarisation, the tension across them was transmitted by stable intercellular junctions during the experiment. To examine the tension on individual cells, the monolayer tension was monitored for over 200 min. Results showed that tension reached its maximum at the time when the stress was applied and decreased by 75% within 2 min (Figure 6.3 (C)). Then monolayer tension decreased at a slower rate until it remained at around 40 nN per cell for the duration of these experiments (Figure 6.3 (D)).

Another test to determine the relationship between the orientation of mechanical stretch and the post-stretch orientation of cell elongation was carried out by laser perturbation. Cellular junctions were visualised by using MDCK cells which expressed E-cadherin-GFP. Before perturbation, cells elongated either in the direction of stretch or in a direction perpendicular

to stretch. In each perturbation, a cell was exposed to a pulsed 405-nm laser for 30 sec. Local recoil for a tissue under tension was observed (Figure 6.3 (E)). The local stress field was closely aligned with the direction of stretch, disregarding the orientation of the long axis of the target cells (Figure 6.3 (F)).

On the whole, these data show that the change in cell shapes was significant and cell oriented by a 30-35% uniaxial stretch. The mean cell aspect ratio was around 1.4, with 55% of cells oriented within 20° of the stretch axis. In contrast, cells in the non-stretched monolayer divided without exhibiting any directional bias (Figure 6.3 (B)). Further, cells within the stretched monolayer were exposed to a sustained local stress which was closely aligned with the stretch axis. This resulted in a tension of ~ 40 nN per cell (Figure 6.3 (D)). Hence cells in stretched monolayers are both elongated and subjected to significant tension. Regardless of the direction of cell elongation, it is likely that cell tension is aligned with the applied stretch.

6.3.2 Effect of Stretch on Cell Division

Mitotic progression within suspended monolayers was visualised using E-cadherin-GFP (Figure 6.4 (A)). The imposition of a uniaxial stretch was accompanied by a transient inhibition of mitotic entry in the epithelium. Nevertheless, mitosis resumed some 60 min later. Then cells all divided in the plane of the epithelium. In the 30-35% strain tissue, cell division was oriented and 56% of cells divided within 20° of the stretch axis (Figure 6.4 (B)). Whereas cells in non-stretched monolayers divided without exhibiting any directional bias (Figure 6.4 (A)) and only 20% of cells oriented their division axis with respect to the stretch axis (Figure 6.4 (B)). It suggests that the amount of strain was sufficient to induce a global bias in the orientation of division.

Although previous work has shown that mechanical forces oriented cell divisions in epithelial tissues, the relative contribution of interface shape and tension on oriented divisions was unravelled. To address this question, the orientation of tissue stress axis, interphase long cell axis and cell division axis in the presence and absence of stretch were compared (Figure 6.4 (D)). In both stretched and non-stretched monolayers, cells divided along their interphase long cell axis (the aspect ratio is measured as $r > 1.4$), with $82 \pm 2\%$ and $77 \pm 4\%$ of divisions, respectively, within 20° of the interphase long cell axis (Figure 6.4 (C)). In addition, mitotic cells were polarised in both stretched and non-stretched monolayers, with their spindles aligned with the long cell axis and with known cortical regulators of spindle orientation concentrated at each pole.

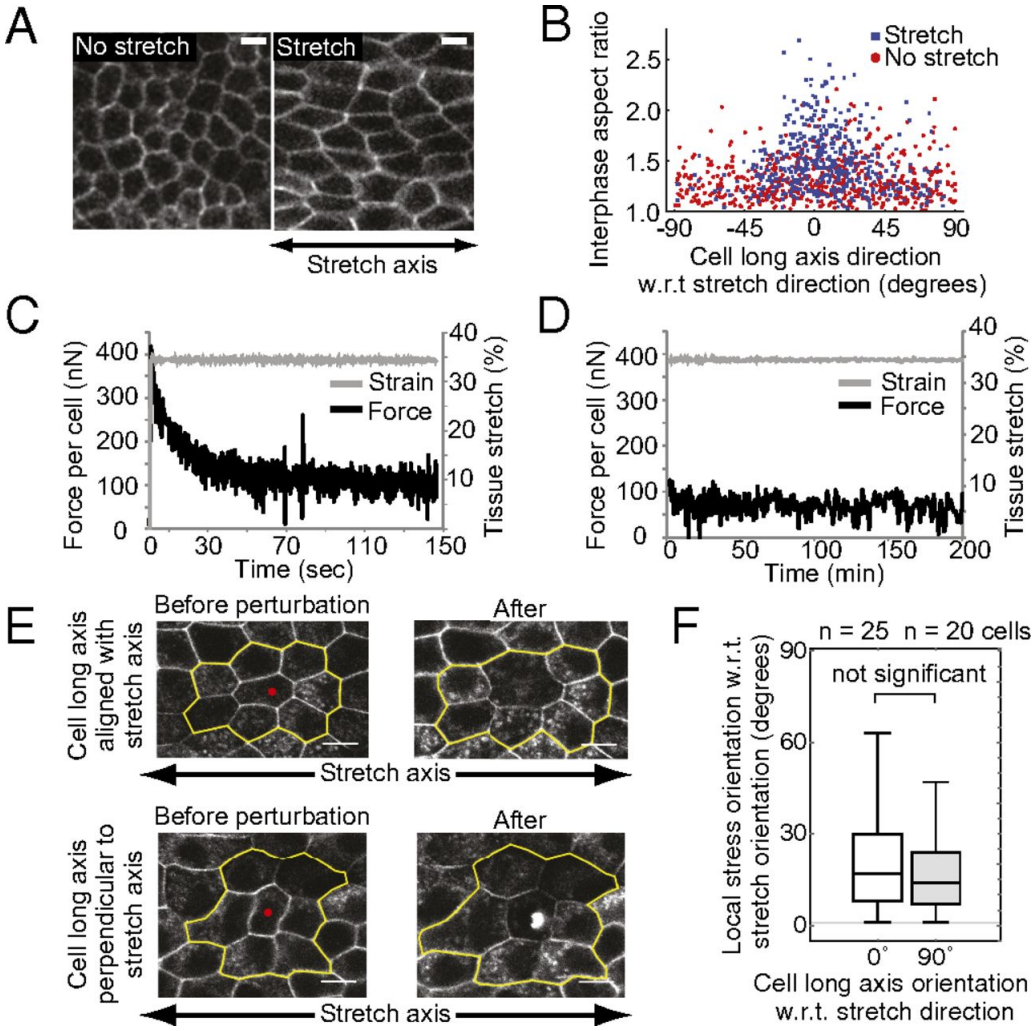

Fig. 6.3 Uniaxial stretch results in long-term cellular elongation and monolayer stress. (A) Monolayers expressing E-cadherin-GFP before and after a 30% stretch. Scale bars: 10 μm. (B) Orientation and aspect ratio of cells in stretched (blue) and non-stretched (red) monolayers, as calculated from the orientation and major-to-minor axis ratio of the best-fit ellipse to the cell shape. w.r.t., with respect to. The evolution of strain (gray) and force (black) in a stretched monolayer for short (C, up to 150 s) and long (D, up to 200 min) time scales is shown. (E) Cells expressing E-cadherin-GFP in a stretched monolayer before and after perturbation of their mechanical integrity by a pulsed-UV laser. Cells with shapes oriented 0° (Top) and 90° (Bottom) to the direction of stretch were chosen. Red dots indicate the area where the laser was applied. Yellow outlines mark the region including the nearest neighbours of the perturbed cell. (Scale bars: 10 μm.) (F) Local orientation of stress, as measured from recoil after laser perturbation, for cells with shapes oriented 0° and 90° to the stretch direction. The horizontal line and top and bottom of boxes represent the median, 75th percentile, and 25th percentile in all box plots, respectively. The whiskers demarcate the range ($n \geq 20$ cells and $n \geq 12$ monolayers for each condition) [110].

To isolate the effects of tension from the effects of cell shape, the small group ($\sim 5\%$) of elongated cells whose interphase long cell axis was misoriented ($> 35°$) with respect to the stretch axis was analysed (Figure 6.4 C (points in red), D, E (points in red)). In this case, it is significant that these cells always divided along their interphase long cell axis, rather than the axis of the applied stretch (Figure 6.4 (E)). This was the same case in Figure 6.3 (E) and (F), although the local stress field was aligned with the global stretch. Hence we can conclude that the combination of a stretch-induced global bias in the orientation of long cell axes and the tendency of cell division along their long axis results in the alignment of divisions in stretched monolayers.

6.3.3 Effect of Monolayer Stress on Mitotic Rounding

Given these observations, we measured the changes in cell shape before and after mitosis in both stretched and non-stretched monolayers and investigated how these changes contributed to the relief of tissue stress in the stretched monolayers. Cells within non-stretched monolayers entered mitosis and kept a nearly isotropic metaphase shape (aspect ratio $r_{-stretch} = 1.16 \pm 0.02$; Figure 6.4 (A) and 6.5 (A)). By contrast, cells within stretched monolayers were unable to fully round prior to division (aspect ratio $r_{+stretch} = 1.256 \pm 0.02$; Figure 6.4 (A) and 6.5 (A)), and their interphase long axis decreased (Figure 6.5 (B)). *In vitro* measurements show that the rounding force generated by cells when entering into mitosis is ~ 80 nN per cell [43]. However, we have measured the force in stretched monolayer is ~ 40 nN per cell (Figure 6.3 (D)), and thus, cells failed to round up completely due to residual monolayer tension.

Next, we investigated the relative dimensions of each cell in the directions parallel and perpendicular to the axis of division at 5-min interval. In stretched monolayers, the aspect ratio was measured with respect to the division direction. Initially, cells were more elongated. When cells entered mitosis, the aspect ratio decreased as cell rounded up before division (Figure 6.5 (D), i), and then increased rapidly during anaphase elongation (Figure 6.5 (D), ii), before being approximately halved at division (t=0). In the end, daughter cells gradually increased their aspect ratio in the 25 min after division (Figure 6.5 (D), iii). Differently, in non-stretched monolayers, cells retained a roughly constant aspect ratio until anaphase, when it increased sharply (Figure 6.5 (D), ii). Then the aspect ratio was halved at abscission and remained constant (Figure 6.5 (D), iii). When cells exited mitosis, they elongated in the direction of the applied stretch (Figure 6.5 (E)) rather than the orientation of division, as a consequence of extrinsic tension. Hence, these data suggest that monolayer stress

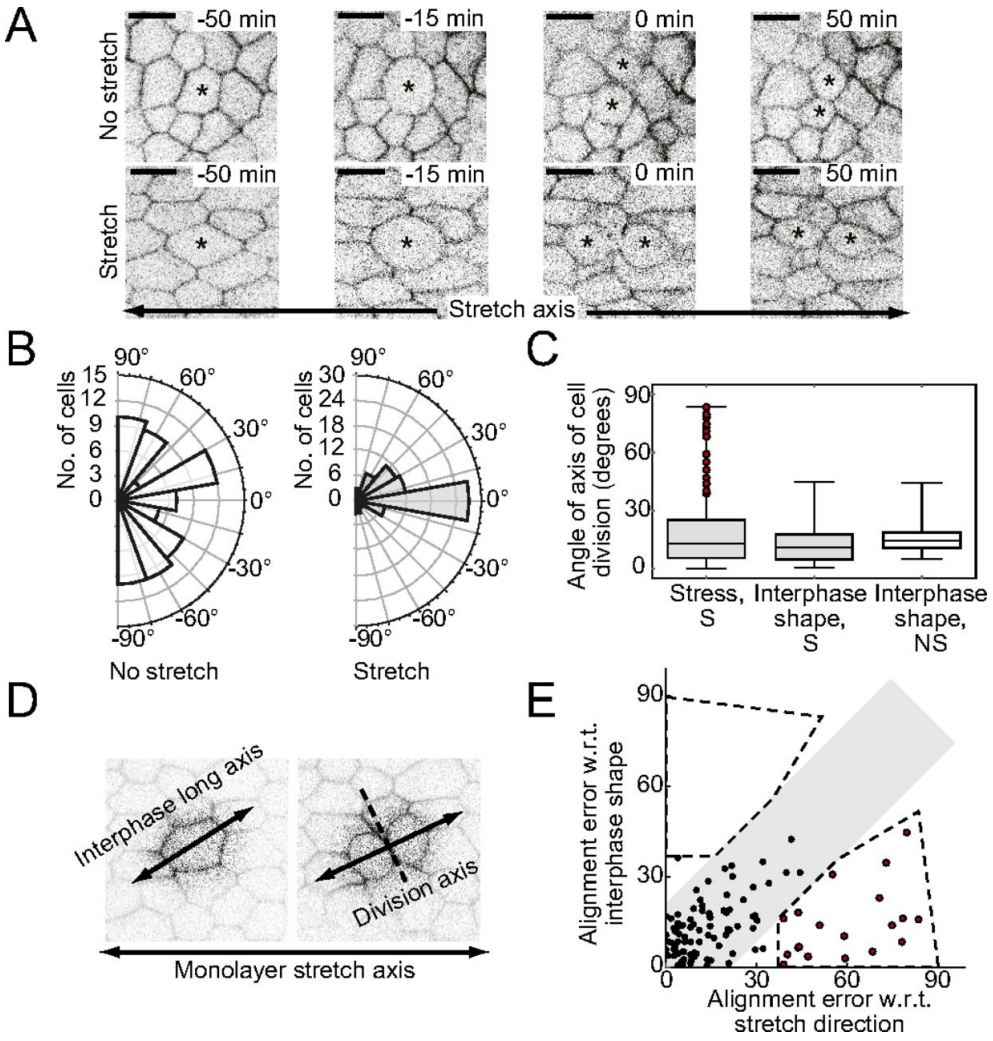

Fig. 6.4 Divisions align along the interphase long cell axis in monolayers. (A) Time series of a dividing cell in a non-stretched monolayer and a stretched monolayer. Time is measured from the start of the division. Asterisks mark dividing and daughter cells. (Scale bars: 10 μm.) (B) Orientation of division with respect to the direction of stretch or with respect to the direction perpendicular to the test rods in the no-stretch case ($n \geq 72$ divisions and $n = 3$ monolayers for each condition). (C) Orientation of division with respect to the axis of stretch (stress, Left), to the interphase shape orientation in stretched monolayers (Middle), and to the interphase orientation in non-stretched monolayers (Right) for elongated cells ($r > 1.4$). Cells marked by a red point correspond to those appearing in red in E. NS, non-stretched; S, stretched. (D) Dividing cell in a stretched monolayer. The interphase shape is misaligned with the direction of monolayer stress, and the division follows the interphase shape rather than the monolayer stress direction. (E) Error in alignment of division with the monolayer stress axes plotted against the error in alignment with interphase shape for elongated ($r > 1.4$) cells in stretched monolayers. The gray shading shows the region in which divisions align equally well with monolayer stress and interphase shape. Dotted lines demarcate regions where divisions align significantly better with interphase shape than stress, and vice versa [110].

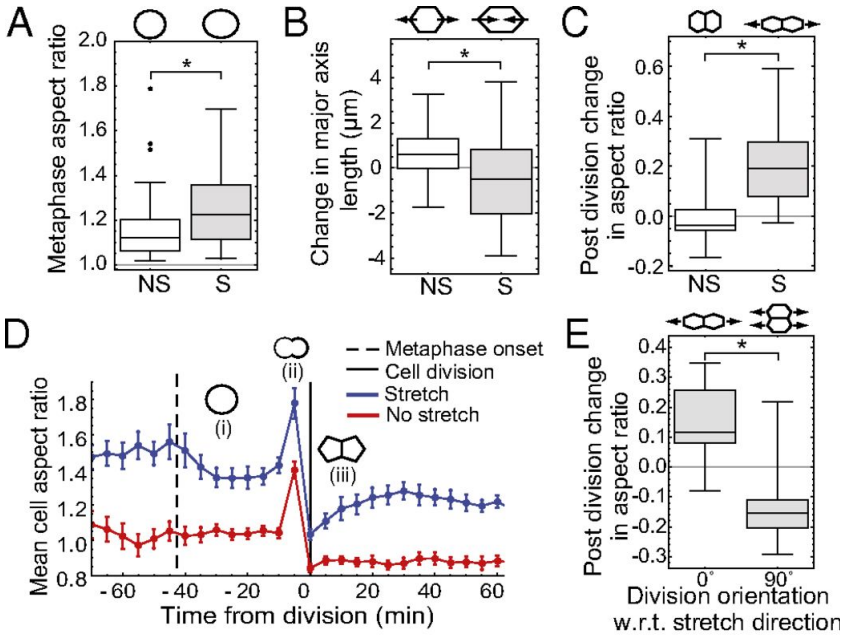

Fig. 6.5 Effect of monolayer stress on mitotic rounding. (A) Box-whisker plots showing the metaphase aspect ratio of dividing cells in non-stretched and stretched monolayers ($*P < 0.002$). (Top) Diagrams show the median shape of rounded cells in each condition. (B) Changes in the long cell axis length during rounding in non-stretched and stretched monolayers. (Top) Diagrams show the most frequent direction of shape change during rounding in each condition ($n \geq 48$ cells and $n = 3$ monolayers for each condition; $*P < 0.001$). (C) Change in cell aspect ratio (measured with respect to the direction of division) between division ($t = 0$) and $t = 25$ min ($n = 20$ cells for each condition; $*P < 0.001$). (D) Temporal evolution of the mean cell aspect ratio (measured with respect to the direction of division) of dividing cells. Data points are averaged over $n = 10$ cells in both stretched (blue) and non-stretched (red) monolayers. Division was taken as time 0 (solid vertical line). Rounding onset (dashed line), anaphase, and daughter cell reintegration are marked by (i), (ii), and (iii), respectively, and are represented by pictograms. From time 0 onward, the values represent the average over all individual daughter cells. Error bars indicate SE. (E) Change in cell aspect ratio (measured with respect to the direction of division) between division ($t = 0$) and $t = 25$ min for cells without a well-defined long axis ($r < 1.25$) in stretched monolayers ($n \geq 18$ cells were characterized for each condition; $*P < 0.001$ [110].

impedes mitotic rounding but promotes elongation of daughter cells following abscission. Cell elongation at anaphase was relatively less affected by extrinsic tension.

6.3.4 Cell Division Leads to a Global Redistribution of Mass

Next, we investigated the relationship between oriented division and monolayer stress relaxation. The shape changes of dividing cells and the organisation of surrounding cells were first explored. We calculated the mean cell length and mean cell width throughout division, including late G_2 into mitosis (t = -60 min and t = -50 min), division (t = 0) and epithelium reintegration (t = 50 min and t = 60 min) (Figure 6.6 (A) and (B)). By comparing these data at 50-60 min before and after division, the net effect of cell division is to redistribute cell mass along the division axis, regardless of in either stretched or non-stretched monolayer. The combined daughter cell length at the division point was larger than the mother cell length before division by $35 \pm 3\%$ in stretched monolayers and $37 \pm 4\%$ in non-stretched monolayers (Figure 6.6 (A)). After division, at t = 50-60 min, combined daughter cell lengths decreased slightly but remained notably larger than mother cell lengths before division by $21 \pm 3\%$ in stretched monolayer and $18 \pm 3\%$ in non-stretched monolayer. As a consequence of a significant decrease in cell widths and an increase in cell lengths, the aspect ratio of combined daughter cells was significantly increased, compared with mother cells, by $+41 \pm 5\%$ in stretched monolayers and $+42 \pm 5\%$ in non-stretched monolayers. Thus, these data indicate that individual divisions lead to the redistribution of mother cell mass along the interphase long axis regardless of the monolayer tension.

Then we examined the influence of individual divisions on local tissue organisation. By visualising junctional movements in the vicinity of dividing cells in image overlays, the positions of intercellular junctions before (green, Figure 6.6 (C)) and after (red, Figure 6.6 (C)) division were compared. Both the overlays and the corresponding fluorescence intensity line profiles showed that the division was accompanied by an inward movement of neighbouring junctions in a direction perpendicular to the axis of division, together with an outward movement in the direction of the division. These patterns of deformation were observed in the division regions regardless of whether in stretched or non-stretched monolayers, but not in control areas of the monolayer, where no divisions took place. Taken both analyses together, cell division redistributes tissue mass, which results in an expansion in the direction of division and a contraction in the perpendicular direction. As there is a global bias in division orientation in stretched monolayers, the effects of individual cell

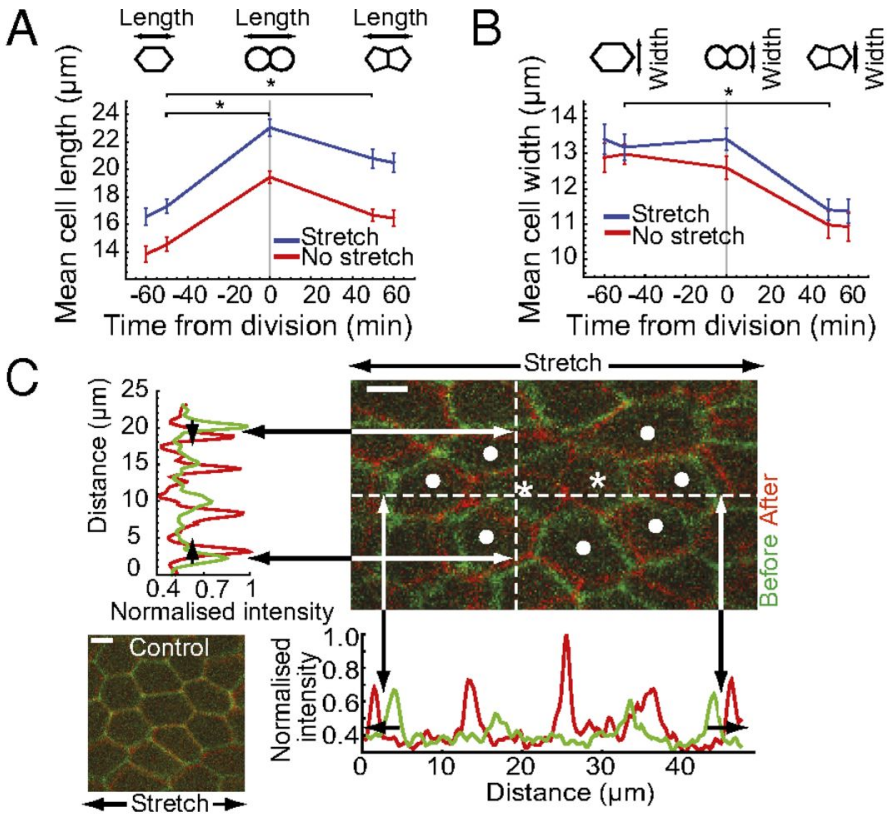

Fig. 6.6 Effects of stress-induced oriented division on local cell packing and monolayer stress. Temporal evolution of mean cell length (A) and mean cell width (B) of the mother cell (before division) and of the combined spatial envelope of the daughters (after division) in stretched (blue) and non-stretched (red) monolayers showing mass redistribution in the direction of division. (Top) Diagrams depict the measurements taken. Asterisks denote a significant difference between medians ($*P < 0.01$; $n \geq 38$ cells from $n = 3$ monolayers for each condition). Error bars denote SE. (C) Overlays of mitotic cells 10 min before (green) and 30 min after (red) furrowing onset. Asterisks mark daughter cells, and dots mark first neighbours. Fluorescence intensity line profiles taken along the dotted lines show shifts in the position of junctions in cells neighbouring the dividing cell (black arrows in the fluorescence profile). Junctions shift away from the dividing cell along the axis of division (Bottom Right) and toward it in the direction perpendicular to division (Upper Left). (Bottom Left) No such shifts were observed in overlays of areas containing no division. (Scale bars: 10 μm.) [110].

division accumulate to expand the monolayer in the direction of stretch and to contract it in the perpendicular direction, which is a similar effect to tissue convergent extension behaviour.

6.3.5 Summary

These experimental results show that cell division both generates disorder and alters tissue-scale stresses and strains within an epithelial monolayer. However, within epithelia, intrinsic forces such as the increased cortical contractility and osmotic pressure [92] are challenging to quantify through experiments. The information is insufficient to explain the shape changes of individual cells entering mitosis and to predict the interplay between intrinsic cellular-scale forces and the external tissue-scale forces. Under these circumstances, we propose that the differences in the path of cell shape change in stretched and non-stretched monolayers could be a result of simple mechanics. We suggest that cells do not sense and transduce the mechanical signals from the extrinsic forces, and the changes in the tissue stress are merely a consequence of changes in cell shapes and the orientation of the division.

In order to understand this, we implemented cell division in the mechanical model to investigate cell shape changes within an epithelial monolayer at rest or subjected to a uni-axial stretch. The details are introduced in the following sections.

6.4 Computational Methods

In the experiments, only the changes observed in the monolayer plane were taken into account. The monolayer can be modelled by the 2D mechanical model to explore the role of cell divisions on tissue stress relaxation. Hence, we implemented cell growth and cell division in a passive system, where no active cell movements were considered. The methods are described in this section.

6.4.1 Defining Cell Division

In the model, cell growth can be realised by simply increasing the size of the division cell, and cell division is modelled as splitting a mother cell into two daughter cells by introducing a new edge, along either long cell axis or short cell axis. As the two daughter cells observed in the experiments were approximately of the same size, the daughter cells in the model were identical. Hence, before division, the mother cell is represented by one ellipse with one centre, one shape and one area. After division, daughter cells are described by two identical

ellipses with two new cell centres. The sum of the area of these two ellipses is equal to the area of the mother cell. We start from defining the new cell centres of daughter cells.

Centre of Mass

In the model, the area of the daughter cells is half the size of the mother cell. The positions of new cells could be determined by moving the centre of mass of the mother cell by an equal displacement but in different directions along the division axis. The displacement set to match the centroid of a semi-elliptical area is $\frac{4a}{3\pi}$ [28], where a is half the length of the division axis (Figure 6.7 (A) and (B)).

Division Axis

Here we use two orthogonal unit vectors, **u** and **n**, to represent the direction of the long cell axis and short cell axis of the mother cell, and we have $\mathbf{n}.\mathbf{u} = 0$. As we have calculated the centres of mass of two daughter cells (x_1, y_1) and (x_2, y_2), the two orthogonal unit vectors can be calculated by Equation (6.1) to (6.4).

$$\mathbf{u} = [dx, dy]^T, \tag{6.1}$$

$$\mathbf{n} = [-dy, dx], \tag{6.2}$$

$$dx = \frac{x_2 - x_1}{norm}, \tag{6.3}$$

$$dy = \frac{y_2 - y_1}{norm}, \tag{6.4}$$

where the norm is $\sqrt{(x_2 - x_1)^2 + (y_2 - y_1)^2}$.

Cell Shape

According to Voronoi tessellation, a division is modelled as the introduction of a new edge which divides the mother cell into two daughters. Before division, the lengths of the long and short axes of the mother cell are a and b, which are defined as the mother length and mother width. If the division is along the long axis, the daughter cell lengths and widths will be $\frac{a}{2}$ and b, respectively (Figure 6.7 (C)).

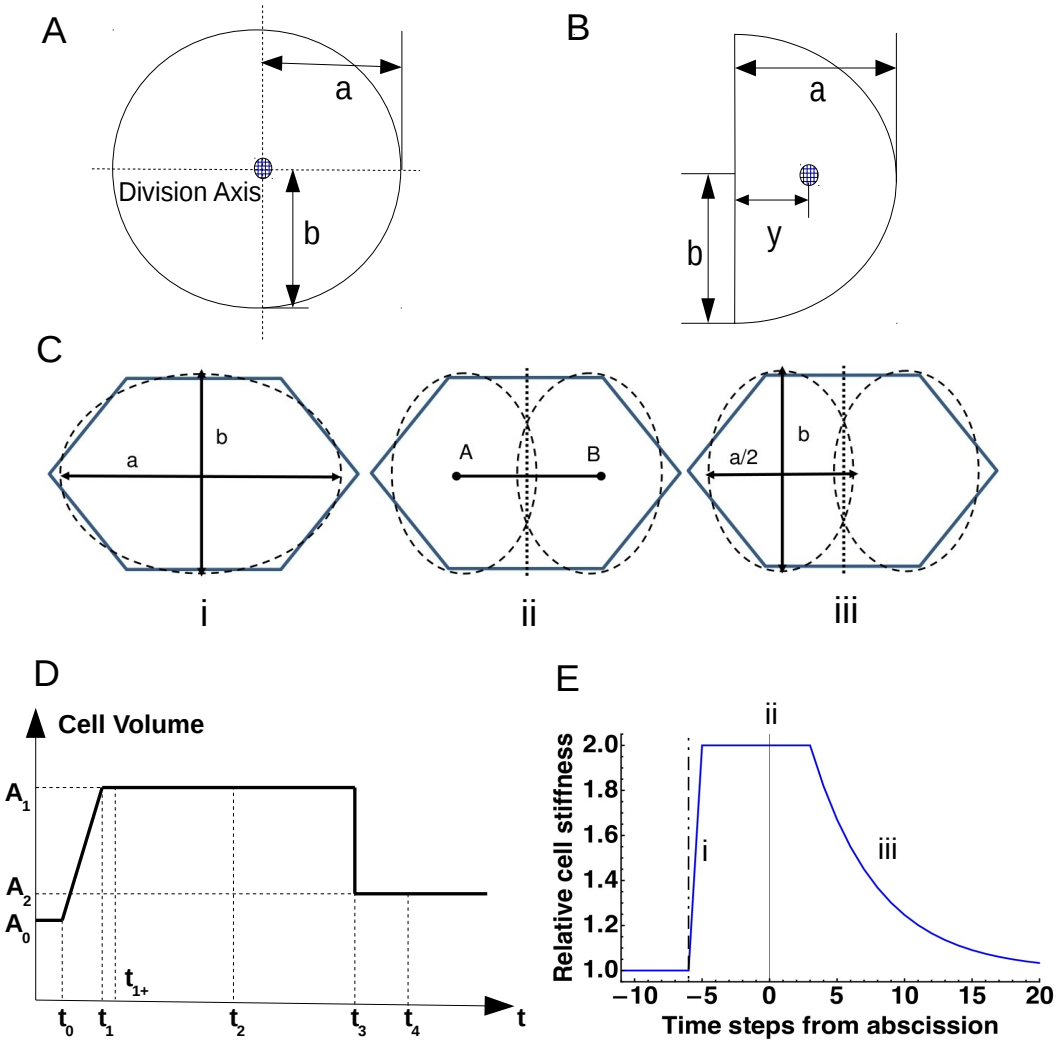

Fig. 6.7 Cell growth and cell division in the model. (A) The cell is represented by an ellipse. a and b represent a half length of two perpendicular axes across the centroid. (B) Cell divides equally. The new position of the centroid of daughter cell is moved by a distance of y from the centroid of the mother cell. This can be calculated from the displacement set to match the centre of mass of half an ellipse. (C) Schematic diagram of an example of cell division along long cell axis. The hexagon and the ellipse are two configurations of cells. (i) The axes of the mother cell, a: long cell axis; b: short cell axis. (ii) A and B denote the centres of mass of two daughter cells. The axis of division is defined by a line going through A and B. (iii) The axes of daughter cells, $\frac{a}{2}$: long cell axis, which is half the long axis of the mother cell; b: short cell axis. (D) The volume (area) of dividing cell over time. The initial cell volume is A_0. At t_0, cell begins growth and reaches a new cell volume of A_1. At t_{1+} the cell–cell viscosity is increased. At t_2, the stiffness of mother cell is increased. Cell division takes place at t_3 and daughter cells have a size of A_2. (E) An example of the temporal evolution of cell stiffness during mitosis imposed on all dividing cells in simulations. Cell divides at $t = 0$. The time points marked by (i), (ii) and (iii) correspond to points on Figure 6.5 (D).

6.4.2 Simulation Protocols

In this section, we introduce the protocols used in the model to simulate the experimental observations. As cell–cell junctions were stable at their initial positions in the experiments, we increased cell–cell viscosity η to a sufficiently high value when the step strain is applied. In this case, cells were difficult to rearrange with their neighbours. Upon entering mitosis, the mother cell rounded up. The cortical stiffness of the division cell was increased to generate a significant rounding force, which was derived from measurements in isolated cells [52, 92]. In the model, the change in cortical (surface) tension ($\Delta\Gamma$) was realised by the change in the shear modulus (ΔG) as $\Delta\Gamma = \Delta G \cdot R$ (where R is the cell radius). After cell division, the stiffness of the daughters was gradually returning to interphase levels (Figure 6.7 (E)).

In the 2D model, cell volume is represented by the area of the ellipse. Figure 6.7 (D) illustrates the change in cell volume of the dividing cell against time:

- t_{0-}: Cells maintain normal configuration and have no division. The initial cell size is A_0
- t_0: Mother cell starts to grow at a constant rate r ($r > 1$).
- t_1: Mother cell stops growing and reaches a new size A_1.
- t_{1+}: A step strain is applied in the stretched simulation. Cell–cell viscosity η is increased and maintained until the end of the simulation in both stretched and non-stretched cases.
- t_2: The stiffness (shear modulus) of mother cell is increased.
- t_3: Cell divides. The stiffness of the two daughter cells keeps high.
- t_4: Post-division cell re-integration. The stiffness of the two daughter cells exponentially returns to interphase level.

Stretched and Non-stretched Simulation

We used a system of 256 identical cells with periodic boundary conditions. Similar to the experiments, two groups of simulation were carried out, one was a system deformed by an instantaneous step strain, while the other was the control group in which no extrinsic strain was applied. In both groups, we had over 180 simulations, in each of which a different cell was selected as division cell. A 30% stretch was applied in the horizontal direction while the

area of the system was preserved by reducing the length of the tissue in the perpendicular direction.

Oriented Division and Misoriented Division

Another test was performed to examine the effects of tissue stress dissipation as a consequence of oriented divisions. We also used a system of 256 identical cells with periodic boundary conditions. Divisions along both long cell axis and short cell axis in stretched and non-stretched tissues were taken into consideration. For each group we had over 180 simulations, in each of which one cell was selected as division cell. In oriented division groups, all selected cells divided along their long axis. In misoriented groups, 50% of the division cells were randomly selected to divide along the long cell axis, and the other half of cells divided perpendicularly along the short cell axis.

6.4.3 Data Collection

In general, we had four simulation groups applied with different conditions. The total number of cells in the model tissue before division was 256. In each group, individual simulation was repeated by selecting one different cell as division cell and the total number of simulations is $n > 180$.

- Group 1: Oriented division in stretched tissue.
- Group 2: Misoriented division in stretched tissue.
- Group 3: Oriented division in non-stretched tissue.
- Group 4: Misoriented division in non-stretched tissue.

We are interested in cell shape evolution and tissue stress change during mitosis. Similar to the methods used in analysing experimental data, the length l and width w of cells are defined as the projection of cell long axis and short axis onto the stretch direction and the perpendicular direction, respectively. Then the aspect ratio of cells is the ratio of the length and the width $\frac{l}{w}$.

In each simulation, we recorded the time evolution of the average stress tensor $\bar{\sigma}$ of the tissue, the strain tensor ε, the radius R and the cell aspect ratio ρ of the mother and daughter cells. In the next section, we introduce the simulation results and compare with the observations in the experiments.

6.5 Results

6.5.1 Behaviour of the System

In the simulation, the 30% step strain is in the direction of the x-axis. The area of the tissue is preserved by reducing the length of the tissue in the perpendicular direction. A typical system is shown in Figure 6.8. Cells are deformed to match exactly and instantaneously the step strain after the system is stretched. Because the stretch is applied much more quickly before cells can respond to it and rearrangement takes place, the average strain of cells remains the same as the tissue strain (Figure 6.8 (B)).

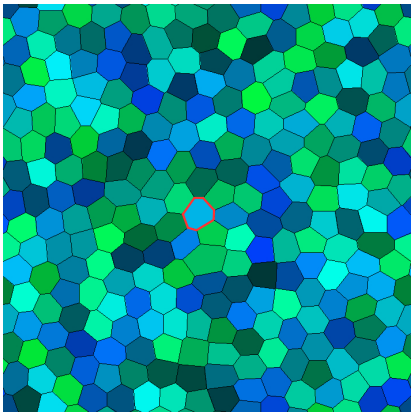

(A)

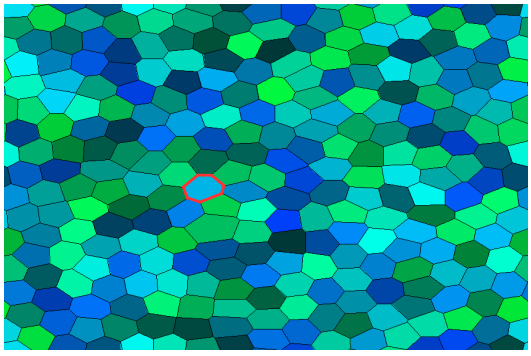

(B)

Fig. 6.8 A 30% step strain is applied to a system of cells. The edge of one cell in both pictures was marked in red to compare the shape change before and after the application of stretch. (A) The pre-strained system of cells. (B) The system of cells immediately after the applied stretch. In (B) cells elongated in the direction of the applied stretch by a strain approximately identical to that at the tissue level.

We computed the new monolayer-scale mechanical equilibrium at each time point during division. Figure 6.9 (A) shows an example of the simulation of cell division in both stretched

(S) and non-stretched (NS) monolayers. In the stretched monolayer, cells are elongated in the direction of the extrinsic stretch. The deformation is roughly equal to that at the tissue level. Cell–cell viscosity in the system is high and cells hardly move so as to maintain this configuration of cells before division. Over the simulation time, there was no obvious cell rearrangement and hence, cells kept the same amount of deformation afterwards (the time step from t_0 to t_4 is related to Figure 6.7 (D)).

After growing to approximately twice the initial size at t_1, cell entered into mitosis and its stiffness increased abruptly as cell rounding was recognised at t_2. This sharp increase in stiffness drove complete rounding in non-stretched monolayers but only partial rounding in stretched monolayers. At abscission, daughter cells were separated along the long cell axis and identical in size at t_3. In the example, we could obviously observe that the cell long axis was aligned with the stretch axis. At t_4, new cells re-integrated and cell mass was redistributed after division. In non-stretched monolayers, daughter cells maintained their shape, while in stretched monolayers, daughter cells gradually elongated in the direction of the applied strain.

6.5.2 Changes in Cell Shape Accompanying Mitotic Progression

We have seen that cells in both stretched and non-stretched monolayers follow a similar path of shape changes during mitotic progression. Similar to the experiment, we calculated cell aspect ratio to determine the evolution of cell shape that accompanied divisions and compared that at each division phase in both monolayers. Significantly, while in simulations experimentally measured changes were introduced in the mechanics of isolated mitotic cells into a model epithelium, these changes in aspect ratios of cells were qualitatively and quantitatively comparable to the observations in suspended monolayers.

In simulations, following the stretch, cells within the stretched tissue were subjected to a tension oriented along the axis of extension. The long axes of cells were primarily oriented along the direction of extension (Figure 6.9 (B)). As the dividing cell entered mitosis, the cell aspect ratio decreased in both monolayers due to the increased cell cortical stiffness (Figure 6.9 (C) (i)). At $t = 0$, the cell divided (Figure 6.9 (C) (ii)) and the aspect ratios of the daughter cells were roughly equal to half of their mothers'. After division, the cell aspect ratio tended to increase in stretched monolayers because of the tensile stretch but kept approximately the same level in non-stretched ones (Figure 6.9 (C) (iii)).

More specifically, cells within non-stretched monolayers assumed a near circular metaphase shape (mean aspect ratio $= 1.08 \pm 0.03$). By contrast, in stretched monolayers, cells were

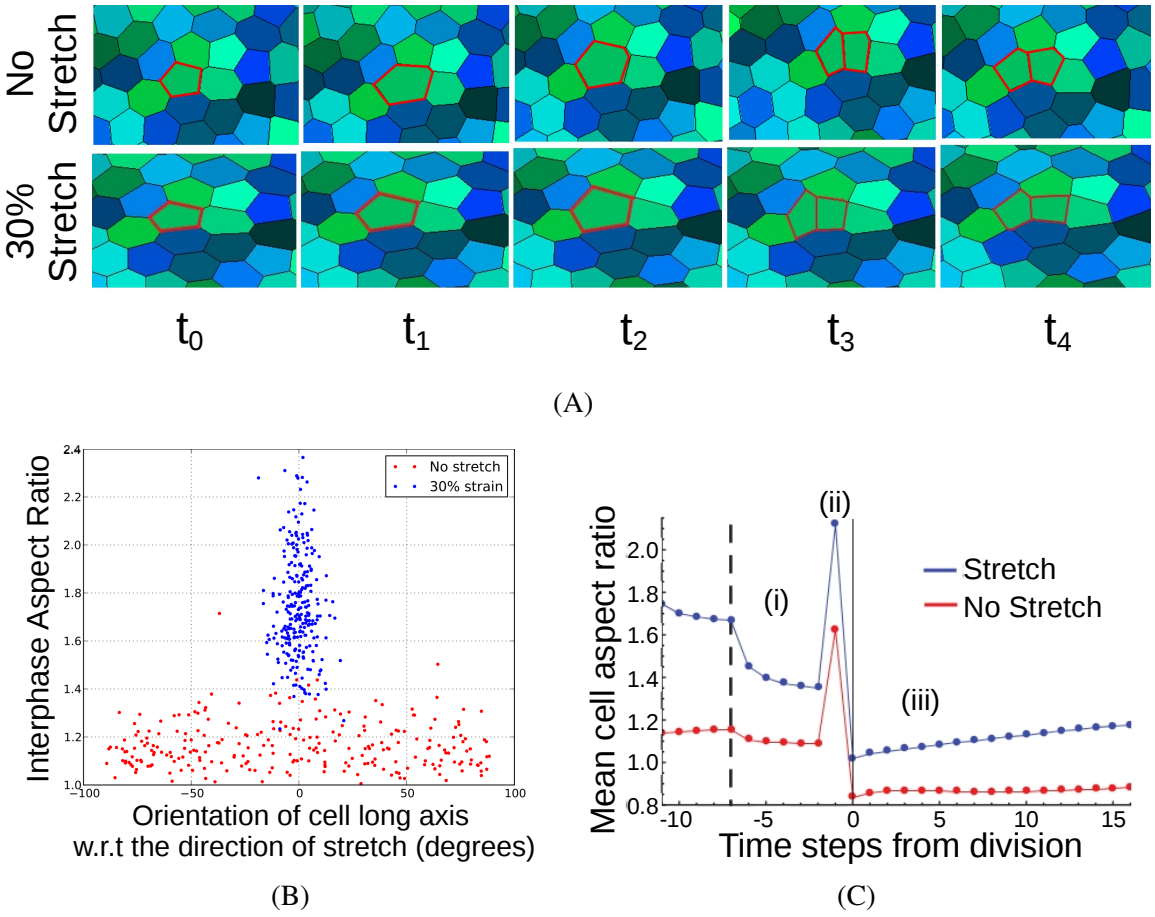

Fig. 6.9 Simulation: balance of cell-autonomous and extrinsic mechanical forces explains changes in cell shape accompanying mitotic progression. (A) An example of time series of simulated division in stretched (bottom) and non-stretched (top) tissues with the dividing and daughter cells highlighted with red junctions. t_0: before division, t_1: cell growth, t_2: mitotic rounding up, t_3: cell division, t_4: post-division. (B) The orientation and aspect ratio of cells in stretched (blue) and non-stretched (red) monolayers, as calculated the same way from the orientation and major to minor axis ratio of the best-fit ellipse of the cell shape. (C) The progression of mean cell length/width over time of cells in stretched (blue) and non-stretched (red) simulated monolayers. The times marked with (i), (ii) and (iii) correspond to points on Figure 6.5 (D). The SE is less than 0.02, and so is not shown in the plot. Each data point represents $n \geqslant 180$ divisions.

unable to fully round prior to division (mean aspect ratio $= 1.32 \pm 0.05$; Figure 6.10 (A)). Some time after division, daughter cells underwent a significant but gradual increase (0.18 ± 0.1) in their aspect ratio as the cell stiffness returned to the initial value, which denoted an elongation in the direction of applied stretch (Figure 6.10 (B)). In non-stretched monolayers, the time course of cell deformation appeared comparatively featureless, with little change (-0.03 ± 0.05) in aspect ratio prior to division or elongation of the daughter cells.

These findings suggest that experimentally observed changes in cell shape during division are the simple consequence of well-understood autonomous changes in mitotic cell mechanics, removing the need to invoke additional mechanisms.

6.5.3 Effect of Stretch on Daughter Cell Aspect Ratio

In order to examine mass redistribution during divisions, we then compared the aspect ratio of daughter cells with the aspect ratio of their mothers in both experiments and computational simulations (Figure 6.11).

In experiments (Figure 6.11 (A)), mother cells had an average aspect ratio of $\rho = 1.09 \pm 0.03$ and divided into daughter cells with an aspect ratio of $\rho = 0.91 \pm 0.02$, in non-stretched monolayers. Hence, the long cell axes of mothers' were perpendicular to the long axes of daughter cells. However, in stretched monolayers, mother cells had an aspect ratio of $\rho = 1.34 \pm 0.05$ and their daughters remained elongated in the same direction with an aspect ratio of $\rho = 1.10 \pm 0.03$. These data suggest that although division redistributes mass along the division axis in both non-stretched and stretched monolayers, the orientation of daughter cells was affected by the stretch. Assuming homogeneous cell growth throughout the monolayer, the next round of divisions will tend to be oriented with the first round in stretched monolayers but perpendicular to the first round in non-stretched monolayers.

Significantly, we have obtained qualitatively and quantitatively similar results from the model (Figure 6.11 (B)). Before division, mother cells in stretched monolayers had an aspect ratio of $\rho = 1.60 \pm 0.05$ and in non-stretched monolayers mother cells had an aspect ratio of $\rho = 1.10 \pm 0.02$. Immediately after division, daughter cells in stretched monolayers were approximately isotropic ($\rho = 1.03 \pm 0.03$), whereas cells displayed marked anisotropy in control tissues ($\rho = 0.84 \pm 0.03$). Thus, the alignment of mother cells and daughter cells appears to be a simple by-product of the application of stretch.

Since the model replicates what we have observed in the experiments with sufficient evidence, the model could predict the influence of divisions on monolayer stress.

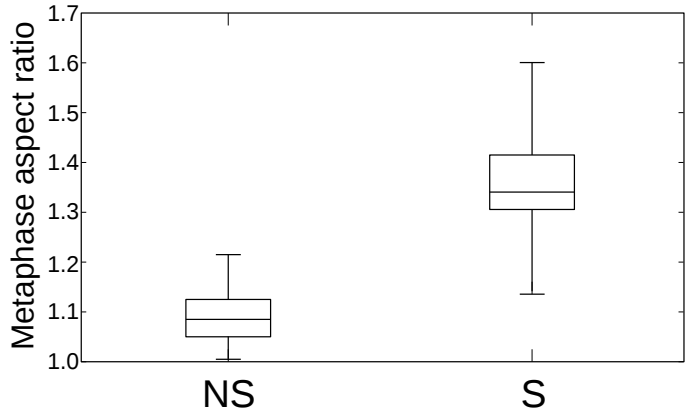

(A)

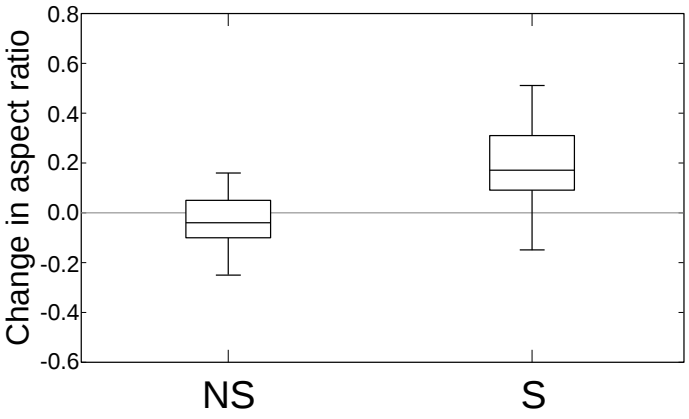

(B)

Fig. 6.10 Simulated results of the effect of tissue stress on mitotic rounding. (A) Box-whisker plots showing the metaphase aspect ratio of dividing cells in non-stretched (NS) and stretched (S) monolayers. (B) Box-whisker plots showing the change in cell aspect ratio (with respect to the direction of division) between division ($t = 0$) and post division ($t = 20$). Number of divisions is $n \geqslant 180$.

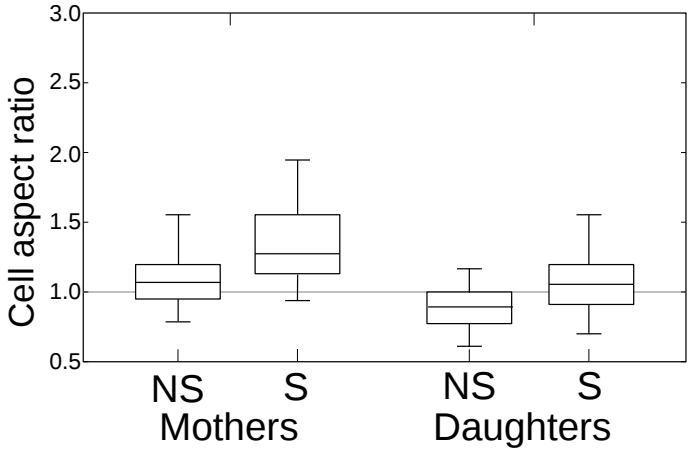

(A)

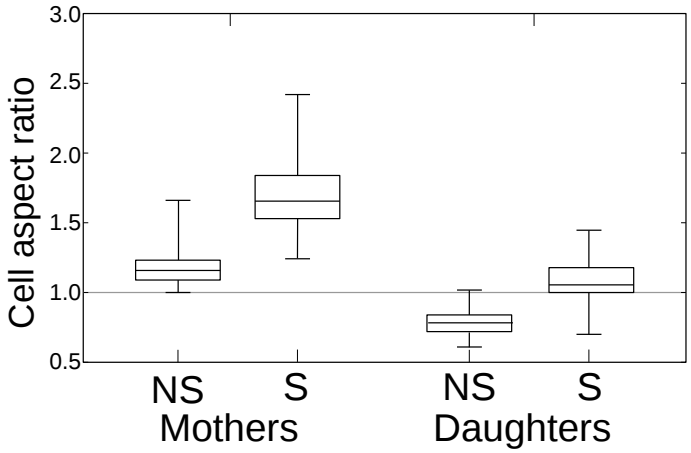

(B)

Fig. 6.11 Effects of stretch-induced oriented division in both experiments and simulations. (A) Aspect ratio (measured with respect to the direction of division) of stretched and non-stretched cells at 50 min before division (mothers) and 50 min after division (individual daughters) ($n \geqslant 35$ cells and $n = 3$ monolayers for each condition). (Top) Diagrams depict measurement taken. (B) Same as A, but in simulated monolayers ($n \geqslant 180$ divisions).

6.5.4 Effect of Oriented Divisions on Monolayer Stress

We first quantified the global changes in the tissue mean shear stress in both stretched and non-stretched monolayers (Figure 6.12 (A)). In stretched monolayers, a step decrease in monolayer stress at the division point was noticed, whereas in non-stretched monolayers, the change in tissue stress before and after division was insignificant.

Next, we compared the changes in monolayer stress induced by misoriented divisions (Figure 6.12 (B)). In non-stretched monolayers, either oriented divisions or misoriented divisions did not lead to significant changes in overall tissue stress, as expected under conditions of isotropic tissue growth. Conversely, in stretched monolayers, divisions oriented along the axis of stretch dissipated significantly more stress than misoriented divisions.

These data suggest that under extrinsic stretch, the orientation of cell division is critical and it contributes to the relaxation of global stresses. They explain how isotropic monolayer growth and the restoration of homoeostasis following a stretch can both be understood as emergent properties resulting from the simple ability of cells to orient their division along their interphase long axis.

6.6 Discussion

Animal tissues are mechanosensitive [93], but the physical parameters that control cells have not been defined. One of the typical biological examples is oriented cell division, which plays an important role in tissue morphogenesis [25] and tissue stress relaxation [20]. However, this process was not clearly explained. Firstly, the influence of tissue stress on morphological changes during cell division was unknown. Further, it is unclear if divisions respond to tension and/or cellular deformation, in a stretched monolayer. Finally, the effects of individual oriented divisions on tissue stress and homoeostasis remain unknown. These questions motivated us to carry out the research.

The reason for choosing suspended monolayers as an ideal system with which to begin exploring the mechanisms guiding the return to homoeostasis is that one can impose a well-controlled deformation, accurately measure the evolution of tissue-level forces, and track changes in cell shape. As the substrate was removed, monolayer-level forces were transmitted through cell–cell junctions. Further, cells did not change neighbours during the study of division. In our analysis, we chose experimental conditions under which cells were forced to elongate by a 30% strain in the direction of stretch. Consequently, monolayers experienced a tension of ~ 40 nN per cell. There are two cues that orient cell divisions: the

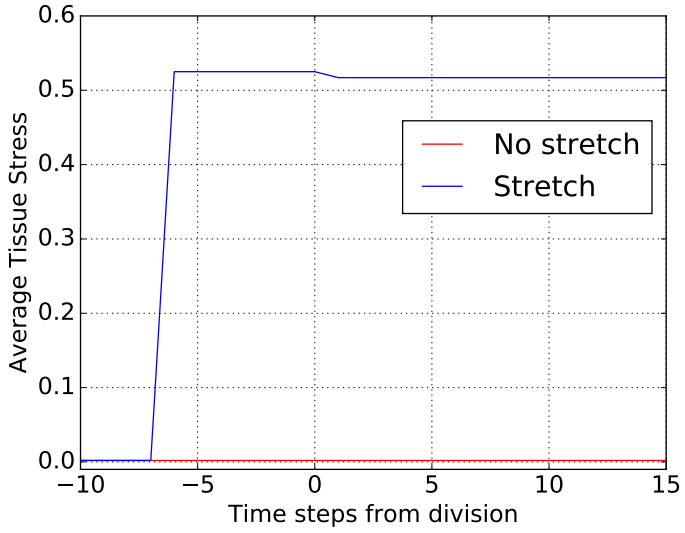

(A)

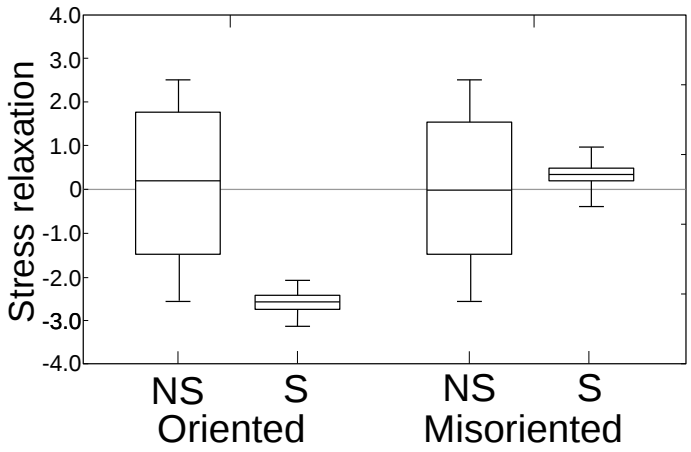

(B)

Fig. 6.12 The effect of oriented divisions on monolayer stress in the model. (A) Average monolayer stress at each time step during division period in non-stretched monolayers (red) and stretched monolayers (blue) (cell division at $t = 0$). (B) The change in monolayer stress caused by simulated divisions in stretched (S) and non-stretched (NS) monolayers in cases where the division is oriented with the cell shape orientation (oriented) or 90° from it (misoriented). The magnitude of stress relaxation given corresponds to 1% of the cells in the tissue dividing. ($n \geqslant 180$ divisions were examined).

tissue-scale tension and cellular-scale topological deformation. However, we suggest that topology dominates over stress in the control of division so that we observed that in most cases cell oriented in line with cell shape rather than tissue tension, although the two cues were identical.

Therefore, in the model, we assumed that cell divided along their long cell axis. When subjected to prolonged stretch, cells within monolayers elongated in proportion to the applied tissue stretch, oriented their long axes along the direction of extension, and underwent oriented divisions but not cell intercalation. Since we do not need to consider the changes in the third direction, our 2D mechanical model takes this advantage and by adjusting the parameters, it is able to faithfully replicate the observed changes in cell shape occurring during division. For instance, we set a high cell–cell friction to prevent cell rearrangement and increased the shear modulus of dividing cells to increase the cortical tension. Strikingly, simulations produced qualitatively and quantitatively similar changes in the aspect ratio of the spatial envelope of dividing cells observed experimentally in both stretched and control monolayers (a 29% and 34% increase in aspect ratio in stretched and non-stretched monolayers, respectively). Moreover, we calculated the reduction in average tissue stress per division in the simulated monolayer (Figure 6.12 (A)). After division, the average monolayer stress decreased by ~ 0.008 per cell per division in stretched monolayers, while in non-stretched ones there was no significant reduction in tissue stress. As we know that in stretched monolayers daughter cells recover cell shape, each oriented division in monolayers contributes to the dissipation of stress through redistribution and reintegration. The order of magnitude is determined by the stiffness of division cell and the total number of cells in the monolayer. We suggest that the change in tissue stress per division in oriented divisions is proportional to

$$\Delta\overline{\sigma} \propto \frac{G}{N}, \tag{6.5}$$

where G is the shear modulus of the division cell and N is the total number of cells in the tissue. In the simulation, we have $G = 2$ for the mother cell and $N = 256$ before division. Hence, the rate of stress dissipation is 0.0078 per cell per division.

Within both stretched and non-stretched monolayers, cell division redistributed cell mass along the long cell axis. This mass redistribution appeared to be triggered by the process of anaphase elongation, which led to the elongation and narrowing of the spatial envelope of the two daughter cells, compared to their mothers'. The model, incorporating only cell autonomous changes in the stiffness of division cells and cell division along the long interphase axis, was able to qualitatively and quantitatively reproduce the experimental observations,

suggesting that no mechanosensitive signalling was involved. However, simulations showed that the mass redistribution concomitant with each division led to the relaxation of stress when divisions were oriented along the axis of extension but not if they were misoriented (Figure 6.11). Importantly, these data suggest that there is a dialogue between intrinsic forces, which were generated during mitotic rounding and division, and tissue-scale forces. Thus, the forces generated upon entry into mitosis were sufficient to drive rounding, even if they were not large enough to generate cells with an isotropic shape in a tissue under tension. Then, upon exit from mitosis, as cells relaxed back in the epithelium, the tension in the tissue was sufficient to cause cells to partially elongate in the axis of tension, enabling oriented division to contribute to the restoration of normal cell packing and resting tension.

In addition, we have only applied two levels of tissue strain in the model. With 0% strain which is the non-stretched case, cells did not change shapes, while with 30% strain cell oriented with the stress. This implies that there might exist a transition between the two cases. The applied stretch is not restricted to these two levels. Simulations could be performed with different strain levels from 0% to 50% imposed on the tissue to explore how cell shape change is related to the applied stress. This suggests that higher stress causes larger cell shape disorder which results in more significant oriented divisions in the tissue.

6.7 Research Updates

The recent work by Bosveld et al. [15] shows that tricellular junctions (TCJs) in epithelial tissues are able to sense mechanical cues which orient the direction of cell division. In epithelial tissues, cell shapes depend on cell adhesion and cortical tension. When an extrinsic mechanical stress is applied, TCJ bipolarity and cell shape orientations are aligned in most elongated cells, thus accounting for orientation of divisions along the global stress axis. This behaviour is an important geometric feature of epithelial tissues. TCJs play a core role as sensors of cell shape and mechanical strain orientation which orient mitosis when the interphase cell shape is defined.

In our research, we have assumed that epithelial cells do not sense mechanical signals from the extrinsic forces, and the shape changes of individual cells entering mitosis are a simple consequence of the tissue-scale tension. Hence, as oriented division is a result of a combination of cell shape changes and the tendency to divide along long cell axis, we initialised that cell oriented their long axes along the direction of mechanical stress and underwent oriented divisions in the mechanical model. The work by Bosveld et al. [15] provides evidence of the interplay between intrinsic cellular-scale forces and the external

tissue-scale forces, and supports the initial assumptions in the model. Combining both studies, we could conclude that global mechanical perturbations induce oriented divisions which consequently dissipate extrinsic mechanical stresses.

Chapter 7

Conclusion

Introduction

At the beginning of the thesis, we asked how are the changes in the mechanical properties of tissues related to tissue deformations during active developmental processes, and how cells within the tissue behave when a local or global perturbation occurs. We focused on the mechanical interactions within living tissues throughout the thesis and used both experimental techniques and computational modelling to address these questions.

The magnetic tweezers have been used to probe the rheology in early zebrafish embryos between high stage and the onset of gastrulation. The tissue response to the applied force is modelled as viscoelastic. The embryo becomes stiffer and more viscous during this period of development, showing that a loose collection of cells becomes cohesive tissues. In this chapter, the main findings are discussed, followed by a discussion on possible directions of extension for this study in the future.

7.1 Main Results

7.1.1 The Instrument for Micromechanical Measurement in Living Embryos

A tetrapolar electromagnet was developed to probe the mechanical properties of embryonic tissues that are undergoing morphogenetic development. The device can apply a 3D remote force to an injected bead without disrupting the normal development of the embryo. This new design allocates sufficient space for the biological sample and the mounting chamber

and enables the device to accommodate different imaging systems, for instance, the bright field microscope for calibration and the LSFM microscope. The probe used for embryo manipulation is the superparamagnetic beads, which experience a magnetic force in a magnetic field induced by the electrical currents in the coils. 3D forces in the order of a few pica-newtons to nano-newtons can be generated on beads with diameters of 20 to 50 μm using different current configurations.

The most challenging part was the instrument calibration, aimed at establishing the relationship between the electrical currents in the coils and the resulting forces on the bead. Our approach was to select six basic current configurations which were able to move the bead in the directions of $\pm x$, $\pm y$ and $\pm z$. The force calibration process for each configuration combined experimental measurement and data regression modelling. Magnetic forces were measured by moving the bead in the calibrated viscous liquid and calculating the bead velocity at each sampling point within the imaging volume. These sampling trajectories were uniformly collected within the volume and the average distance between every two adjacent trajectories was 10 μm. The measured force data were learned by the multi-variate Gaussian Process regression model. Based on the information provided by the measurement, the model established a relationship between the positions in the imaging volume and the corresponding 3D magnetic force vector for each configuration.

Nevertheless, the relationship between the current and the forces was not fully established. We could add new variates in the Gaussian Process model such as the four currents. Since non-parametric learning algorithms require a large amount of data, we have to measure forces for a large number of configurations. However, this is very time-consuming. More variates in the model may influence the accuracy of the prediction results. An analytical approach is discussed in Section 7.5.2.

7.1.2 Characterisation of Local Rheology in Early-stage Embryonic Tissues

The magnetic tweezers were used to probe the mechanical properties of zebrafish embryos during the late blastula stages when the first morphogenetic transformations occurred after the intense period of cleavage. It was observed that the embryo transformed from an elliptical shape to a spherical shape. A constant force was applied to the grafted bead. The displacement curves were consistent with a simple rheological model, showing that the tissue is viscoelastic. The model suggests that the tissue consists of two mechanical components, a soft viscoelastic component representing the cytoskeleton and a more viscous component

describing the cell–cell adhesion. The results show that the embryo becomes stiffer and more viscous during this period of development.

Experiments were also performed with mutants in which the corresponding expressions of cellular properties were blocked. Results suggest that during early embryogenesis, cells become motile and induce a change of the embryo shape. Furthermore, these morphogenetic movements occurred between high stage and the onset of gastrulation in WT embryos are under the control of cell motility via the actomyosin network, through the activities of Rac1 and Rho-kinase, and cell–cell adhesion through E-Cadherin activity.

In the experiment, the magnitude of the applied force was constant. Although the rheological model indicates that the tissue is viscoelastic, the linearity with forces remains unknown. Forces in different orders of magnitudes can be applied to test how the tissues behave with a varying force. Besides, forces in different directions can be applied to examine whether the embryo mechanical property is isotropic.

7.1.3 Local Cell Stress Disorder in Response to External Perturbations

A significant mismatch between the experimental curves and the modelling curves was noticed from ~ 60 sec after the current was switched off. The experimental curves had a long and slow secondary relaxation. A mechanical model was used to investigate this mismatch, since it provided a larger-scale system to predict viscoelastic tissue behaviours by simply varying the control parameters. An external force was applied to one of the cells in the tissue as the probe. The cell was pulled to slide through its neighbours. The displacement curve in the simulation was qualitatively similar to the experimental curve. This result has further verified the viscoelastic property of the embryonic cells.

We suggested that the secondary relaxation was induced by the stress disorder in local cells caused by the bead creep. The simulation results show that the bead displacement during the secondary relaxation is correlated with the bead creep distance. The secondary relaxation is a result of cell intercalation and is controlled by the characteristic time constant of the system. The patterns of local cell stress during the creep indicate that the main stress experienced by the cells in the direction of the applied force is elastic stress, while for the cells on both sides of the bead the main stress is shear stress. The response of the early-stage embryo to the local perturbation demonstrates the mechanical characteristics of history dependent materials.

7.1.4 Oriented Cell Division Contributes to Tissue Stress Relaxation

The regulation and function of cell division orientation in animal tissues were investigated through both experiments and computational modelling. Results show that cell division is aligned better with long, interphase cell axis than with the monolayer stress axis. This phenomenon, combined with the alignment of cellular long axes induced by the stretch, results in a global bias in the orientation of divisions in the direction of tissue extension. In addition, the mass redistribution concomitant with each division leads to a process of tissue stress relaxation when divisions are oriented along the axis of extension, but not if they are misoriented. Thus, when oriented across a monolayer, divisions act collectively to redistribute mass along the axis of the stretch, helping to return the monolayer to its resting state. Importantly, as the application of a stretch naturally results in changes in the shape of cells and in their elongation along the stretch axis, tissue relaxation in the monolayer is an emergent property of the propensity of cells to divide along their interphase long axis. It does not require that cells read and interpret other mechanical cues.

7.2 Implications and Future Work

The two key techniques used in the thesis are the magnetic tweezers and the mechanical model. The magnetic device allows us to probe the rheology in living tissues, and the model can be used to complement these experiments and to help to tease out the mechanical processes driving morphogenesis. Based on these main findings, we formulate new hypotheses and discuss the main directions for future work to test them.

7.2.1 Frequency Sweeps Test

In the experiment, we used a constant force to investigate the evolution of the mechanical properties of the zebrafish embryos during development. DC currents were applied to the coils to generate a stable magnetic field that does not change with time. Although the experimental data fitted a linear rheological model, whether the tissue properties are linear was unclear.

To further examine the cytoskeletal plasticity and passive cell intercalation, frequency sweeps test can be carried out by generating sequences of force oscillations at frequencies ranging from 1 mHz to 10 Hz. This can be realised by applying AC currents at different frequencies to the coils. As a result, the force on the bead changes both its magnitude and direction. Bead displacement can be measured and fitted to suitable rheological models.

As introduced in Chapter 2, the strain of the spring changes instantaneously with the applied stress, while for the dashpot the strain rate changes rapidly with the applied stress. It illustrates that the elastic deformation of the material changes consistently with the force and the viscous deformation lags the change in the applied force. Hence, the frequency sweeps test allows us to investigate the viscoelastic properties from the tissue deformation in response to the varying forces. However, the test is restricted to three factors: the capability of the power supply, the imaging frame rate of the camera and the heat generated by the eddy current. AC currents applied to four coils require a multi-channel AC current supply. The imaging frame rate should be higher than the frequency of the current to detect the changes in the magnitude. Moreover, a changing magnetic field in the coil induces eddy currents which generate heat rapidly. These factors should be carefully assessed when the frequency sweep test is designed.

7.2.2 Magnetic Force Calibration

To realise the frequency sweeps test, it is necessary to calibrate magnetic forces for a varying current configuration. The ultimate goal of the calibration is to establish the relationship between the current in the coils and the resulting force on the magnetic bead. Currently, we have only calibrated a limited number of current configurations. Although the learning algorithm is capable of higher dimensional data interpolation, measuring forces for a large number of configurations is extremely time-consuming. Hence, one possible approach to link the current with the magnetic forces is to combine the magnetic circuit topology and the monopole force model.

The electrical current in the coil generates a magnetomotive force (MMF) which is the cause of the magnetic flux in the magnetic circuit. The MMF can be described by Hopkinson's law as:

$$\mathscr{F} = NI, \tag{7.1}$$

where N is the number of turns in the coil and I is the electrical current through the circuit. Hence, the reluctance of the circuit $\mathfrak{R}$ can be expressed by:

$$\mathfrak{R} = \frac{NI}{\Phi}, \tag{7.2}$$

where Φ is the magnetic flux.

Figure 7.1 shows a simplified model of the magnetic tweezers. The magnetic circuit is analogous to the electrical circuit, in which the MMFs are represented by voltage sources

and the reluctances of different parts of the magnetic paths are analogous to resistors. In this topology, the parasitic reluctances between every pair of circuit nodes are assumed to be negligible. Four coils are connected at the ends of the pole cores in a circle and encircle four return paths. R_f and R_p are the lumped reluctances of a quarter of the frames and a magnetic pole. R_a denotes the lumped reluctance from the tip of the pole to the bead in the air. In this case, the specimen space reluctance R_a dominate. The magnetic reluctance of an object is proportional to its length l_R and inversely proportional to its magnetic permeability μ, where $\mu = \mu_0\mu_R$, and the cross-sectional area A_R [112]:

$$\Re = \left(\frac{l_R}{\mu_0\mu_R A_R}\right). \tag{7.3}$$

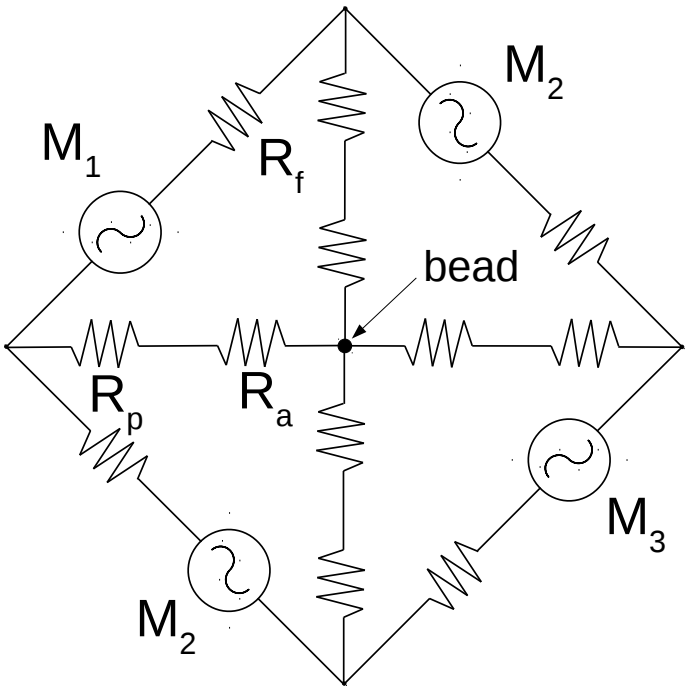

Fig. 7.1 Schematic diagram of magnetic paths of the magnetic tweezers analogous to the electrical circuit where the coils wrap around the flux return path segments. R_f is the flux return leg reluctance, R_p is the pole tip reluctance, and R_a is the reluctance of the gap between the pole tip and the bead. M_i is the magnetomotive forces in each coil.

Equation (7.3) allows us to estimate the values of these reluctances in the magnetic circuit from the geometry of the magnetic tweezers. By applying Kirchhoff's circuit laws [57], the relationship between the electrical current I in the coils and the flux through each pole Φ (the flux through R_p and R_a in each branch in the circuit) could be derived. In the monopole model, the magnetic force on the bead is determined by the values of the magnetic charges

q. Based on the measured force data, the correlation between the magnetic flux and the magnetic charges can be obtained. To summarise, the relationship between the electrical current and the resulting forces is established as:

$$I \longrightarrow \Phi \longrightarrow q \longrightarrow \mathbf{F}.$$

7.2.3 The Computational Model

The computational model enables us to investigate the patterning of the cellular movements under different boundary conditions. A few areas of extension for the model to make it applicable to a wider range of systems are briefly discussed.

First, the model can be developed to use finite boundaries rather than periodic, rectangular boundaries. For instance, in the experiment upon the zebrafish embryo, the embryo was fixed in the capillary and contacted with the capillary wall. The interactions within these boundaries should be taken into account.

Besides, the morphogenetic events during the embryo development are mainly in three dimensions. Although we only examined the bead displacement and cell shape changes in the *x*-*y* plane, the interactions in the third dimension is worth examining. To apply the model to studies of three-dimensional systems, we need to move the model entirely to 3D.

Above all, the mechanical parameters used in the model are homogeneous for all cells. The model could be modified to fit a heterogeneous system where cellular properties vary in the tissue. For instance, the cell–cell viscosity can be changed for different cell contact surfaces.

7.2.4 Patterning of the Zebrafish Forebrain Neural Plate

In the thesis, we have discussed the tissue rheology between high stage and the onset of gastrulation. Once gastrulation begins (from 5 hpf), more complex morphogenetic movements take place in the zebrafish embryo. Tissues begin to autonomously reshape by a combination of growth, cell shape changes, and cell intercalation, under the influence of the embryonic patterning system. The mechanism of local tissue activities and long-range mechanical interactions in these patterns remained a challenge.

In Section 1.3.3, we have introduced a study which used tissue tectonics techniques to characterise the morphogenetic patterning of the forebrain neural plate during the development of the brain [29, 79, 111]. The shape and the structure of the forebrain are complex. In

the zebrafish forebrain, the anterior neural plate (ANP) contracts and thickens during gastrulation by decreasing planar cell area. In lateral domains, the cell shape changes are isotropic but the extension is mediolateral, which could be interpreted as passive cell rearrangement induced by the cell shape changes caused by active contractions within the plane of the tissue. We suggest that these changes might be a consequence of the anisotropy of the boundary conditions; laterally connected to similar contracting neural tissues but anteriorly bounded with non-neural ectoderm that might be relatively soft and deformable (Figure 7.2).

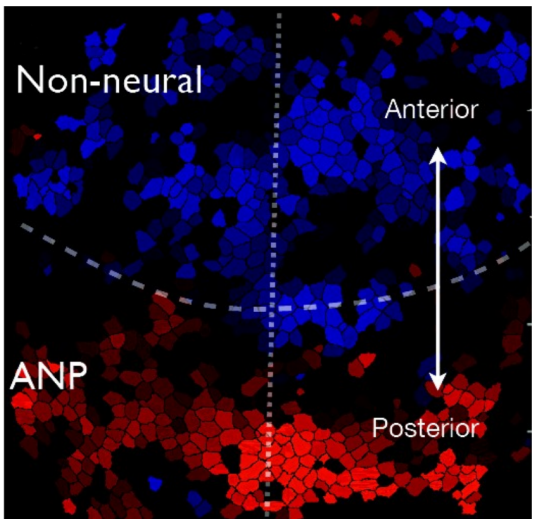

Fig. 7.2 Spatial patterning of the neural ectoderm. Timing: 8 hpf. The colour code quantifies the rate of cell area change: blue = increase, red = decrease. The image is taken from Young et al. [111].

To verify this hypothesis, direct measurement is required. Experiments can be carried out to implant beads in various regions to construct a map of mechanical properties in the forebrain neural plate. We will examine cell deformations caused by the magnetic bead to see if they induce similar cell rearrangement rates to those observed during forebrain formation. This will validate the hypothesis of passive intercalation. In addition, the mechanical properties of the non-neural ectoderm are measured to see if it is softer than the neural tissues.

References

[1] Alberts, B., Bray, D., Hopkin, K., Johnson, A., Lewis, J., Raff, M., Roberts, K., and Walter, P. (2013). *Essential cell biology*. Garland Science.

[2] Alberts, B., Johnson, A., Lewis, J., Raff, M., Roberts, K., and Walter, P. (2002). *Molecular biology of cells*. Garland Science.

[3] Amblard, F., Yurke, B., Pargellis, A., and Leibler, S. (1996). A magnetic manipulator for studying local rheology and micromechanical properties of biological systems. *Review of Scientific Instruments*, 67(3):818–827.

[4] Ashkin, A., Dziedzic, J., Bjorkholm, J., and Chu, S. (1986). Observation of a single-beam gradient force optical trap for dielectric particles. *Optics letters*, 11(5):288–290.

[5] Baena-López, L. A., Baonza, A., and García-Bellido, A. (2005). The orientation of cell divisions determines the shape of *Drosophila* organs. *Current biology*, 15(18):1640–1644.

[6] Balanis, C. A. (2012). *Advanced engineering electromagnetics*. John Wiley & Sons.

[7] Batchelor, G. K. (2000). *An introduction to fluid dynamics*. Cambridge university press.

[8] Beysens, D., Forgacs, G., and Glazier, J. (2000). Embryonic tissues are viscoelastic materials. *Canadian Journal of Physics*, 78(3):243–251.

[9] Binnig, G., Quate, C. F., and Gerber, C. (1986). Atomic force microscope. *Physical review letters*, 56(9):930.

[10] Blanchard, G. B., Kabla, A. J., Schultz, N. L., Butler, L. C., Sanson, B., Gorfinkiel, N., Mahadevan, L., and Adams, R. J. (2009). Tissue tectonics: morphogenetic strain rates, cell shape change and intercalation. *Nature Methods*, 6(6):458–464.

[11] Boal, D. and Boal, D. H. (2012). *Mechanics of the Cell*. Cambridge University Press.

[12] Bock, M., Tyagi, A. K., Kreft, J.-U., and Alt, W. (2010). Generalized Voronoi tessellation as a model of two-dimensional cell tissue dynamics. *Bulletin of mathematical biology*, 72(7):1696–1731.

[13] Bonnet, I., Marcq, P., Bosveld, F., Fetler, L., Bellaïche, Y., and Graner, F. (2012). Mechanical state, material properties and continuous description of an epithelial tissue. *Journal of The Royal Society Interface*, 9(75):2614–2623.

[14] Bosveld, F., Bonnet, I., Guirao, B., Tlili, S., Wang, Z., Petitalot, A., Marchand, R., Bardet, P.-L., Marcq, P., Graner, F., et al. (2012). Mechanical control of morphogenesis by Fat/Dachsous/Four-jointed planar cell polarity pathway. *Science*, 336(6082):724–727.

[15] Bosveld, F., Markova, O., Guirao, B., Martin, C., Wang, Z., Pierre, A., Balakireva, M., Gaugue, I., Ainslie, A., Christophorou, N., et al. (2016). Epithelial tricellular junctions act as interphase cell shape sensors to orient mitosis. *Nature*.

[16] Bourguignon, L. Y., Zhu, H., Shao, L., Zhu, D., and Chen, Y.-W. (1999). Rho-kinase (ROK) promotes CD44v3, 8–10-ankyrin interaction and tumor cell migration in metastatic breast cancer cells. *Cell motility and the cytoskeleton*, 43(4):269–287.

[17] Bray, D. (2001). *Cell movements: from molecules to motility*. Garland Science.

[18] Brodland, G. W. and Veldhuis, J. H. (2002). Computer simulations of mitosis and interdependencies between mitosis orientation, cell shape and epithelia reshaping. *Journal of biomechanics*, 35(5):673–681.

[19] Campàs, O., Mammoto, T., Hasso, S., Sperling, R. A., O'Connell, D., Bischof, A. G., Maas, R., Weitz, D. A., Mahadevan, L., and Ingber, D. E. (2014). Quantifying cell-

generated mechanical forces within living embryonic tissues. *Nature methods*, 11(2):183–189.

[20] Campinho, P., Behrndt, M., Ranft, J., Risler, T., Minc, N., and Heisenberg, C.-P. (2013). Tension-oriented cell divisions limit anisotropic tissue tension in epithelial spreading during zebrafish epiboly. *Nature cell biology*, 15(12):1405–1414.

[21] Cetl, G. (2009). The Cell Cycle, Mitosis and Meiosis. *The Cell Cycle*.

[22] Chassot, M. (2009). *Magnetic Field Optimization From Limited Data*. PhD thesis, Master Thesis. University of Edinburg.

[23] Chen, X. (2007). *Multiscale modeling of Amphibian neurulation*. PhD thesis, University of Waterloo.

[24] Chmielewski, A. K., Kyrsting, A., Mahou, P., Wayland, M. T., Muresan, L., Evers, J. F., and Kaminski, C. F. (2015). Fast imaging of live organisms with sculpted light sheets. *Scientific reports*, 5.

[25] da Silva, S. M. and Vincent, J.-P. (2007). Oriented cell divisions in the extending germband of *Drosophila*. *Development*, 134(17):3049–3054.

[26] Dao, M., Lim, C. T., and Suresh, S. (2003). Mechanics of the human red blood cell deformed by optical tweezers. *Journal of the Mechanics and Physics of Solids*, 51(11):2259–2280.

[27] Ebarasi, L., Oddsson, A., Hultenby, K., Betsholtz, C., and Tryggvason, K. (2011). Zebrafish: a model system for the study of vertebrate renal development, function, and pathophysiology. *Current opinion in nephrology and hypertension*, 20(4):416–424.

[28] Efunda (2016). Centroid, area, moments of inertia, polar moments of inertia and radius of gyration of a half circle. *URL: http://www.efunda.com/math/areas/CircleHalf.cfm*.

[29] England, S. J., Blanchard, G. B., Mahadevan, L., and Adams, R. J. (2006). A dynamic fate map of the forebrain shows how vertebrate eyes form and explains two causes of cyclopia. *Development*, 133(23):4613–4617.

[30] Etournay, R., Merkel, M., Popović, M., Brandl, H., Dye, N. A., Aigouy, B., Salbreux, G., Eaton, S., and Jülicher, F. (2016). Tissueminer: A multiscale analysis toolkit to quantify how cellular processes create tissue dynamics. *Elife*, 5:e14334.

[31] Etournay, R., Popović, M., Merkel, M., Nandi, A., Blasse, C., Aigouy, B., Brandl, H., Myers, G., Salbreux, G., Jülicher, F., et al. (2015). Interplay of cell dynamics and epithelial tension during morphogenesis of the drosophila pupal wing. *Elife*, 4:e07090.

[32] Evans, E. and Yeung, A. (1989). Apparent viscosity and cortical tension of blood granulocytes determined by micropipet aspiration. *Biophysical journal*, 56(1):151.

[33] Every, A. (1994). Displacement field of a point force acting on the surface of an elastically anisotropic half-space. *Journal of Physics A: Mathematical and General*, 27(23):7905.

[34] Fink, J., Carpi, N., Betz, T., Bétard, A., Chebah, M., Azioune, A., Bornens, M., Sykes, C., Fetler, L., Cuvelier, D., et al. (2011). External forces control mitotic spindle positioning. *Nature cell biology*, 13(7):771–778.

[35] Fisher, J., Cummings, J., Desai, K., Vicci, L., Wilde, B., Keller, K., Weigle, C., Bishop, G., Taylor II, R., Davis, C., et al. (2005). Three-dimensional force microscope: a nanometric optical tracking and magnetic manipulation system for the biomedical sciences. *Review of scientific instruments*, 76(5):053711.

[36] Fisher, J. K., Cribb, J., Desai, K. V., Vicci, L., Wilde, B., Keller, K., Taylor II, R., Haase, J., Bloom, K., O'Brien, E. T., et al. (2006). Thin-foil magnetic force system for high-numerical-aperture microscopy. *Review of Scientific Instruments*, 77(2):023702.

[37] Forgacs, G., Foty, R. A., Shafrir, Y., and Steinberg, M. S. (1998). Viscoelastic properties of living embryonic tissues: a quantitative study. *Biophysical journal*, 74(5):2227–2234.

[38] Gibson, M. C., Patel, A. B., Nagpal, R., and Perrimon, N. (2006). The emergence of geometric order in proliferating metazoan epithelia. *Nature*, 442(7106):1038–1041.

[39] Gibson, W. T., Veldhuis, J. H., Rubinstein, B., Cartwright, H. N., Perrimon, N., Brodland, G. W., Nagpal, R., and Gibson, M. C. (2011). Control of the mitotic cleavage plane by local epithelial topology. *Cell*, 144(3):427–438.

[40] Guevorkian, K., Gonzalez-Rodriguez, D., Carlier, C., Dufour, S., and Brochard-Wyart, F. (2011). Mechanosensitive shivering of model tissues under controlled aspiration. *Proceedings of the National Academy of Sciences*, 108(33):13387–13392.

[41] Guirao, B., Rigaud, S. U., Bosveld, F., Bailles, A., Lopez-Gay, J., Ishihara, S., Sugimura, K., Graner, F., and Bellaïche, Y. (2015). Unified quantitative characterization of epithelial tissue development. *Elife*, 4:e08519.

[42] Hardin, J. (2005). Images and movies to enhance understanding of animal development. *URL: http://worms.zoology.wisc.edu/dd2/echino/gast/morph/morph.html*.

[43] Harris, A. R., Peter, L., Bellis, J., Baum, B., Kabla, A. J., and Charras, G. T. (2012). Characterizing the mechanics of cultured cell monolayers. *Proceedings of the National Academy of Sciences*, 109(41):16449–16454.

[44] Henon, S., Lenormand, G., Richert, A., and Gallet, F. (1999). A new determination of the shear modulus of the human erythrocyte membrane using optical tweezers. *Biophysical journal*, 76(2):1145–1151.

[45] Hertwig, O. (1983). About the value of the first cleavage for the organisation of the embryo: experimental studies on frog and triton eggs. *Arch. Mikr. Anat*, 35(xlii):66–807.

[46] Hochmuth, R. M. (2000). Micropipette aspiration of living cells. *Journal of biomechanics*, 33(1):15–22.

[47] Huskins, C. L. (1933). Mitosis and meiosis. *Nature*, 132:62–63.

[48] Jackson, J. D. (1999). *Classical electrodynamics*. Wiley.

[49] Jennings, J. N. (2014). *A new computational model for multi-cellular biological systems*. PhD thesis, University of Cambridge.

[50] Keller, R., Shook, D., and Skoglund, P. (2008). The forces that shape embryos: physical aspects of convergent extension by cell intercalation. *Physical biology*, 5(1):015007.

[51] Kimmel, C. B., Ballard, W. W., Kimmel, S. R., Ullmann, B., and Schilling, T. F. (1995). Stages of embryonic development of the zebrafish. *Developmental dynamics*, 203(3):253–310.

[52] Kunda, P. and Baum, B. (2009). The actin cytoskeleton in spindle assembly and positioning. *Trends in cell biology*, 19(4):174–179.

[53] Landau, L. D. (2013). *The classical theory of fields*, volume 2. Elsevier.

[54] Lecuit, T., Lenne, P.-F., and Munro, E. (2011). Force generation, transmission, and integration during cell and tissue morphogenesis. *Annual review of cell and developmental biology*, 27:157–184.

[55] Lee, L. M. and Liu, A. P. (2014). The application of micropipette aspiration in molecular mechanics of single cells. *Journal of nanotechnology in engineering and medicine*, 5(4):040902.

[56] LeGoff, L., Rouault, H., and Lecuit, T. (2013). A global pattern of mechanical stress polarizes cell divisions and cell shape in the growing *Drosophila* wing disc. *Development*, 140(19):4051–4059.

[57] Li, W. and An, G. (2013). Application of Kirchhoff's Voltage Law in circuit analysis. *Electronic Science and Technology*, 7:042.

[58] Lin, F. (2011). Picture of zebrafish embryo development. *URL: http://www.linfishlab.webs.com/zebrafish.htm*.

[59] Lodish, H., Baltimore, D., Berk, A., Zipursky, S. L., Matsudaira, P., and Darnell, J. (1995). *Molecular cell biology*, volume 3. Scientific American Books New York.

[60] Luxenburg, C., Pasolli, H. A., Williams, S. E., and Fuchs, E. (2011). Developmental roles for Srf, cortical cytoskeleton and cell shape in epidermal spindle orientation. *Nature cell biology*, 13(3):203–214.

[61] MacKay, D. J. (2003). *Information theory, inference and learning algorithms*. Cambridge university press.

[62] Mao, Y., Tournier, A. L., Bates, P. A., Gale, J. E., Tapon, N., and Thompson, B. J. (2011). Planar polarization of the atypical myosin dachs orients cell divisions in *Drosophila*. *Genes & development*, 25(2):131–136.

[63] Martin, A. C., Gelbart, M., Fernandez-Gonzalez, R., Kaschube, M., and Wieschaus, E. F. (2010). Integration of contractile forces during tissue invagination. *The Journal of cell biology*, 188(5):735–749.

[64] Meyer, G. and Amer, N. M. (1988). Novel optical approach to atomic force microscopy. *Applied physics letters*, 53(12):1045–1047.

[65] Meyers, M. A. and Chawla, K. K. (2009). *Mechanical behavior of materials*, volume 2. Cambridge university press Cambridge.

[66] Moller, W., Nemoto, I., and Heyder, J. (2003). Effect of magnetic bead agglomeration on cytomagnetometric measurements. *IEEE transactions on nanobioscience*, 2(4):247–254.

[67] Moore, S. W., Keller, R. E., and Koehl, M. (1995). The dorsal involuting marginal zone stiffens anisotropically during its convergent extension in the gastrula of xenopus laevis. *Development*, 121(10):3131–3140.

[68] Muhamed, I., Wu, J., Sehgal, P., Kong, X., Tajik, A., Wang, N., and Leckband, D. E. (2016). E-Cadherin-mediated force transduction signals regulate global cell mechanics. *J Cell Sci*, 129(9):1843–1854.

[69] Neuman, K. C. and Nagy, A. (2008). Single-molecule force spectroscopy: optical tweezers, magnetic tweezers and atomic force microscopy. *Nature methods*, 5(6):491.

[70] O'Connor, C. M., Adams, J. U., and Fairman, J. (2010). Essentials of cell biology. *Cambridge: NPG Education*.

[71] Overby, D. R., Matthews, B. D., Alsberg, E., and Ingber, D. E. (2005). Novel dynamic rheological behavior of individual focal adhesions measured within single cells using electromagnetic pulling cytometry. *Acta Biomaterialia*, 1(3):295–303.

[72] Özkaya, N., Nordin, M., Goldsheyder, D., and Leger, D. (2012). *Fundamentals of biomechanics: equilibrium, motion, and deformation*. Springer Science & Business Media.

[73] Pedregosa, F., Varoquaux, G., Gramfort, A., Michel, V., Thirion, B., Grisel, O., Blondel, M., Prettenhofer, P., Weiss, R., Dubourg, V., Vanderplas, J., Passos, A., Cournapeau, D., Brucher, M., Perrot, M., and Duchesnay, E. (2011). Scikit-learn: Machine learning in Python. *Journal of Machine Learning Research*, 12:2825–2830.

[74] Planus, E., Fodil, R., Balland, M., Isabey, D., et al. (2002). Assessment of mechanical properties of adherent living cells by bead micromanipulation: comparison of magnetic twisting cytometry vs optical tweezers. *Journal of biomechanical engineering*, 124(4):408–421.

[75] Puech, P.-H., Taubenberger, A., Ulrich, F., Krieg, M., Muller, D. J., and Heisenberg, C.-P. (2005). Measuring cell adhesion forces of primary gastrulating cells from zebrafish using atomic force microscopy. *Journal of cell science*, 118(18):4199–4206.

[76] Rappaport, R. (1961). Experiments concerning the cleavage stimulus in sand dollar eggs. *Journal of Experimental Zoology*, 148(1):81–89.

[77] Rasmussen, C. E. and Williams, C. K. I. (2006). *Gaussian processes for machine learning*. The MIT Press,.

[78] Rauzi, M. and Lenne, P.-F. (2011). 4 cortical forces in cell shape changes and tissue morphogenesis. *Current topics in developmental biology*, 95:93.

[79] Rembold, M., Loosli, F., Adams, R. J., and Wittbrodt, J. (2006). Individual cell migration serves as the driving force for optic vesicle evagination. *Science*, 313(5790):1130–1134.

[80] Reynaud, E. G., Peychl, J., Huisken, J., and Tomancak, P. (2015). Guide to light-sheet microscopy for adventurous biologists. *Nature methods*, 12(1):30–34.

[81] Roylance, D. (2001). Engineering viscoelasticity. *Department of Materials Science and Engineering–Massachusetts Institute of Technology, Cambridge MA*, 2139:1–37.

[82] Sadd, M. H. (2014). *Elasticity: theory, applications, and numerics*. Academic Press.

[83] Santi, P. A. (2011). Light sheet fluorescence microscopy a review. *Journal of Histochemistry & Cytochemistry*, 59(2):129–138.

[84] Santner, T. J., Williams, B. J., and Notz, W. I. (2013). *The design and analysis of computer experiments*. Springer Science & Business Media.

[85] Savin, T., Shyer, A. E., and Mahadevan, L. (2012). A method for tensile tests of biological tissues at the mesoscale. *Journal of Applied Physics*, 111(7):074704.

[86] Sekimura, T., Noji, S., Ueno, N., and Maini, P. (2003). *Morphogenesis and pattern formation in biological systems*. Springer.

[87] Selchow, O. and Huisken, J. (2013). Light sheet fluorescence microscopy and revolutionary 3D analyses of live specimens. *BioPhotonik*.

[88] Shigehito Yamada, Mark Hill, T. T. (2015-10-21). Human embryology. *New Discoveries in Embryology*.

[89] Shivakumar, P. C. and Lenne, P.-F. (2016). Laser ablation to probe the epithelial mechanics in *Drosophila*. *Drosophila: Methods and Protocols*, pages 241–251.

[90] Solnica-Krezel, L. and Driever, W. (1994). Microtubule arrays of the zebrafish yolk cell: organization and function during epiboly. *Development*, 120(9):2443–2455.

[91] Steinberg, M. and Poole, T. (1982). Liquid behavior of embryonic tissues. *Cell behavior*, pages 583–607.

[92] Stewart, M. P., Helenius, J., Toyoda, Y., Ramanathan, S. P., Muller, D. J., and Hyman, A. A. (2011). Hydrostatic pressure and the actomyosin cortex drive mitotic cell rounding. *Nature*, 469(7329):226–230.

[93] Streichan, S. J., Hoerner, C. R., Schneidt, T., Holzer, D., and Hufnagel, L. (2014). Spatial constraints control cell proliferation in tissues. *Proceedings of the National Academy of Sciences*, 111(15):5586–5591.

[94] Sumner, A. T. (2008). Mitosis, Meiosis and the Cell Cycle. *Chromosomes: Organization and Function*, pages 5–23.

[95] Sun, Y., Duthaler, S., and Nelson, B. J. (2005). Autofocusing algorithm selection in computer microscopy. In *2005 IEEE/RSJ International Conference on Intelligent Robots and Systems*, pages 70–76. IEEE.

[96] Tanase, M., Biais, N., and Sheetz, M. (2007). Magnetic tweezers in cell biology. *Methods in cell biology*, 83:473–493.

[97] Thomson, J. J. (1904). On the structure of the atom: an investigation of the stability and periods of oscillation of a number of corpuscles arranged at equal intervals around the circumference of a circle; with application of the results to the theory of atomic structure. *The London, Edinburgh, and Dublin Philosophical Magazine and Journal of Science*, 7(39):237–265.

[98] Tofallis, C. (2015). A better measure of relative prediction accuracy for model selection and model estimation. *Journal of the Operational Research Society*, 66(8):1352–1362.

[99] Ulrich, F. and Heisenberg, C.-P. (2008). Probing E-cadherin endocytosis by morpholino-mediated Rab5 knockdown in zebrafish. *Exocytosis and Endocytosis*, pages 371–387.

[100] Vicci, L. (2001). A 3D magnetic force manipulator dc prototype. *UNC Chapel Hill Dept. Comp. Sci. Tech. Rep*.

[101] Vicci, L. (2003). Analytical bead force model for the 3DFM. Technical report, UNC Technical Report TR03-029.

[102] Vincent, O. and Folorunso, O. (2009). A descriptive algorithm for sobel image edge detection. In *Proceedings of Informing Science & IT Education Conference (InSITE)*, pages 97–107.

[103] Wahlström, N., Kok, M., Schön, T. B., and Gustafsson, F. (2013). Modeling magnetic fields using Gaussian processes. In *2013 IEEE International Conference on Acoustics, Speech and Signal Processing*, pages 3522–3526. IEEE.

[104] Wallingford, J. B., Fraser, S. E., and Harland, R. M. (2002). Convergent extension: the molecular control of polarized cell movement during embryonic development. *Developmental cell*, 2(6):695–706.

[105] Wang, N., Butler, J. P., Ingber, D. E., et al. (1993). Mechanotransduction across the cell surface and through the cytoskeleton. *Science*, 260(5111):1124–1127.

[106] Welch, W. J., Buck, R. J., Sacks, J., Wynn, H. P., Mitchell, T. J., and Morris, M. D. (1992). Screening, predicting, and computer experiments. *Technometrics*, 34(1):15–25.

[107] Wiebe, C. and Brodland, G. W. (2005). Tensile properties of embryonic epithelia measured using a novel instrument. *Journal of biomechanics*, 38(10):2087–2094.

[108] Williams, D. A., Tao, W., Yang, F., Kim, C., Gu, Y., Mansfield, P., Levine, J. E., Petryniak, B., Derrow, C. W., Harris, C., et al. (2000). Dominant negative mutation of the hematopoietic-specific Rho GTPase, Rac2, is associated with a human phagocyte immunodeficiency. *Blood*, 96(5):1646–1654.

[109] Wu, Y., Liu, K., Song, K., and Pan, S. (2011). Three powerful research tools from single cells into single molecules: AFM, laser tweezers, and Raman spectroscopy. *Applied biochemistry and biotechnology*, 165(2):485–496.

[110] Wyatt, T. P., Harris, A. R., Lam, M., Cheng, Q., Bellis, J., Dimitracopoulos, A., Kabla, A. J., Charras, G. T., and Baum, B. (2015). Emergence of homeostatic epithelial packing

and stress dissipation through divisions oriented along the long cell axis. *Proceedings of the National Academy of Sciences*, 112(18):5726–5731.

[111] Young, S., Jennings, J. N., Blanchard, G. B., Kabla, A. J., and Adams, R. (2015). Tissue dynamics of the forebrain neural plate. *bioRxiv*, page 016303.

[112] Zhang, Z., Huang, K., and Menq, C.-H. (2010). Design, implementation, and force modeling of quadrupole magnetic tweezers. *IEEE/ASME Transactions on Mechatronics*, 15(5):704–713.